On the Development of Scaffolds for Bone Tissue Engineering

Conor Timothy Buckley, B.A., B.A.I.

A thesis submitted to the University of Dublin in partial fulfilment of the requirements for the degree of

Doctor in Philosophy

School of Engineering

Trinity College Dublin

Ireland

September 2007

Supervisor

Dr. Kevin U. O'Kelly

External Examiner

Prof. Brian J. Meenan

Internal Examiner

Dr. Garret E. O'Donnell

Declaration

I declare that I am the sole author of this thesis and that all the work presented in it, unless otherwise referenced, is my own. I also declare that this work has not been submitted, in whole or in part, to any other university or college for any degree or other qualification.

I authorise the library of Trinity College Dublin to lend and copy this thesis.

Conor Buckley

September, 2007

"To see a world in a grain of sand

And a heaven in a wild flower

Hold infinity in the palm of your hand

And eternity in an hour"

- William Blake

Table of Contents

Declaration i

Contents iii

List of Figures ix

List of Tables xvii

Nomenclature & Abbreviations xx

Acknowledgements xxiv

Publications and presentations resulting from this study xxvi

Abstract xxviii

1 Introduction 1

1.1 Bone grafting and bone implants 1

1.2 Future advancement of scaffold based tissue engineering for 21st century medicine 3

1.2.1 Current scaffold limitations 4

1.3 Focus of present investigation 6

2 Literature Review 8

2.1 Anatomy of bone 9

2.1.1 Structure 9

2.1.2 Matrix of bone 9

2.1.3 Bone formation 10

2.2 Current tissue engineering strategies 11

2.2.1 Implant material criteria 13

2.3 Biomaterials 15

2.3.1 Introduction 15
2.3.2 Commonly employed biomaterials 16
2.4 Scaffold properties 18
2.4.1 Porosity 18
2.4.2 Microporosity 20
2.4.3 Pore size 22
2.4.4 Interconnectivity 26
2.4.5 Surface characteristics and cell surface engagement 28
2.5 Scaffold architectures 31
2.5.1 Introduction 31
2.5.2 Single random porous domain scaffolds 31
2.5.3 Single regular porous domain scaffolds 34
2.5.4 Multi-domain porous scaffolds 36
2.6 Traditional scaffold fabrication techniques 39
2.7 Solid free form (SFF) fabrication technologies 41
2.8 Fluid conductance and permeability 43
2.9 Cell seeding 47
2.9.1 Static cell seeding 47
2.9.2 Dynamic cell seeding and culturing 47
2.10 *In vivo* assessment of scaffolds 51
2.10.1 Single random porous domain scaffolds 51
2.10.2 Single regular porous domain scaffolds 55
2.10.3 Multi-domain porous scaffolds 58
2.11 *In vivo* environments: diffusion and cellular consumption of nutrients 61
2.11.1 Introduction 61
2.11.2 *In vivo* nutrient environment 62
2.11.3 Theoretical numerical modelling 66
2.11.4 Cellular consumption 69
2.12 Chapter summary 70

3 Materials & Methods **73**

3.1 Introduction 74

3.2 Elastomeric polymer based scaffolds 76

3.2.1 Poly(dimethylsiloxane) (PDMS) scaffold fabrication 76

3.2.2 Chemical surface treatments 78

3.2.3 Contact angle measurements 79

3.2.4 Cell seeding of PDMS substrates 81

3.2.5 Poly(1,12-dodecanediol-co-citric acid) (PDDC) scaffolds 82

3.2.6 Polymer synthesis 82

3.2.7 PDDC scaffold fabrication 83

3.2.8 PDDC scaffold pore morphology 84

3.2.9 Tensile mechanical properties 86

3.2.10 Summary of elastomeric scaffolds 87

3.3 Hydroxyapatite ceramic scaffold processing 89

3.3.1 Starting materials for foamed slip and freeze-drying methods . 90

3.3.2 Fabrication of flat HA substrates 90

3.3.3 Mould design using rapid-prototyping 91

3.3.4 Preparation of porous ceramic scaffold- foamed slip method . 93

3.3.5 Preparation of porous ceramic scaffold- freeze-drying method . 93

3.3.6 Wax infiltration 96

3.3.7 Introduction of a parallel macro-channel array 97

3.3.8 Wax removal and sintering regime 99

3.4 Anorganic bone matrix preparation 100

3.5 Determination of scaffold properties 101

3.5.1 Determination of effective diffusion coefficient 101

3.5.2 Direct permeability analysis 104

3.5.3 Fluid retention properties 106

3.5.4 Embedding of scaffold samples in JB-4 Plus® glycol methacrylate 106

3.5.5 Scanning electron microscopy (SEM) . . . 107
3.5.6 Pore size analysis . . . 108
3.5.7 Determination of porosity . . . 108
3.5.8 Mechanical properties . . . 109
3.6 Preparation and Procedures for Cell Culture . . . 110
3.6.1 Material sterility . . . 110
3.6.2 Sterilisation procedure - Equipment . . . 110
3.6.3 Sterilisation procedure - Reagents . . . 111
3.6.4 Culture environment . . . 111
3.6.5 MC3T3-E1 cell culture . . . 111
3.6.6 Cell passaging . . . 112
3.6.7 2D Time-dependent cell attachment . . . 112
3.6.8 Static cell seeding of scaffolds . . . 113
3.6.9 Dynamic rotational cell seeding of scaffolds . . . 114
3.6.10 XTT cell proliferation and viability assay- standard curve . . . 115
3.6.11 XTT cell proliferation and viability assay- 2D and 3D . . . 116
XTT correction factor . . . 116
3.6.12 DNA quantification using Hoechst 33258- standard curve . . . 117
3.6.13 Cell digestion and DNA assay- HA scaffold . . . 118
3.6.14 Cell seeding suspension volume dependency . . . 118
3.6.15 Examination of cell proliferation-2D . . . 119
3.6.16 MTT assay . . . 119
3.6.17 Static and dynamic culturing of HA scaffolds . . . 120
3.6.18 Examination of cellular oxygen consumption . . . 120
3.7 Finite element modelling of *in vitro* oxygen concentration profiles . . . 123
3.7.1 Initial and boundary conditions . . . 124
3.7.2 Numerical methods . . . 125
3.8 Statistical and error analysis . . . 126

4 Results **128**

4.1 Introduction 129

4.2 Characterisation of scaffold properties 129

4.2.1 Scaffold and pore architecture 129

4.2.2 Pore size analysis 138

4.2.3 Determination of porosity 147

4.2.4 Determination of effective diffusion coefficient 149

4.2.5 Direct permeability analysis 151

4.2.6 Mechanical properties 154

4.2.7 Fluid retention properties 159

4.3 Cellular response to HA scaffolds and substrates 160

4.3.1 XTT correction factor 160

4.3.2 2D Time-dependent cell attachment 162

4.3.3 Examination of cell proliferation-2D 163

4.3.4 Static cell seeding of 3D scaffolds 165

4.3.5 Dynamic rotational cell seeding of scaffolds 171

4.3.6 Static and dynamic rotational culturing of scaffolds- Examination of cell distribution 173

4.3.7 Static and dynamic rotational culturing of scaffolds- Examination of cell proliferation 179

4.3.8 Examination of cellular oxygen consumption 181

4.3.9 Summary of cellular response to hydroxyapatite scaffolds . . . 185

4.4 Finite element modelling of *in vitro* oxygen concentration profiles . . 186

4.4.1 Summary 198

5 Discussion **199**

5.1 Introduction 200

5.2 Scaffold fabrication and architecture 201

5.3 Permeability of scaffolds 205

5.4 Diffusion coefficients 208

5.5 Mechanical properties 210
5.6 Cell seeding 212
5.7 Dynamic vs. static culturing 216
5.8 Finite element modelling of *in vitro* oxygen concentration profiles . . 218

6 Conclusions and future work **224**
6.1 Summary of project 224
6.2 Future work 227

Bibliography **230**

Appendices **244**
A SEM micrographs of PDDC scaffolds 244
B Hydroxyapatite powder data 246
C CNC machining G-code 249
D Image analysis code 250
E Threshold images of HA scaffolds 255

List of Figures

1.1 Various cancellous bone architectures (adapted from Singh, 1978). . . 5

2.1 The anatomical structure of bone tissue (adapted from Martini, 2001). 10

2.2 Idealised tissue engineering approach. 12

2.3 Compressive strengths of porous HA ceramics. 20

2.4 Interconnected plate structures yielding 5-11 μm void openings within PLA material (Taboas *et al.*, 2003) 21

2.5 Water retention characteristics of porous β-TCP replicas of bovine cancellous bone (Tancred *et al.*, 1998a). 22

2.6 SEM images of porous HA implants post-implantation (Chang *et al.*, 2000). 24

2.7 Example of pore fenestration (Murphy *et al.*, 2002). 27

2.8 Single random porous domain scaffold architectures. 33

2.9 Single regular porous domain scaffold architectures. 35

2.10 Multi domain porous scaffold architectures. 37

2.11 Biphasic scaffold architectures (Taboas *et al.*, 2003). 43

2.12 Permeability values for various ceramic scaffolds (Li *et al.*, 2003). . . 45

2.13 Bioreactor devices used for cell seeding and *in vitro* culturing (adapted from Martin *et al.*, 2004). 49

2.14 Comparative MTT staining of ChronOS^{TM} porous ceramic scaffolds subjected to both perfusion and static seeding techniques (Wendt *et al.*, 2003). 50

2.15 Macromorphology of commercially available bone implant materials (Tadic and Epple, 2004) 52
2.16 SEM photomicrograph of the microstructure of a synthetic porous HA scaffold fabricated through foaming of a HA slurry (Dong *et al.*, 2001a). 54
2.17 Replicated β-TCP scaffold implanted in the alveolar ridge (Al-Souhail *et al.*, 2000) 55
2.18 Illustrations showing the designs for *in vivo* implantation (A) Radial channels specimen (B) Orthogonal channels specimen (Chu *et al.*, 2002). 56
2.19 SEM demonstrating signs of bone regeneration within HA regular architecture scaffolds fabricated through solid free-form fabrication (Chu *et al.*, 2002). 57
2.20 Images of HA scaffolds produced using the Theirform^{TM} process (adapted from Roy *et al.*, 2003). 59
2.21 Histology sections of a multi-domain porous HA scaffold (adapted from Roy *et al.*, 2003). 60
2.22 Percentage bone ingrowth in coronal sections as a function of defect area for the various scaffold implants (adapted from Simon *et al.*, 2003). 61
2.23 Conceptual illustration of the biological processes involved within and around a porous scaffold implanted *in vivo* (Muschler *et al.*, 2004). . . 62
2.24 Illustration of an idealised cell-scaffold matrix after implantation and resulting oxygen profile (adapted from Muschler *et al.*, 2004). 64
2.25 The tissue oxygen concentration (line graph) and the oxygen consumption (bar graph) values obtained for healing rib defects as a function of time (Heppenstall *et al.*, 1975). 66

3.1 Flow chart of the experimental methods employed for the development of elastomeric scaffolds. 76
3.2 (A) Single nylon layer of parallel fibers (B) Nylon mesh structure creating the mould prior to infiltration. 77

3.3 Orthogonal PDMS structures fabricated through nylon stacking. . . . 78
3.4 Spin coating set-up for the fabrication of PDMS substrates. 79
3.5 (A) (B) and (C) Culture plates seeded with MC3T3-E1 cells (D) (E) and (F) PDMS substrates seeded with MC3T3-E1 cells. 81
3.6 Experimental set-up for PDDC pre-polymer synthesis. 83
3.7 PTFE mould with fused-salt particles (250-300 μm) infiltrated with PDDC polymer. 84
3.8 SEM micrographs of cross-sections of ethanol-fused particulate leached PDDC scaffold. Pore size range (150-250 μm). 85
3.9 SEM micrographs of ethanol-fused particulate leached PDDC scaffold (A) and (B) Top surface, (C) and (D) Bottom surface . Pore size range (150-250 μm). 86
3.10 Experimental set-up for tensile testing of Poly(1,12-dodecanediol-co-citric acid) (PDDC) scaffolds. 87
3.11 Stress-strain curves for Poly(1,12-dodecanediol-co-citric acid) (PDDC) scaffolds fabricated through a ethanol-fused particulate salt-leaching method. 87
3.12 Flow chart of the experimental methods employed for the development and characterisation of ceramic-based scaffolds. 89
3.13 Solid free form (SFF) fabricated scaffold produced using selective laser sintering (SLS) technique. 91
3.14 Light micrograph of the typical architecture of HA scaffolds (post-sintering) produced via the foam-gel method. 94
3.15 Experimental arrangement for freeze drying of HA scaffolds. 95
3.16 Graph of the freeze-drying program cycle for HA scaffolds. 96
3.17 Stainless steel mould and resulting freeze-dried HA green body. . . . 96
3.18 Experimental set-up for the introduction of macropores into freeze-dried HA scaffolds. 97
3.19 Illustration of the unidirectional macrochannel pattern array. 98

3.20 Process overview 98
3.21 Sintering regime 99
3.22 Diagram of Wheaton-soxhlet apparatus for the removal of organic matrix from cancellous bone samples. 101
3.23 Schematic representation of the Franz diffusion cell. 102
3.24 Peripheral sealing of a bimodal scaffold with heatshrink. (A) Bimodal HA scaffold (B) Heatshrink. 103
3.25 Experimental setup for the direct measurement of permeability of scaffolds. 105
3.26 Experimental setup for the determination of compressive mechanical properties of HA scaffolds and ABM samples. 110
3.27 Schematic of the experimental arrangement for 2D time-dependent cell attachment 113
3.28 PDMS scaffold seeding chambers. 114
3.29 Experimental setup for dynamic rotational seeding of HA scaffolds. . 115
3.30 Schematic illustrating the experimental arrangement for determining cellular oxygen consumption. 121
3.31 Schematics of finite element model geometry. 125

4.1 Light micrograph of the scaffold architectures of trimodal scaffolds produced through the freeze drying process. 130
4.2 SEM of scaffold architecture of ⌀ 5 mm with pore size and spacing of 500 μm. 131
4.3 Higher magnification (x80) image of a unidirectional channel (⌀ 500 μm , surrounded by the mesoporous region, which also contains micropores within the base material. 132
4.4 SEM showing the top surface region of a trimodal scaffold with unidirectional macrochannels of ⌀ 800 μm, with a spacing of 800 μm. . . 132
4.5 SEM illustrating the typical mesoporous architecture obtained through freeze drying. 133

4.6 Higher magnification (x350) SEM showing the micro and mesoporosity. 133
4.7 High magnification SEM (x1.8k) showing micropores (indicated by white arrow heads) within the base material of a mesopore strut. . . . 134
4.8 SEM of a cross-sectioned macrochannel demonstrating an open interconnected structure. 134
4.9 SEM of a trimodal scaffold showing two cross-sectioned macrochannels. 135
4.10 SEM showing a disrupted cross-section area of a macrochannel. . . . 135
4.11 SEM showing the bottom surface of a bimodal scaffold typically observed. 136
4.12 Higher magnification (x3k) SEM of the bottom surface of a bimodal scaffold. 136
4.13 SEM of a trimodal scaffold showing evidence of pile up occurring around the periphery of the macrochannels. 137
4.14 Light stereo-micrograph (Magnification x 4) images of scaffolds sliced in the traverse direction. Scale bar is 1 mm. 139
4.15 Light stereo-micrograph (Magnification x 4) images of scaffolds sliced in the longitudinal direction. Scale bar is 1 mm. 139
4.16 Light micrograph (Magnification x 10) images of scaffolds sliced in the traverse direction prior to thresholding used for pore size image analysis. Scale bar is 400 μm. 140
4.17 Light micrograph (Magnification x 10) images of scaffolds sliced in the longitudinal direction prior to thresholding used for pore size image analysis. Scale bar is 400 μm. 140
4.18 Representative images of thresholded scaffold sections used for image analysis. 141
4.19 Frequency distribution of pore intercept lengths from a single slice for images as shown in Figure 4.18. 145
4.20 Frequency distribution graph based on the combined horizontal and vertical mean intercept measurements. 146

4.21 Plot of experimental data (red line) for the change in oxygen partial pressure (%) occurring in the lower chamber versus time (s) of a bimodal scaffold structure. 150
4.22 Fluid conductivity of various scaffold types. 153
4.23 Permeability of various scaffold types. 153
4.24 Typical stress-strain response of trimodal, bimodal and ABM (Anorganic bone matrix) samples. 154
4.25 Ultimate compressive strengths of porous trimodal, bimodal scaffolds and anorganic cancellous bone. 155
4.26 Graph of strain to failure for porous trimodal, bimodal scaffolds and anorganic cancellous bone. 156
4.27 Images of both bimodal and trimodal scaffolds pre- and post- mechanical testing. 158
4.28 Viable cell number for the different groups as presented in Table 4.10. 161
4.29 Time course of MC3T3-E1 osteoblastic cell attachment to 2D nonporous HA substrates. 162
4.30 Comparative growth kinetics of MC3T3-E1 cells cultured on control and HA substrates. 164
4.31 Seeding efficiency (%) of cells within bimodal scaffolds post-seeding at 30, 60, 120 and 180 min. 166
4.32 Seeding efficiency (%) of cells within trimodal scaffolds 3 hrs post-seeding. 168
4.33 Comparative MTT staining of longitudinal bimodal cross-sections seeded with 25 and 50 μL of cell suspension. Scale bar is 1mm. 169
4.34 Schematic to illustrate a possible reason of lower seeding efficiencies of trimodal scaffolds compared to bimodal scaffolds for the same given seeding volume. 170
4.35 Illustration of orientations assessed to enhance seeding efficiency of trimodal scaffolds. 171

4.36 Seeding efficiency of trimodal scaffolds subjected to normal, horizontal (no rotation) and horizontal rotation seeding. 172
4.37 Comparative MTT staining of surface and longitudinal cross-sections of trimodal (A, B) and bimodal scaffolds (C, D) 4 hours post seeding. Scale bar is 1mm. 173
4.38 Comparative MTT staining of surface and longitudinal cross-sections of bimodal and trimodal scaffolds 1 day post seeding. Scaffolds were subjected to either static or dynamic culturing. Scale bar is 1mm. . . 175
4.39 Comparative MTT staining of surface and longitudinal cross-sections of bimodal and trimodal scaffolds 3 days post seeding. Scaffolds were subjected to either static or dynamic culturing. Scale bar is 1mm. . . 176
4.40 Comparative MTT staining of surface and longitudinal cross-sections of bimodal and trimodal scaffolds 5 days post seeding. Scaffolds were subjected to either static or dynamic culturing. Scale bar is 1mm. . . 177
4.41 Comparative MTT staining of surface and longitudinal cross-sections of bimodal and trimodal scaffolds 7 days post seeding. Scaffolds were subjected to either static or dynamic culturing. Scale bar is 1mm. . . 178
4.42 Comparative growth kinetics over 7 days of MC3T3-E1 cells cultured on bimodal and trimodal HA scaffolds subjected to either static or dynamic culture conditions. 179
4.43 The depletion of oxygen concentration (O_2) measured at the base of oxygen sensitive wells for three different cell densities. 181
4.44 Oxygen consumption rate per cell (OCR) (fmol min^{-1} $cell^{-1}$) over time for three different initial seeding densities. 182
4.45 Total cell number versus time of MC3T3-E1 cells cultured on porous HA bimodal scaffolds initially seeded with three different cell densities. 183
4.46 Illustration of the 3D scaffold geometry to highlight the longitudinal plane and centre line from which oxygen concentrations were extracted for planar plots. 188

4.47 Day 1 oxygen concentration plot for bimodal scaffolds. 190
4.48 Day 3 oxygen concentration plot for bimodal scaffolds. 190
4.49 Day 5 oxygen concentration plot for bimodal scaffolds. 191
4.50 Day 7 oxygen concentration plot for bimodal scaffolds. 191
4.51 Day 1 oxygen concentration plot for trimodal scaffolds. 192
4.52 Day 3 oxygen concentration plot for trimodal scaffolds. 192
4.53 Day 5 oxygen concentration plot for trimodal scaffolds. 193
4.54 Day 7 oxygen concentration plot for trimodal scaffolds. 193
4.55 Changes in oxygen concentration along the centre line of scaffold constructs for various time points (1, 3, 5 and 7 days) (A) Bimodal and (B) Trimodal. 194
4.56 Solution convergence test using increasing mesh refinements from 35138 to 460812 elements. 196
4.57 Cell density sensitivity analysis for (A) Bimodal and (B) Trimodal scaffolds. 197

List of Tables

2.1 Types of tissue attachment of biomaterials (adapted from Cao and Hench, 1996). 16

2.2 Definitions of parameters involved in describing porous scaffold features (Li *et al.*, 2003). 18

2.3 Summary of pore size and porosity of the porous HA implants (Chang *et al.*, 2000). 23

2.4 Biomechanical analysis of porous HA implants (Chang *et al.*, 2000). . 25

2.5 Conventional scaffold processing techniques for tissue engineering (Yang *et al.*, 2001; Leong *et al.*, 2003). 40

2.6 Advantages and limitations of SFF fabrication techniques 42

2.7 Permeabilities for a given anatomic site (Nauman *et al.*, 1999). 45

2.8 Permeability of PLGA scaffolds of varying porosity (Agrawal *et al.*, 2000). 46

2.9 Oxygen tensions in % and mmHg and corresponding relationship to *in vivo* and *in vitro* environments (compiled from Brighton *et al.*, 1991). 65

2.10 Comparison of the oxygen consumption rates of various cell types. . . 70

3.1 H_2SO_4 chemical treatments of PDMS substrates and resulting contact angles measurements. 80

3.2 APTES chemical treatments of PDMS substrates and resulting contact angles measurements. 80

3.3 Freeze-drying program cycle for HA scaffolds produced 95

3.4 Summary of the different groups used for XTT correction with respective absorbance values and corresponding cell numbers. 117

4.1 Scaffold terms used to define various scaffold architecture types . . . 129

4.2 Horizontal and vertical mean intercept lengths (MIL) of different scaffold samples in the longitudinal and traverse directions. 143

4.3 Mean pore intercept lengths (MIL) of all horizontal and vertical measurements within a sample, separated by slice orientation in the longitudinal and traverse directions. 144

4.4 Summary of the porosities for both bimodal and trimodal scaffolds. . 148

4.5 Sample data and calculated diffusion coefficient (D, m^2s^{-1}) obtained for a specimen with initial conditions of C_0= 4.5 %, C_1= 19.6 and x= 2.97 mm. 149

4.6 Conductivity data for various scaffold types. 152

4.7 Permeability data for various scaffold types. 152

4.8 Ultimate compressive strength data of porous trimodal, bimodal scaffolds and anorganic cancellous bone. 155

4.9 Strain to failure data for porous trimodal, bimodal scaffolds and anorganic cancellous bone. 156

4.10 Summary of the different groups used for XTT correction with respective absorbance values. 161

4.11 Percentage increase per hour (% h^{-1}) of viable cell numbers for discrete time frames, $\triangle$ t (hrs), for both HA and control substrates. . . 165

4.12 Seeding efficiency (%) of cells of bimodal scaffolds at various time points (30, 60, 120 and 180 min) post-seeding. 167

4.13 Seeding efficiency (%) of cells within trimodal scaffolds 3 hrs post-seeding. SE = standard error of the mean, n= number of samples. . . 168

4.14 Data for the oxygen consumption rate per cell (OCR) (fmol min^{-1} $cell^{-1}$) at different time points for three different initial seeding densities (0.5, 1 and 2 x 10^5 cells). 182

4.15 Model parameters used to calculate the oxygen concentration profiles in bimodal and trimodal scaffolds. 187
4.16 Cell density parameters used to determine oxygen concentration profiles for bimodal and trimodal scaffolds for various time points. 188

Nomenclature & Abbreviations

Greek

Symbol	Definition	Units
α	Solubility coefficient of oxygen	non-dimensional
σ	Stress	MPa
σ_0	Zero porosity strength	MPa
κ	Permeability	m^2
μ	Viscosity	Pa·s
ϵ	Void fraction	non-dimensional
τ	Tortuosity	non-dimensional
ρ	Density	kg m^{-3}
ρ_{app}	Apparent density	g cm^{-3}
ρ_{real}	Real density	g cm^{-3}

Roman

Symbol	Definition	Units
b	Pore geometry parameter	non-dimensional
c	Concentration	mol m^{-3}
h	Diffusion path length	cm
m	Mass flow rate	kg s^{-1}
p	Pore volume fraction	non-dimensional
r	Specimen radius	cm
t	Time	s

Symbol	Definition	Units
A	Area	m^2
C	Fluid conductance	$m^3s^{-1}Pa^{-1}$
D_{eff}	Effective diffusion coefficient	m^2s^{-1}
I	Normalised fluorescent intensity	non-dimensional
K_m	Michaelis-Menten constant	mol m^{-3}
K_{SV}	Stern-Volmer constant	non-dimensional
L	Length	m
M_{dry}	Dry mass	g
M_{wet}	Wet mass	g
O_2	Oxygen concentration	mol m^{-3}
P	Pressure	Pa
P_{app}	Apparent porosity	non-dimensional
P_{real}	Real porosity	non-dimensional
PO_2	Partial pressure of oxygen	atm
Q	Volumetric flow rate	m^3s^{-1}
R	Reaction rate	mol m^3 s−1
S	Surface area	m^2
V_m	Molar volume of oxygen at standard temperature	L
V_{max}	Maximal rate of oxygen consumption per cell	mol $cell^{-1}$ s^{-1}

Abbreviations

3-DP	Three dimensional printing
ABM	Anorganic bone matrix
ALP	Alkaline phosphatase, a marker of osteogenic differentiation
APTES	3-Aminopropyltriethoxysilane, a coupling agent to improve cell adhesion
BCP	Biphasic calcium phosphate
BMP	Bone morphogenetic protein
BMSC	Bone marrow stromal cell
BRM	Bone replacement material

BSE	Bovine spongiform encephalopathy
CCD	Charge coupled device
CG	Collagen-glycosaminoglycan
CNC	Computer numeric control
CT	Micro computer tomography
ECM	Extracellular matrix
FDA	Food and drug administration
FDM	Fused deposition modelling
HA	Hydroxyapatite
HIV	Human immunodeficiency virus
HOS	Human osteosarcoma
MTT	3-(4,5-Dimethylthiazol-2-yl)-2,5-diphenyltetrazolium bromide, a tetrazolium salt reduced to purple formazan in the mitochondria of living cells
NB	New bone
OBS	Oxygen biosensor system
OCR	Oxygen consumption rate
PCL	Polycaprolactone
PE	Polyethylene
PEGT/PBT	Polyethyleneglycol terephtalate and polybuthylene terephtalate
PEI	Polyoxyethylenelaurylether
PDDC	Poly(1,12-dodecanediol-co-citric acid)
PDMS	Poly(dimethylsiloxane)
PGA	Polyglycolic acid
PLA	Polylactic acid
PLDL	Poly(L/DL-lactide)
PLG	Poly(lactide-co-glycolide)
PLGA	Poly(lactic-co-glycolic acid)
PTFE	Poly(tetrafluoroethylene)
RP	Rapid prototyping
RUNX2	A key transcription factor associated with osteoblast differentiation

SB	Surrounding bone
SD	Standard deviation
SE	Standard error
SEM	Scanning electron microscope (microscopy)
SFF	Solid free form
SL/SLA	Stereolithography
SLS	Selective laser sintering
TCP	Tricalcium phosphate
TZP	Tetragonal zirconia polycrystal
XTT	2,3-bis[2-methyloxy-4-nitro-5-sulfophenyl]-2H-tetrazolium-5-car-boxanilide, a tetrazolium salt reduced by metabolically active cells to a colored-water-soluble formazan derivative that can be easily quantified colorimetrically

Acknowledgements

I would first like to thank my supervisor Dr. Kevin O'Kelly, for providing me with the opportunity to carry out research and for allowing me the intellectual freedom to explore new avenues, supporting me throughout with guidance and advice. Thank you Kevin. My thanks must also go to Prof. Patrick Prendergast and Dr. Veronica Campbell for their supervision for a period of time during this work.

I'd like to lend my gratitude to all the technical staff (Tom Haveron, Gabriel Nicholson, Sean Doonan, JJ Ryan, Paul Normoyle, Gerry Byrne, Danny Boardman, John Gaynor, Peter O' Reilly and Alan Reid) for their specialist skills in solving technical problems and the administrative staff (Joan Gillen, Nicole Byrne and Sheena Brown) for aiding me in carrying out every day administrative tasks.

I've made many great friends throughout my postgraduate years, friends I hope I have made for life. To Linda, Laoise, Triona, Danny, Mary, Richie, Kevin, Tadhg, Orla, Alex, John B., John V., John G., James, Paul, Niamh, Melanie, Karen, Geraldine, Damien, Brianne, Jennifer, Orlaith, Oran, Paddy, Louise, Eric, Emma, Elaine, Paula and Adriele. Thank you for making life so much fun and for making my time at Trinity so enjoyable. I would especially like to thank all my friends from the Tissue Engineering group for their expertise and assistance with this work. It has been an absolute pleasure working with you all.

I'm eternally grateful to my family, for their unstinting support, dedication, love and encouragement throughout. Without their help, I would not have been able to return to university to pursue this adventure. Mum and Dad, thank you for awarding me every opportunity in life.

This work was supported by the HEA under the Programme for Research in Third Level Institutions (PRTLI).

Publications and presentations resulting from this study

C.T. Buckley and K.U. O'Kelly (2006): Assessment of a Novel Hydroxyapatite Bone Tissue Engineering Scaffold Incorporating a Tri-Modal Pore Distribution. Proceedings of the Fifth World Congress of Biomechanics, Munich, Germany. Paper #6563
(Oral Presentation)

C.T. Buckley and K.U. O'Kelly (2006): Fabrication of a Hydroxyapatite Scaffold with a Tri-Modal Pore Distribution for Bone Tissue Engineering. Bioengineering in Ireland- Proceedings of the twelfth Annual Conference of the Section of Bioengineering of the Royal Academy of Medicine in Ireland. P.E. McHugh, D. O'Mahoney & D. FitzPatrick, (Eds.), p89 ,ISBN 1-905-254-075.
(Oral Presentation)

C.T. Buckley, A. Prina-Mello, K.U. O'Kelly (2005): Development of Biodegradable Elastomeric Scaffolds for Mechanobiology Investigations. Bioengineering in Ireland- Proceedings of the eleventh Annual Conference of the Section of Bioengineering of the Royal Academy of Medicine in Ireland. D.P. FitzPatrick & M. Senouci, (Eds.), p13.
(Oral Presentation)

C.T. Buckley and K.U. O'Kelly (2004): Development of Regular Architecture Scaffolds for 3D Culturing Systems. Proceedings of the 14th Conference of the European Society of Biomechanics, 's Hertogenbosch, The Netherlands.
(Oral Presentation)

C.T. Buckley and K.U. O'Kelly (2004): A New Technique for Fabricating Regular 3D Scaffolds for Bone Tissue Engineering Applications. Bioengineering in Ireland- Proceedings of the tenth Annual Conference of the Section of Bioengineering of the Royal Academy of Medicine in Ireland. D.P. Fitzpatrick, B.A.O. McCormack & T.M. McGlouhlin, (Eds.), p19 ,ISBN 1-902277-83-X.
(Oral Presentation)

C.T. Buckley and K.U. O'Kelly (2004): Regular Scaffold Fabrication Techniques for Investigations in Tissue Engineering. Proceedings of the first symposium on Biomechanical Engineering held between the Trinity Centre for Bioengineering and the National Centre for Biomedical Engineering Science under the Programme for Research in Third Level Institutions. P.J. Prendergast & P.E McHugh (Eds.), pp 147-166, TCBE & NCBES, Ireland.

C.T. Buckley and K.U. O'Kelly (2003): Direct Permeability Measurements in Cross-Species Trabecular Bone with Varying Anatomic Location. Bioengineering in Ireland- Proceedings of the ninth Annual Conference of the Section of Bioengineering of the Royal Academy of Medicine in Ireland. D.P. FitzPatrick, B.A.O. McCormack & D. McCormack, (Eds.), p19 , ISBN 1-902277-72-4. (Oral Presentation)

Abstract

Many of the current tissue-engineering scaffold-based strategies have suffered from limited cell depth viability when cultured *in vitro*, with viable cells existing within the outer 250-500 μm from the fluid-scaffold interface. This is primarily believed to be due to the lack of nutrient delivery into and waste removal from the inner regions of the scaffold construct. Other issues associated with scaffolds involve poor seeding efficiencies and limited cell penetration resulting in heterogenous cellular distributions.

This work focused on developing a novel hydroxyapatite multi-domain porous scaffold architecture (*i.e.* a scaffold providing a discrete domain for cell occupancy and a separate domain for nutrient delivery) with the specific objectives of embodying in one scaffold the structures required to optimise cell seeding, cell proliferation and migration and potentially to facilitate vascularisation once implanted *in vivo*.

It has been demonstrated that incorporating unidirectional macrochannels into a porous scaffold material significantly enhances initial cell seeding distribution, while maintaining relatively high seeding efficiencies. This work has also demonstrated that for seeding of three-dimensional porous scaffolds, appropriately matching the seeding volume to the saturation capacity of the scaffold is the optimum approach in terms of promoting homogeneous cell seeding while maintaining relatively high seeding efficiencies.

Through *in vitro* static culturing it has been shown that providing a discrete domain for nutrient diffusion and metabolic waste removal is insufficient to maintain cell viability throughout the entire scaffold depth. Finite element analysis incorporating measured effective diffusion coefficients, cellular oxygen consumption

rates and cellular distributions demonstrate that the formation of this necrotic core cannot be solely due to oxygen diffusion limitations and is possibly due to other diffusive limited species concentrations such as glucose or metabolic waste products. Therefore, in order to overcome these diffusion based limitations it has been shown that dynamic rotational culturing of multi-domain porous scaffolds can maintain uniform cell viability throughout the scaffold depth with increasing culturing time and increase the rate and extent of cell proliferation ($\sim$ 2 fold) compared to static culturing.

This work provides significant insight into current tissue engineering strategies and raises important questions regarding scaffold architecture and short-term conditioning of scaffolds *in vitro* prior to *in vivo* implantation.

Chapter 1

Introduction

Contents

1.1 Bone grafting and bone implants 1

1.2 Future advancement of scaffold based tissue engineering for 21st century medicine 3

1.3 Focus of present investigation 6

1.1 Bone grafting and bone implants

Bone is used annually in more than 450,000 graft procedures in the United States and in 2.2 million procedures worldwide to repair bone defects (Lewandrowski *et al.*, 2000). The term graft refers to the transplantation of living cells usually in tissue that can survive and grow in a new location. Cancellous bone grafting is required in a number of surgical procedures (*e.g.* to fill voids left after the removal of diseased bone, or in the reconstruction of the alveolar ridge in the jaw due to excessive bone resorption). The graft not only replaces missing bone, but also aids in the formation of new bone. This new bone growth strengthens the grafted area by forming a bridge between existing bone and the graft material. Over time, as the bone under goes the remodelling process, most of the grafted tissue is replaced by newly formed bone. There are four main types of bone graft available to surgeons. These include:

- Autografts: those where the bone to be grafted is harvested from one part of the body and placed in another site of the same individual.
- Allografts: grafts obtained from human donors.
- Xenografts: grafts harvested from one species onto or into individuals of unlike species.
- Synthetic substitutes: grafts made from synthetic substitute materials.

Grafting of the patient's own bone is ideal from the perspective of minimising host rejection and optimising osteogenic potential. However harvesting autogenous bone requires additional surgery and there is a limit to the amount that can be harvested. Also harvesting can cause site morbidity associated with infection, pain and haematoma (Tancred *et al.*, 1998b; Burg *et al.*, 2000; Yoshikawa, 2000).

Allografts, which provide most of the desirable tissue characteristics as autografts, introduce the possibility of disease transmission such as HIV (human immunodeficiency virus) and hepatitis. Xenografts, typically bovine in origin, can provide ample bone volume, but the risk of bovine spongiform encephalopathy (BSE) transmission is possible (Tancred *et al.*, 1998b). Thus, in theory an entirely synthetic graft offers the best alternative to fill bony defects without causing disease transmission or site morbidity. For a synthetic graft to be successful it must provide a suitable environment in which osteoprogenitor cells are permitted to adhere, proliferate, differentiate and create extra-cellular matrix (ECM). However, to date, there has been no single synthetic bone graft developed that surpasses or even equals the success of an autograft.

1.2 Future advancement of scaffold based tissue engineering for 21st century medicine

A paradigm shift has taken place in modern regenerative medicine from using synthetic implants and tissue grafts to a tissue engineering approach that uses degradable porous material scaffolds integrated with biological cells or molecules to regenerate tissues (Hollister *et al.*, 2005).

Tissue engineering has been defined by Laurencin *et al.* (1999) as "The application of biological, chemical, and engineering principals towards the repair, restoration and regeneration of living tissue using biomaterials, cells and factors alone or in combination". This paradigm shift requires scaffolds that have the architectural ability to temporarily support mechanical function with sufficient mass transport to aid and facilitate nutrient delivery and metabolic waste removal in order to facilitate biological delivery and tissue formation or regeneration. Little is known quantitatively about this optimised balance as first generation scaffolds were not fabricated with precise porous architecture which allows for direct comparison or ease of quantification.

Recent advances in both computational topology design (CTD) and solid free-form fabrication (SFF) have made it possible to create scaffolds with well defined architectures. The benefits of these technological advancements include the enhancement of interconnected porosity which can improve cell seeding and the incorporation of channels to guide cell migration and tissue ingrowth (Hollister *et al.*, 2005).

Despite these advances in fabrication methods significant questions with respect to the efficacy of designed scaffold architectures on tissue regeneration remain unanswered to date. For example, does increased permeability enhance tissue regeneration? Is there an optimal material for regeneration of specific tissues? What are the optimised nutrient conditions to enhance and facilitate new tissue formation? Is it essential to seed scaffolds with cells prior to implantation? Is it necessary to promote matrix synthesis prior to *in vivo* implantation? Can the surface topography of 3D scaffolds be modified to enhance cellular migration? Answering these

and other questions requires both *in vitro* and subsequent *in vivo* experiments using scaffolds made with controlled characteristics and quantifiable architectures. Once these questions are sufficiently answered, scaffold based tissue engineering can make a significant impact on regenerative medicine treatments, which cannot be resolved using traditional random architecture scaffolds.

1.2.1 Current scaffold limitations

A recurring limitation of bone tissue scaffolds is that most studies have shown that bone forms only in the outer 250 μm - 500 μm region of scaffolds. This may be explained by the lack of nutrient delivery to and waste removal from the inner regions of a scaffold (Ishaug-Riley *et al.*, 1998). If the pore size or interconnectivity is too small, cells can occlude them, preventing further cell penetration and widespread bone formation (Leong *et al.*, 2003). It is essential that a scaffold possess suitable interconnectivity and pore size distribution to minimise diffusion limitations and avoid pore occlusion prior to vascularisation.

Scaffold characteristics such as interconnectivity (Chang *et al.*, 2000; Hui *et al.*, 1996), pore size (Ishaug-Riley *et al.*, 1998), microporosity, macroporosity (Ishaug-Riley *et al.*, 1998) and surface roughness (Hench and Ethridge, 1982; Cao and Hench, 1996; Ducheyne and Qiu, 1999; Anselme, 2000) all influence cellular responses, as they collectively control the degree of nutrient delivery, penetration depth of cells and rate of metabolic waste removal. Ideally, a tissue engineered scaffold must provide a germane environment during *in vitro* cell culturing and during subsequent *in vivo* implantation. However, these two environments differ dramatically in terms of nutrient concentration gradients, pressure gradients and fluid velocities. *In vivo*, diffusion is the primary mechanism for transporting nutrients, whereas *in vitro*, through the use of perfusion bioreactors, it is an imposed fluid flow. A clinically relevant scaffold must provide a nutrient rich environment within the scaffold core in order for cells to lay down new matrix and minimise cell necrosis in conditions similar to the *in vivo* environment. It has been shown that scaffolds with defined interconnected channels enhance cell nutrient delivery, waste removal and vascular

invasion (Baksh and Davies, 2000). Ideally, a scaffold should (1) be highly porous and interconnected; (2) be biocompatible and/or bioresorbable with a controlled degradation and resorption rate to match cell/tissue growth *in vitro*/*in vivo*; (3) have suitable surface chemistry for cell attachment, proliferation, and differentiation; (4) have an architecture suitable for initial cell seeding; (5) have mechanical properties to support the graft and allow clinical manipulation/shaping.

Many researchers have been successful in replicating identical cancellous structures (Tancred, 1996) or even mimicking the random porous nature of cancellous bone (Ishaug-Riley *et al.*, 1998). But by doing this, the understanding of what constitutes an ideal nutrient environment has not been answered. Since the architecture of cancellous bone differs from one location to another within an individual (Figure 1.1), it is hypothesised here that a scaffold with properties which are tailored to suit the location of the defect within an individual offers the greatest potential for successful filling of bony defects (Hollister *et al.*, 2000).

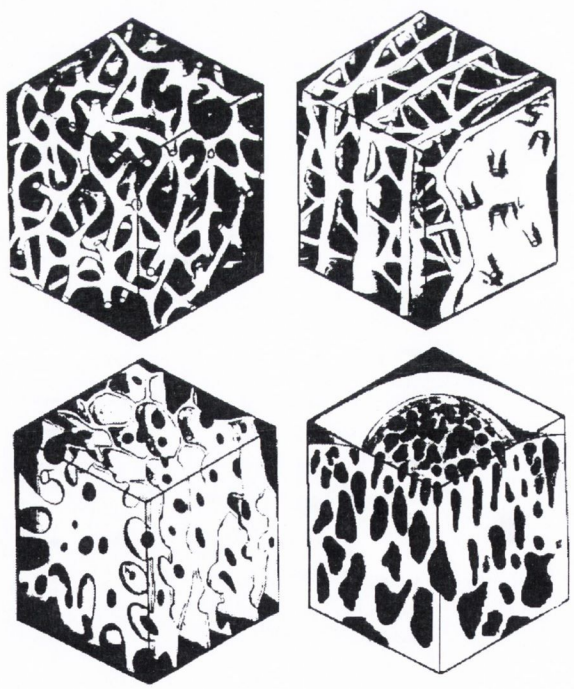

Figure 1.1. Various cancellous bone architectures (adapted from Singh, 1978).

This could perhaps be considered as a rather *naive* approach to developing synthetic bone grafts. Cancellous bone can be considered as an initially random porous structure that has been remodelled throughout an individual's life in response to *in vivo* stimuli. It is in effect an end product derived from embryonic mesenchyme which has undergone development, growth and the remodelling process. It does not necessarily provide a suitable scaffold for new bone formation. Therefore it is necessary to develop a scaffold that facilitates culturing *in vitro* and so that once implanted *in vivo* will provide an environment which will allow cells to remain viable.

1.3 Focus of present investigation

In light of the issues described in the previous sections, it is the aim of this work to advance the fundamental work in bone tissue engineering and accelerate the development of scaffolds for *in vivo* applications.

This work focuses on developing a novel hydroxyapatite multi-domain porous scaffold architecture (*i.e.* a scaffold providing a discrete domain for cell occupancy and a separate domain for nutrient delivery) with the specific aim to embody in one scaffold the structures required to optimise cell seeding, cell proliferation and migration and potentially to facilitate vascularisation once implanted *in vivo*.

It is hypothesised that this is best achieved with engineered scaffolds incorporating regular and interconnected pore structures (rather than solely random pore arrangements). The specific objectives of this work include:

- Fabrication and characterisation of scaffolds in terms of porosity, pore size, permeability, effective diffusion coefficient and mechanical properties of both bimodal and trimodal scaffold architectures.

- Biocompatibility: The influence of 2D hydroxyapatite substrate material on the time dependent cell attachment and subsequent cellular proliferation compared to normal tissue culture plastic.

- Optimisation of cell seeding efficiency and distribution will be investigated by comparing the seeding volume and the influence of macrochannels on the resulting cell distribution post static seeding.

- The influence of *in vitro* static and dynamic (rotational) culturing conditions on the proliferation and distribution of viable cells during short term culturing.

- Finite element analysis on the influence of multi-domain type scaffolds on the local oxygen concentrations which is hypothesised to minimise the steep gradients that normally exist for single random porous domain scaffolds. This work also includes the determination of oxygen consumption rates of osteoblast-like cells (MC3T3-E1) when cultured on hydroxyapatite substrates.

Chapter 2

Literature Review

Contents

2.1 Anatomy of bone 9

2.2 Current tissue engineering strategies 11

2.3 Biomaterials 15

2.4 Scaffold properties 18

2.5 Scaffold architectures 31

2.6 Traditional scaffold fabrication techniques 39

2.7 Solid free form (SFF) fabrication technologies 41

2.8 Fluid conductance and permeability 43

2.9 Cell seeding 47

2.10 *In vivo* assessment of scaffolds 51

2.11 *In vivo* environments: diffusion and cellular consumption of nutrients 61

2.12 Chapter summary 70

2.1 Anatomy of bone

2.1.1 Structure

Bone is generally classified into one of two types: 1) cortical bone, also known as compact or dense bone and 2) cancellous bone, also known as trabecular or spongy bone (Figure 2.1). These two types are classified on the basis of their respective porosity and the unit microstructure. Cortical bone is denser with a porosity ranging between 5 and 10% and is primarily found in the shaft of long bones and forms the outer shell around cancellous bone at the end of joints and in the vertebrae. Cancellous bone is less dense than compact bone with porosities ranging between 20 and 80%, and occurs near the ends of long bones, at the interior of small bones and between the surfaces of flat bones. The orientation of the plates and rods is such that cancellous bone is anisotropic in most locations, but can also exist in isotropic form in regions such as the vertebral bodies (Yaszemski *et al.*, 1996). Cancellous bone is located where bones are heavily stressed or where stresses arrive from many directions. The trabeculae are orientated along stress lines but with extensive cross bracing (Martini, 2001).

2.1.2 Matrix of bone

Calcium phosphate, $Ca_3(PO_4)_2$, accounts for almost 50% of the volume of bone. Calcium phosphate interacts with calcium hydroxide, $Ca(OH)_2$, to form crystals of hydroxyapatite (HA), $Ca_{10}(PO_4)_6(OH)_2$. As the crystals form they also incorporate other calcium salts such as calcium carbonate, $CaCO_3$, and ions such as sodium, magnesium and fluoride. Collagen fibres contribute to about 45% of the volume of bone (Martini, 2001).

The mineral crystals are deposited along, and in close relation to the bone collagen fibrils. The result is a protein-crystal nano-composite with properties intermediate between those of collagen and those of pure mineral crystals. It is for this reason that bone is strong, somewhat flexible and very resistant to shattering.

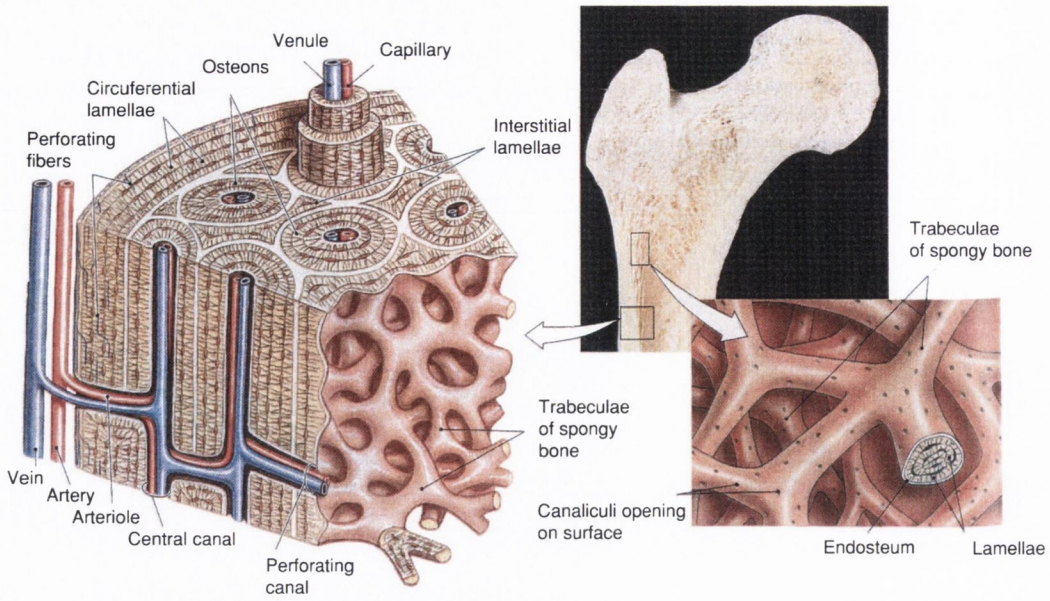

Figure 2.1. The anatomical structure of bone tissue (A) Illustration of the relationships between trabecular and cortical bone (B) Illustration of the organisation of trabecular bone (adapted from Martini, 2001).

2.1.3 Bone formation

The process of bone formation (osteogenesis) involves three main steps:

- Production of the extracellular organic matrix (osteoid)
- Mineralisation of the matrix to form bone
- Bone remodelling by resorption and reformation

Newly formed bone is either formed *via* intramembranous ossification or endochondral ossification. Intramembranous ossification is the formation of woven bone directly from condensed mesenchymal tissue without the intermediate formation of a cartilaginous framework. Endochondral ossification involves a cartilaginous intermediate, formed from mesenchymal tissue. This cartilage is then ossified to form the new bone. The bones that result from intramembranous ossification include the flat bones of the skull, the mandible, and the clavicle. Endochondral ossification occurs

in the embryonic formation of the long bones, in fracture repair, in physeal growth of the immature skeleton, and in the incorporation of bone grafts (Yaszemski *et al.*, 1996; Martini, 2001).

Mature bone is lamellar bone. New bone, whether formed at the physis, during fracture repair, in neoplasia, in embryonic life, or as a result of bone graft incorporation, is woven bone. Woven bone becomes lamellar bone through the process of remodelling. The randomly orientated collagen fibres of woven bone are replaced by parallel fibres in lamellar bone. The mineral phase is organised around these collagen fibres; it is this organised, remodelled mineral phase that gives lamellar bone its anisotropic properties (Yaszemski *et al.*, 1996).

The cellular activities of osteoblasts, osteoclasts and osteocytes are essential to the process of bone formation and remodelling. Osteoblasts synthesise the collagenous precursors of bone matrix and also regulate its mineralisation. Osteoclasts (formed by the fusion of cells of the monocyte-macrophage cell line) remove bone tissue by removing the bone's mineralised matrix in a process known as bone resorption. As the process of bone formation progresses, the osteoblasts come to lie in tiny spaces (lacunae) within the surrounding mineralised matrix and are then called osteocytes. The cell processes of osteocytes occupy minute canals (canaliculi), which permit the circulation of tissue fluids. To meet the requirements of skeletal growth and mechanical function, bone undergoes dynamic remodelling by a coupled process of bone resorption by osteoclasts and reformation by osteoblasts.

2.2 Current tissue engineering strategies

Bone tissue engineering is the use of a scaffolding material to either induce formation of bone from the surrounding tissue or to act as a carrier or template for implanted bone cells or other agents (Burg *et al.*, 2000). The scaffold or three-dimensional (3D) construct provides the necessary support for cells to proliferate and maintain their differentiated function, and its architecture defines the ultimate shape of the new bone.

The development of synthetic bone grafts has evolved from providing an inert macroporous biocompatible construct to allow for revascularisation and cell invasion (Begley *et al.*, 1995; Boyde *et al.*, 1999; Tamai *et al.*, 2002; Grynpas *et al.*, 2002) to a tissue engineered approach as illustrated in Figure 2.2. In this approach cells are harvested from a patient or donor and expanded *in vitro*. A three-dimensional scaffold is then seeded with these expanded cells with possible *in vitro* culturing (statically or in a bioreactor device) and finally implanted *in vivo*. This tissue engineering approach is envisaged to allow the development of scaffolds with increased osteogenic potential and hence improve clinical success (Yoshikawa, 2000; Dong *et al.*, 2001a). It is therefore essential to provide a biological environment in which cells can readily attach, proliferate and maintain their differentiated phenotype and to allow deposition of bone matrix throughout the entire construct.

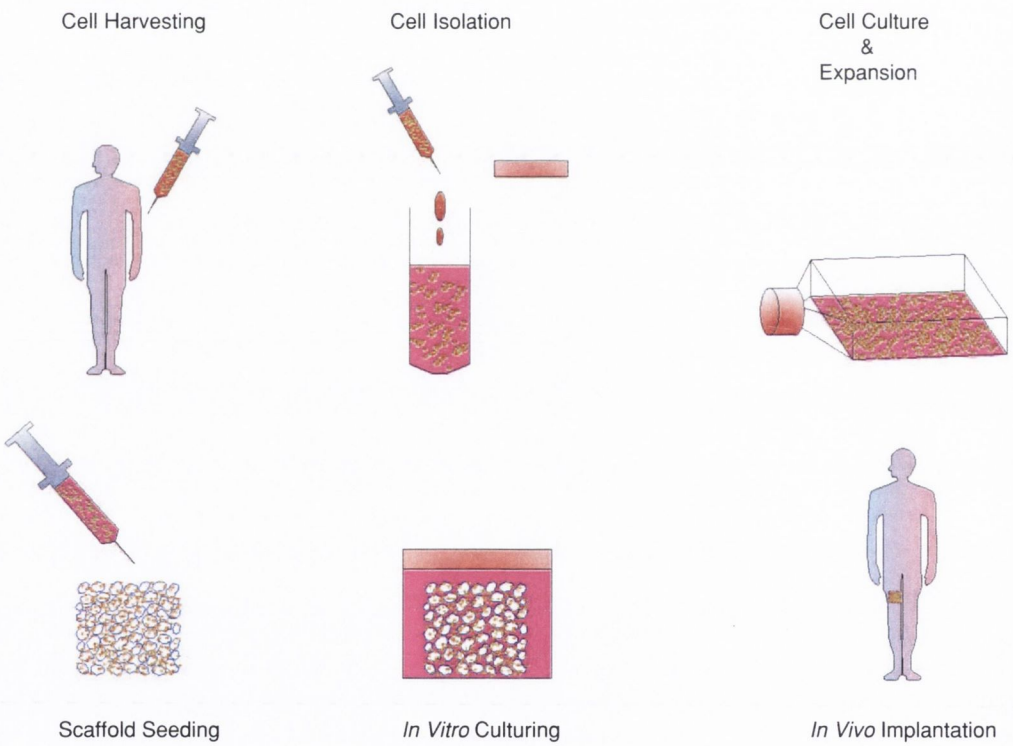

Figure 2.2. Idealised tissue engineering approach.

2.2.1 Implant material criteria

Cancellous bone has an open porous network allowing for easier vascularisation, which is important for the maintenance of cells and the development of new bone. A cancellous autograft begins to revascularise within hours of transplantation, and revascularisation is usually complete in two weeks. New fibrovascular granulation tissue moves through the porous trabecular network and occupies the graft (Yaszemski *et al.*, 1996). The more porous the graft the easier it is for vascularisation to occur. Failure to develop an adequate vascular network will mean that only peripheral cells may survive or develop, supported by diffusion (Tancred, 1996). The biological response to a macroporous bone replacement material (BRM) may be osteogenic, osteoinductive, or osteoconductive as defined below:

- Osteogenic: contains viable cells which aid in the process of bone regeneration
- Osteoinductive: induces bone through the presence of growth factors, to form in an area in which it would not otherwise have formed
- Osteoconductive: includes HA and β-TCP, possess the ability to passively facilitate bone healing. For a cancellous BRM this typically involves allowing the development and growth of bone throughout a porous matrix

A synthetic cancellous BRM should be bioactive, osteoinductive, osteoconductive and osteogenic: *i.e.* it should possess the ability to allow direct deposition of new bone and either allow, or encourage bone to form throughout its matrix. Ideally a scaffold should have the following characteristics to bring about the desired biologic response (Hutmacher, 2001):

(i) three-dimensional and highly porous with an interconnected pore network for cell/tissue growth and flow transport of nutrients and metabolic waste

(ii) biodegradable or bioresorbable with a controllable degradation and resorption rate to match cell/tissue growth *in vitro* and/or *in vivo*

(iii) suitable surface chemistry for cell attachment, proliferation and differentiation

(iv) mechanical properties to match those of tissues at the site of implantation

(v) be easily processed to form a variety of shapes and sizes

Scaffolds should be fabricated from a highly biocompatible material, which does not have the potential to elicit an immunological or clinically detectable primary or secondary foreign body reaction (Hutmacher, 2001). Controlling the degradation rate of the scaffold is an important factor in creating an optimum construct. If the rate of bone ingrowth is exceeded by the rate of resorption, then the implant is likely to fail (Tancred, 1996; Hutmacher, 2000). Higher resorption or dissolution rates may also have a detrimental effect on the formation of new tissue. Yuan *et al.* (2001) implanted two types of tri-calcium phosphate ceramic scaffolds, α-TCP and β-TCP, into dorsal muscles of dogs. Higher cell populations were found to exist within the pores of β-TCP ceramics compared to α-TCP. Bone formation was observed to occur in β-TCP implants at 45 and 150 days, however, no bone formation was found in any of the α-TCP implants. Interestingly, newly formed bone tissue in β-TCP implants was observed to degenerate at 150 days. The authors concluded that porous β-TCP can induce bone formation, while the rapid dissolution of α-TCP, resulting in higher local concentrations of Ca^{2+} and PO_4^{3-}, may resist bone formation in α-TCP, and the less rapid dissolution of β-TCP may be detrimental to already formed bone in β-TCP.

Yamada *et al.* (1997) conducted *in vitro* studies to assess the influence of a calcium phosphate ceramic's solubility on osteoclastic resorption. Neonatal rabbit bone cells were cultured on HA, β-tricalcium phosphate (β-TCP) and two types of biphasic calcium phosphate (BCP) with HA/β-TCP ratios of 25/75 and 75/25. Osteoclasts resorbed BCP most extensively, with an HA/β-TCP ratio of 25/75

whereas pure β-TCP, which had the highest solubility in acid was not resorbed to the same degree. The authors concluded that the extent of osteoclastic resorption of calcium phosphate ceramics might, to a certain degree, be proportional to their solubility, but this finding may not be valid for ceramics with very high dissolution rates.

2.3 Biomaterials

2.3.1 Introduction

No material implanted into living tissues is inert; all materials elicit a response from the host tissue (Cao and Hench, 1996). According to the different types of implant-attachment, biomaterials are classified into four types (Table 2.1).

The tissue response to a biologically inactive, nearly inert implant is formation of a non-adherent fibrous capsule, and the thickness of the layer formed is dependent on the implant, host tissue, motion and fit at the interface and the mechanical load. More chemically reactive metallic implants elicit thicker interfacial fibrous layers. Because the interface is not chemically or biologically bonded, micromotion can occur and this results in progressive development of the non-adherent fibrous capsule which eventually leads to deterioration in function of the implant or the host tissue at the interface or both.

Microporous biomaterials provide interfacial fixation by ingrowth of bone tissue into pores on the surface or throughout the implant. This attachment is termed biological fixation (Cao and Hench, 1996).

A bioactive material is one that elicits a specific biological response at the interface of the material which results in the formation of a bond between the tissues and the material (Hench and Ethridge, 1982). It is intermediate between resorbable and bioinert. A bioactive material creates an environment compatible with osteogenesis, with the mineralising interface developing as a natural bonding junction between living and non-living materials.

Table 2.1. Types of tissue attachment of biomaterials (adapted from Cao and Hench, 1996).

Implant	Type of attachment	Example
Biotolerant	Mechanical interlock (morphological fixation)	Metals, Alumina, Zirconia, Polyethylene (PE)
Porous coated	Ingrowth of tissues into pores (biological fixation)	HA coated porous metals
Bioactive	Interfacial bonding with tissues (bioactive fixation)	Bioactive glasses, HA, Bioactive glass-ceramics
Resorbable	Replacement with tissues	Tricalcium Phosphate, Polylactic acid (PLA)

Resorbable implants are designed to degrade gradually with time and to be replaced with natural host tissues, thus eliminating any long-term functional or biocompatibility problems. For example tricalcium phosphate (TCP) ceramics degrade to calcium and phosphate salts. A disadvantage in employing a resorbable ceramic is that the material used is restricted in composition to physiological constituents because of the large concentration of ions released during the resorption process. As mentioned in section 2.2.1, for a resorbable implant to be successful the resorption rate of the material must be matched to the repair rates of body tissues (Cao and Hench, 1996; Tancred, 1996; Hutmacher, 2000).

2.3.2 Commonly employed biomaterials

The three main material types which have been successfully investigated for use in developing scaffolds include:

(i) natural polymers, such as collagens, glycosaminoglycan, starch, chitin and chitosan

(ii) synthetic polymers, based on polylactic acid (PLA), polyglycolic acid (PGA) and their co-polymers (PLGA)

(iii) ceramics, such as HA and β-tricalcium phosphate (β-TCP)

While naturally occurring biomaterials offer the greatest potential in terms of biocompatibility, large batch-to-batch variations can exist as well as poor mechanical performance. A concern of material supply limitations has prompted researchers to investigate the use of synthetic polymers.

Synthetic polymers have been widely used for over 20 years as surgical sutures, with long established clinical success and many are approved for human use by for example the Food and Drug Administration (FDA) in the United States. However, synthetic polymers of the poly(α-hydroxy acids) family release acidic by-products as they undergo degradation by bulk erosion *via* hydrolysis when exposed to aqueous environments (Lin *et al.*, 2003). Although these degradation products are naturally present in the human body and are removed by natural metabolic pathways (Sachlos and Czernuszka, 2003), the local pH of the surrounding microenvironment can be reduced below that of the natural physiological pH and thus elicit an immunological response. The effect of this acidic environment can cause cell and tissue necrosis as well as acting as an autocatalyst, further accelerating the degradation of the polymer.

Ceramics have also been widely used, due to their high biocompatibility and resemblance to the natural inorganic component of bone and teeth (Chang *et al.*, 2000; Chu *et al.*, 2002). Because of their natural brittleness, HA and β-TCP porous ceramic structures have very low strength and toughness. Thus, despite their favourable biological properties and architectural features, the poor mechanical properties of these ceramic materials have severely limited their use for clinical applications. As synthetic polymers are deemed to be ductile with insufficient rigidity, some researchers have developed composite materials (e.g. polymers with ceramic particles embedded within the polymer matrix) to improve mechanical performance and render the material more suitable for load bearing applications. This provides an added advantage since the embedded ceramic particles act as a buffer to the degradation by-products produced (Laurencin and Lu, 2000).

The development of materials for tissue engineering scaffolds presents many chal-

lenges in obtaining specific mechanical and bioresorbable properties in addition to developing materials suitable for various fabrication processes.

2.4 Scaffold properties

Scaffold properties such as pore size, interconnectivity, microporosity, macroporosity and surface characteristics have been shown to influence the rate and degree at which bone formation occurs. This section explores the influence of these properties in more detail. Parameters that are discussed in the following sections are defined in Table 2.2.

Table 2.2. Definitions of parameters involved in describing porous scaffold features (Li *et al.*, 2003).

Parameter	Definition
Porosity	Percentage of volume of voids over total volume (voids & solid)
Pore	Cell space of a void
Pore size	Diameter of a spherical pore or cylindrical channel
Interconnectivity	Extent of a pore connected with its neighbors
Fenestration	Window between adjacent pores

2.4.1 Porosity

There have been many methods developed to impart porosity to a ceramic body. Such methods are mainly based on the admixing of foreign materials, which are then pyrolysed during sintering, resulting in structures containing voids (Engin and Tas, 1999). Other methods include particulate leaching, a method whereby for example salt granules of a pre-determined size obtained through sieving, are added to either a ceramic or polymer mixture, and are then leached out to form a porous structure (Murphy *et al.*, 2002; Taboas *et al.*, 2003).

It is the porosity of a scaffold into which cells are seeded, that allows them to attach, proliferate and differentiate. This open porosity provides an available volume for new matrix deposition and nutrient delivery. It is thus favourable to have a high degree of porosity to allow full ingrowth of new tissue. The porosity in conjunction with the pore size and interconnectivity should also be sufficient to prevent pore occlusion and peripheral tissue formation. However, as the porosity of a scaffold increases the overall mechanical properties decrease exponentially as depicted in Figure 2.3 A. Based on the minimum solid area approach, Rice (1993) proposed that the resulting porosity-strength dependence can be approximated closely by an exponential function as described by Eqn. 2.1

$$\sigma = \sigma_0 e^{-bp} \tag{2.1}$$

where σ_0 is zero-porosity strength, σ is the strength at pore volume fraction p, and the constant b is related directly to the pore characteristics.

Liu (1997) also demonstrated that for a given porosity volume, the compressive strength of a porous ceramic decreases linearly with increasing macropore size and the degree of strength degradation tends to decrease with increased porosity volume (Figure 2.3 B). Specimens with smaller micropores exhibit higher strength than those with larger macropores. However, the strength tends to become insensitive to macropore size at higher levels of porosity.

Development of scaffolds for bone tissue engineering with sufficient mechanical properties presents many challenges with respect to design criteria. The two competing criteria of developing a mechanically suitable, yet highly porous scaffold is difficult to achieve. Thus, compromises must be made in the design and fabrication processes. This will inevitably lead to the production of scaffolds for different functional uses, *i.e.* load- and non load- bearing scaffold constructs for bone tissue engineering purposes.

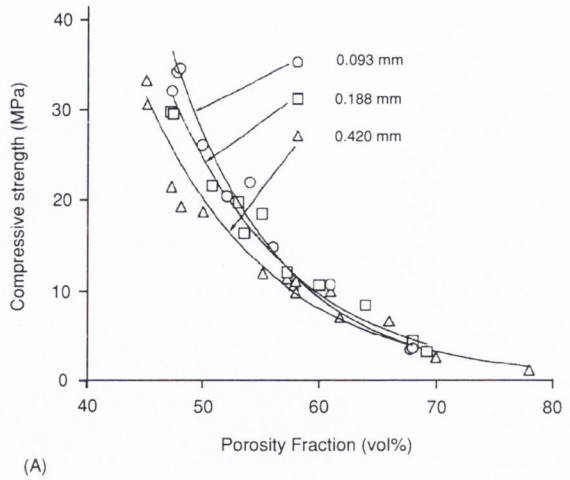

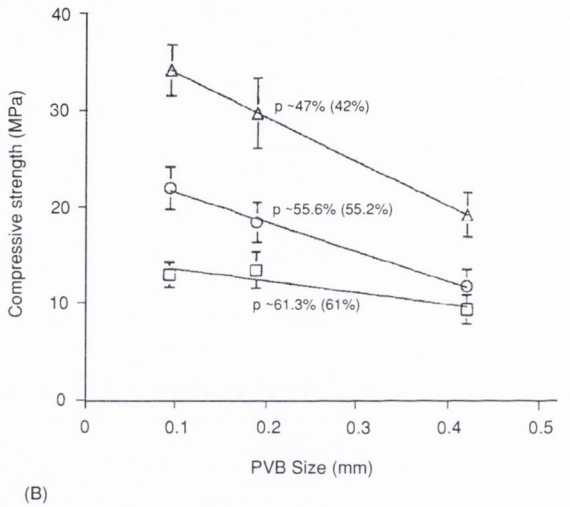

Figure 2.3. Compressive strengths of porous HA ceramics (A) Illustrates the relationship between porosity and resulting compressive strength (B) Illustrates a decreasing linear relationship of compressive strength with increasing macropore size for a given porosity (Liu, 1997).

2.4.2 Microporosity

The incorporation of microporosity within the scaffold material may have added advantages with regard to nutrient delivery and cellular response. Taboas *et al.* (2003) successfully incorporated microporosity within a scaffold material (PLA) consisting of interconnected plate structures, yielding 5-11 μm void openings (Figure 2.4), through an emulsion-solvent diffusion technique. The microporosity of a scaffold gives it the potential to be preconditioned with bone morphogenetic proteins (BMPs) (Asahina *et al.*, 1997) and anti-inflammatory drugs (Dexamethasone) (Yoon *et al.*,

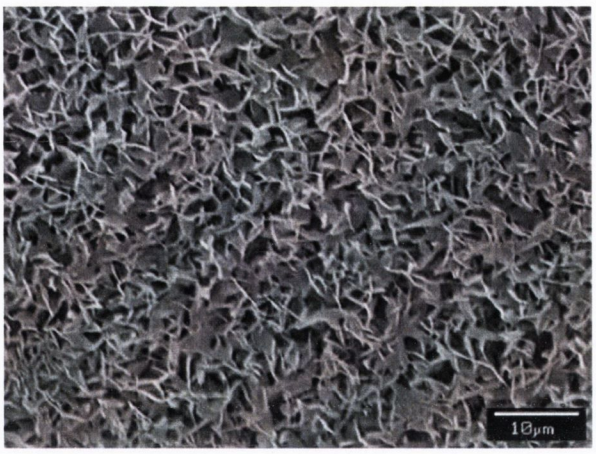

Figure 2.4. Interconnected plate structures yielding 5-11 μm void openings within PLA material (Taboas *et al.*, 2003)

2003), which may be beneficial for clinical applications and promote the formation of a specific tissue type.

Tancred *et al.* (1998a) assessed the fluid-retention characteristics (Figure 2.5) of ceramic based scaffolds produced by identically replicating the architecture of bovine cancellous bone and observed that these scaffolds were capable of retaining water at the level of at least 50 wt% of the mass of the mineral, at less than 65% porosity, to about 150 wt% of the mass of the mineral at 80-85% porosity, indicating that β-TCP replicated structures could also be useful as a carrier for osteogenic agents such as bone morphogenetic proteins (BMP's).

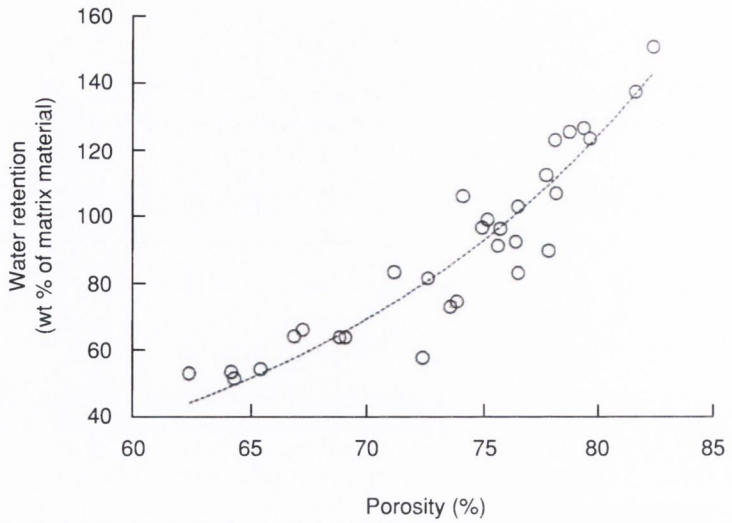

Figure 2.5. Water retention characteristics of porous β-TCP replicas of bovine cancellous bone showing the increase in water retention (wt% of matrix mineral) with increasing construct porosity (Tancred *et al.*, 1998a).

2.4.3 Pore size

The optimal pore size for maximum osteoconduction has not been determined. Many investigators have defined scaffold pore size as either micro (pore diameter < 100 μm) or macro (pore diameter > 100 μm). For colonisation of macropores to occur, the minimum pore size in which bone will form is claimed to be approximately 100 μm (Hulbert *et al.*, 1972). Other researchers have created scaffolds with pore sizes of between 150-300 μm and 500-710 μm to promote bone formation (Mikos *et al.*, 1993; Ishaug-Riley *et al.*, 1998). Mikos *et al.* (1993) observed that the rate of tissue ingrowth increased as the porosity and/or the pore size of implanted devices increased. Ishaug-Riley *et al.* (1998) performed *in vitro* studies using a foam type polymer (75:25 PLGA, 90 % porosity) scaffolds seeded with neonatal rat calvarial osteoblasts. A maximum penetration depth of osseous tissue of 220 $\pm$ 40 μm was reached after 56 days in the osteoblast/foam constructs with a pore size of 150-300 μm. For constructs of 500-710 μm pore size, the penetration depth was 190 $\pm$ 40 μm under the same conditions. The authors concluded that scaffold pore size and thickness did not significantly affect the proliferation or function of osteoblasts. However many of these pore sizes were determined using random pore geometries,

and hence do not define optimum pore sizes accurately; rather they define the range of pore sizes in which bone formation was observed.

Chang *et al.* (2000) conducted experiments to assess the differences in osteoconduction according to pore sizes and the influence of interconnectivity. Cylindrical porous HA specimens containing regular conduits, with pore diameters ranging from 50 to 500 μm, which were not interconnected (*i.e.* unidirectional channels), were fabricated using polyester fibres coated with HA slurry and compacted into a block shape. The fibers describing the pore architecture were then pyrolysed out *via* thermal sintering. In an attempt to evaluate the effects of interconnectivity and pore arrangement, cylindrical-, sponge- and cross-type scaffolds were also fabricated. Sponge-type scaffolds were fabricated using polyurethane foam with pores of 340 μm and for the cross-type scaffolds a polypropylene net (100x120 μm) was used. Both these structures were infiltrated with HA slurry and pyrolyzed as described previously. A summary of pore size and porosity of the porous HA implants is given in Table 2.3.

Table 2.3. Summary of pore size and porosity of the porous HA implants (Chang *et al.*, 2000).

Implant type (μm)	**Measured pore size (μm)**	**Total porosity (%)**	**Macropore porosity (%)**
Cylinder, 50	49.3 ± 1.63	42.3 ± 0.47	12.9 ± 0.79
Cylinder, 100	94.1 ± 1.28	49.9 ± 2.72	20.3 ± 3.96
Cylinder, 300	272.4 ± 5.4	42.1 ± 2.83	23.6 ± 1.63
Cylinder, 500	472.2 ± 8.2	47.3 ± 1.97	32.8 ± 1.81
Sponge	250.0 ± 5.0	83.9 ± 2.31	———
Cross	116.7 ± 5.9	67.6 ± 3.61	24.9 ± 4.51

Scaffolds were implanted for *in vivo* evaluation. After eight weeks, active osteoconduction was evident in each graft type. In the 100-500 μm cylindrical channel

groups, the bone ingrowth patterns resembled Haversian canal structures. For the sponge-type constructs, the new bone formed consisted of an irregular woven bone structure. The cross-type grafts showed an intermediate form of bone, between the cylindrical- and sponge-types. The amount of bone formation did not increase from four to eight weeks. Despite this finding, remodelling and bone marrow formation was found within the larger cylindrical types (300, 500 μm), and the sponge- and cross-types. The direction of bone formation within the cylindrical types was found to be parallel to the long axis of the pores, while an irregular bone pattern with no directionality was observed along the surface of the pores for the sponge-type. For the cross-type, bone ingrowth showed patterns of both the cylindrical and sponge-type at the same time. Scanning electron microscopy (SEM) images of the porous implants are shown in Figure 2.6. A biomechanical analysis was also carried out, in order to determine the maximum compressive strength before and after *in vivo* implantation for each scaffold type. A summary of the results obtained is shown in Table 2.4.

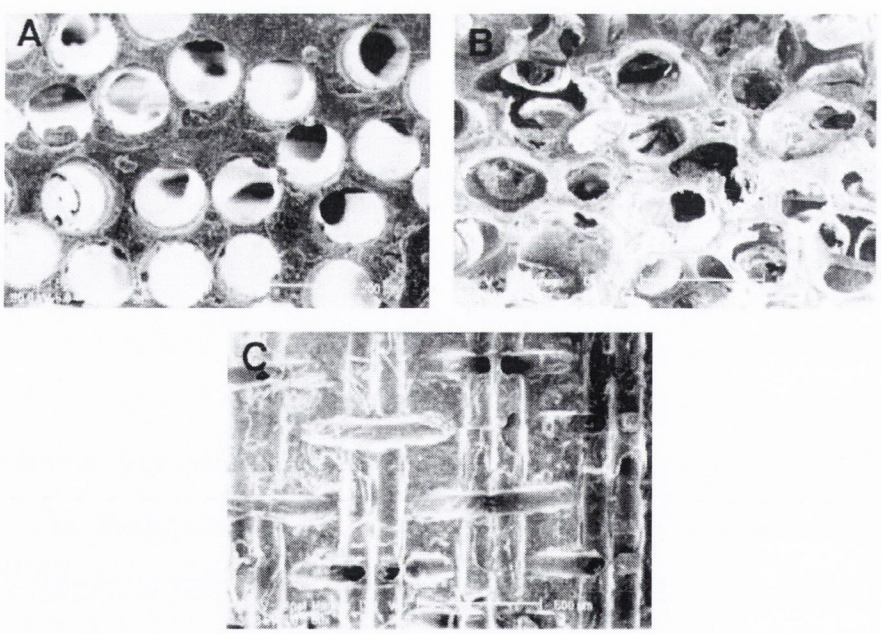

Figure 2.6. SEM images of porous implants. (A) Transverse cut of ∅ 100 μm sized cylindrical-type 120, (B) sponge-type and (C) longitudinal cut of cross-type porous HA (Chang *et al.*, 2000).

Table 2.4. Biomechanical analysis of porous HA implants (Chang *et al.*, 2000).

Implant type (μm)	**Pre-implant (MPa)**	**Post-implant (MPa)**	**$\triangle$ (MPa)**
Cylinder, 50	12.7 $\pm$ 1.36	14.5 $\pm$ 7.33	1.8 $\pm$ 8.69
Cylinder, 100	6.12 $\pm$ 2.02	8.65 $\pm$ 4.87	2.5 $\pm$ 6.89
Cylinder, 300	7.98 $\pm$ 1.66	15.8 $\pm$ 5.73	7.8 $\pm$ 7.39
Cylinder, 500	10.3 $\pm$ 3.58	11.5 $\pm$ 4.52	1.2 $\pm$ 8.10
Sponge	0.24 $\pm$ 0.05	4.53 $\pm$ 2.14	4.3 $\pm$ 2.19
Cross	0.19 $\pm$ 0.07	7.83 $\pm$ 3.26	7.6 $\pm$ 3.33

As can be seen from Table 2.4, the cylindrical configuration with 300 μm and the cross-type (100x120 μm) exhibited greater increases in mechanical strength than the other test configurations. It is interesting to note that in the cross-type (100x120 μm) constructs, a large increment in mechanical strength was observed also. It could be hypothesised that enhanced diffusion effects due to complete interconnectivity assisted this result. A more detailed study with varying pore sized cross-type implants may perhaps prove the importance of interconnectivity more clearly. A negative point to note with this study is that no detailed image analysis of the spatial distribution of the new bone formed was carried out. Compressive strengths alone do not provide any information on the penetration depths of the bone formed. For a graft to be considered entirely successful, a homogeneous distribution of bone should be observed throughout an entire construct.

Howe *et al.* (1974) implanted Teflon® scaffolds containing a single cylindrical pore with diameters ranging from 274 to 670 μm. The amount of ingression and spatial distribution of bone tissue was assessed for each pore diameter at weekly intervals over a sixteen week period. An optimum pore diameter of between 400 to 450 μm was observed to promote maximum bone ingression. It was also observed that bone deposition within the cylindrical channels appeared to be initiated at the pore walls.

Hollister *et al.* (2005) created HA scaffolds (8 mm diameter, 6 mm height) using an indirect solid free form (SFF) fabrication technique. Scaffolds with three different pore designs, including a circular pore, square pore and circular strut, each with three different pore diameters (*i.e.* nine designs) were implanted in a Yucatan minipig mandibular defect. Pore diameters for the circular and square pores were 400, 600 and 900 μm and for the circular strut were 600, 900 and 1200 μm. Scaffolds were assessed through micro-computed tomography (μ-CT) techniques. Bone was observed to occupy 40-50 % of the available pore volume at six weeks and 70-80 % of the available pore volume at eighteen weeks. There was no significant difference in the amount of bone fill based on either pore size or pore geometry. Based on these results the authors conclude that overall bone growth does not depend on pore sizes between the range of 400 and 1200 μm.

The pore size employed may also be dependent on the tissue-type desired. For example scaffolds with pore sizes less than 150 μm have been successfully used for regeneration of skin in burn patients (O'Brien *et al.*, 2004). Osteoblasts appear to exhibit greater cellular response when pore sizes of between 200 and 400 μm are employed (Chang *et al.*, 2000; Dennis *et al.*, 1992). This may be due to the curvature of the pore which may provide optimum compression and tension on the cells mechanoreceptors which allows them to migrate into openings of such a size (Boyan *et al.*, 1996).

2.4.4 Interconnectivity

A scaffold should provide an open porous network structure allowing for easier vascularisation, which is important for the recruitment and maintenance of penetrating cells from surrounding tissues and the development of new bone *in vivo*. The greater the degree of interconnectivity the easier it is for vascularisation to occur. Failure to develop an adequate vascular network will mean that only peripheral cells may survive or differentiate, supported by diffusion. Chang *et al.* (2000) proposed that the degree of interconnectivity rather than the actual pore size has a greater influ-

ence on osteoconduction. Interconnectivity is a physical characteristic that aids in the delivery of nutrients and removal of metabolic waste products. Some studies have shown that bone normally forms in the outer 250 μm periphery of scaffolds and that this may be explained by the lack of nutrient delivery and waste removal (Ishaug-Riley *et al.*, 1998). When the pore size of the scaffold is too small, pore occlusion can occur by cells preventing further cell penetration and bone formation (Leong *et al.*, 2003). Many of the scaffolds created through traditional fabrication techniques produce systems with pores of specific diameter. However, the contact area between adjacent pores, which is termed fenestration, is sometimes limited and influences the degree of interconnectivity of a scaffold construct. An example of this in relation to salt particulate leaching is shown in Figure 2.7, although many of the foaming techniques currently used also produce poor spherical fenestrations between adjacent pores.

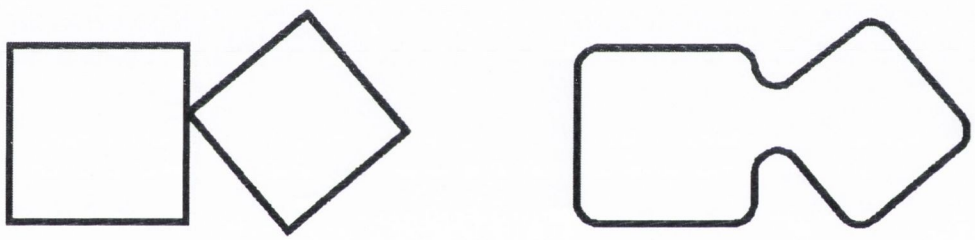

Figure 2.7. Example of pore fenestration (A) Poor contact between adjacent pores due to small areas of contact and sharp radii at edges and corners. (B) Improved contact between adjacent pores due to the formation of thick salt bridges between particles, as well as an increase in the radius of curvature at the edges and corners of each salt particle (Murphy *et al.*, 2002).

Reduced fenestration between adjacent pores may also be responsible for peripheral tissue formation commonly observed in tissue engineering scaffolds due to nutrient transport limitations and possible pore occlusion. It is therefore essential that a scaffold possess a high degree of interconnectivity with sufficiently large pore fenestration windows in conjunction with a suitable pore size and macroporosity in order to minimise diffusion limitations and prevent pore occlusion.

2.4.5 Surface characteristics and cell surface engagement

The cellular response to a substrate material is of significant interest in order to determine optimal surface characteristics to promote osteointegration and cell viability. Attachment, adhesion and spreading of cells belong to the first phase of cell/material interactions and the quality of this first phase will influence the cells capacity to proliferate and to differentiate on contact with the substrate (Anselme, 2000). This first phase depends on the adsorption of proteins onto the materials surface. Cells interact with their substrate through focal contacts. The focal contacts are specialized microstructures anchored within the cell to cytoskeletal microfilaments, which underlie the cytoplasmic membrane. Components of the microstructure traverse the cytoplasmic membrane, permitting the cell to bind to its extracellular matrix *via* proteins called integrins (Boyan *et al.*, 1996). A material is conditioned by the components of the fluid in which it is immersed, whether it be serum, saliva or cell culture media. From this serum, proteins are adsorbed onto the surface of the substrate.

The energy at the surface of a biomaterial is defined by its general charge density and the net polarity of the charge. Thus, a surface with a net positive or negative charge may be hydrophilic in character, whereas a surface with a neutral charge may be more hydrophobic (Boyan *et al.*, 1996). Hydrophilic surfaces such as glass therefore have high surface energies, whereas hydrophobic surfaces such as PTFE or polystyrene have low surface energies. Cells do not interact with a naked material either *in vitro* or *in vivo*. At each step, the material is conditioned by the biological fluid components. Initially, the role of surface energy, as dictated by the surface roughness, topography, and composition of the substrate may play a major role in determining which proteins are adsorbed onto the surface, as well as whether or not the cells themselves adhere to the surface (Kieswetter *et al.*, 1996). Osteoblast/material interaction depends on the surface characteristics which determine how biological molecules will adsorb to the surface and more particularly determine the orientation of adsorbed molecules which in turn determines the cell behaviour on contact with

the substrate. Cells in contact with a surface will firstly attach, adhere and spread. This first phase depends on previously described adhesion proteins. Thereafter, the quality of this adhesion will influence their morphology, and their capacity for proliferation and differentiation.

Presently, there is a lack of understanding of how material properties, including chemistry, surface energy, wettability, roughness, and topography, as well as percent porosity and pore size in 3-D substrates, influence cell behaviour and differentiation (Ciapetti *et al.*, 1996).

Based on the available literature it appears that key critical parameters of scaffold design on cellular response include the following: open porosity, pore size, pore interconnectivity, substrate material chemistry, scaffold permeability and surface roughness.

A significant challenge in developing porous scaffolds is the ability to homogeneously seed cells within the core of the scaffold construct. The available methods of improving cell material interaction are through modifying the material as well as adjusting the porosity (Cerroni *et al.*, 2002). Furthermore, cell attachment and adhesion are critical factors determining the proliferation and function of cells (Malik *et al.*, 1992). Cells loaded as suspensions to the surface of the scaffold will firstly adhere, grow and then migrate (Anselme, 2000).

The initial responses of cells in contact with a substrate material are attachment, adhesion and spreading. Cells that are seeded in the interior regions of a scaffold construct tend to migrate towards the surface or periphery where the nutrient concentrations are significantly higher (Salgado *et al.*, 2004). Formation of cell colonies on the periphery of scaffolds limits the adhesion of remaining cells on the surface of the scaffold and prevents the migration of cells into the scaffold (Anil-Kumar *et al.*, 2005), and is also hypothesised to be responsible for peripheral tissue formation due to mass transfer limitations (Martin *et al.*, 1998).

Surface treatment of HA, by sintering at various temperatures, results in the variation of its chemical and crystallographic characteristics which are reported to

influence osteoblastic activity. Frayssinet *et al.* (1997) sintered HA disks at different temperatures ranging from 850 to 1350 °C to determine the effects on cell growth rates. It was observed that the cell growth correlated with the ceramic sintering temperatures, although no significant differences were noted in cell adhesion from the different samples. The calcium and phosphorus concentration in the culture medium in contact with ceramics sintered below 1050 °C decreased during the culture period, and increased for the ceramics sintered at higher temperatures. Ceramics sintered between 1100 °C and 1250 °C brought about an increase in Ca and P concentrations while ceramics sintered at higher temperatures did not induce any changes. SEM examination showed that ceramic samples sintered at 850 °C consisted of small grains with pores between them. Conversely samples sintered at 1200 °C were made of larger grains without any visible pores, thereby decreasing the surface area of material in contact with the culture medium. The authors concluded that the modification of the culture medium brought about by high-surface area ceramics could influence the growth of cells when in contact with such ceramics.

Deligianni *et al.* (2001) conducted a study in an attempt to examine the effect of surface roughness of HA on cellular adhesion, proliferation, differentiation and detachment strength. Parameters known to influence cell response such as surface chemical composition and crystallinity were maintained constant, while three different values of surface roughness were assessed. Human bone marrow cells were plated onto HA disc-shaped pellets prepared from synthetic HA powder. The pellets were sintered and polished with three grades of silicon carbide (SiC) paper (180-, 600- and 1220-grit). Tissue culture plates were used for control purposes. The authors found that cells attached and grew faster on culture plastic in comparison with HA. No statistically significant differences were observed in the expression of ALP (alkaline phosphatase, a marker of osteogenic differentiation) activity on all three surfaces, although lower ALP activity was observed on the roughest HA surface until the eighth day, and another culture of the same roughness showed similar low ALP activity after thirteen days. After sixteen days ALP activity was expressed similarly on all

surfaces tested. These results suggest that there is a time delay in the expression of ALP activity on the rougher surfaces. The authors found that cell adhesion, proliferation and detachment strength were sensitive to surface roughness and increased as the roughness of HA increased. The authors concluded that since surface roughness enhances surface wetting properties, this facilities cell attachment directly *via* enhanced formation of focal contacts or indirectly through selective adsorption of serum proteins required for cell attachment.

From the literature it is apparent that cells respond differently (in terms of adhesion, proliferation, activity *etc.*) depending on the properties (surface chemistry and surface roughness) of the substrates they are attached to and present many challenges in developing and optimising scaffolds with tailored affinity for cell growth.

2.5 Scaffold architectures

2.5.1 Introduction

This section describes the main types of scaffold architectures that are commonly used for tissue engineering purposes and discusses the resulting associated issues. Techniques for creating various types of scaffold architectures will be addressed in Sections 2.6 and 2.7. The response of these scaffold-types when implanted *in vivo* will be reviewed in Section 2.10.

2.5.2 Single random porous domain scaffolds

Many of the sponge-type scaffolds provide a single domain into which cells are seeded and, during *in vitro* culturing, proliferate and migrate to a small extent into the available pores. The populating cells cannot migrate into the interior regions of the scaffold as discussed earlier. This is believed to be due to insufficient delivery of nutrients and oxygen, and also removal of metabolic waste products (Galban and Locke, 1999).

In these scaffolds, a single pore system must accommodate the conflicting effects

of cell proliferation and matrix formation with the need for greater nutrient delivery and metabolic waste removal (*i.e.* with increasing cell proliferation, the availability of nutrients becomes diminished). This inevitably leads to a thin layer of bone at the periphery of the scaffold (Cartmell *et al.*, 2003), and a necrotic region at the core of the scaffold. The formation of this thin layer of tissue (approximately 500 μm thick) forming at the periphery of a scaffold, with diminished cell matrix deposition in the interior regions, has been referred to as the "M&M effect". This is analogous to the popular brand of chocolate sweet, having a dense crust and a soft core (Karande *et al.*, 2004).

Exclusive peripheral tissue formation may be a manifestation of the fact that as cells within the pores of the scaffold begin to proliferate and secrete extracellular matrix (ECM), they simultaneously begin to occlude the pores and decrease the supply of nutrients to the interior (Karande *et al.*, 2004). Scaffolds with limited interconnectivity/fenestration may also accelerate this phenomenon. It is also pertinent to note that much higher rates of mass transfer exist at the periphery of a scaffold, and that these higher rates promote mineralisation, further limiting the mass transfer of nutrients to the core of a scaffold (Martin *et al.*, 1998).

The key parameter responsible for this phenomenon is believed to be the limited transport of oxygen to the interior regions of a scaffold construct (Ishaug-Riley *et al.*, 1998; Martin *et al.*, 1998; Obradovic *et al.*, 2000; Carrier *et al.*, 2002; Martin *et al.*, 2004; Malda *et al.*, 2004a; Dunn *et al.*, 2006). Some examples of single random porous domain scaffold architectures are shown in Figure 2.8.

Creation of scaffolds with well defined internal architectures is essential to overcome limitations of mass transfer. Previous researchers have also demonstrated that control over the interior architecture is crucial to ensure scaffold vascularisation and bone deposition (Mikos *et al.*, 1993; Chu *et al.*, 2002). Non-uniform micro environments can produce regions with insufficient nutrient concentrations which can inhibit cellular activity and prevent the formation of new tissue.

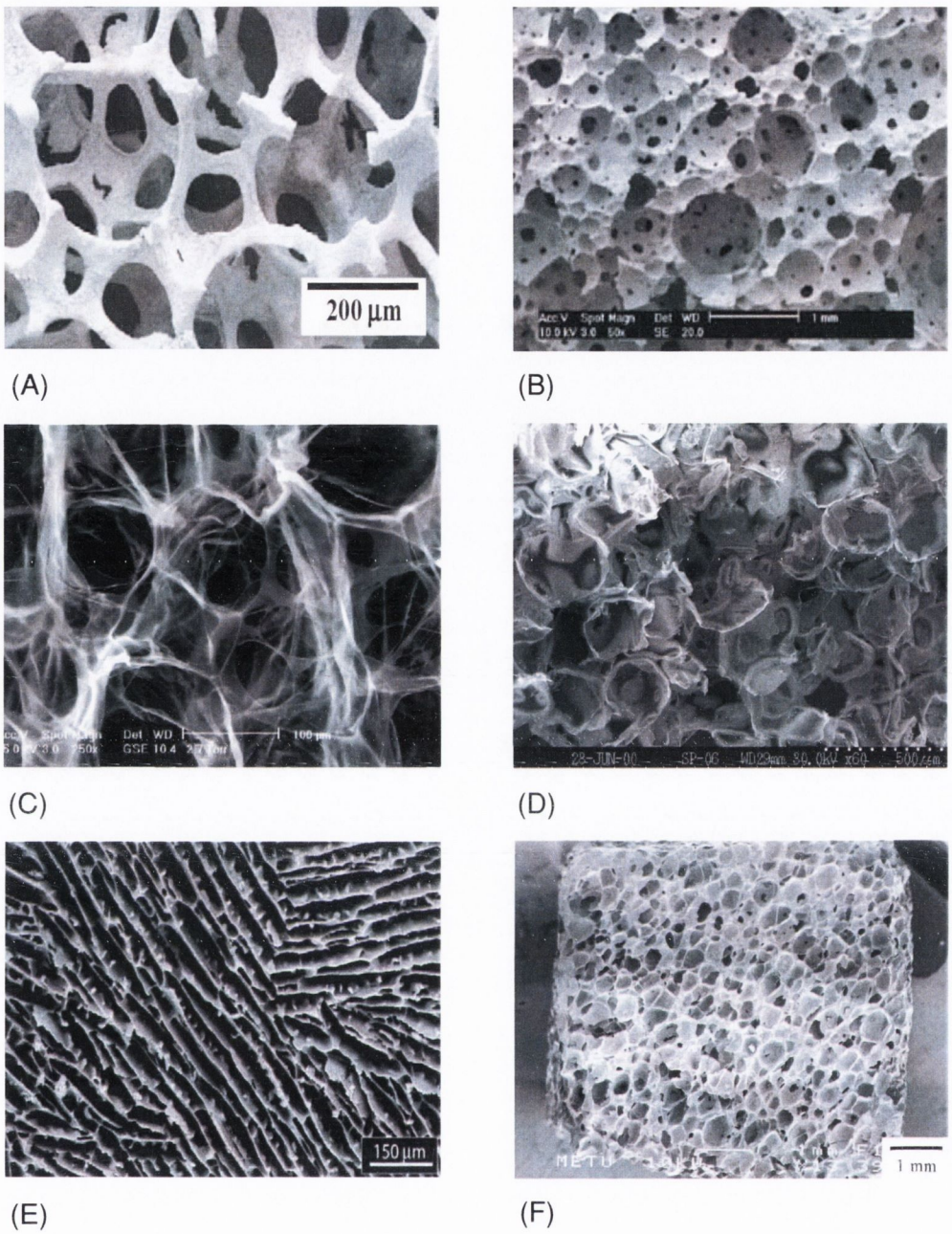

Figure 2.8. Single random porous domain scaffolds (A) SEM morphologies of a HA porous scaffold fabricated through a polyurethane foam reticulate method (Kim *et al.*, 2004) (B) Porous HA ceramic prepared using a modified slip casting technique incorporating foaming of the slip and setting using methylcellulose (Cyster *et al.*, 2005) (C) ESEM micrographs of collagen-glycosaminoglycan (CG) scaffolds produced through freeze-drying using a constant cooling rate technique (O'Brien *et al.*, 2004) (D) Electron micrographs of the cross-section of solvent cast PLG polymer scaffolds prepared using the salt fusion process (Murphy *et al.*, 2002) (E) Cross-sectioned microstructure of porous HA scaffolds (64% porosity) fabricated through freeze-casting (Deville *et al.*, 2006) (F) SEM micrographs of HA bioceramics (60% porosity) fabricated through foaming of ceramic slip (Engin and Tas, 1999).

2.5.3 Single regular porous domain scaffolds

The limitations of single random porous domain scaffolds has prompted researchers to develop and fabricate scaffolds with a single macro-pore phase of regular morphology (*e.g.* orthogonal arrays of channels) through rapid-prototyping techniques. This removes the tortuosity of random pore structures which impedes the predictable diffusion or flow of nutrients through the structure and it offers a unidirectional macropore arrangement for initial cell seeding (Rose *et al.*, 2004). Interestingly, these scaffold structures have suffered the same performance limitations of the random pore structure; bone forms in the peripheral regions of the scaffold but not in the interior when implanted *in vivo* (Chu *et al.*, 2002). This will be explored in greater detail in Section 2.10.2.

Regular architecture scaffolds permit cells to be seeded in the core much more readily than random architecture scaffolds and create environments which encourage uniform conditions for promoting cell viability. The added advantage of developing regular architecture scaffolds is that they permit parametric analyses to be conducted, which is essential in developing scaffolds that can repeatedly provide a germane cell environment. Finite element diffusion/perfusion studies are more feasible when regular architecture-type scaffolds are employed. Some examples of single regular porous domain scaffold architectures are shown in Figure 2.9. Advantages and limitations of these fabrication techniques are compared in more detail in Section 2.7. The increasing capabilities of μCT technology in conjunction with rapid-prototyping techniques offers great potential in automating the development of scaffolds with geometries tailored to a specific defect site for individuals.

However, with respect to these single regular porous domain scaffolds, the underlying limitations of uniform cell seeding, nutrient delivery and peripheral bone tissue formation have not been investigated sufficiently. The *in vivo* response to these single regular domain scaffolds will be addressed in Section 2.10.

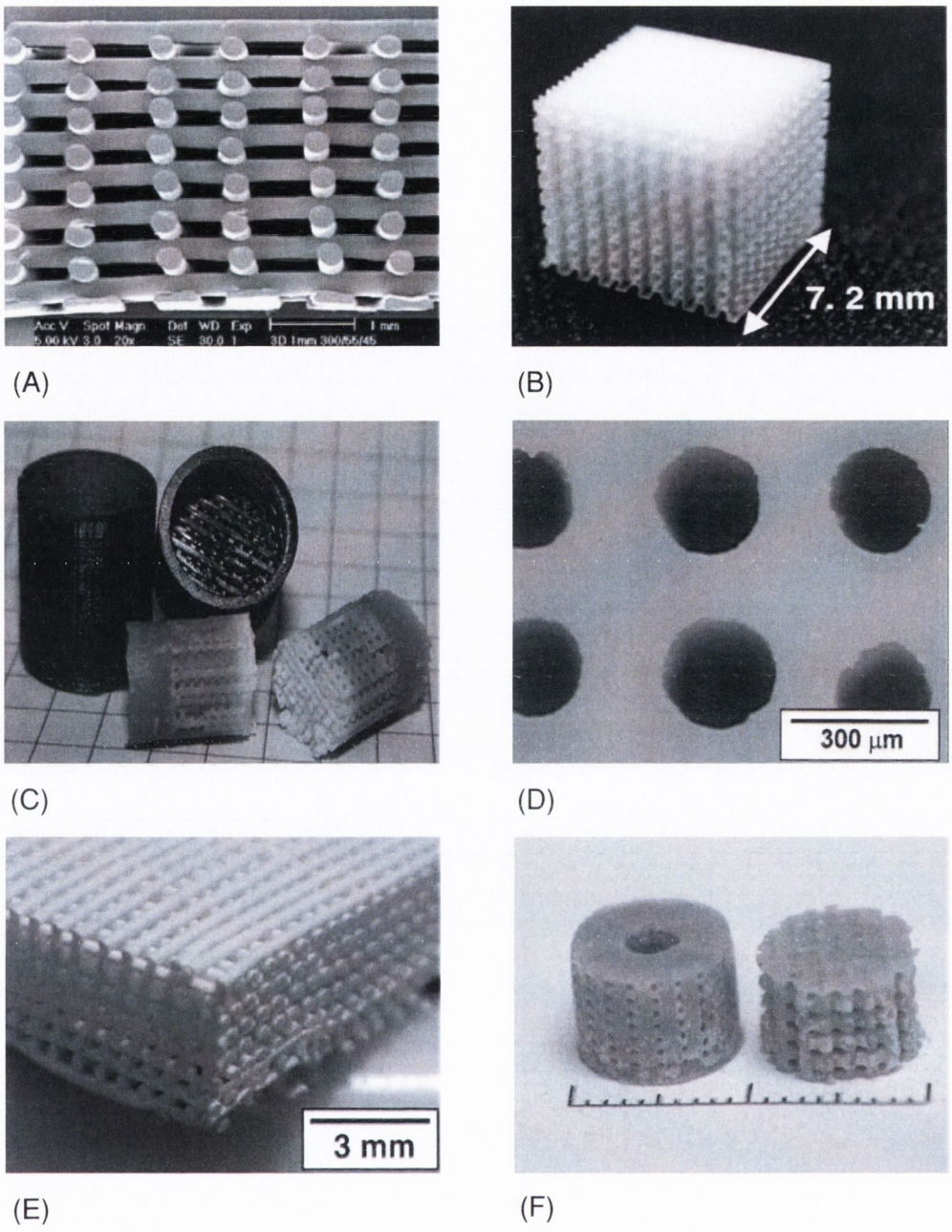

(A) (B)

(C) (D)

(E) (F)

Figure 2.9. Single regular porous domain scaffolds (A) SEM section of a 3D poly(ethylene glycol)-terephthalatepoly(butylene terephthalate) scaffold employing a fiber deposition technique (Woodfield *et al.*, 2004) (B) Optical micrograph of a tetragonal zirconia polycrystal (TZP) ceramic structure fabricated through CNC-machining and lamination and dip-coating (Jun *et al.*, 2006) (C) Resin casting moulds (made through stereo lithography (SL)) and sintered structures made of hydroxylapatite (Woesz *et al.*, 2005) (D) Optical micrograph of the cross section of a HA macrochannelled scaffold formed through a coextrusion process (Koh *et al.*, 2002) (E) Macrochanneled PCL/HA scaffold fabricated using the rapid direct deposition process (Koh *et al.*, 2006) (F) Sintered HA scaffolds fabricated through indirect casting of epoxy molds made by stereo lithography (SL). Scale bar is 2 cm (Chu *et al.*, 2002).

2.5.4 Multi-domain porous scaffolds

In an attempt to overcome the limitations outlined previously, scaffolds have been developed with distinct and separate domains. In this configuration a scaffold can possess meso-pores (90-100 μm) in which cells proliferate and lay down new matrix and also macro-channels (300-500 μm) which provide higher levels of nutrient and oxygen delivery and metabolic waste removal through diffusion. The macro-channels may also permit uniform cell seeding and facilitate vascularisation. Depending on the pore size, the meso-pores may also facilitate vascularisation to some extent. Examples of multi-domain porous scaffold architectures are shown in Figure 2.10. Rose *et al.* (2004) assessed the *in vitro* response of human osteosarcoma (HOS TE85) cells when seeded onto porous HA scaffolds (fabricated through a foam-gel method) with a centrally aligned channel in the centre (Figure 2.10 A). A series of scaffolds with channel diameters ranging from 170 to 421 μm were produced. The authors observed that cell coverage within these centrally aligned channels increased with increasing channel diameter; from 22 $\pm$ 3 % in the 170 μm diameter channel to 38 $\pm$ 6 % coverage in the 421 μm channel. The authors suggest that this incorporation of a specific macroarchitecture (*i.e.* centrally aligned channel) into a porous scaffold improves nutrient transfer to the scaffold centre. However, in this study no comparison was made to scaffolds without a centrally aligned channels, and therefore warrants further investigation.

Lin *et al.* (2003) fabricated poly(L-lactide-co-30%-DLlactide) PLDL porous structures by using a unique process that combined the use of a blowing agent (azodicarbonamide) to create open-cell reticulated foams with axially aligned wires that were removed to create continuous unidirectionally oriented channels measuring 100 μm in diameter (Figure 2.10 B). Osteoblast-like cells (MC3T3-E1) were seeded onto these scaffold structures to assess the biocompatibility of the material. Viable cells were largely seen on the periphery of the scaffold although some viable cells were observed in the interior. No detailed investigations or comparisons were made to scaffolds that did not contain unidirectionally oriented channels.

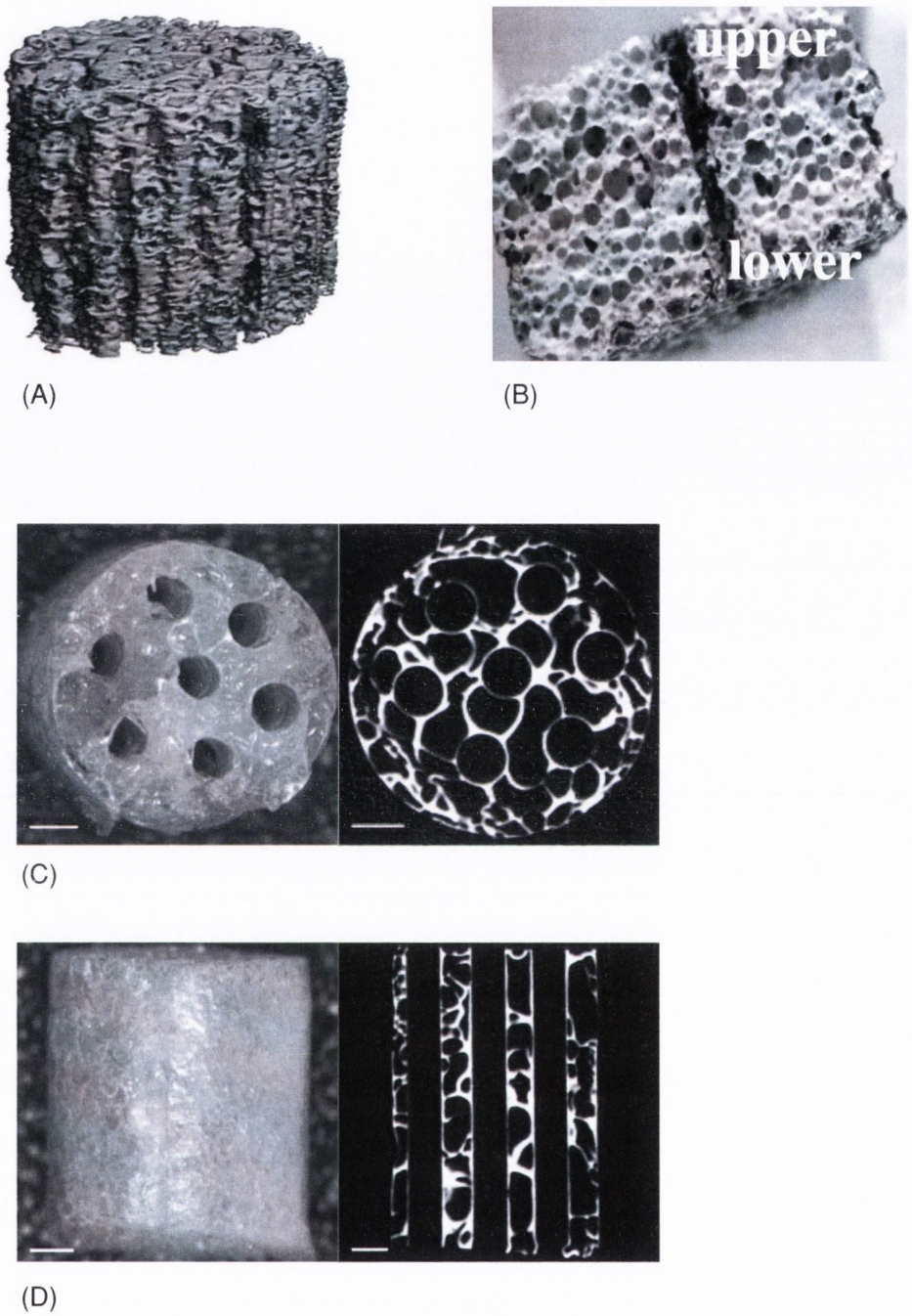

Figure 2.10. Multi domain porous scaffolds (A) Random porous HA scaffold with single centrally aligned channel (421 μm) (Rose *et al.*, 2004) (B) Micro-CT images of oriented porous PLDL scaffolds created using a solution coating and porogen decomposition technique (Lin *et al.*, 2003) (C) and (D) Cross-sectional and longitudes views of a PLGA scaffold created from parallel wire moulds (left=micrograph, right=μCT slices), scale bar is 500 μm (Moore *et al.*, 2006).

Until recently, few researchers have adopted this approach of creating scaffolds with distinct and separate domains. An area of research with increasing application is in nerve generation where such channels have been used to provide spatial guidance and increased surface area for neuron growth (Hadlock *et al.*, 2000) and spinal cord axon regeneration (Moore *et al.*, 2006). One of the reasons for this lack of development of multi-domain scaffolds for bone tissue engineering purposes may be due to the difficulty in developing techniques to create such architectures in a manner suitable for clinical applications. Therefore, there is limited information on the *in vitro* and *in vivo* response to scaffolds with such architectures.

2.6 Traditional scaffold fabrication techniques

Several techniques have been developed to fabricate scaffolds. These include solvent-casting and particulate-leaching, gas foaming, fibre meshes/fibre bonding, phase separation, melt moulding, emulsion freeze drying, solution casting and freeze drying (Table 2.5). Traditional methods of fabricating scaffolds, through material processing and casting, have largely been unsuccessful in controlling the internal architecture to a high degree of accuracy or homogeneity, since the resulting interior architectures are determined by the processing technique. For example, particulate leaching is a process whereby the internal architecture is determined by embedding a high density of salt crystals into a dissolved polymer or ceramic matrix. The dissolved mixture is then poured into a mould and treated under heat and pressure to form the external shape. The salt particles are then leached out to leave interconnecting interior pores. Running the salt crystals through a sieve to obtain a specific range of pore size can control the pore diameters; although the agglomeration of salt particles can alter the eventual pore size and pore distribution during leaching (Leong *et al.*, 2003). The fenestration windows between adjacent salt crystals can also be limited, since salt crystals are inherently cuboidal. Particulate leaching techniques are limited to producing thin membranes (2-3 mm), due to the difficulty in ensuring complete removal of the embedded particles. Also, there is little control over the orientation and the degree of interconnectivity. However the degree of interconnectivity can be improved by having a high density of salt particles (Hollister *et al.*, 2000; Ishaug-Riley *et al.*, 1998) and also by fusion of the salt crystals prior to infiltration (Murphy *et al.*, 2002), to improve pore fenestration.

Tancred *et al.* (1998a) developed a lost wax process to create exact replicas of select bovine cancellous structures using HA, β-TCP, and bio-glasses. Although an exact replica of bone, the structure has the same limitations as other scaffolds with random porosity and interconnectivity.

Table 2.5. Conventional scaffold processing techniques for tissue engineering (Yang *et al.*, 2001; Leong *et al.*, 2003).

Process	Advantages	Disadvantages
Solvent casting and particulate leaching	Large range of pore sizes	Limited membrane thickness (3 mm)
	Independent control of porosity and pore size	Limited interconnectivity
	Crystallinity can be tailored	Residual porogens
	Highly porous structures	Poor control over internal architecture
Fibre bonding	High porosity	Limited range of polymers
		Residual solvents
		Lack of mechanical strength
Phase separation	Highly porous structures	Poor control over internal architecture
	Permits incorporation of bioactive agents	Limited range of pore sizes
Melt moulding	Independent control of porosity and pore size	High temperature required for nonamorphous polymer
	Macro shape control	Residual porogens
Membrane lamination	Macro shape control	Lack of mechanical strength
	Independent control of porosity and pore size	Limited interconnectivity
Polymer/ceramic fibre composite foam	Independent control of porosity and pore size	Problems with residual solvent
	Superior compressive strength	Residual porogens
High-pressure processing	No organic solvents	Nonporous external surface
		Closed-pore structure
Freeze drying	Highly porous structures	Limited to small pore sizes
	High pore interconnectivity	
Hydrocarbon templating	No thickness limitation	Residual solvents
	Independent control of porosity and pore size	Residual porogens

2.7 Solid free form (SFF) fabrication technologies

Rapid prototyping (RP) or solid free form (SFF) fabrication technologies are currently being used by investigators to manufacture tissue engineering scaffolds (Bose *et al.*, 1999; Chu *et al.*, 2001; Hollister *et al.*, 2000; Hutmacher, 2000; Wintermantel *et al.*, 1996; Xiong *et al.*, 2001). Each SFF fabrication process has its own advantages and disadvantages in fabricating scaffolds as summarised in Table 2.6. SFF methods are based on the technique that a material in either powdered or liquid form is solidified one layer at a time. It is thus an additive process unlike traditional methods of manufacturing which are subtractive based. Each layer is created as defined by a computer-generated file. Once the layer is complete, the build platform is indexed downward by one layer thickness and the process is repeated. The main systems that fall under this category are:

(i) Stereolithography (SLA)

(ii) Selective laser sintering (SLS)

(iii) Fused deposition modelling (FDM)

(iv) Three-dimensional printing (3-DP)

The main limitations here include the use of toxic binders, poor feature symmetry and limited material choice. Due to these material limitations, researchers have also used SFF techniques to indirectly cast scaffolds with controlled internal and external architecture by means of a lost mould process (Chu *et al.*, 2001; Taboas *et al.*, 2003). Manufacturing of these scaffolds consists of three different types of development and optimisation work. They include:

(i) Mould design and sacrificial mould fabrication

(ii) Material casting

(iii) Thermal or chemical removal of mould

Table 2.6. Advantages and limitations of SFF fabrication techniques

Technique	Advantages	Limitations
SLA	Relatively easy to remove support materials	Limited by the development of photopolymerizeable and biocompatible, biodegradable liquid polymer material
	Accurate small features	
SLS	Good compressive strengths	High processing temperatures
	Greater material choice	Materials trapped in small inner features are difficult to remove
	Solvent free	
FDM	No material trapping within small features	Requires support material for irregular structures
	Solvent free	Anisotropy between XY and Z direction
	Good compressive strengths	
3D-P	Greater material choice	Materials trapped in small inner features are difficult to remove
	Low heat effect on raw material	Use of toxic organic solvents
		Lack of mechanical strength

Lost mould processes are mainly suited to ceramic infiltrates as ceramics are typically sintered to temperatures in excess of 1000 °C, which ensures complete removal of the polymer mould. When attempting to fabricate polymer scaffolds through indirect fabrication methods, an extra step of creating a ceramic-type mould is required. This ceramic mould is infiltrated through melt or solvent casting depending on the desired polymer. Once cured, the ceramic mould can be removed through solvent dissolution. The choice of solvent for mould dissolution is dependent on the cast and mould material. This iteration further reduces the quality of the final scaffold in terms of pore symmetry and material properties due to polymer exposure to solvents. An advantage of indirect casting is the production of discrete composite scaffolds in which material regions are mechanically interdigitated (Figure 2.11), as

well as the incorporation of microporosity within the scaffold material which allows for preconditioning with bioactive agents and manipulation of the surface roughness.

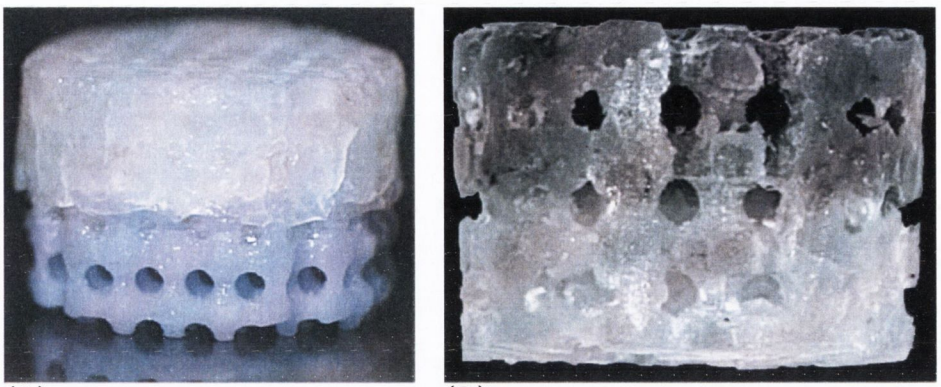

(A) (B)

Figure 2.11. Biphasic scaffold architectures. (A) Biphasic PLA/HA scaffold (top=PLA, bottom=HA). PLA global pores are 600 μm, HA global pores are 500 μm. (B) Biphasic PLA/PGA scaffold (top=PGA, bottom=PLA), 800 μm orthogonal pores (Taboas *et al.*, 2003).

2.8 Fluid conductance and permeability

Fluid flow within the pore spaces of scaffolds or between individual trabeculae in the case of bone samples is of great importance with respect to tissue engineering. Hui *et al.* (1996) observed that the fluid conductance in cylindrical trabecular bone grafts was found to be the best predictor of their clinical success as scaffolds in the rabbit tibial diaphysis. The authors tested the hypothesis that graft-host union depends on the fluid conductance of the graft. Cylindrical cancellous bone specimens were trephined from fresh porcine femoral heads in a direction either parallel or perpendicular to the femoral axis. Each specimen was inserted in tightly fitted silicone tubing and connected to a perfusion apparatus. The conductance (C) [$m^3s^{-1}Pa^{-1}$] to fluid flow of the graft was calculated as

$$C = \frac{dQ}{dP} \tag{2.2}$$

where Q [m^3s^{-1}] is the induced flow and P [Pa] is the pressure drop across the graft.

The grafts (still fitted inside the silicone tubing) were transplanted into 35 rabbits and examined after nine weeks post-implantation. The tibia graft junctions were examined *via* light microscopy and classified into union or non-union categories. Grafts with union were defined as those having fusion with at least the proximal tibia and having osteoblasts, microvessels and fibrous tissues, but no blood clots at the graft-host interface. The authors observed that the graft-host union is not affected by the effect of the length, porosity or orientation of the graft alone, but rather by their simultaneous effect expressed as conductance. A threshold conductance was found to be around 1.5 x 10^{-10} $m^3s^{-1}Pa^{-1}$

Permeability (κ) [m^2] can be considered as the conductance of the graft normalised by the physical size of the graft and the viscosity of the fluid.

$$\kappa = \frac{CL\mu}{A} \tag{2.3}$$

where A is the cross-sectional area of the graft [m^2], L is the length of the graft [m], μ is the viscosity of the fluid [Pa·s] and C is the conductance of the graft [$m^3s^{-1}Pa^{-1}$].

Nauman *et al.* (1999) conducted experiments to determine the dependence of intertrabecular permeability on flow direction and anatomical site. The intertrabecular permeabilities obtained ranged from 2.68 x 10^{-11} to 2.00 x 10^{-8} m^2. The transverse permeabilities obtained were, in general, lower than the respective longitudinal values. The ratio of longitudinal to transverse permeabilities depended strongly on anatomical site. A longitudinal to transverse permeability ratio of 2.05 was found for the human vertebrae and a ratio of 23.3 was found for the human proximal femur, which is thus greater by an order of magnitude. As can be seen from Table 2.7, the permeabilities of specimens from the bovine tibia and human femur were not significantly different.

Radisic *et al.* (2005) evaluated the permeability of a porous poly(glycerol-sebacate) scaffold fabricated by means of the particulate salt leaching technique and obtained a value of 8.1 $\pm$ 0.4 x 10^{-12} m^2. This value of permeability, which is approximately three orders of magnitude lower than that of cancellous bone is indicative of a poorly

Table 2.7. Permeabilities for a given anatomic site (Nauman *et al.*, 1999).

Anatomic site	**Longitudinal** K_L ($x10^{-9}$ m^2)	**Transverse** K_T ($x10^{-9}$ m^2)	**Permeability ratio** K_L / K_T
Human vertebral body	7.22	3.52	2.05
Human proximal femur	5.13	0.22	23.3
Bovine proximal tibia	3.17	0.48	6.60

interconnected structure.

In another study by Li *et al.* (2003), the permeabilities of various ceramic porous structures including commercially available scaffolds, bone and coral were measured. These porous structures of varying porosity (50-80%) had a range of permeabilities (Figure 2.12) between 0.03 and 0.53 x 10^{-9} m^2. The authors found a positive correlation existed between porosity and permeability, provided that similar pore interconnectivity existed. Also for structures with the same porosity, permeability values decreased for smaller pore sizes.

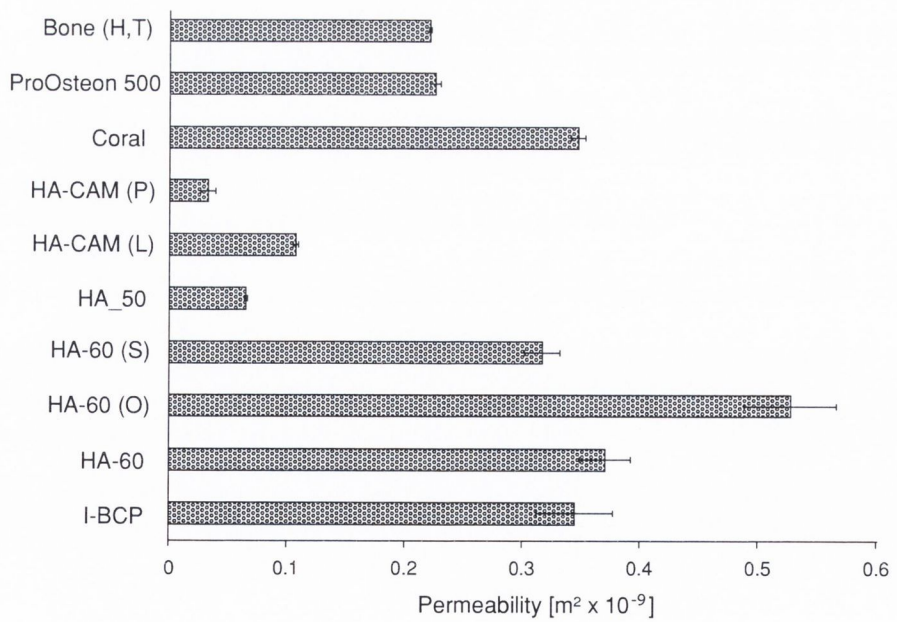

Figure 2.12. Permeability values for various ceramic scaffolds (Li *et al.*, 2003).

Another study by Agrawal *et al.* (2000) measured the permeability for PLGA scaffolds (50:50) and observed a positive correlation with increasing porosity. The values for permeability in Table 2.8 are expressed in units of m^4/Ns, which is the specific hydraulic permeability. Assuming a viscosity coefficient for water as .001 Pa·s, the range of hydraulic permeabilities is 2.1 - 16.1 x 10^{-12} m^2. These low values of permeability might suggest structures with a poorly interconnected structure, or structures with limited pore fenestrations and hence may not facilitate vascularisation when implanted *in vivo*.

Table 2.8. Permeability of PLGA scaffolds of varying porosity (Agrawal *et al.*, 2000).

Salt:Polymer ratio (w/w)	**% Porosity**	**Permeability (m^4/Ns)**
14:1	92.4 ± 0.4	16.1 ± 6.4 x10^{-9}
7:1	87.3 ± 1.6	9.1 ± 2.3 x10^{-9}
3.5:1	80.3 ± 2.3	2.1 ± 2.8 x10^{-9}

From a tissue engineering perspective, the variation of permeability with anatomic site may have important implications for the geometric design of synthetic bone substitutes. It is likely that the critical conductance depends on the ability of blood to pass through the bone substitute relative to that of the surrounding bone. This suggests that permeability may be more appropriate than conductance for determining the clinical success of bone grafts. The optimal bone substitute must have a greater permeability than the surrounding bone. If the principle direction of blood flow is not known, the permeability of the substitute must be greater than the average longitudinal permeability for that anatomic site.

2.9 Cell seeding

Cell seeding of scaffolds is an important step for tissue engineering systems and is often overlooked as a design parameter in scaffold fabrication. A geometrically small 3D scaffold (e.g. 5 mm diameter x 2 mm thick), can present a significant challenge to distributing a high density of cells efficiently and uniformly throughout the scaffold volume (Martin *et al.*, 2004). In order to develop cell-seeded scaffolds for successful clinical applications using high initial cell densities, cells should be seeded with a high efficiency in order to limit the biopsy sizes required and/or the extent of cell expansion (Wendt *et al.*, 2005). The initial cellular distribution is important insofar as a homogeneously seeded scaffold forms the basis for subsequent uniform tissue formation, provided the transport of nutrients is not limited.

2.9.1 Static cell seeding

Static seeding is by far the most common method of seeding scaffolds with cells. Essentially cells are suspended in a specific volume of medium (typically at a concentration of 1 x 10^6 cells/mL) and delivered directly onto the surface of the scaffold by means of a micropipette. This technique is often associated with low seeding efficiencies and non-uniform cell distributions within scaffolds. This is partially due to the manual- and operator-dependent nature of the process (Wendt *et al.*, 2005). Bioreactor systems have been developed to overcome some of these issues and these are discussed in the next section.

2.9.2 Dynamic cell seeding and culturing

Some researchers have attempted to overcome the non-homogeneous cell distribution of random single phase scaffolds by employing perfusion systems (Wendt *et al.*, 2003), orbital shaker systems (Almarza and Athanasiou, 2004; Rose *et al.*, 2004), spinner-flasks (Vunjak-Novakovic *et al.*, 1999; Wendt *et al.*, 2003; Almarza and Athanasiou, 2004), rotating wall vessels (Vunjak-Novakovic *et al.*, 1999) and low

pressure vacuum systems (Dong *et al.*, 2001b; Wang *et al.*, 2006) with some success. Examples of some of these devices are shown in Figure 2.13.

Spinner-flasks: Cells are delivered to the scaffold by convection. During subsequent culture, medium stirring enhances the mass transfer to the scaffold. Turbulent flows exist at the periphery of the scaffolds, which can result in the formation of fibrous outer capsules (Vunjak-Novakovic *et al.*, 1999).

Rotating-wall vessels: The vessel walls are rotated such that the drag force (F_d), centrifugal force (F_c) and the net gravitational force (F_g) acting on the construct are in equilibrium. The scaffold construct remains in a continuous state of free-fall.

Hollow-fiber bioreactors: Enhance the mass transfer during culture of highly metabolically active cells such as hepatocytes. Cells are typically embedded in a gel and placed in the lumen of a permeable hollow fiber and medium is perfused over the exterior boundaries of the fibers.

Direct perfusion bioreactors: Medium is perfused directly through a porous scaffold using a pump system. This system has been used to initially seed scaffold constructs (Wendt *et al.*, 2003), but also for subsequent culturing purposes (Cartmell *et al.*, 2003; Janssen *et al.*, 2006).

Vacuum systems: This type of device has been used in attempt to facilitate the perfusion of a larger number of cells into a porous scaffold by using a low pressure (100 mmHg) system for a short period of time (100 secs.) (Wang *et al.*, 2006).

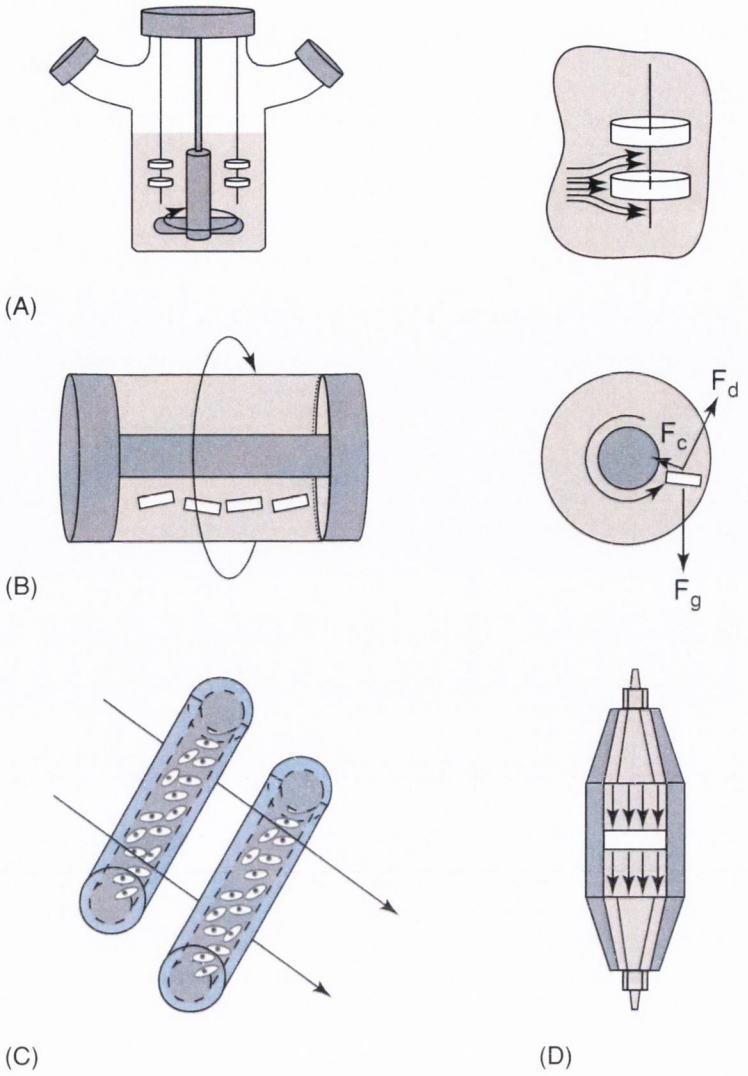

Figure 2.13. Bioreactor devices used for cell seeding and *in vitro* culturing (A) Spinner-flask (B) Rotating-wall vessels (C) Hollow-fiber bioreactor (D) Direct perfusion bioreactor (adapted from Martin *et al.*, 2004).

Wendt *et al.* (2003) developed an oscillating perfusion system and assessed the efficacy of this perfusion technique for different scaffolds and cell types compared to static and spinner flask seeding methods. For chondrocytes seeded onto Polyactive foams, the viable cell seeding efficiency (defined as the percentage of initially loaded cells that were seeded and remained viable, was significantly higher for the perfusion method (75 ± 6 %) than those subjected to static (57 ± 5 %) and spinner flask (55 ± 8 %) methods. Bone marrow stromal cells were seeded using the oscillatory perfusion system onto porous ceramic scaffolds (ChronOS^{TM}) and compared to the

static seeding method. It was observed that cells were homogeneously distributed throughout the scaffold volume following the perfusion method, whereas cells were predominantly located near the top surface of the ceramic scaffold for the statically seeded constructs (Figure 2.14).

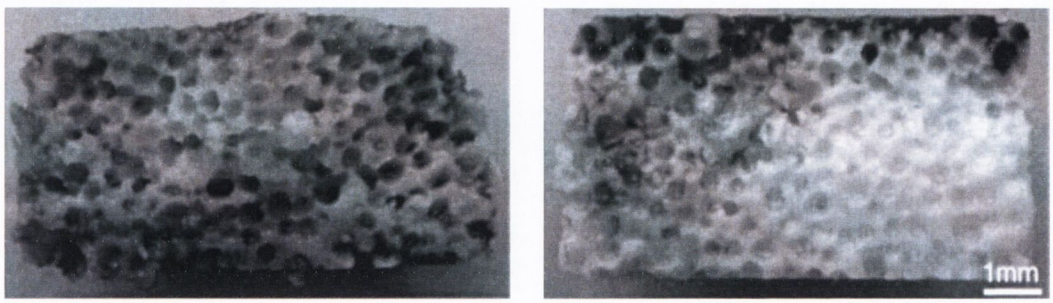

(A) (B)

Figure 2.14. Comparative MTT staining of seeded ChronOS^{TM} porous ceramic scaffolds (A) Scaffold seeded by perfusion, relatively homogeneous staining through scaffold depth (B) Statically seeded scaffold, staining predominantly confined to the top surface (Wendt *et al.*, 2003).

Cartmell *et al.* (2003) perfused human trabecular bone scaffolds seeded with MC3T3-E1 osteoblast-like cells for one week in a custom made perfusion system. The influence of the applied flow rates (0.01, 0.1, 0.2, and 1.0 mL/min) were investigated. It was observed that a flow rate of 1.0 mL/min resulted in substantial cell death throughout the constructs whereas lowering the flow rate led to an increasing proportion of viable cells, particularly at the centre of the constructs. DNA analysis also showed increases in cell proliferation at a flow rate of 0.01 mL/min relative to 0.2 mL/min and static controls. Conversely, mRNA expressions of Runx2, osteocalcin, and alkaline phosphatase were upregulated at 0.2 mL/min compared with lower flow rates. These observations suggest that perfusion of constructs may benefit the development of 3-D tissues *in vitro* by enhancing transport of nutrients and waste within the constructs and providing flow-mediated mechanical stimuli.

Wang *et al.* (2006) observed that seeding scaffolds through applying a low pressure (100 mmHg) to porous β-TCP scaffolds resulted in significantly higher cell seeding efficiency, alkaline phosphatase (ALP) activity and DNA content compared

to the control group. Scanning electron microscopy (SEM) revealed that scaffolds exposed to low pressure also had a large number of cells (BMSCs) in the central parts of the scaffolds, while few or no cells were observed in the central portions for scaffolds not exposed to low pressure. However, there were no differences between the two groups by SEM analysis in the number of cells located at the periphery of the scaffolds, where large number of cells were consistently observed.

Bioreactor systems may provide for better cell distribution initially, however, they still do not provide the higher nutrient concentrations required to support proliferating cells. While significant attempts have been made by many researchers to improve the cell seeding uniformity and efficiency of scaffolds using various methods as outlined in the preceding section, a more viable or germane approach might be to develop a scaffold that can initially facilitate better cell seeding (by providing regular channels throughout the scaffold depth) and therefore overcome the existing limitations that single domain scaffolds inherently possess.

2.10 *In vivo* assessment of scaffolds

This section reviews the *in vivo* performance of single random porous domain, single regular porous domain and multi-domain porous scaffolds.

2.10.1 Single random porous domain scaffolds

There are many types of single random porous domain scaffolds that have been used for *in vivo* implantation, with some degree of success (Gauthier *et al.*, 1998; Chistolini *et al.*, 1999; Dong *et al.*, 2001a; Tamai *et al.*, 2002; Ito *et al.*, 2004; Mastrogiacomo *et al.*, 2006). Bone scaffold products such as bovine bone matrix have also been extensively studied, have undergone clinical trials and are commercially available under such brand names as BioOss®, Tutoplast®, Endobon®, Vitoss® and Osteograft® (Tadic and Epple, 2004). Examples of these products are shown in Figure 2.15.

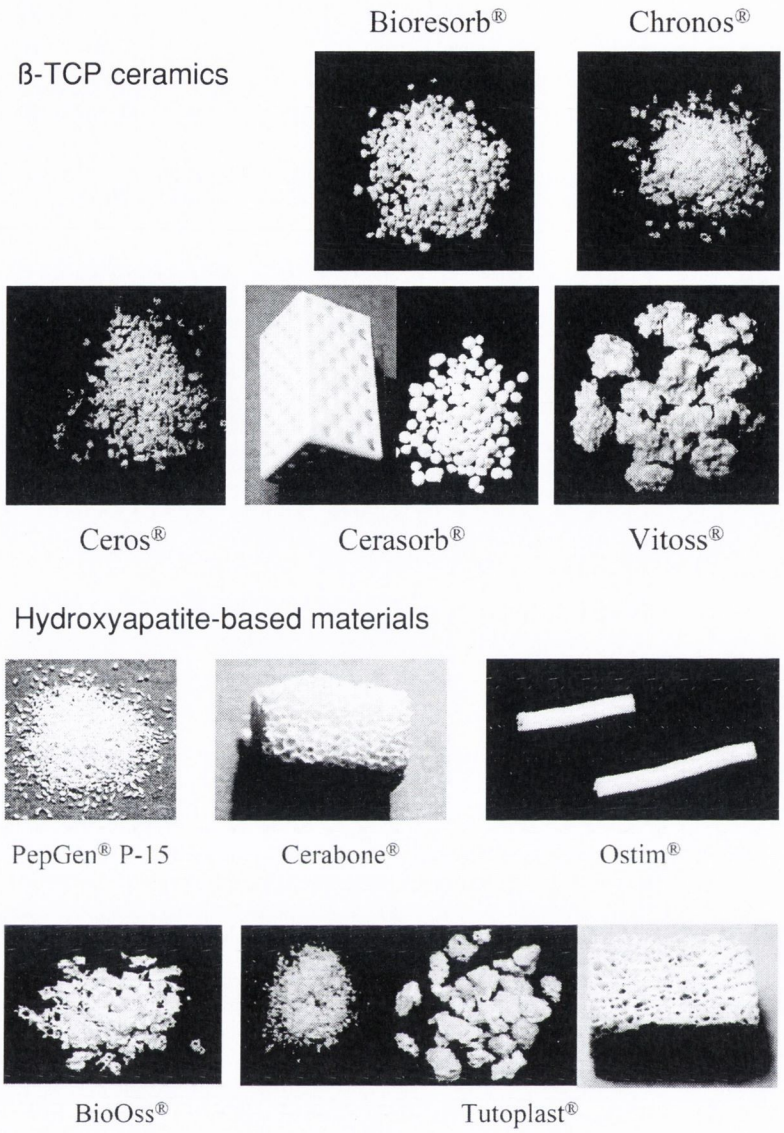

Figure 2.15. Macromorphology of commercially available bone implant materials (Tadic and Epple, 2004)

Gauthier *et al.* (1998) implanted macroporous biphasic calcium phosphate (BCP) scaffolds with two different randomly oriented macropore diameters (300 and 565 μm) and two different porosities (40 and 50 %) into the distal end of rabbit femurs at the epiphyso-metaphyseal junction. The authors observed that new bone was deposited directly on the surface of peripheral pores for all implants and only scaffolds with a macropore diameter of 565 μm showed evidence of bone colonisation in deep pores, while no significant difference was observed between implants with 40 or 50 % macroporosity.

Chistolini *et al.* (1999) implanted HA scaffolds (20 mm in diameter and 35 mm in height, with a central bore of 10 mm in diameter), 70-80 % porosity with a pore size distribution of: < 10 μm ~ 3 vol %; 10-150 μm ~ 11 vol %; > 150 μm ~ 86 vol % into diaphyseal tibia segments of sheep and secured by external fixators. Prior to implantation, two HA carriers were seeded with autologous *ex vivo* expanded bone marrow stromal cells BMSCs; the other two implants were cell-free and used as controls. After 8 weeks, bone tissue was found within the internal macropores of cell-loaded HA carriers, and in the control implants. However, bone formation was mostly limited to the outer surface, although substantially greater amounts of bone was formed in cell-seeded implants compared to non-seeded constructs (~ 50 % versus ~ 7 %).

Dong *et al.* (2001a) fabricated HA scaffolds through foaming of a HA slurry with polyoxyethylenelaurylether (PEI). These scaffolds had a porosity of ~ 77 % and average pore diameter of 500 μm with an interconnecting path (fenestration) of diameter 200 μm (Figure 2.16). Scaffolds were seeded with osteoblastic primary cells obtained from the bone shaft of femorae of Fischer 344 male, 7-week-old rats, and subcultured for two weeks with osteogenic medium. Cell seeded scaffolds and cell-free scaffolds (control) were implanted in subcutaneous pouches created in the back of syngeneic 7-week-old male Fischer rats.

In the cell seeded scaffolds, after 2 weeks post-implantation, bone formation was observed to occur in some of the pores, with the amount of bone formed increasing after 4 weeks and becoming more extensive by 8 weeks. In contrast, no bone formation was observed to occur in the cell-free scaffolds after 4 or 8 weeks. These observations highlight the potential benefits of seeding scaffolds prior to implantation.

Tancred *et al.* (1998b) developed a process for the replication of bovine cancellous bone in synthetic bioceramic materials. These replicas had a pore morphology and interconnectivity almost identical to the original bovine cancellous bone. *In vivo* studies using a canine jaw model were also carried out using these replicated scaffolds

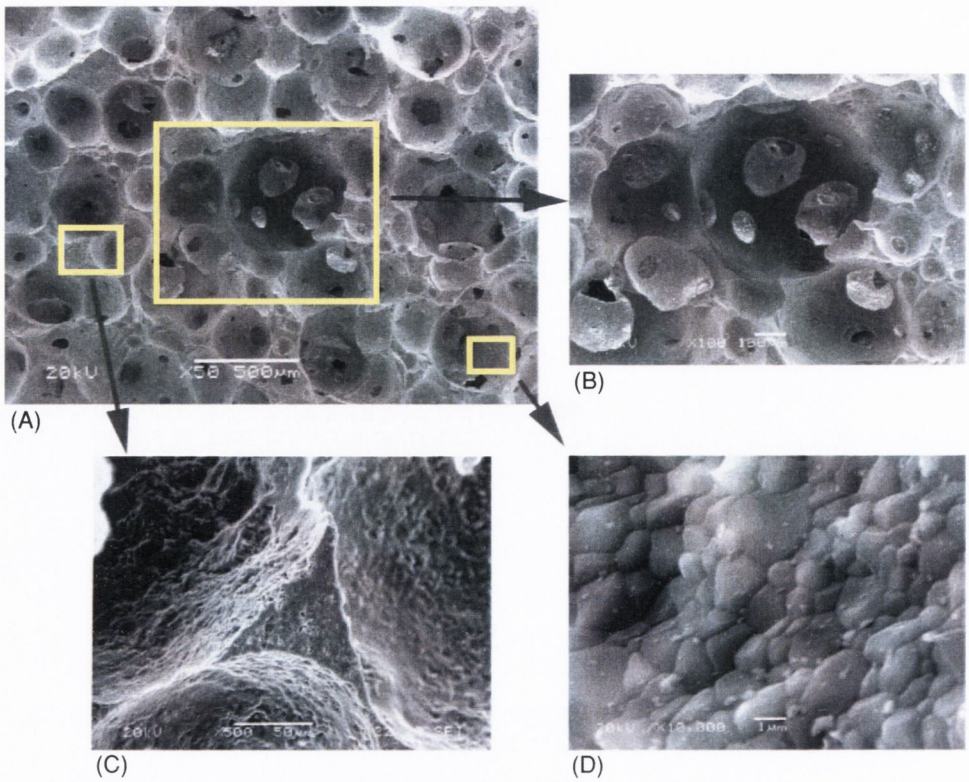

Figure 2.16. (A) SEM photomicrograph of the microstructure of a synthetic porous HA scaffold fabricated through foaming of a HA slurry with polyoxyethylenelaurylether (PEI). Scalebar = 500 μm; (B) Interconnecting path. Scalebar = 100 μm; (C) Surface of pore. Scalebar = 1 μm; (D) Skeleton of pore. Scalebar = 10 μm (Dong *et al.*, 2001a).

to assess their suitability for alveolar ridge reconstruction in Labrador dogs (Al-Souhail *et al.*, 2000). Replicated β-TCP scaffolds (9 mm x 6 mm x 4 mm) were placed into surgically prepared cavities in alveolar bone from which the teeth had been extracted (Figure 2.17). Inflammatory cell infiltrates were the predominant feature at four weeks. Vascularisation and new bone formation were seen within the scaffold at eight weeks. By sixteen weeks the formation of woven bone was observed. The authors provided no information on the degree of bone penetration or regional formation of bone deposition. Quantitative comparison of explanted scaffolds may prove difficult, since each replicated scaffold has a slightly different internal architecture. Also it must be remembered that the replicated scaffolds were based on the cancellous architecture from femoral condyles, which may differ from that of alveolar bone, in terms of porosity, permeability and conductivity.

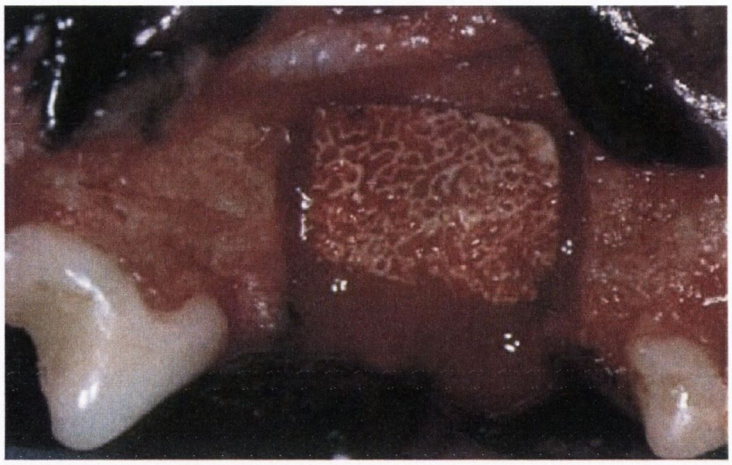

Figure 2.17. Replicated β-TCP scaffold implanted in the alveolar ridge (Al-Souhail *et al.*, 2000)

It is hypothesised by many researchers that a scaffold or bone substitute with architectures similar to that of the defect tissue to be replaced is optimal for *in vivo* success. However, bone can be considered as an initially random porous structure that has been remodelled throughout an individual's life in response to *in vivo* stimuli; the architecture is in effect an end result of the *in vivo* remodelling process. Therefore, it may not necessarily provide a suitable scaffold for new bone formation.

2.10.2 Single regular porous domain scaffolds

Few studies have investigated the *in vivo* response to scaffolds with controlled architectures. Chu *et al.* (2002) conducted one of the few such studies of implants using scaffolds with two different internal regular architectures. The specimens used were cylindrical in shape, with a diameter of 8 mm and a height of 6 mm. The radial design contained a central column of about 3 mm in diameter in the Z-direction with channels of 366 μm extending from the centre toward the surface in radial directions, with a porosity of 38% (Figure 2.18 A). The orthogonal design contained channels of 444 μm penetrating in the X, Y and Z planes, with a porosity of 44% (Figure 2.18 B). These scaffolds (radial and orthogonal designs) were implanted for *in vivo* evaluation and assessed at five and nine weeks. It was observed that the

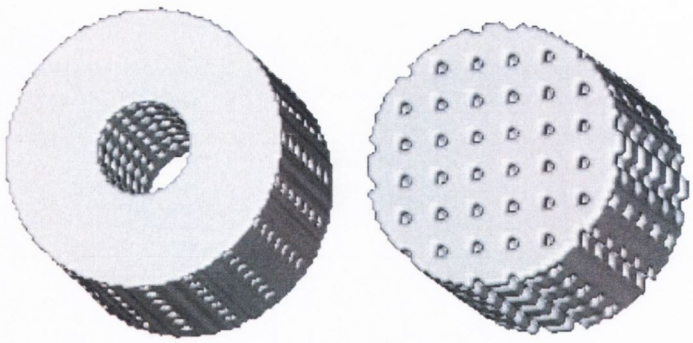

(A) (B)

Figure 2.18. Illustrations showing the designs for *in vivo* implantation (A) Radial channels specimen (B) Orthogonal channels specimen (Chu *et al.*, 2002).

distribution of the regenerated bone was not homogeneous throughout the implants. A large difference was seen between the two end sections and the two central zones. For the end sections, regenerated bone tissue was observed across the entire implant and for the central zones of the scaffolds, the regenerated tissue was only found at the periphery of the implant (Figure 2.19).

The explanation provided for this observation is based on the accessibility of these regions to osteoprogenitor cells. Since the end surfaces of the implant are in direct contact with periosteum, all the channels on the surface are accessible to the osteoprogenitor cells. The osteoprogenitor cells are able to migrate from the periosteum into the HA implant and regenerate bone tissue. For the end sections the direction of bone penetration is perpendicular to the sectioning plane. For the middle sections of the scaffolds, only the peripheral channels are accessible to the osteoprogenitor cells. The cells are expected to migrate from the periphery towards the core of the implant and form new bone. As was observed, this only occurred to a limited extent.

The new bone tissue penetration depth measured in the middle sections was 1.08 $\pm$ 0.49 mm for the orthogonal design and 1.28 $\pm$ 0.60 mm for the radial design. The difference between the two designs was not statistically different ($p > 0.05$).

The comparable bone penetration depths observed in the end and side sections

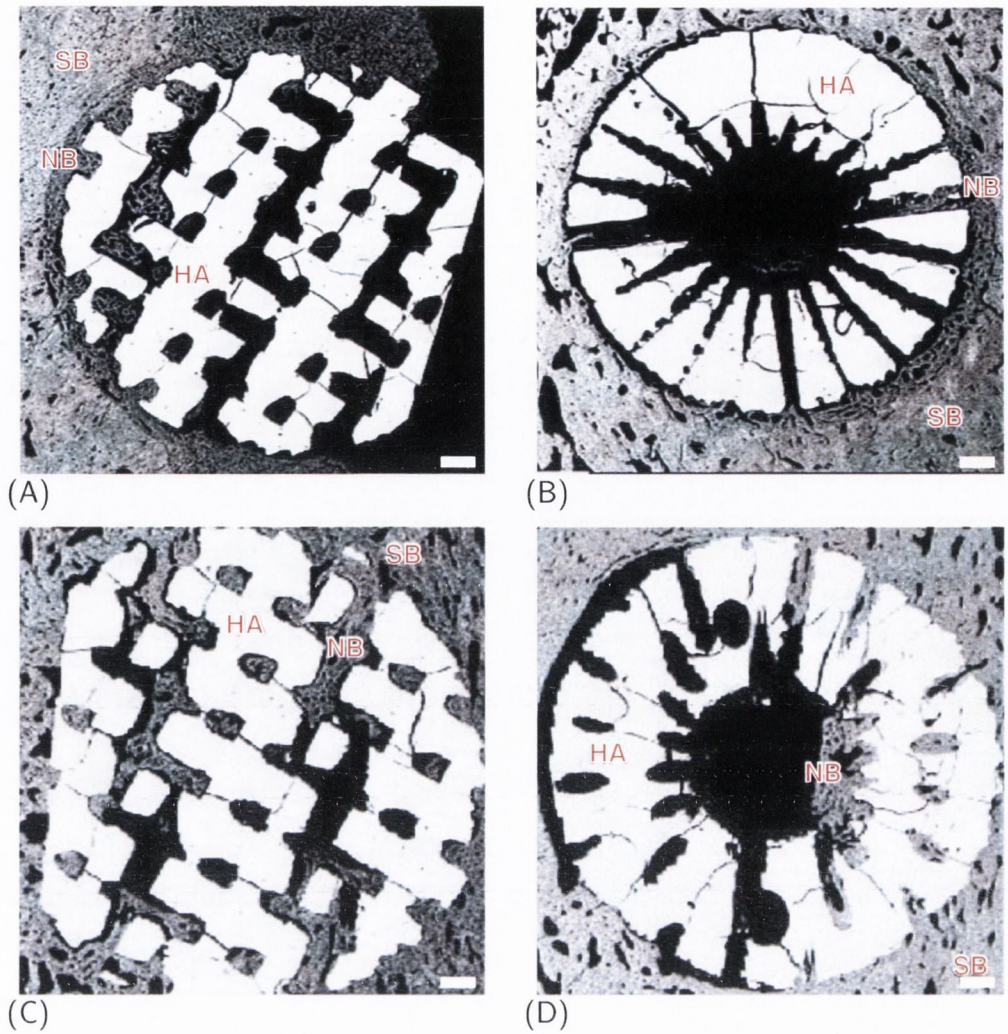

Figure 2.19. SEM showing signs of bone regeneration inside the implants. (A) Orthogonal design at 5 weeks, (B) radial design at 5 weeks, (C) orthogonal design at 9 weeks, and (D) radial design at 9 weeks (HA: HA implant, NB: new bone, SB: surrounding bone, Scale bar is 1 mm) (Chu *et al.*, 2002).

in the orthogonal design were an expected result due to the identical architecture in these locations. The authors observed that for the same locations in the radial design where the channel sizes were different, the bone penetration observed was comparable, and thus suggests that the depth of bone penetration is independent of the channel size. This statement may be valid to a small extent, but the difference in pore size was only 78 μm, and the pore sizes used were above the required threshold for bone formation as defined by (Hulbert *et al.*, 1972).

The percentage of bone ingrowth from the side penetration zone in the radial design was lower though not statistically different from that of the end penetration

zone. This observation may be explained by the fact that the side channels in the radial design were not interconnected. A non-interconnected pore configuration is not as favourable in terms of cell nutrient delivery, waste removal and vascular invasion processes (Baksh and Davies, 2000).

A significant conclusion that can be formed from this study is that it appears that cells do not migrate to a great extent from the surrounding tissues into the scaffolds. Bone formation was observed at the end and periphery surfaces, possibly due to the proximity of cells and nutrients available in the periosteum. Perhaps the radial designs could have been improved by packing the central core with autograft pulp to provide a more abundant supply of cells in that region. A positive point to note, is that a direct comparison of the results obtained for each scaffold can be made since the internal architecture for each scaffold group was identical.

2.10.3 Multi-domain porous scaffolds

Roy *et al.* (2003) assessed the *in vivo* performance of porous sintered HA scaffolds as shown in Figure 2.20. These scaffolds were created using the Theriform^{TM} solid free form (SFF) fabrication process. Scaffolds ($\varnothing$ = 8 mm, H = 3 mm) with macrochannels (axial channel size of 1.6 x 1.6 mm and radial channel size of 1.6 x 1.0 mm) and scaffolds without macrochannels were implanted in a rabbit calvarial defect and assessed at eight weeks. Circular defects ($\varnothing$ 8 mm) were created with a hand drill and trephine bit in the parietal bones of the skull on either side of the sagittal suture line.

All scaffolds were positioned so that the axial channels faced the dura on the endocranial side and the periosteum and skin were sutured in layers. After eight weeks implantation it was observed that scaffolds containing engineered macroscopic channels had a significantly higher percentage of new bone area compared to those scaffolds without engineered macroscopic channels. The base material of the scaffolds contained pores which were less than 20 μm in size with a pore volume of 45 %. This was an artifact of the manufacturing process and was not created intentionally.

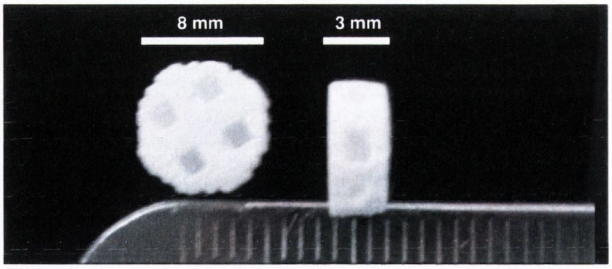

(A)

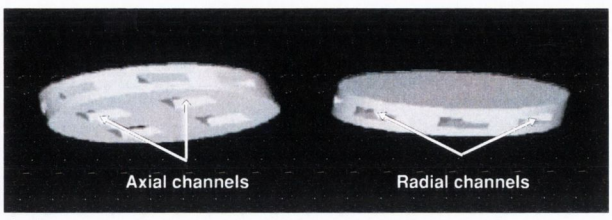

(B)

Figure 2.20. Images of HA scaffold produced using the Theirform^{TM} process (A) Orthogonal pore structure (B) Axial channel size of 1.6 x 1.6 mm and radial channel size of 1.6 x 1.0 mm (adapted from Roy *et al.*, 2003).

An unexpected finding in this study was the abundance of new bone within this secondary porosity as shown in Figure 2.21.

Another study from the same laboratory (Simon *et al.*, 2003) used a trephine defect model to assess the *in vivo* potential of various architecture designs. Of interest in this study is the difference between two of the designs employed. The first design having a grid structure of 500 μm square axial pores and two layered sets of four 1.6 x 0.6 mm channels on the horizontal plane of the implant. A second design used an identical structure to that of the first but with salt-leached porous walls yielding an 80 % wall porosity. This was termed a bimodal pore distributed scaffold. No data or images on the pore size for this phase were provided by the authors, but it was stated that it had a wider distribution than the measurements for the regular channels. The designed scaffolds had a diameter of 8 mm and were 3 mm in height and the material used was poly(DTE carbonate). A control scaffold, Interpore 500, which is a commercially available coralline bone scaffold made from HA *via* the replamineform process was also implanted for comparison purposes. At eight weeks, the mineral apposition rate (MAR) for all specimens ranged between 2.1 μm/day (control) and 2.8 μm/day for the scaffold with the bimodal pore design.

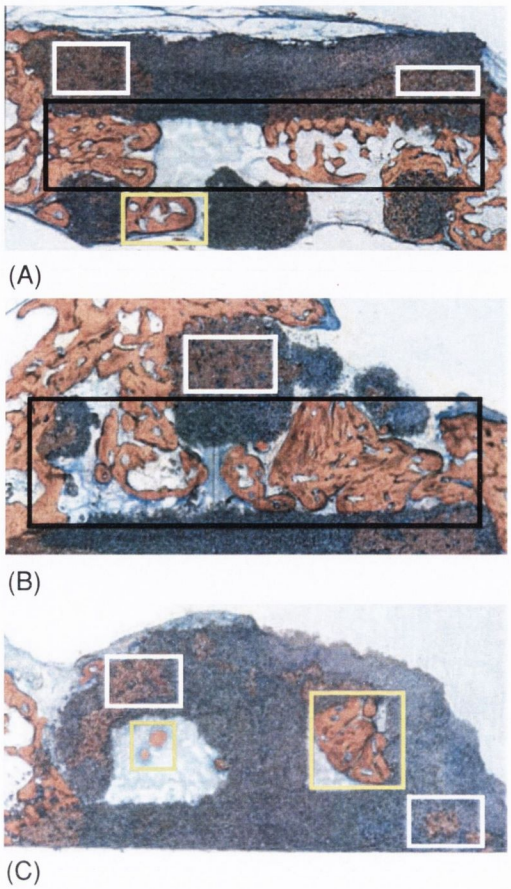

Figure 2.21. Histology sections of a multi-domain porous HA scaffold (A) Coronal section (B) & (C) Horizontal sections going toward the bottom of the scaffold. The black boxes indicate new bone growth through the radial channels, the yellow boxes indicate new bone growth through the axial channels and the white boxes indicate new bone growth through the micro pores (adapted from Roy *et al.*, 2003).

At sixteen weeks the MAR for the control (Interpore 500) and that for the design with solid walls decreased below 2 μm/day while the scaffolds with the bimodal pores had a rate of 2.6 μm/day. The area of ingrowth as a function of defect area into coronal sections, assessed histomorphometrically revealed the bimodal porous scaffold had bone ingrowth area of 16.3 % $\pm$ 0.9 % SE, while the other implants had less, between 9 and 13.5 % (Figure 2.22).

These findings give rise to the potential that multi domain type configurations of scaffolds could prove advantageous in the development of tissue engineering scaffolds by providing discrete domains for bone formation in the porous base material itself.

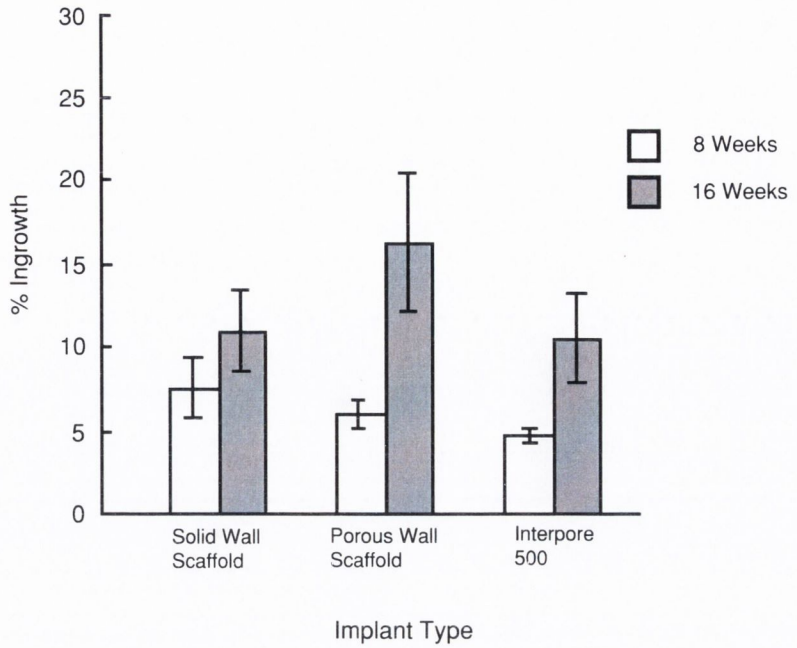

Figure 2.22. Percentage bone ingrowth in coronal sections as a function of defect area for the various scaffold implants (adapted from Simon *et al.*, 2003).

2.11 *In vivo* environments: diffusion and cellular consumption of nutrients

2.11.1 Introduction

As previously described, in situations where cells are transplanted into a three-dimensional (3D) environment there is a necessity for the delivery of nutrients and removal of metabolic waste products. The movement of such molecules into and away from the scaffold is collectively referred to as mass transport. This section will review the importance of the local nutrient environment, with an emphases on the influence of oxygen concentrations. The diffusion coefficient of oxygen through cell culture media at 37 °C is approximately 2.5-3 x 10^{-9} m^2s^{-1} (Pettersen *et al.*, 2005) and through blood is approximately 2.2 x 10^{-9} m^2s^{-1} (Hershey and Karhan, 1968) at 25 °C, thus, as a result of normal respiration, a decrease in oxygen tension can develop in the vicinity close to proliferating cells, influencing the activities of the exposed cells due to lower oxygen concentrations, and as such, altering the future performance in terms of proliferation and matrix deposition.

2.11.2 *In vivo* nutrient environment

Passive diffusion along concentration gradients is the principal mechanism for mass transport, particularly for small molecules (Muschler *et al.*, 2004). With respect to *in vivo* tissues such as cancellous bone and bone marrow, the distance that oxygen molecules must diffuse between a capillary lumen and a cell membrane is between 40 and 200 μm (Chow *et al.*, 2001).

Oxygen gradients in physiologic systems play an important role in maintaining homeostasis and inducing acute cellular response (Allen and Bhatia, 2003). Once a scaffold is implanted into a defect site a sequential progression of events takes place involving inflammation, revascularisation and remodelling (Cypher TJ, 1996). Figure 2.23 illustrates the biological processes involved within and around a porous scaffold implanted *in vivo*.

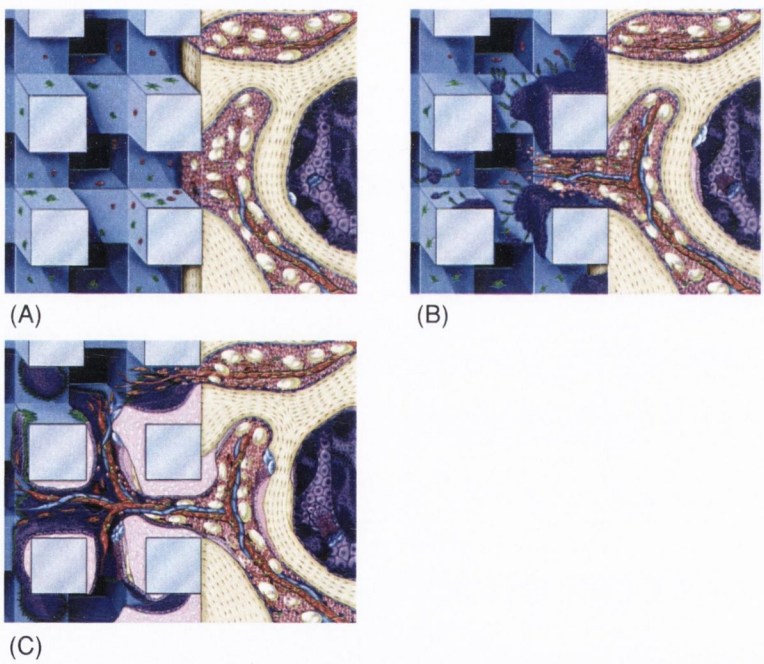

Figure 2.23. Conceptual illustration of the biological processes involved within and around a porous scaffold implanted *in vivo* (Muschler *et al.*, 2004). (A) immediately after implantation (B) Invasion of inflammatory cells, osteoblastic stem cells and vascular endothelial cells. After time, the invading osteoblastic stem cells begin to differentiate to form a network of new woven bone. (C) Bone and vascular remodelling occur within the implanted site. Initial woven bone is replaced with lamellar bone, forming an interconnected network.

During the inflammatory stage, a hematoma develops within the site during the first few hours and days. Inflammatory cells and fibroblasts infiltrate the region resulting in the formation of granulation tissue, ingrowth of vascular tissue, and migration of mesenchymal cells. During this early stage and prior to vascularisation, the primary nutrient and oxygen supply is provided by the exposed cancellous bone and muscle tissue (Kalfas, 2001). For an implanted scaffold, this implies that vessels that deliver oxygen are initially confined to the periphery or outer surface of the scaffold. Therefore, immediately after implantation of a cell-seeded scaffold, the diffusion distance is critical in maintaining the degree of oxygen delivery to the site. With increasing distance from the oxygen source, cells compete for oxygen and other nutrients, as well as competing with other cell types that are recruited as part of the local inflammatory response (Muschler *et al.*, 2004). For a clinically relevant scaffold of thickness 5 mm, the diffusion distance for oxygen from the periphery to the central region is approximately 25 times the normal diffusion distance. This situation inevitably leads to the formation of oxygen concentration gradients within the scaffold (Figure 2.24) and therefore a heterogenous micro-environment. Cells that are residing on the peripheral domain experience much greater nutrient delivery, than their counterparts at the central core. Depending on the degree of the oxygen concentration gradient, the proliferation and subsequent matrix deposition by the cells is affected. As mentioned in Section 2.5.3, Martin *et al.* (1998) suggested that these higher rates of mass transfer at the periphery of a scaffold promote mineralisation, further limiting the mass transfer of nutrients to the core of a scaffold.

Brighton *et al.* (1991) subjected rat calvarial bone cells to various oxygen tensions (1, 3, 5, 9, 13, 21 and 60% O_2), corresponding to 7.6, 22.8, 38, 68.4, 98.8, 159.6 and 456 mm Hg respectively (Table 2.9), using modified Cooper culture dishes. The authors observed that low oxygen concentrations (1 - 9 %) in the gaseous environment favoured bone cell proliferation, whereas high oxygen concentrations (9 - 21 %) favoured macromolecular synthesis (alkaline phosphatase activity, collagen and proteoglycan synthesis), in agreement with previous pO_2 measurements of healing in

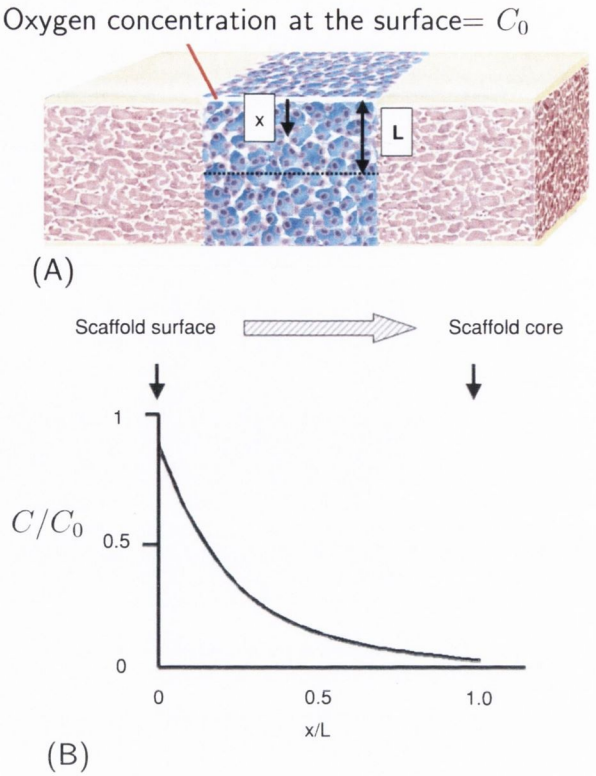

Figure 2.24. Illustration of an idealised cell-scaffold matrix after implantation and (B) Resulting oxygen profile indicating decreasing oxygen concentration with increasing depth to the central axis of the scaffold (adapted from Muschler *et al.*, 2004).

the fracture callus (Brighton and Krebs, 1972). Based on their experimental findings the authors suggested a sequence of events that take place in a healing fracture:

(i) immediate loss of blood supply to the local fracture site

(ii) ingrowth of osteoprogenitor cells

(iii) increase in cellular proliferation accompanied by initial macromolecular synthesis

(iv) with increasing levels of pO_2, a slowing of cellular proliferation, and a greater increase in macromolecular synthesis

Heppenstall *et al.* (1975) investigated the role of oxygen content and the oxygen consumption in a large area of healing osseous tissue as a function of time in an attempt to determine the gaseous conditions under which new bone is formed *in*

Table 2.9. Oxygen tensions in % and mmHg and corresponding relationship to *in vivo* and *in vitro* environments (compiled from Brighton *et al.*, 1991).

Oxygen Tension (%)	**Oxygen Tension (mm Hg)**	**Relating pO_2 environment**
1	7.6	Fracture hematoma
3	22.8	Hypoxic tissue
5	38	Venous supply
9	68.4	Mixed arterial-venous supply
13	98.8	Arterial supply
21	159.6	Normal *in vitro* culture conditions
60	456	Hyperoxic or toxic state

vivo. The authors observed that the tissue oxygen tension was very low in the beginning, with an initial value of 8.0 mm Hg recorded at three days, showing a gradual rise to 32 $\pm$ 2 mm Hg by three weeks and a further rise to 46 $\pm$ 2 mm Hg by six weeks. New bone formation was observed to take place under low oxygen tension (hypoxic condition), with rapid new bone formation occurring between two and four weeks, corresponding to a range of oxygen tensions of $\sim$ 24-40 mm Hg, respectively.

It is clear from the above findings that when a scaffold is initially implanted into a defect site, low oxygen tensions exist, and these oxygen concentrations increase over time. It is therefore pertinent that a scaffold provides a homogeneous oxygen environment throughout the scaffold depth in order that all cells within the construct experience the same oxygen concentrations. By doing this, variable changes in cell proliferation are minimised, and deposition of new bone matrix is permissible. In the early stages of scaffold implantation, prior to vascularisation, a cell seeded scaffold relies solely on the diffusion of oxygen through the blood itself. The presence of a scaffold will reduce the effectiveness of this nutrient delivery, since a porous construct will have an effective diffusion coefficient value less than that of the blood itself. Higher concentrations will exist at the periphery or on the surface of the

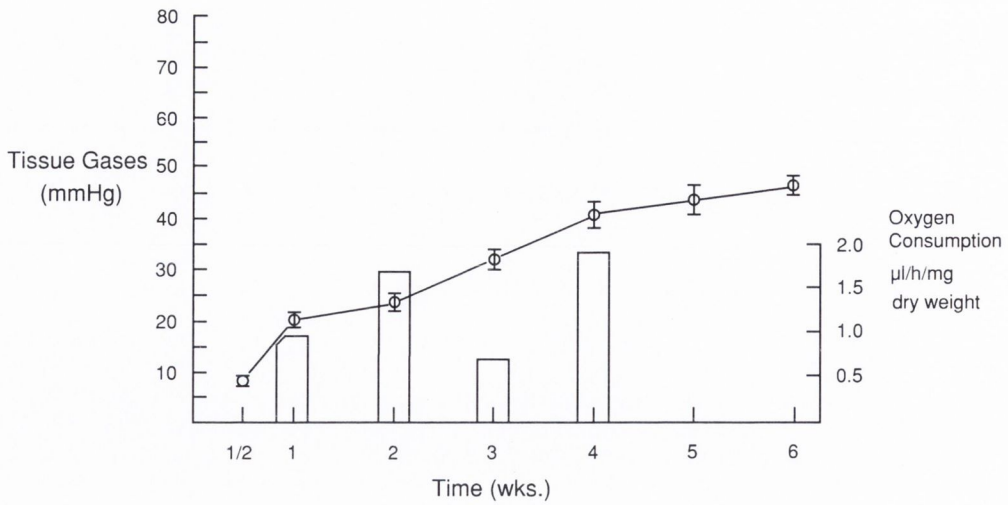

Figure 2.25. The tissue oxygen concentration (line graph) and the oxygen consumption (bar graph) values obtained for healing rib defects as a function of time (Heppenstall *et al.*, 1975).

scaffold, with steep oxygen gradients being formed with increasing depth into the scaffold. It is therefore necessary to develop scaffolds which can provide higher oxygen concentrations (*i.e.* minimise the existence of steep concentration gradients) throughout the scaffold depth.

2.11.3 Theoretical numerical modelling

Theoretical modelling has been used by many researchers to explore the relationships that exist for oxygen concentrations with respect to cell density (Malda *et al.*, 2004a,c; Radisic *et al.*, 2005; Croll *et al.*, 2005; Radisic *et al.*, 2006) and proliferation (Pisu *et al.*, 2003; Lewis *et al.*, 2005; Dunn *et al.*, 2006), diffusion distance (Nehring *et al.*, 1999) and macromolecular synthesis (Obradovic *et al.*, 2000). These models are mainly diffusion-reaction type models, in which oxygen is diffusing into the scaffold and the reaction is the activity of the cells consuming this nutrient. Mathematical modelling is useful, since it can predict the influence of specific cellular parameters such as cell density and cellular oxygen consumption rates as well as the influence of important scaffold parameters such as scaffold geometry and effective diffusion coefficients on the developing oxygen profiles.

Malda *et al.* (2004a) experimentally measured the *in vitro* oxygen gradients that exist within a polyethylene glycol terephthalate/polybutylene terephthalate (PEGT/PBT) polymer scaffold (80 % porosity) fabricated through a compression moulding and salt leaching method. A glass microelectrode system was used to measure the oxygen concentrations at specific depths within the porous scaffold. Low oxygen concentrations, between 2-5 % were measured within the centre of the scaffold. A mathematical model was developed to predict the oxygen profiles within the scaffold constructs and were compared to the experimental findings. This model used a heterogeneous cell distribution which was obtained experimentally. However the diffusion coefficient that was used to obtain a good oxygen profile correlation with the measured experimental values was estimated based on the rule of mixtures theory. The oxygen consumption rates of the chondrocytes was also adjusted in order to fit the experimental oxygen profile. A value of 3.8 x 10^{-10} m^2s^{-1} was estimated for the overall diffusion coefficient through the scaffold construct which is approximately 13 % of the diffusion coefficient through water at 37 °C (3.0 x 10^{-9} m^2s^{-1}). This diffusion coefficient appears to be extremely low for an 80 % porous scaffold and would possibly indicate a scaffold which has poor interconnectivity or high pore tortuosity.

Dunn *et al.* (2006) assessed the *in vitro* cell growth of MC3T3-E1 cells in a PLGA polymer scaffold (10 mm diameter, 1 mm height), produced through particulate leaching. Scaffolds were seeded with cells (1 x 10^5) and incubated for ten days. Scaffolds were embedded (porcine skin gelatin), cryosectioned, and the cell distribution was determined within the scaffolds. After ten days, it was observed that the cell density increased from 2.1 x 10^5 cells/cm^3 to 1.3 x 10^7 cells/cm^3 at the fluid-scaffold interface. However, the increase in cell density was mostly confined to the outermost 200 μm from the fluid-scaffold interface.

A mathematical diffusion model was developed in order to predict the cell distributions within the scaffolds after ten days in culture. The growth of the cells within the scaffold was modelled using the logistic law which prevents the cell population

from growing too big for its environment by including an inhibiting factor (*e.g.* nutrient concentration). The rate of cell growth was assumed to be proportional to the cell density modified by the logistic law until the maximal cell density was reached, with the specific rate of cell growth being assumed proportional to the concentration of the limiting molecule, in this case oxygen. A good agreement was found for the cell density profile for the simulated mathematical model, using cell growth based on the local oxygen tension. In the mathematical model the diffusion coefficient of oxygen through the scaffold was assumed to be the same as that of water (3.0 x 10^{-9} m^2s^{-1}). However, this is a highly unrealistic and improbable value to employ. According to Cussler (1997) (p173), the effective diffusion coefficient (D_{eff}) through a porous material is a function of both porosity and tortuosity of the pore structure as described by Eqn. 2.4.

$$D_{eff} = \epsilon \frac{D}{\tau} \tag{2.4}$$

in which D is the diffusion coefficient within the pores, ϵ is the void fraction and τ is the tortuosity. The tortuosity accounts for the longer diffusion path of the diffusing species and is defined as the actual distance a molecule must travel through a substance divided by the thickness (shortest path length) of that substance. Tortuosities usually range between two and six, averaging about three (Cussler, 1997).

Lewis *et al.* (2005) developed a mathematical diffusion-reaction model that showed for scaffolds seeded with chondrocytes, which rely solely on diffusion for the supply of nutrients, will inevitably produce proliferation-dominated regions near the outer edge of the scaffold.

Radisic *et al.* (2005) modelled the oxygen distribution in engineered cardiac tissue with a parallel channel array perfused with culture medium with and without oxygen carriers (perfluorcarbons) which were perfused to enhance the formation and development of cardiac tissue and therefore were not relying solely on diffusion but on a bioreactor environment. These models were used to optimise scaffold geometry and flow conditions necessary to cultivate cardiac constructs of high cell density (x

10^8 cells/mL) and of clinically relevant thickness (5 mm).

It is essential when developing mathematical models, that realistic experimental parameters are used. This implies that experimental measurement of effective diffusion coefficients is vital as is the determination of cellular oxygen consumption rates for cells cultured on various substrates. Only with this complete experimental data can realistic and valid models be formulated.

In all these diffusion-dependent mathematical models, only single domain type structures have been considered. Therefore it is necessary to develop mathematical models which characterise the influence of multi-domain type scaffolds (*i.e.* scaffolds providing a discrete domain for cell occupancy and a separate domain for nutrient delivery) in an attempt to minimise the steep oxygen concentration gradients that normally exist for single random porous domain scaffolds, as outlined in this section.

2.11.4 Cellular consumption

From Section 2.11.2 it is clear that cells respond to oxygen over a wide range of oxygen environments from anoxia to hyperoxia. Oxygen consumption has been shown to vary with cell type. Table 2.10 shows different cell types and their corresponding oxygen consumption rates. The diffusion coefficient of oxygen in tissue ranges between 2-2.5 x 10^{-9} m^2s^{-1} at 37 °C (Chow *et al.*, 2001).

Many methods have been employed to determine the oxygen consumption rates of various cell types both in two and three dimensions. These include microelectrode measurements (Metzen *et al.*, 1995; Mamchaoui and Saumon, 2000; Pettersen *et al.*, 2005), Clark polarographic oxygen electrodes (Balis *et al.*, 1999), fiber optic oxygen sensors (Allen *et al.*, 2001; Griffith *et al.*, 2005) and fluorescence techniques (Haselgrove *et al.*, 1993; Guarino *et al.*, 2004; Heywood *et al.*, 2006).

Much of the work on determining cellular oxygen consumption rates has focused on chondrocytes, endothelial cells, alveolar type cells, hepatocytes and cancerous cells. Minimal data exists for the consumption rates of osteoblast type cells. Guarino *et al.* (2004) measured the oxygen consumption rate of MC3T3-E1 cells (an

Table 2.10. Comparison of the oxygen consumption rates of various cell types.

Cell type	**Oxygen consumption rate (mol/cell.s)**	**Reference**
Bovine articular cartilage chondrocytes (4 % agarose scaffolds)	5.11×10^{-19}	(Heywood *et al.*, 2006)
Bovine cartilage chondrocytes	1.9×10^{-18}	(Obradovic *et al.*, 2000)
Bovine chondrocytes on microcarriers	$2\text{-}4 \times 10^{-17}$	(Malda *et al.*, 2004b)
MC3T3-E1 (mouse myoblast) on polysaccharide scaffolds	1.33×10^{-17}	(Guarino *et al.*, 2004)
Hematopoietic stem cells	$0.47\text{-}3.33 \times 10^{-17}$	(Collins *et al.*, 1998)

osteoblast-type immortalised cell line) cultured on polysaccharide scaffolds using a fluorescence technique. It is important to quantify the various oxygen consumption rates of cells so that valid mathematical models can be developed. The oxygen consumption rates of cells may also be dependent on the material substrate to which they are attached. This may be especially important for mammalian adherent cells as substrates may influence metabolic activities and therefore oxygen consumption rates.

2.12 Chapter summary

As is evident from this chapter, there are many scaffold parameters (*e.g.* material, porosity, pore size, interconnectivity) that may influence the formation of new bone tissue when implanted *in vivo*. Immediately after implantation of a cell-seeded scaffold, the diffusion distance is critical in maintaining the degree of oxygen delivery to the site. With increasing depth, away from the oxygen source, cells compete for oxygen and other nutrients, as well as competing with other cell types that are recruited as part of the local inflammatory response. The oxygen concentrations in such *in*

vivo healing defects can initially be as low as 1-2%. This evidence emphasises the need to develop scaffolds which can deliver more homogeneous nutrient concentrations throughout a scaffolds volume, thereby creating more favourable conditions for new bone formation, and preventing exclusive peripheral bone formation.

Many of the scaffolds which have been developed provide a single porous domain which must accommodate the conflicting effects of cell proliferation and matrix formation with the need for greater nutrient delivery and metabolic waste removal. Even with the advent of rapid-prototyping technologies, fabrication techniques have not been sufficiently developed to date which facilitate the creation of scaffold architectures which may overcome these limitations. As presented in Sections 2.5.4 and 2.10.3, evidence exists from both *in vitro* and *in vivo* studies for the development of multi-domain porous scaffolds as an alternative avenue of research, which may aid in developing scaffolds which provide better architectural structures for cell seeding, cellular proliferation and maintenance of oxygen concentrations and which may enhance the potential of scaffolds to promote bone formation to a greater extent when implanted *in vivo*. Therefore, it is necessary to develop these scaffold-type structures further and characterise their properties to optimise such structures for the development of the next generation of tissue engineering scaffolds.

It is the aim of this work to advance the fundamental work in bone tissue engineering and accelerate the development of scaffolds for *in vivo* applications. Moreover this work aims to develop a novel hydroxyapatite multi-domain porous scaffold architecture (*i.e.* a scaffold providing a discrete domain for cell occupancy and a separate domain for nutrient delivery) to embody in one scaffold the structures required to optimise cell seeding, cell proliferation and migration and potentially to facilitate vascularisation once implanted *in vivo*. It is hypothesised that this will best be achieved with engineered scaffolds incorporating regular and interconnected pore structures, (rather than solely random pore arrangements).

The specific objectives of this work include the fabrication and characterisation (porosity, pore size, permeability, effective diffusion coefficient and mechanical prop-

erties) of multi-domain scaffolds and assess their biocompatibility in terms of proliferation, distribution and oxygen consumption rates when seeded with osteoblast-like cells (MC3T3-E1). Optimisation of cell seeding techniques to increase cell seeding efficiency will also be investigated. Scaffolds will also be assessed *in vitro via* both normal static diffusion-based and dynamic rotational culturing methods. Finally, finite element methods will be employed in a limited fashion to characterise the influence of multi-domain type scaffolds on the local oxygen concentrations in an attempt to minimise the steep gradients that normally exist for single random porous domain scaffolds.

Chapter 3

Materials & Methods

Contents

3.1 Introduction 74

3.2 Elastomeric polymer based scaffolds 76

3.3 Hydroxyapatite ceramic scaffold processing 89

3.4 Anorganic bone matrix preparation 100

3.5 Determination of scaffold properties 101

3.6 Preparation and Procedures for Cell Culture 110

3.7 Finite element modelling of *in vitro* oxygen concentration profiles 123

3.8 Statistical and error analysis 126

3.1 Introduction

This chapter details the experimental methods that were employed throughout the investigation. There are two distinct approaches that were undertaken for the development of scaffolds. These being:

(i) Development of elastomeric scaffolds (Sections 3.2)

(ii) Development of ceramic based scaffolds (Section 3.3)

Initial work of developing scaffolds with defined regular architectural features was attempted with the use of elastomeric materials such as Poly(dimethylsiloxane) (PDMS) and Poly(1,12-dodecanediol-co-citric acid) (PDDC) polymers. The feasibility of producing regular orthogonal repeating unit structures with PDMS was successfully achieved.

Since PDMS is inherently hydrophobic, attempts were made using chemical treatments to render the material hydrophilic in order to facilitate cell attachment. However, chemical treatments proved ineffective and therefore the substrate material could not be effectively seeded with cells. Other researchers have employed plasma treatment for 2D PDMS substrates with some success (Moretti *et al.*, 2004). Further work investigating the use of plasma treatment and possible surface coating with collagen solutions for 3D PDMS scaffold structures may therefore warrant further investigation. However, such optimisation was outside the scope of the present investigation.

PDDC scaffolds were also successfully fabricated utilising the commonly used particulate leaching technique. Further advancement of this technique was achieved by fusing of the salt grain crystals prior to polymer infiltration to improve the pore interconnectivity, which is an essential design parameter when fabricating porous scaffold architectures. Technical issues were encountered when attempting to introduce unidirectional macrochannels into these porous materials, which could not be overcome. Other researchers have shown some success when adopting laser cutting methods. For example (Radisic *et al.*, 2005) created porous poly(glycerolsebacate)

scaffolds by means of a salt-leaching technique, with parallel channels in a square array bored using a 120 W CO2 laser cutting/engraving system (model X-660, Universal Laser Systems, Scottsdale, AZ). Due to the technical difficulties associated in the development of elastomeric scaffolds with defined internal architecture (*i.e.* unidirectional macrochannels), this avenue of research was aborted in favour of developing more clinically relevant ceramic-based (hydroxyapatite) scaffolds for bone tissue engineering purposes. However, the methods and the preliminary results pertaining to the work conducted for the fabrication of elastomeric scaffolds is given in the following sections. The methods, and a more in depth investigation involved in the development, fabrication and characterisation of ceramic based scaffolds begins in Section 3.3.

3.2 Elastomeric polymer based scaffolds

The following sections describe the methods employed in the development of elastomeric scaffolds. A process flow chart for the experimental methods is shown in Figure 3.1.

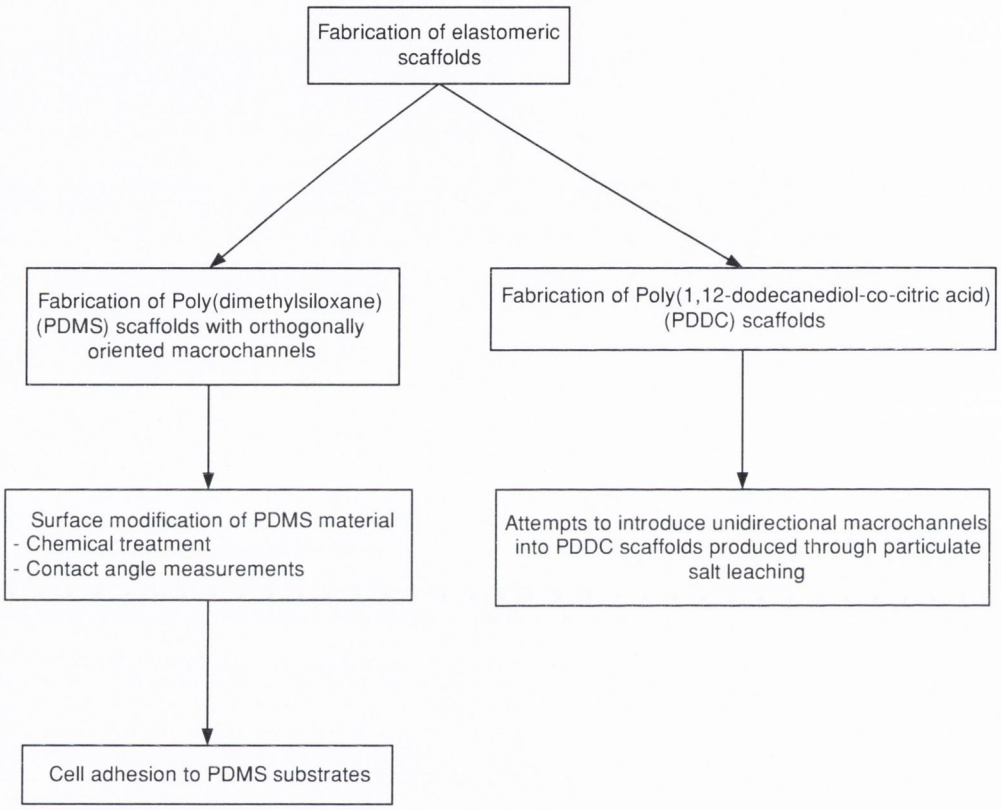

Figure 3.1. Flow chart of the experimental methods employed for the development of elastomeric scaffolds.

3.2.1 Poly(dimethylsiloxane) (PDMS) scaffold fabrication

The process is essentially a lost mould process, in which orthogonal layers of parallel unidirectional nylon fibres of equal spacing create the mould (Figure 3.2 A). The layers are created by winding nylon fibre around a plate with defined notches of equal spacing. Each layer of the unidirectional fibers is stacked orthogonally (90 °) to the previous layer, thus creating a mould architecture in the form of a 3D mesh-

like structure (Figure 3.2 B). This mould is then infiltrated with a polymer solution. Once the infiltrate has cured (crosslinked), the nylon fibre mould is removed through physical extraction of the fibres.

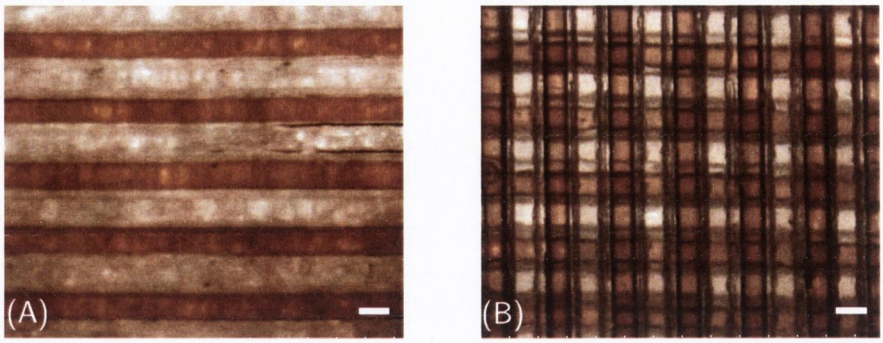

Figure 3.2. (A) Single nylon layer of parallel fibers (B) Nylon mesh structure creating the mould prior to infiltration. White scale bar is 350 μm.

Poly(dimethylsiloxane) (PDMS) is widely used in microfabrication for biological applications and offers biocompatibility, optical transparency, permeability to gases, flexibility, and durability. PDMS produced by Dow Corning, Sylgard®184 was obtained from R W Greef (Glasgow, UK). The notched aluminium recessed plate (Figure 3.3 D) was fabricated in TCD using a diamond saw (Streurs^{TM} Accutom 50) and 400 μm blade (Metprep^{TM} 10-12-50), with a notch spacing of 300 μm. Nylon fiber of 350 μm diameter (Climax®, Germany) was used in this study. PDMS infiltrate was mixed using a 10:1 weight ratio of base to curing agent, and degassed under vacuum for 1 hr. The polymer solution was then introduced using a 10 mL surgical syringe into the fiber mesh matrix (Figure 3.2) and cured for six hrs at 60 °C. After crosslinking of the PDMS polymer, the nylon fibers were extracted from the polymer to reveal a slab (50 mm x 50 mm x 3 mm) with orthogonally oriented channels (Figure 3.3).

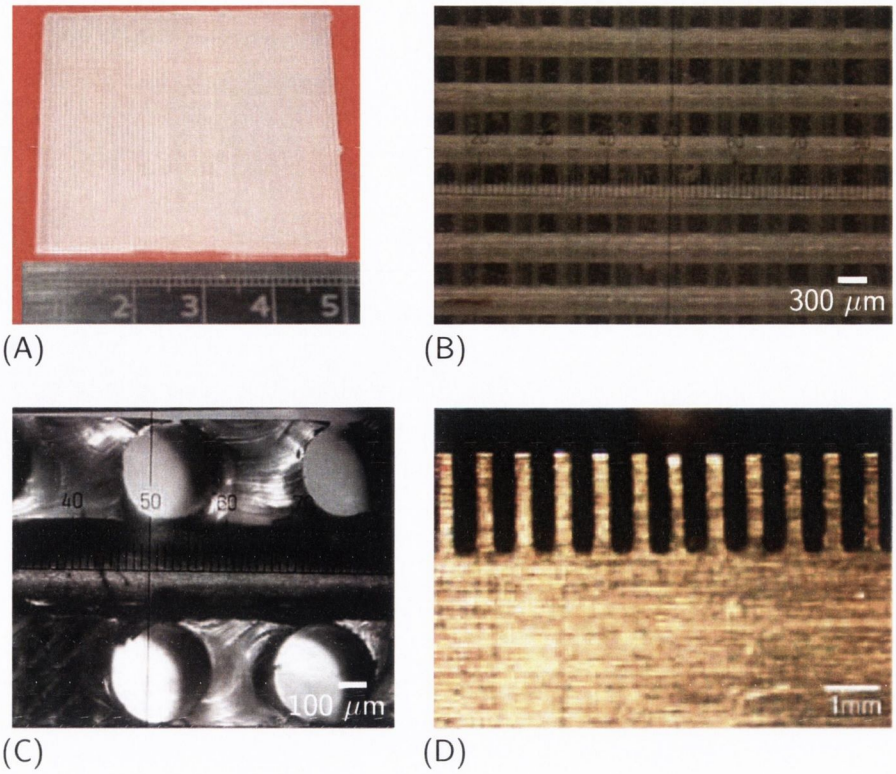

(A) (B)

(C) (D)

Figure 3.3. Orthogonal PDMS structures fabricated through nylon stacking (A) 5 cm square slab of PDMS scaffold (B) & (C) Magnified structure of regular PDMS scaffold 350 μm pore size and 300 μm pore spacing. (D) 400 μm notched aluminium plate, notch spacing of 300 μm.

3.2.2 Chemical surface treatments

A negative aspect of using silicone substrates is that the surfaces are inherently hydrophobic. For this reason attempts were made to render the PDMS substrate hydrophilic through chemical surface treatments. Flat PDMS substrates were created using a spin coating technique (Figure 3.4). PDMS solution was mixed using a 10:1 weight ratio of base to curing agent, and degassed under vacuum for 1 hr.

Silicon wafer substrates were ultrasonicated in acetone and rinsed in ethanol and finally dried using nitrogen in a clean room environment. A small volume of degassed PDMS solution ($\sim$ 5 mL) was poured directly onto the silicon substrate and a speed of 500 r.p.m. was applied for 30 secs. After this stage the silicon wafers were placed directly onto the surface of a hotplate and the PDMS crosslinked for 10 mins. at 110 °C . After this stage of crosslinking, the PDMS layer was peeled gently from the silicon wafer substrate and cut into 10 mm square sections.

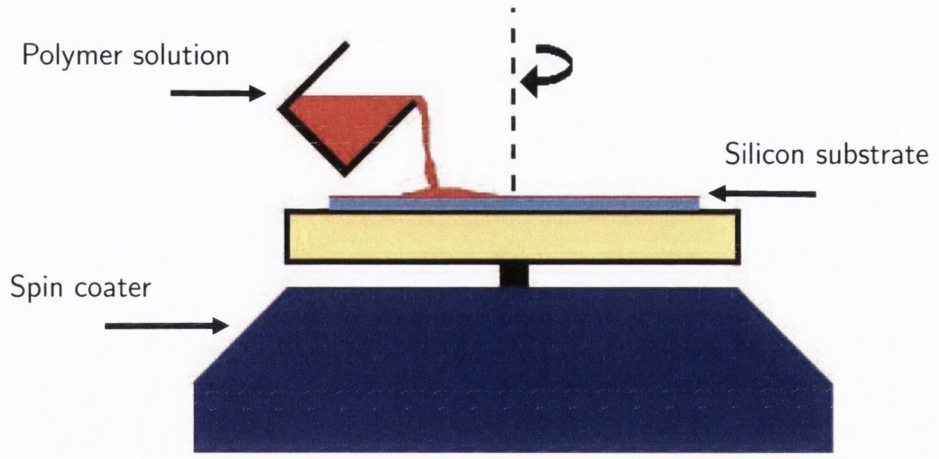

Figure 3.4. Spin coating set-up for the fabrication of PDMS substrates.

These PDMS sections (10 mm^2) were then subjected to two types of surface treatments:

- Sulphuric acid (H_2SO_4), 70, 80 and 90% concentrations in deionised water.
- Piranha solution (Concentrated H_2SO_4 and Hydrogen Peroxide H_2O_2, 3:1 v/v) followed by APTES 1, 2 and 10% concentrations in deionised water/acetone.

3.2.3 Contact angle measurements

Water in air contact angle analysis was carried out on a FTÅ Contact Angle Instrument, using a sessile drop technique, in order to determine the effectiveness of the surface treatments as described in section 3.2.2. Measurements were carried out within 30 mins. of chemical surface treatment. From the results obtained in Tables 3.1 and 3.2 very little effect was observed for any of the chemical treatments, except for the 90 % H_2SO_4 exposed for 30 secs. However, after treatment the surfaces of these samples were highly distorted (foam-like surface) and brittle, no longer possessing any elastic properties.

Table 3.1. H_2SO_4 chemical treatments of PDMS substrates and resulting contact angles measurements.

Treatment	**Immersion Time [secs]**	**Contact Angle[°]**
70% H_2SO_4	120	109.6 ± 2.2
70% H_2SO_4	240	105.1 ± 2.3
80% H_2SO_4	30	109.9 ± 4.3
80% H_2SO_4	60	106.6 ± 3.7
80% H_2SO_4	120	106.4 ± 0.6
90% H_2SO_4	5	89.3 ± 6.4
90% H_2SO_4	10	91.3 ± 2.7
90% H_2SO_4	30	61.9 ± 15.5
Control	n/a	112.3 ± 1.5

Table 3.2. APTES chemical treatments of PDMS substrates and resulting contact angles measurements.

Treatment	**Immersion Time [mins]**	**Temperature**	**Contact Angle[°]**
1% APTES (H_2O)	45	Room Temp.	92.4 ± 2.6
2% APTES (H_2O)	45	Room Temp.	94.4 ± 1.6
10% APTES (H_2O)	120	50 °C	107.1 ± 6.0
1% APTES (C_3H_6O)	45	Room Temp.	91.95 ± 3.1
2% APTES (C_3H_6O)	45	Room Temp.	85.5 ± 5.9
Control	n/a	Room Temp.	97.7 ± 4.3

3.2.4 Cell seeding of PDMS substrates

Experiments were carried out in order to assertain if PDMS substrates which were not subjected to chemical treatments were suitable for cell seeding and attachment. MC3T3-E1 cells were seeded onto PDMS substrates and also onto culture plates for comparison purposes and observed after 3 hrs and after 3 days (Figure 3.5). The initial cell density was adjusted to 2.5 x 10^4 cells/cm^2 and the cell suspension was pippetted directly onto the surfaces of the substrates.

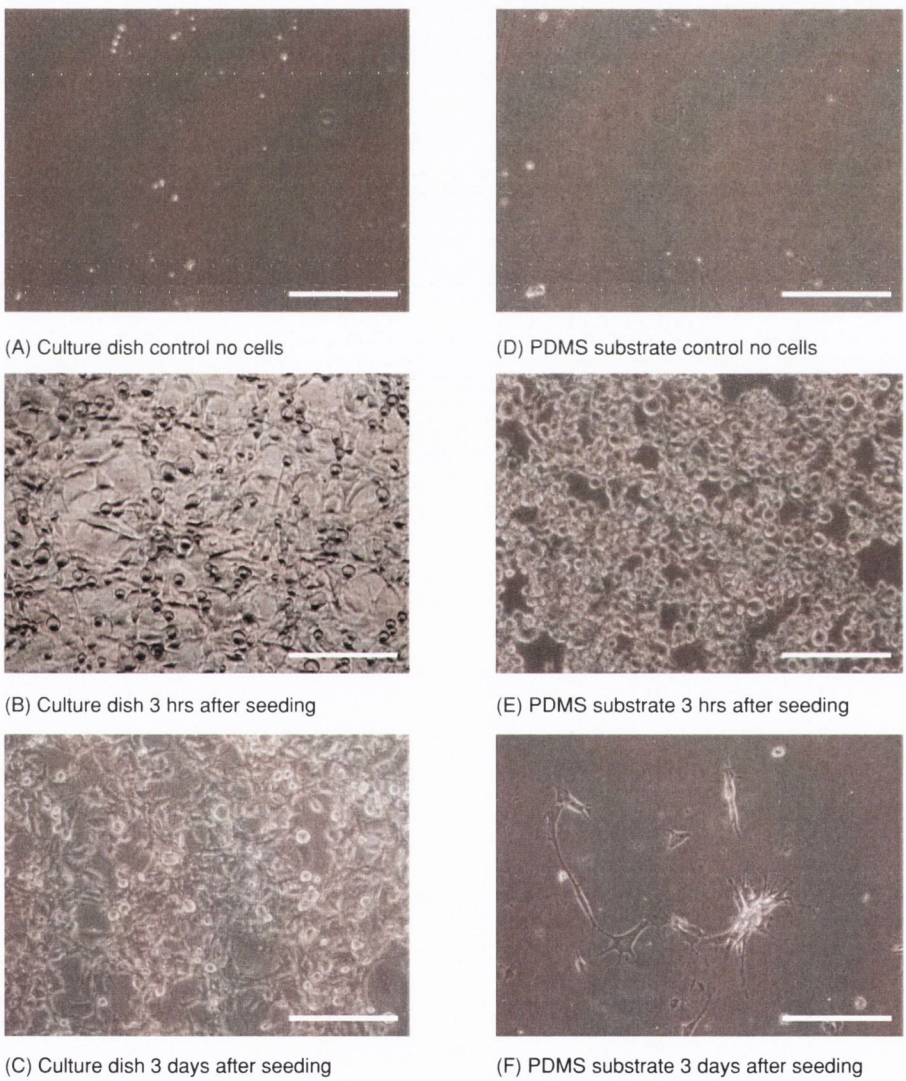

Figure 3.5. (A) (B) and (C) Culture plates seeded with MC3T3-E1 cells (D) (E) and (F) PDMS substrates seeded with MC3T3-E1 cells. White scale bar is 100 μm.

After 3 hrs post-seeding cells have readily attached and spread on the surface of tissue plastic culture plates (Figure 3.5 B). In contrast, cells which were seeded onto the PDMS substrates (Figure 3.5 E) still appear to be mostly spherical in shape indicating that the cells have not attached to the surface at this time point. After 3 days in culture, cells appear to have attached and proliferated on the culture plates, whereas for the PDMS substrates very few cells were observed to have attached and proliferated. Since it was not possible to modify the surfaces of PDMS substrates to reduce the degree of hydrophobicity, and insufficient cell attachment was observed for non-treated PDMS substrates, the approach of creating 3D scaffolds using PDMS in combination with the fiber-winding technique was abandoned in favour of pursuing alternative methods.

3.2.5 Poly(1,12-dodecanediol-co-citric acid) (PDDC) scaffolds

Recent work by Yang *et al.* (2004) has led to the development of a new family of biodegradable polyester elastomers based on polymerisation of a linear diol with citric acid. The work herein describes the fabrication of fused-particulate leached scaffolds in conjunction with this family of polymers. This material which is a citric acid-based biodegradable elastomer, is essentially a polyester network with a controllable number of crosslinks, which allows the elasticity and biodegradability of the material to be easily tailored. These properties can be modulated by controlling synthesis conditions such as cross-linking temperature and time, vacuum and initial monomer molar ratio.

3.2.6 Polymer synthesis

All chemicals were purchased from Sigma-Aldrich (Dublin, Ireland). Preparation of Poly(1,12-dodecanediol-co-citric acid) (PDDC) was carried out as described by Yang *et al.* (2004, 2006). Briefly, a polycondensation reaction between equimolar amounts of citric acid and 1,12-dodecanediol in a 250 mL three-neck round-bottom flask, with an inlet and outlet adapter was carried out (Figure 3.6). The mixture

was melted under a flow of nitrogen gas by stirring at 160 °C in a silicone oil bath, and then the temperature of the system was lowered to 140 °C and stirred for a further hour. This resulted in the synthesis of the pre-polymer solution.

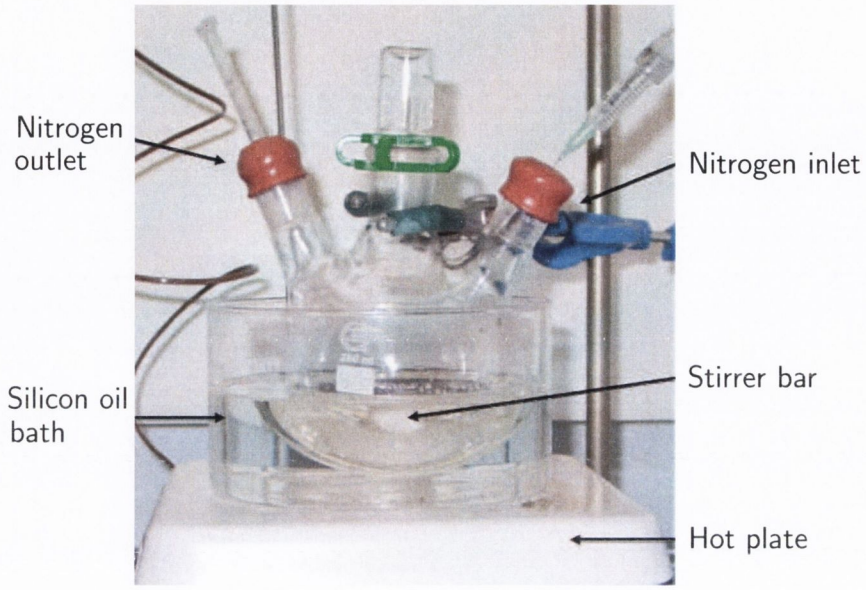

Figure 3.6. Experimental set-up for PDDC pre-polymer synthesis.

3.2.7 PDDC scaffold fabrication

PDDC scaffolds were fabricated utilising the commonly employed particulate salt-leaching method (Ishaug-Riley *et al.*, 1998; Murphy *et al.*, 2002). Poly(tetrafluoroethylene) (PTFE) recessed moulds (4 mm deep recess) containing sieved salt crystals (NaCl, 250-300 μm), were soaked in 80% ethanol to facilitate fusion of the salt crystals, creating an interconnected structure during evaporation (Figure 3.7). PDDC pre-polymer was dissolved in ethanol at 40 wt.-%. and infiltrated into the interconnected salt mould. After solvent evaporation, the moulds were transferred to an oven for post-polymerisation at 120 °C. After 24 hrs, the resulting structures were immersed in deionised water to facilitate the leaching of the salt. Successive incubations were carried out for 48 hrs, to ensure removal of the salt porogen.

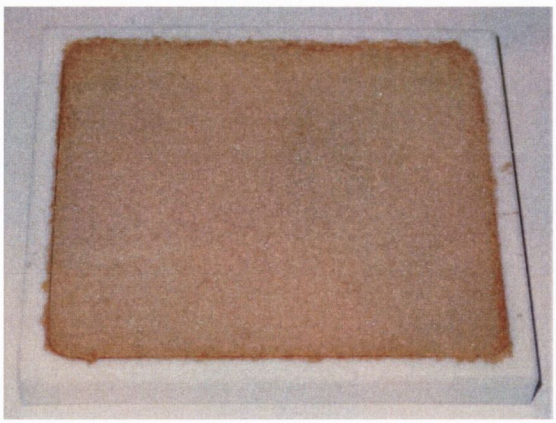

Figure 3.7. PTFE mould with fused-salt particles (250-300 μm) infiltrated with PDDC polymer.

3.2.8 PDDC scaffold pore morphology

Sections of fabricated PDDC scaffolds were serially dehydrated in ethanol, and snap frozen in liquid nitrogen to reveal the cross-section morphology produced through the ethanol fusion particulate-leached technique. The snap-frozen samples were prepared for electron microscopy as described in Section 3.5.5. Figure 3.8 demonstrates the pore morphology of cross-sections produced by this technique. More images can be seen in Appendix A. As can be seen from the SEM images, the scaffolds produced have a random porous structure. Pores have a cuboidal structure consistent with the morphology of salt crystals. At higher magnifications, a significant degree of microporosity is evident (Figure 3.8 C and D) which is possibly due to the evaporation of ethanol prior to crosslinking. Figure 3.8 C, reveals the interconnected pore structure that was formed. The open windows (fenestration) observed between adjacent pores are likely due to the prior fusion of salt-crystals.

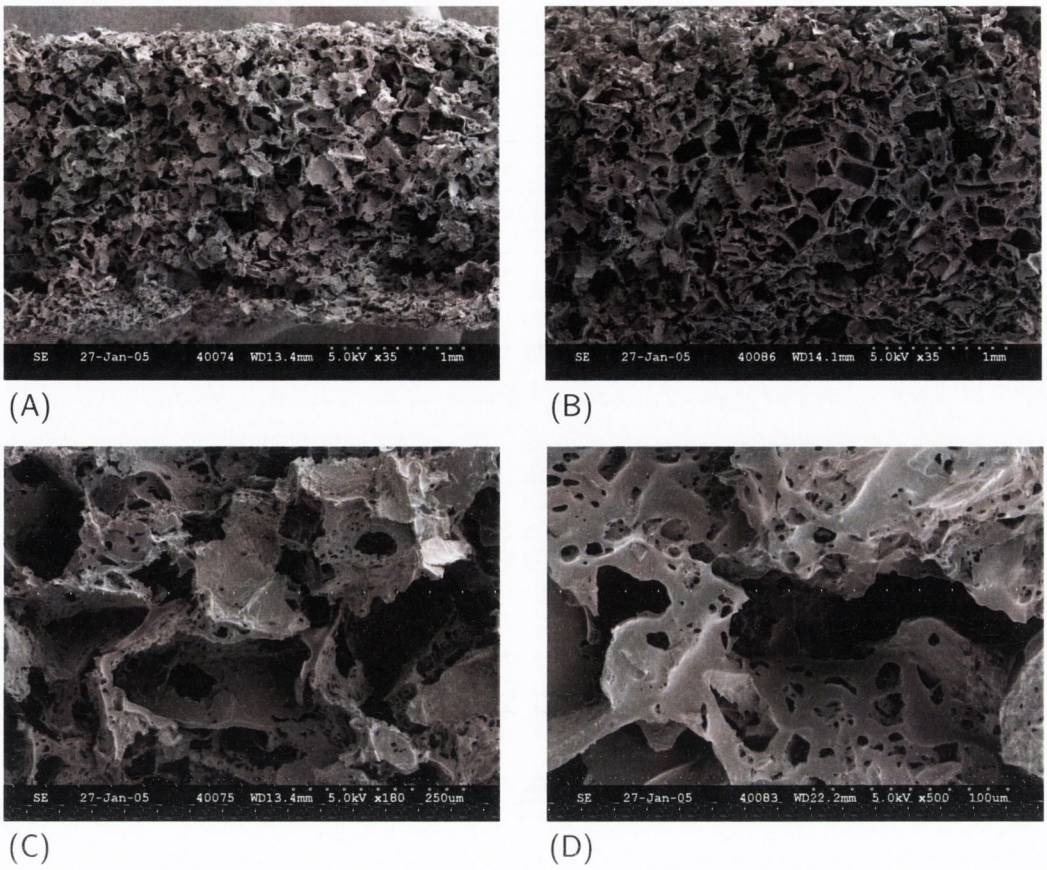

Figure 3.8. SEM micrographs of cross-sections of ethanol-fused particulate leached PDDC scaffold. Pore size range (150-250 μm). Scale bars (A) & (B)=1 mm, (C)=250 μm and (D)=100 μm.

Figure 3.9 reveals the surface morphology of PDDC scaffolds produced. As can be seen, a more closed-type pore structure is present, compared to the more open pore structure that was observed in the cross-sections of scaffold samples. This dense type layer is possibly a result of direct surface contact with the PTFE mould (bottom surface). This denser layer was also observed to occur on the top surface, and may be due to over saturation of the salt moulds with the polymer infiltrate solution.

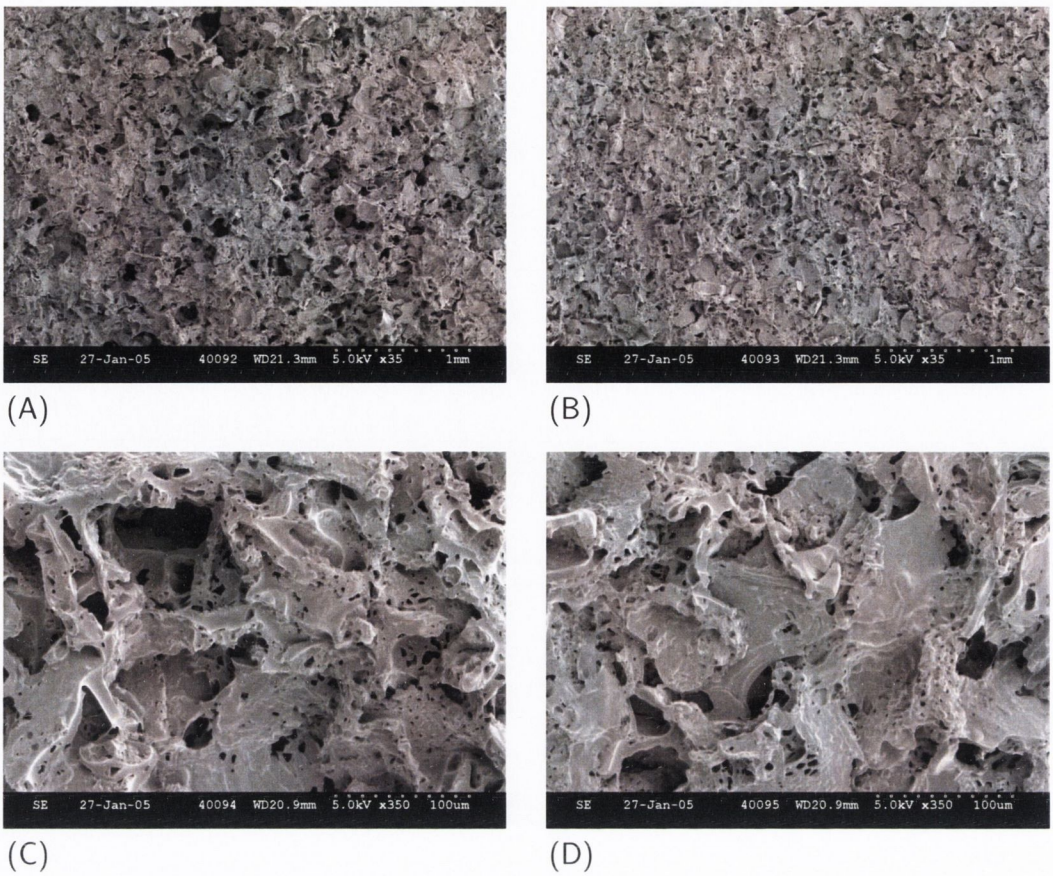

Figure 3.9. SEM micrographs of ethanol-fused particulate leached PDDC scaffold (A) and (B) Top surface, (C) and (D) Bottom surface . Pore size range (150-250 μm). Scale bars (A) & (B)=1 mm, (C) & (D)=100 μm.

3.2.9 Tensile mechanical properties

The tensile properties of PDDC scaffold samples were tested using a Zwick mechanical testing machine (Zwick Testing Machines Ltd , United Kingdom). Samples were stored in deionised water for 48 hrs prior to testing. Scaffold samples (4 x 4 x 20 mm) were clamped between two grip-plates and subjected to a pre-load of 0.01 N. The experimental set-up is shown in Figure 3.10. Samples were then loaded in tension for 10 cycles at 0.1 Hz, and the eleventh cycle was loaded to failure. Values were converted to a stress-strain curve and a Young's modulus was calculated from the initial slope region. The stress-strain curve for each of three scaffold samples is shown in Figure 3.11. As can be seen, a strong linear relationship exists, which is consistent with elastomeric-type materials. Failure was observed to occur at greater than 90 % strain. The Young's modulus was calculated to be 51.3 KPa ($\pm$ 0.84 SE,

n=3) and the tensile strength was calculated to be 41.9 KPa (± 0.88 SE, n=3).

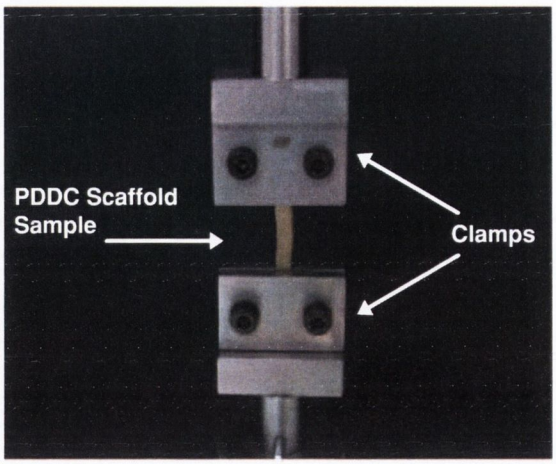

Figure 3.10. Experimental set-up for tensile testing of Poly(1,12-dodecanediol-co-citric acid) (PDDC) scaffolds.

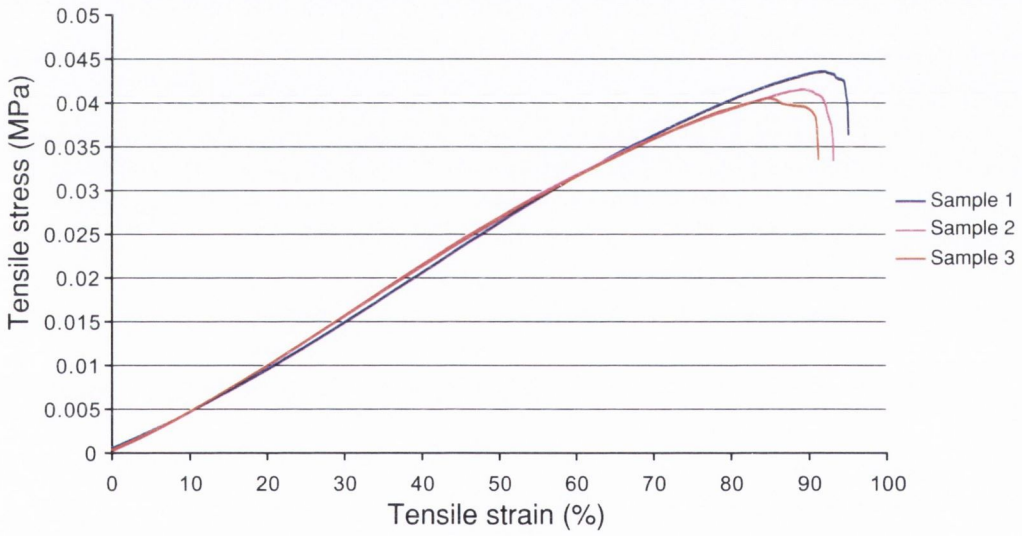

Figure 3.11. Stress-strain curves for Poly(1,12-dodecanediol-co-citric acid) (PDDC) scaffolds fabricated through a ethanol-fused particulate salt-leaching method.

3.2.10 Summary of elastomeric scaffolds

This section reviewed the methods used in developing a biodegradable elastomeric scaffold that may prove beneficial for mechanobiology investigations. The feasibility

of producing regular orthogonal repeating unit structures with PDMS was successfully achieved. However, chemical surface treatments to render PDMS hydrophilic proved ineffective and therefore the substrate material could not be effectively seeded with cells. Other researchers have employed plasma treatment for 2D PDMS substrates with some success (Moretti *et al.*, 2004). Further work investigating the use of plasma treatment and possible surface coating with collagen solutions for 3D PDMS scaffold structures may therefore warrant further investigation.

PDDC scaffolds were also successfully fabricated utilising the commonly used particulate leaching technique. Further advancement of this technique was achieved by fusing of the salt grain crystals prior to polymer infiltration to improve the pore interconnectivity, which is an essential design parameter when fabricating porous scaffold architectures. This approach led to the successful fabrication of elastomeric PDDC scaffolds with an interconnected pore structure and good tensile mechanical properties.

Technical issues were encountered when attempting to introduce unidirectional macrochannels into these porous materials, which could not be overcome. Attempts were made to introduce macrochannels (which may facilitate cell-seeding) into porous PDDC scaffolds using the fiber winding method and also through the insertion of needles. However, both these methods proved to be unsuccessful. Other researchers have shown some success when adopting laser cutting methods (Radisic *et al.*, 2005).

As is evident from the SEM images the poor surface morphology of the scaffolds produced demonstrated a limitation of this technique. Removal of these dense surfaces proved to be unattainable, and thus homogeneous seeding of scaffolds with cells would have proved difficult.

Due to the technical difficulties associated with the development of elastomeric scaffolds with defined internal architecture (*i.e.* unidirectional macrochannels), further fabrication and characterisation of these scaffolds was abandoned in favour of developing more clinically relevant ceramic-based (HA) scaffolds.

3.3 Hydroxyapatite ceramic scaffold processing

The following sections review the experimental methods and protocols for the work carried out for the development and characterisation of HA scaffolds. A flow chart for the avenues of research explored is given in Figure 3.12.

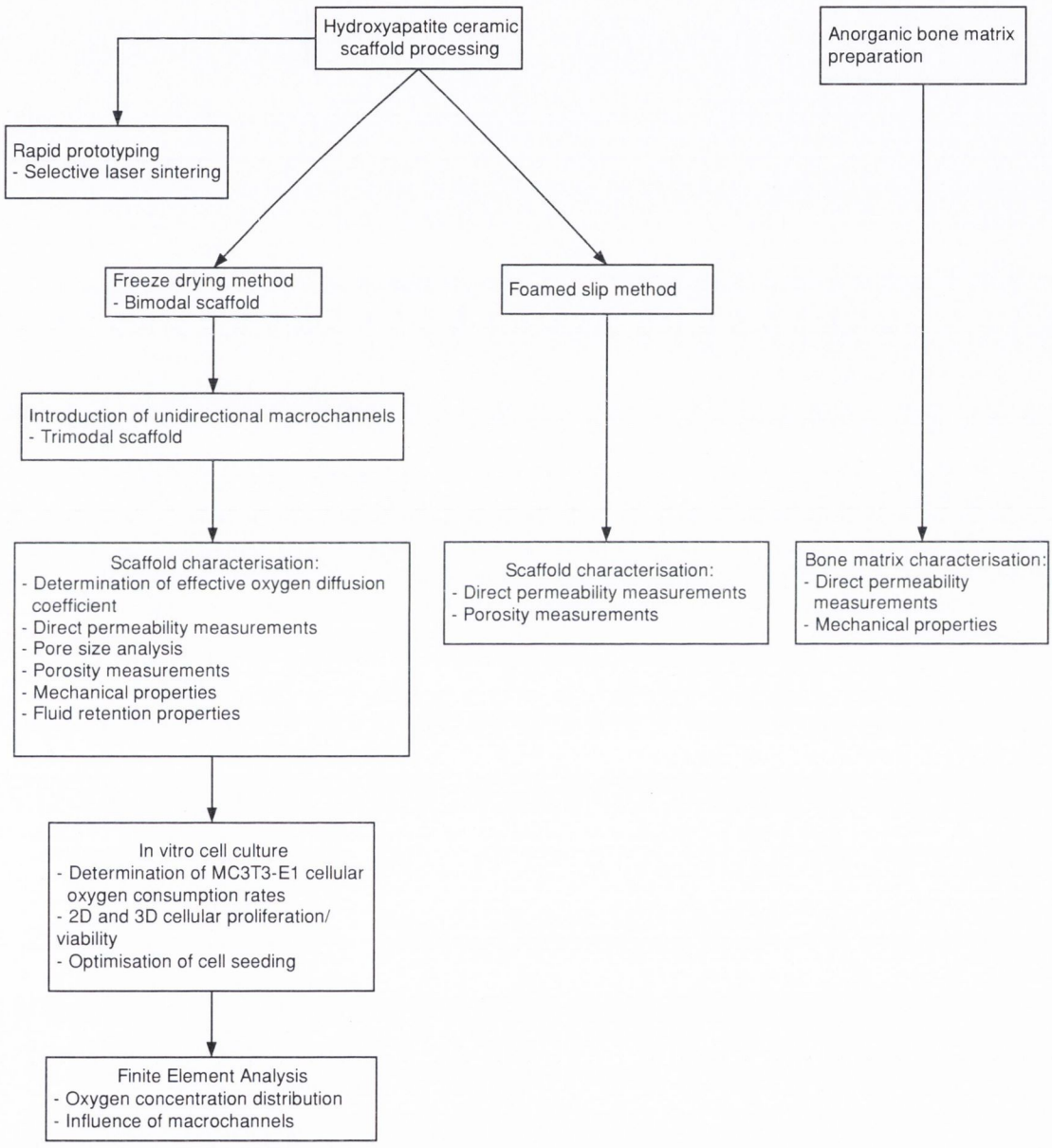

Figure 3.12. Flow chart of the experimental methods employed for the development and characterisation of ceramic-based scaffolds.

3.3.1 Starting materials for foamed slip and freeze-drying methods

Commercially available HA powder (Plasma Biotal., Tideswell, Derbyshire) was used throughout this work. The mean particle size of the HA supplied was $\sim 4\ \mu$m. The ceramic suspension was prepared using HA powder and deionised water employing methylcellulose as a binding agent to improve the green body handleability and preventing collapse of the resulting porous structure during sintering. Darvan® 811 (R.T. Vanderbilt Company, Inc.) was used as the dispersing agent for all ceramic suspensions created.

3.3.2 Fabrication of flat HA substrates

Flat HA substrates were created for assessment of time dependent cell attachment in two dimensions (2D), and for 2D proliferation studies. Hydroxyapatite powder was added to water (78% solids content) containing dispersant, Darvan® 811 with a concentration of 2 wt% (to 100 wt% HA powder) and 4 wt% (to 100 wt% HA powder) of Bindelmittel BV/11 (Degussa, Germany) an organic binding agent based on polyvinyl acetate (binder) and polyethylene glycol (plasticiser) (Tancred, 1996) and manually stirred to form a homogenised slurry. The slurry was poured into 1 mm deep cylindrical silicone wells (⌀ 5 and 16 mm) and placed on a vibration plate for 4 hrs, in an attempt to facilitate grain packing and removal of any micro-bubbles that may have been formed through mixing. The discs were allowed to dry overnight at room temperature. After drying was complete, the discs were carefully removed from their moulds and placed in Almath alumina crucibles (Almath Crucibles Ltd., England) and subjected to a sintering cycle as described in Section 3.3.8.

3.3.3 Mould design using rapid-prototyping

In an attempt to create regular architecture scaffolds, moulds were manufactured through rapid prototyping employing selective laser sintering (SLS). Scaffold designs were created in Pro/ENGINEER Wildfire (Parametric Technology Corporation), a 3D CAD design software package, and exported as stereolithography (.stl) files. The pore size and spacing (edge to edge) dimensions were designed to be 300 μm. Using the .stl files, moulds were fabricated with a Sinterstation 2500 Plus, using Duraform PA - a polyamide based on Nylon 11 as the fabrication material. One of the issues with using the SLS technique is that the pore symmetry and accuracy is limited as shown in Figure 3.13 C.

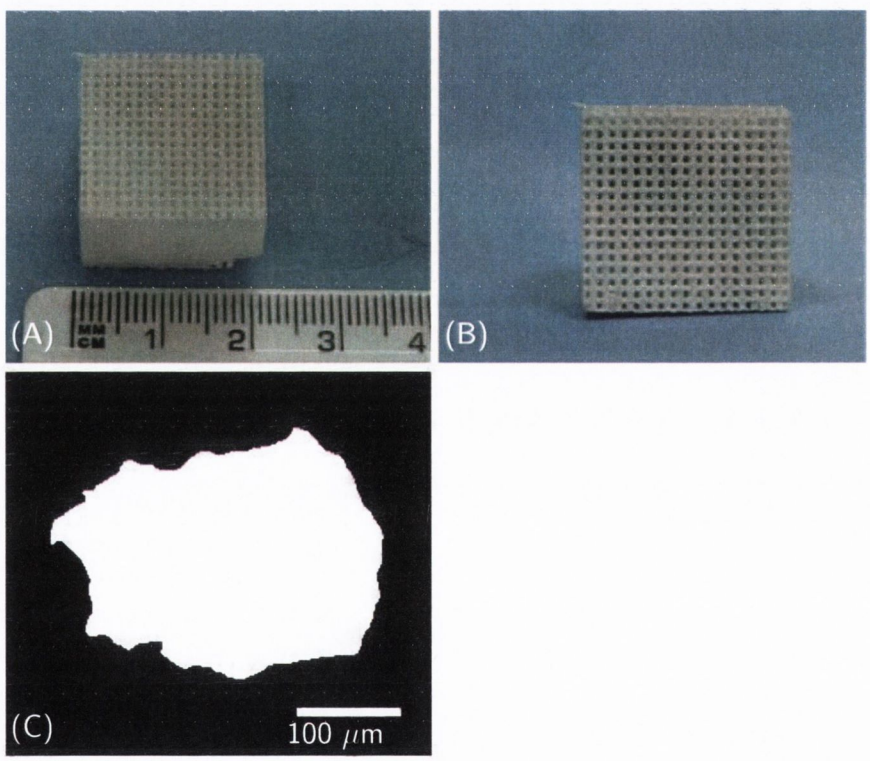

Figure 3.13. (A) and (B) Solid free form (SFF) fabricated scaffold produced using selective laser sintering (SLS) technique. Material is Duraform polyamide. (C) Threshold image of a single pore showing poor symmetry formed through selective laser sintering.

Residual powder is also difficult to remove from the moulds, making it impossible to infiltrate with a ceramic slip. Attempts were made using ultrasonic bath treatment, exposure to air-jetting and insertion of needles to facilitate the removal of residual powder. However all of these post-treatment methods proved ineffective. Due to the poor quality of the moulds obtained using the SLS technique, and the fact that it would be necessary to design scaffold moulds with much larger features to overcome the issue of trapped powder within the pores (of the order of millimeters), the investigation employing this particular method was aborted in favour of pursuing alternative methods.

Similar issues of poor feature symmetry and entrapment of powder particles were observed by Williams *et al.* (2005) when fabricating PCL scaffolds using a similar SLS machine (Sinterstation 2000^{TM}) as used in this work. The smallest attainable feature in SLS is primarily governed by the powder particle size, focused laser beam diameter and heat transfer to the powder bed. Larger particles increase the granularity of edges, layers and surfaces of parts produced by SLS, while smaller particles (10 μm) exhibit poor flow and spreading characteristics (Williams *et al.*, 2005). The authors reported that the Gaussian CO2 laser beam was focused to a 450 μm spot, which also theoretically limits the smallest SLS processed feature. Smaller particles also sinter much faster when trapped inside scaffold pores and at boundaries of designed features, which causes dimensional inaccuracy from thermal growth and makes powder removal post-fabrication difficult to achieve.

Due to these issues many scaffolds fabricated using SLS have pore diameters of approximately 1-2 mm to prevent powder entrapment and to maintain pore geometry. Alternative methods of rapid prototyping such as stereolthography (SLA) (Chu *et al.*, 2002; Taboas *et al.*, 2003) three dimensional printing (3-DP) (Sherwood *et al.*, 2002) and fused deposition modelling (FDM) (Hutmacher, 2001; Zein *et al.*, 2002; Woodfield *et al.*, 2004) have been successfully employed to either directly or indirectly (casting of material and removal of rapid prototyped mould through thermal or chemical means) fabricate scaffolds for tissue engineering purposes. Although

present design/fabrication RP techniques occur at scales above 100 μm, future developments of this technology will lead to machines with capabilities of producing very small features (μm or tens of μm feature sizes), which will inevitably overcome many of the issues that were encountered in the present investigation.

3.3.4 Preparation of porous ceramic scaffold- foamed slip method

A protocol similar to that employed by Rose *et al.* (2004) was utilised in the fabrication of the porous ceramic scaffolds. Methylcellulose 2% (w/v) ($M_n \sim$ 40,000, Sigma; Ireland) was used as the setting agent. Darvan 811, was used as the dispersant at a concentration of 2 wt% (to 100 wt% HA powder). Suspensions were prepared by gradually adding HA powder (final solid content of 40% w/v) to water containing the dispersant and manually stirred. Methylcellulose was then added to the mixture and homogenised in a Turbula® mixer for 1hr at 103 r.p.m. The foaming agent Tergitol® (2% w/v) was subsequently added to the mixture and stirred vigorously using a magnetic stirring unit, creating a foamed slip. The foam was cast into glass petri dishes and immediately placed in an oven at 60 °C to facilitate setting and drying of the foamed structure. On completion of drying, the samples were carefully removed from the glass petri dishes and stored in a desiccator until further use. Wax infiltration to facilitate cutting and sintering of the samples was accomplished as described in Sections 3.3.6 and 3.3.8. The typical architecture produced post-sintering is shown in Figure 3.14.

3.3.5 Preparation of porous ceramic scaffold- freeze-drying method

The freeze-drying method is a two-step process. A ceramic suspension is poured into a mould and then cooled and frozen. The cooling and freezing of the suspension results in the nucleation and growth of ice crystals, which creates the interconnected pores when the sublimable vehicle (typically water) is removed under

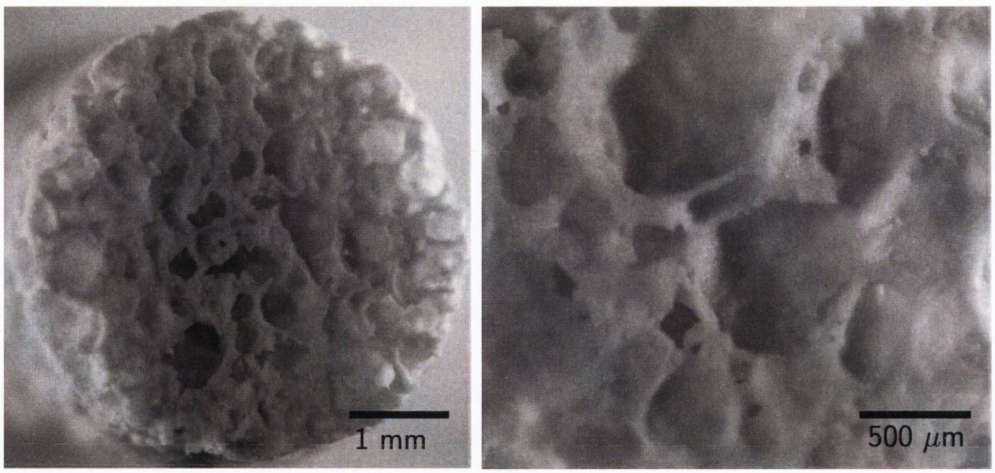

(A) (B)

Figure 3.14. Light micrograph of the typical architecture of HA scaffolds (post-sintering) produced via the foam-gel method. Scale bars, A= 1 mm and B= 500 μm.

vacuum through the second step of the process of drying. This second step of drying avoids drying stresses and shrinkage that may lead to cracks and warping during normal drying (Deville *et al.*, 2006). The green bodies are then subjected to a sintering regime to improve the strength, stiffness and porosity, which produces ceramic scaffold structures with a porous architecture.

Porous HA bimodal (consisting of micro- and meso- pores) scaffolds were fabricated from aqueous suspensions prepared by gradually adding HA powder (final solid content of 36% w/v) to a Nalgene® flask (500 mL) containing the correct volume of water containing the dispersant and mixed through manual stirring. The dispersant, Darvan® 811, concentration was 2 wt% (to 100 wt% HA powder). The binding agent, liquid methylcellulose (Methocel® 60HG, Fluka) was slowly added to the mixture yielding a final binder concentration of 2.5% (w/v). Further homogenisation of the suspension was carried out using a Turbula® mixer at a rotational speed of 23 r.p.m. for 12 hrs. Prior to use for the freeze-drying cycle, the mixture was degassed under vacuum for 1 hr. The suspension was cast into stainless steel rings (∅ 88 mm), (previously sealed on one side using Parafilm®) and placed on the cooling shelf of the freeze-dryer (VirTis Genesis) as depicted in Figure 3.15.

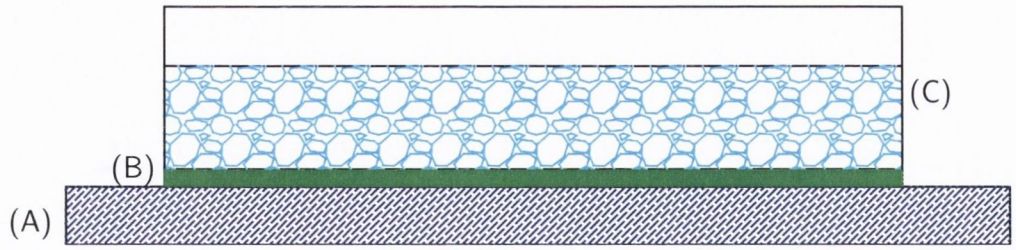

Figure 3.15. Experimental arrangement for freeze drying of HA scaffolds. (A) Cooling shelf, ramped from room temperature to T_f (-40 °C) at 1 °C/min (B) Parafilm® base (C) HA suspension

The ceramic suspension was cooled at a constant cooling rate to a desired final freezing temperature (T_f = -40 °C) as described by O'Brien *et al.* (2004). The frozen suspension was then sublimated under vacuum (200mTorr) for 17 hrs. at a temperature of 0 °C. Table 3.3 shows the freeze-drying program cycle used, and a graph of this program cycle is shown in Figure 3.16. The freeze-drying process resulted in a porous ceramic green body. Samples were carefully removed from the stainless steel rings and stored in a desiccator until further use. An image of the stainless steel mould and resulting freeze-dried HA green body is shown in Figure 3.17.

Table 3.3. Freeze-drying program cycle for HA scaffolds produced

Step	**Temperature [°C]**	**Time [mins.]**	**Ramp/Hold**	**Pressure [mTorr]**
1 (Start)	20	10	Hold	Atm
2 (Ramping)	-40	65	Ramp	Atm
3 (Temp. Hold)	-40	60	Hold	Atm
4 (Drying)	-40	5	Hold	200
5 (Drying)	0	160	Ramp	200
6 (Drying)	0	1020	Hold	200
7 (Drying)	20	40	Ramp	200
8 (Drying)	20	30	Hold	200

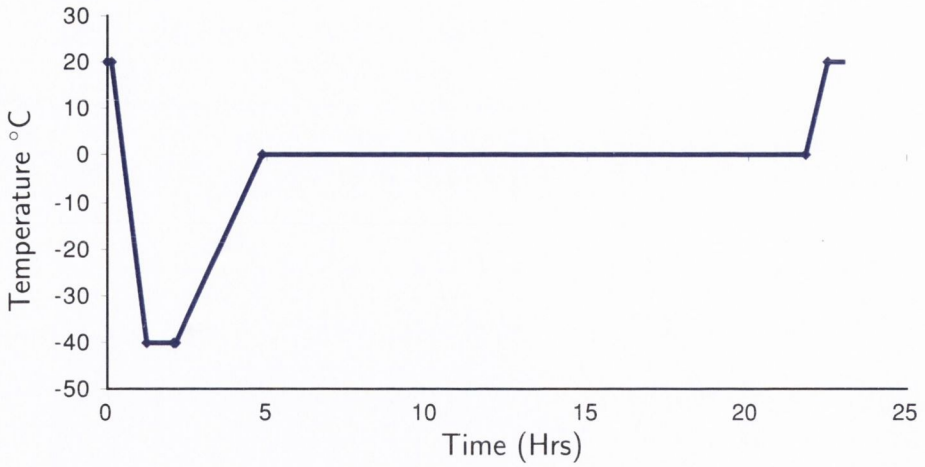

Figure 3.16. Graph of the freeze-drying program cycle for HA scaffolds.

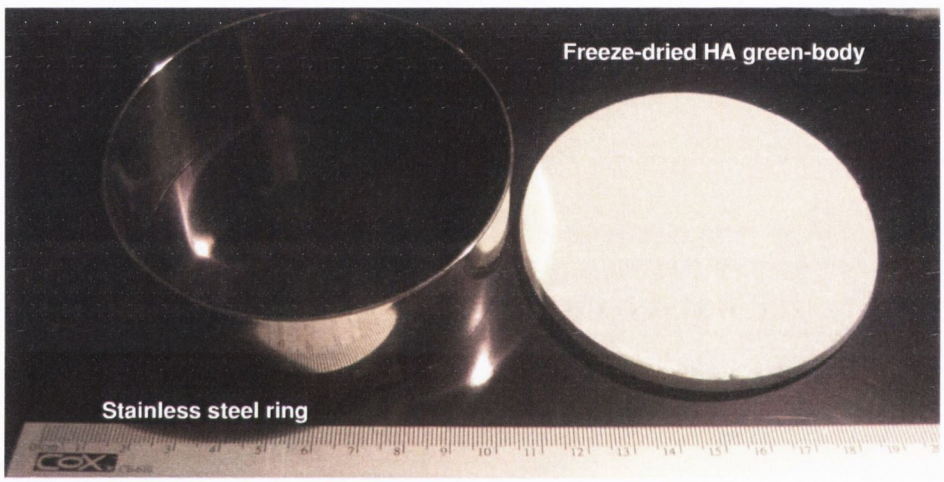

Figure 3.17. Stainless steel mould and resulting freeze-dried HA green body.

3.3.6 Wax infiltration

Due to the fragile nature of the green-body cakes obtained, it was necessary to infiltrate the samples with wax in order to facilitate cutting prior to sintering. Low melting temperature (44-46 °C) paraffin wax (Fluka) was used throughout this work. Impregnation of the green body samples was carried out in a vacuum oven (Binder VD23) at 55 °C. Firstly, the wax was melted in a pyrex bath, the green-body cake was placed on the wax surface and allowed to submerge under its own weight, expelling air from the voids as the wax penetrated the available pore space. Following

complete immersion, a vacuum was applied and held for up to ten minutes at 55 °C. The vacuum was released and the oven was allowed to return to atmospheric pressure. The wax-impregnated cakes were removed from the wax bath and allowed to cool and harden at room temperature. All HA scaffold green-bodies were subjected to the same wax infiltration procedure as outlined in this section.

3.3.7 Introduction of a parallel macro-channel array

Green body cakes obtained from the freeze-drying method (Section 3.3.5) were impregnated with wax as described in Section (3.3.6) in order to allow the introduction of macropores and facilitate the cutting of scaffold discs. This process resulted in the production of a trimodal scaffold, consisting of micro, meso- and macro- pores.

To automate the introduction of macropores into the freeze dried architecture, Computer Numeric Control (CNC) machining was employed. Wax embedded freeze dried HA green-bodies were mounted on a PTFE recessed wax filled base (Figure 3.18) and subjected to a CNC canned cycle (a preset sequence of events initiated by a single G coded command) with a feed of 50 mm/min and drill speed of 3000 r.p.m. using a CNC milling machine (Denford Triac PC Milling Machine, Denford, United Kingdom).

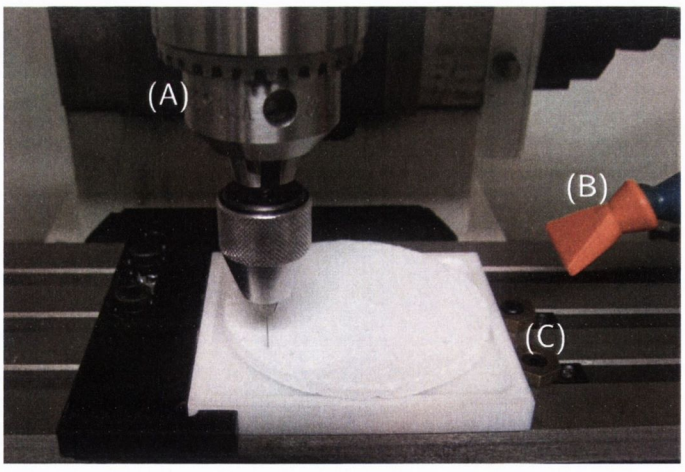

Figure 3.18. Experimental set-up for the introduction of macropores into freeze-dried HA scaffolds;(A) Mandrel and drill (B) Air jet (C) Wax infiltrated HA freeze-dried cake mounted on wax base.

An illustration showing the pattern array of macrochannels is shown in Figure 3.19. Scaffolds with macrochannel diameters of 500 μm and spacing (edge to edge) of 500 μm and scaffolds with 800 μm and spacing (edge to edge) of 500 μm were fabricated. Discs (⌀ 5 mm) were punched out and subjected to a sintering cycle as described in Section 3.3.8. Figure 3.20 summarises the process employed.

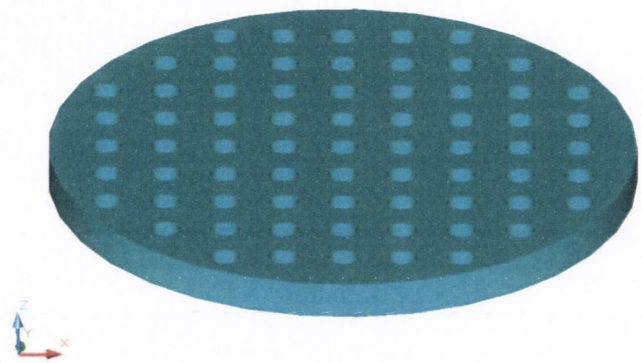

Figure 3.19. Illustration of the unidirectional macrochannel pattern array.

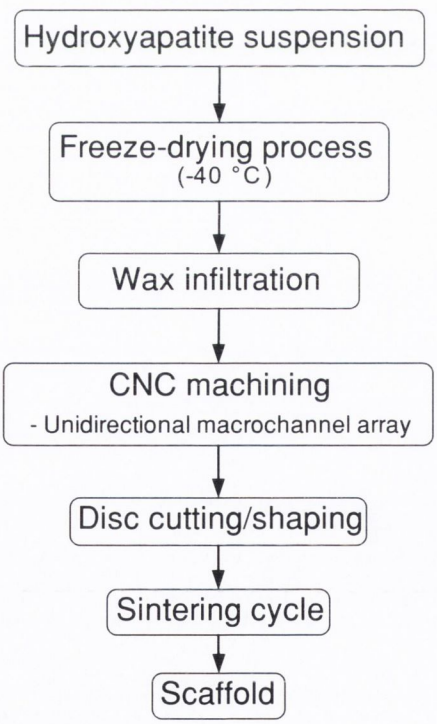

Figure 3.20. Process overview

3.3.8 Wax removal and sintering regime

All scaffold cylinders (⌀ 5 mm) were punched out of the wax-infiltrated green-bodies using cork borers. In order to avoid alteration/destruction of the unsintered pore architecture through the rapid flow of wax, scaffold samples were placed in pyrex dishes and the removal of the wax was accomplished through slow melting in an oven up to 60 °C for 1 hr. Scaffold samples were transferred to Almath alumina crucibles (Almath Crucibles Ltd., England) and sintering was accomplished using a high temperature chamber furnace (UAF 17/27, Lenton, United Kingdom). The green-body ceramic scaffolds were sintered at a rate of 3 °C/min up to 250 °C and held for 1hr. This stage facilitates the complete burnout of the organic components. The ceramic scaffolds or reference discs are then heated in air at the same ramp rate to a final temperature of 1350 °C, and held for three hours and subsequently furnace cooled to ambient temperature (~ 25 °C) at 3 °C/min. All HA fabricated scaffolds and reference discs were subjected to the same sintering regime as outlined in this section.

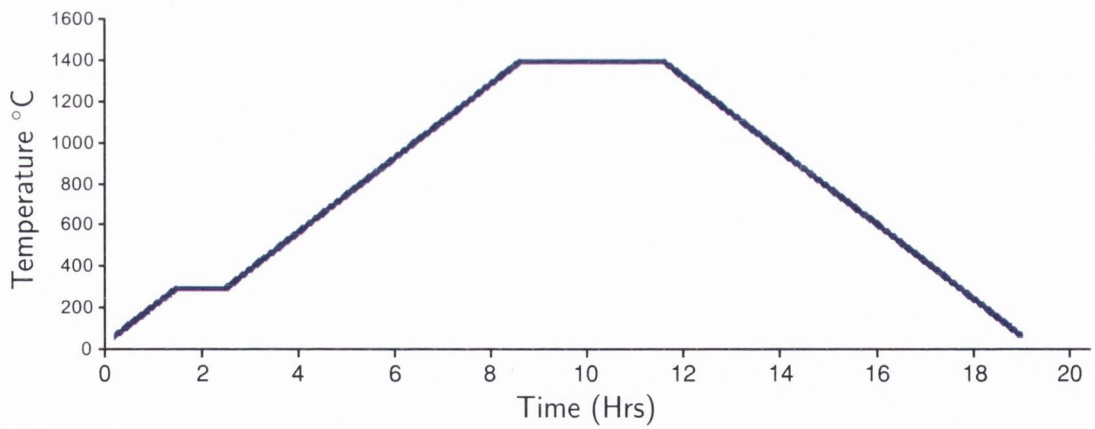

Figure 3.21. Sintering regime

3.4 Anorganic bone matrix preparation

Anorganic bone matrix (ABM) samples were harvested from frozen bovine distal femoral condyles coarsely sliced into sections using a band saw. 5 mm thick sections were then sliced using a diamond saw (Struers^{TM} Accutom 50) and 400 μm blade (Metprep^{TM} 10-12-50). Cancellous samples (4 mm diameter) were physically punched out of each slice. Through visual inspection it was possible to avoid any growth plates and any cortical bone present. Extraction of the organic matrix was performed using a two stage process. Firstly, samples were boiled in water for 24 hrs. The first stage was carried out to enhance the effectiveness of the second treatment (chemical) with ethylenediamine (1,2-diaminoethane; ED) and also to allow visual inspection of the samples to assertain their structural integrity. Samples were then placed in a Wheaton-Soxhlet apparatus (Figure 3.22) and treated for 48 hrs. at 117 °C with ethylenediamine (1,2-diaminoethane; ED) as described by Tancred (1996) and O'Kelly (1999). The soxhlet chamber was encapsulated in a lagging jacket in order to maintain the solvent temperature close to the boiling point, therefore preventing solidification of organic matrix-laden ED within the apparatus. Following completion of the ED treatment, samples were rinsed in deionised water for up to 24 hrs. and finally stored in fresh deionised water until further use.

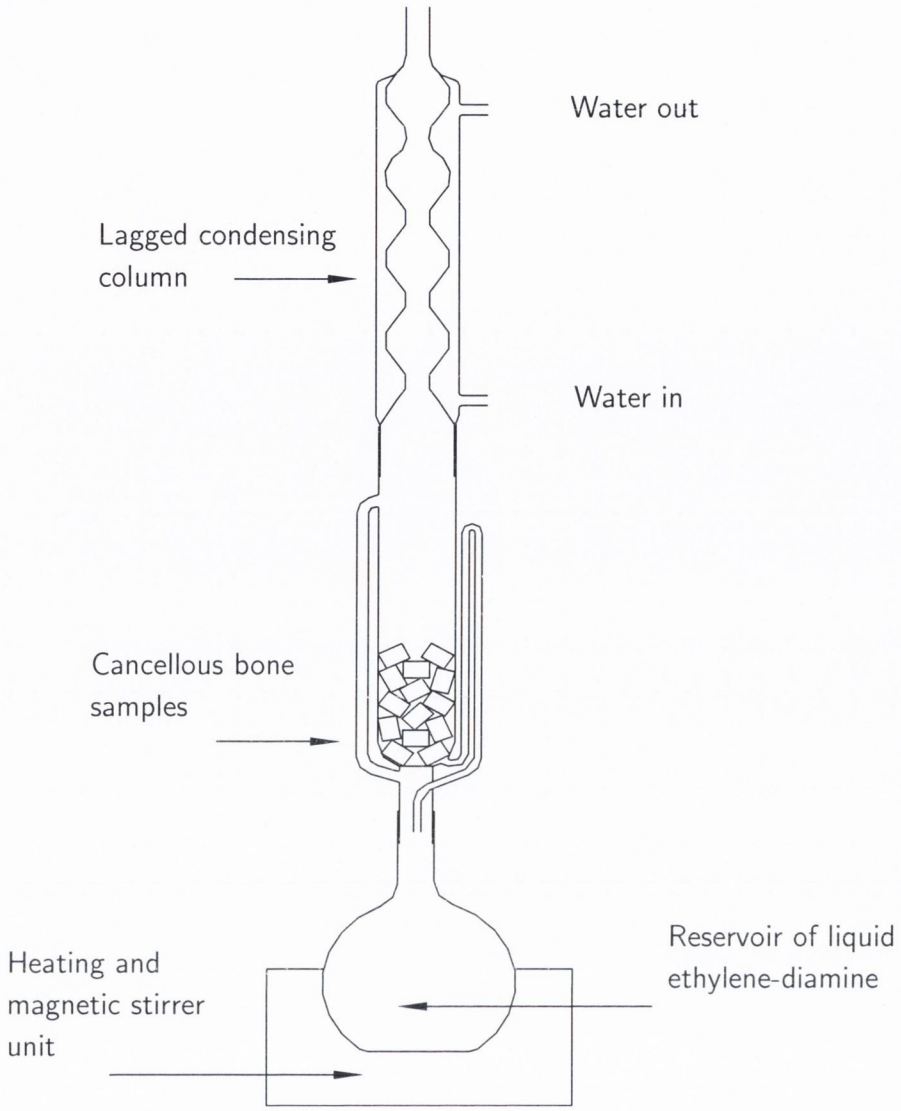

Figure 3.22. Diagram of Wheaton-soxhlet apparatus for the removal of organic matrix from cancellous bone samples, (adapted from O'Kelly, 1999).

3.5 Determination of scaffold properties

3.5.1 Determination of effective diffusion coefficient

The diffusion coefficient of oxygen through bimodal scaffolds (consisting of micro- and meso-pores) obtained through freeze-drying (Section 3.3.5) was measured using a jacketed Franz diffusion cell (PermeGear Inc., USA.) and a dissolved oxygen electrode and meter (ISO2, World Precision Instruments, United Kingdom) as shown in Figure 3.23. The diffusion cell was connected to a circulating pump and maintained at 37 °C by means of a water bath (Grant Instruments, (Cambridge) Ltd., United

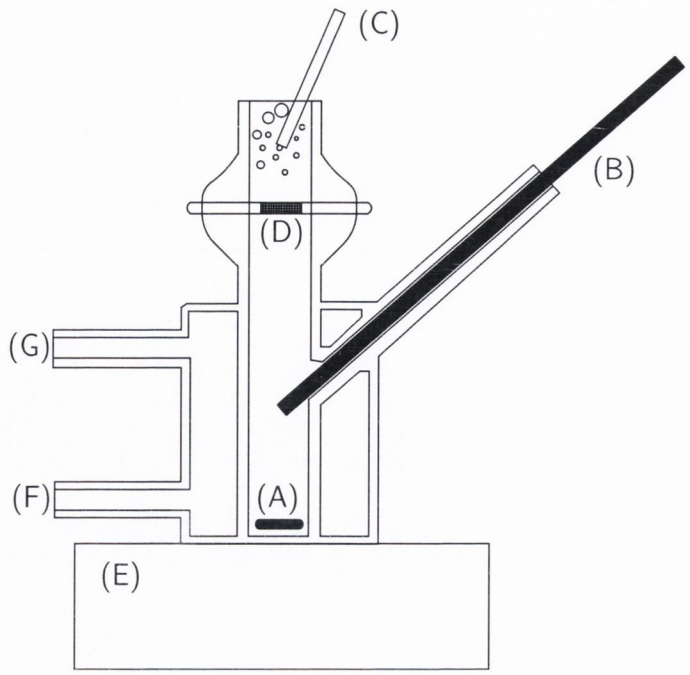

Figure 3.23. Schematic representation of the Franz diffusion cell: (A) magnetic stirrer bar (B) oxygen probe (C) aerator (D)sample (E) magnetic stirrer unit (F) & (G) inlet and outlet to recirculating water bath.

Kingdom). Samples were first sealed in heatshrink tubing, a polymer material (usually PVC with a mixture of polyesters) which decreases in diameter when subjected to heat forming a tight seal. Samples sealed in heatshrink tubing were then inserted into a silicone membrane which was placed in the diffusion chamber (Figure 3.24).

A two point calibration of the oxygen probe was carried out using oxygen saturated water and nitrogen saturated water for the zero point calibration. It was observed that the magnetic stirrer unit influenced the probe readings and therefore all calibrations were carried out in the diffusion cell itself with the magnetic stirrer bar rotation speed set at 400 r.p.m. (VWR S75 Digital Hotplate Stirrer, VWR Int., United Kingdom), to ensure negligible mass transfer resistance in the liquid phase. The bottom chamber of the diffusion cell was filled with nitrogen saturated water, and the top chamber with oxygen rich water. The chambers were separated by the sample to be tested. The upper chamber was kept at 21% oxygen by continuous sparging with air, which also ensured good mixing and good mass transfer in the top chamber (Malda *et al.*, 2004a). The change in the oxygen concentration occurring

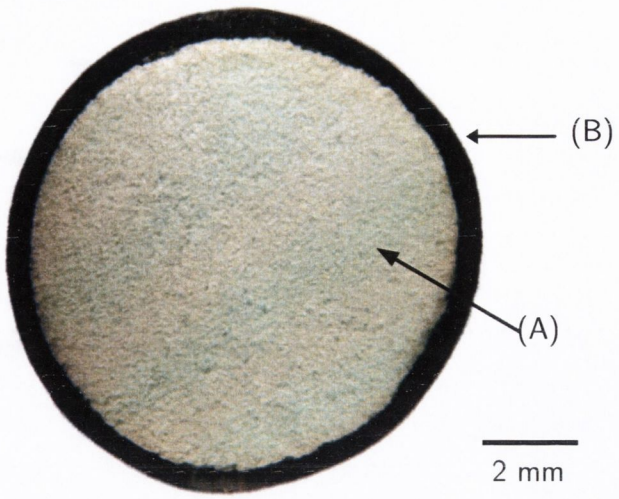

Figure 3.24. Peripheral sealing of a bimodal scaffold with heatshrink. (A) Bimodal HA scaffold (B) Heatshrink.

in the lower chamber was recorded every five mins. for a period of 60 mins. From these data and the measured geometrical properties, the oxygen diffusion coefficient (D) through the bimodal scaffold samples was calculated using the unidirectional diffusion equation (Eqn. 3.3). By making the assumption of unidimensional diffusion in the x direction, the unsteady state diffusion of oxygen into a stationery slab can be reduced to the partial differential form

$$\frac{\partial C}{\partial t} = D\frac{\partial^2 C}{\partial x^2} \tag{3.1}$$

The initial and boundary conditions, imposed by the experimental conditions, for the solution of this equation are

$$\begin{aligned} t = 0, \quad & x > 0, \quad & C = C_0 \\ t > 0, \quad & x = 0, \quad & C = C_1 \\ t > 0, \quad & x > 0, \quad & C = f(t) \end{aligned} \tag{3.2}$$

For a very high mass transfer coefficient facilitated through sparging, the surface resistance will be negligible and the oxygen concentration at the surface will be equal to that in the fluid, which is C_1. If the diffusion chamber is considered to be a semi-infinite medium (in the x direction), Equation 3.1 can be solved to obtain the solution

$$\frac{C_x - C_0}{C_1 - C_0} = 1 \quad - \quad erf\left(\frac{x}{2\sqrt{Dt}}\right) \tag{3.3}$$

where C_x is the oxygen concentration at depth x after time t, C_0 is the initial oxygen concentration within the scaffold, C_1 is the oxygen concentration at the top surface of the scaffold, t is time (s), x is the sample length and D is the diffusion coefficient (m^2s^{-1}).

3.5.2 Direct permeability analysis

The permeability of bimodal, trimodal, foam-gel scaffolds and anorganic bone matrix (ABM) samples was measured using a custom designed permeability chamber. It is essential that the boundary of the sample is completely sealed, thereby preventing the flow of fluid around the scaffold, which would otherwise produce artificially inflated values of permeability. Samples were first sealed in heatshrink tubing, a polymer material (usually PVC with a mixture of polyesters) which decreases in diameter when subjected to heat, forming a tight seal. The permeability chamber (Figure 3.25) consisted of two flange plates, separated by a silicone membrane, with a single punched opening (⌀ 4.9 mm), which provided a tight seal around the sample (⌀ 5.0 mm) when it was inserted. The membrane containing the sample was placed between the two flange plates and assembled and clamped using 3 mm bolts. A constant fluid pressure head was then applied (through the use of an elevated reservoir bath) and the resulting mass flow rate was measured using a mass balance.

With respect to freeze-dried scaffold samples without macrochannels, it was observed that the mass flow rate dropped off with increasing time. It was found that this was due to the formation of micro air bubbles forming on the surface of the

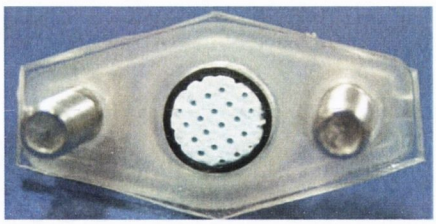

(A)

(B)

Figure 3.25. Experimental setup for the direct measurement of permeability of scaffolds. (A) View of a heatshrink sealed sample inserted into the silicone membrane (B) Full view of the assembled permeability chamber

scaffold which impedes the fluid conductance. To overcome this effect the system was subjected to shock (through light tapping of the vertical column) in order to release the micro bubbles prior to testing. Permeability of the samples was calculated through the application of Darcy's Law. The conductance (C) of fluid flow through the samples was calculated as:

$$C = \frac{\triangle Q}{\triangle P} \tag{3.4}$$

where $\triangle Q$ is the induced flow (mL/s) and $\triangle P$ is the pressure drop (KPa) across the specimen. Applying Darcy's law, we obtain the permeability as:

$$\kappa = \frac{mL\mu}{\rho A \triangle P} \tag{3.5}$$

where κ is the permeability [m^2], m is the mass flow rate [Kg/s], L is the sample length [m], μ is the fluid viscosity [Nsm^{-2}], ρ is the density of the fluid [Kg/m^3], A is the cross-sectional area of the sample [m^2] and $\triangle P$ is the pressure drop across the sample [KPa]. The mass flow rate was determined by measuring the mass of water collected every 30 secs for a period of five mins. using an applied pressure head of 3.5 KPa.

3.5.3 Fluid retention properties

The maximum fluid retention capacities were measured in order to determine the optimal volume of cell suspension that should be applied to scaffolds without causing oversaturation. Scaffolds of each type of known dimensions and dry mass were used. Scaffolds were soaked in deionised water (no vacuum was applied) and excess water was shaken from the scaffolds and subsequently weighed. The maximum water retention volume was calculated and this value was used in order to determine the optimum volume of cell suspension that should be applied to each of the scaffolds.

3.5.4 Embedding of scaffold samples in JB-4 Plus® glycol methacrylate

Embedding of HA ceramic scaffolds for pore size analysis was carried out utilising the JB-4 Plus® embedding kit (Polysciences Europe, Germany). The kit consists of

(i) JB-4 Plus® embedding solution A (monomer)

(ii) JB-4 Plus® embedding solution B (accelerator)

(iii) Benzoyl peroxide (catalyst)

From these stock solutions, the following three types of solutions are required:

(i) Infiltration solution: 1.25 g of catalyst dissolved in 100 mL JB-4 Plus® solution A.

(ii) Equilibration solution: 50:50 (v/v) solution of infiltration solution and 100% ethanol.

(iii) Embedding solution 1.0 mL of JB-4 Plus® solution B, dissolved in 25 mL catalysed solution A.

Samples were equilibrated for 12 hrs. at 4 °C in a solution of ethanol and catalysed JB-4 Plus® solution A, 50:50 (v/v). Samples were then infiltrated in 100% catalysed solution A for one day and stored at 4 °C, with the infiltration solution being changed at 12 hr intervals. Scaffolds were placed in polyethylene molding cup trays (12x16x5 mm) (Polysciences Europe, Germany) and the embedding solution was pipetted into the moulds carefully in order to maintain sample orientation. Labeled plastic block holders (Cat num.15899, Polysciences Europe, Germany) were then placed onto each well and the plastic tray placed in a refrigerator (4 °C) overnight to facilitate curing of the embedded solution.

3.5.5 Scanning electron microscopy (SEM)

Samples for electron microscopy were mounted on 10 mm aluminium stubs using conductive carbon cement (LEIT-C^{TM}) and allowed to dry until all the xylene had evaporated. The samples were then sputter coated with gold at 25 mA for approx 3 minutes (which normally gives a coating of between 10-30 nm depending on the sample surface) using a Polaron sc500 sputter coater. Micrographs were obtained with a Hitachi S-4300 Field Emission Scanning Electron Microscope operating at 5kV acceleration voltage with a tungsten filament and equipped with an energy-dispersive X-ray microanalysis system (EDAX 9100).

3.5.6 Pore size analysis

Embedded scaffold samples (Section 3.5.4) were serially sectioned (5 μm thick sections) on a rotary microtome (Leica RM2255) using a tungsten carbide blade. The sections were picked up by a thick brush and arranged on a clean slide. The sections were air dried and observed under a microscope. Each sample section was imaged using an inverted microscope (Olympus® IX51) and a charge-coupled device (CCD) camera (OLYMPUS DP70, 12.5 megapixel) using image capture software (analySIS® Pro 3.2). Images were analysed using a custom developed linear intercept macro (included in Appendix D) written for Scion Image^{TM} image analysis software (Scion Corp., Frederick, MD), similar to that as previously described by Freyman *et al.* (2001); O'Brien *et al.* (2004). The macro determines the pixel length of each pore that is bisected, when a series of parallel lines (both horizontal and vertical directions), drawn onto an image intercepts a pore wall (black pixel). The raw data from this procedure was exported to a file and subsequently analysed.

3.5.7 Determination of porosity

Both apparent and real densities were calculated for each scaffold sample, where the apparent density includes the open and closed porosity in the volume of a structure and the real density includes only the closed porosity in the volume of the structure (Hing *et al.*, 1999). The apparent density of sintered scaffold samples was calculated from the dry mass and volume for each sample using Eqn. 3.6.

$$\rho_{app} = \frac{M_{dry}}{\pi(r^2)L} \tag{3.6}$$

where ρ_{app} is the apparent density [g/cm^3], M_{dry} is the dry mass [g] of the specimen, r is the specimen radius [cm], L is the specimen length [cm].

Real densities were calculated using Eqn. 3.7. Scaffold samples were placed in a beaker and subjected to a series of brief evacuation-repressurization cycles to force liquid into the pores of the scaffold and to remove any air bubbles that may

have been entrapped within the scaffold. Samples were then carefully removed and shaken vigorously to remove excess liquid and then weighed on a balance (Mettler Toledo AB204-S), accurate to 0.0001 g.

$$\rho_{real} = \left(\frac{M_{dry}}{M_{wet} - M_{dry}} \right) \times \rho_{H_2O} \tag{3.7}$$

where ρ_{real} is the real density [g/cm^3], M_{dry} is the dry mass [g] of the specimen, M_{wet} is the wet mass [g] of the specimen and ρ_{H_2O} is the density of water [g/cm^3]. The apparent (P_{app}) and real porosities (P_{real}), expressed as a %, were then calculated using Eqns. 3.8 and 3.9 respectively.

$$P_{app} = \left(1 - \frac{\rho_{app}}{\rho_{TheoreticalHA}} \right) \times 100 \tag{3.8}$$

$$P_{real} = \left(1 - \frac{\rho_{real}}{\rho_{TheoreticalHA}} \right) \times 100 \tag{3.9}$$

where $\rho_{TheoreticalHA}$ is the theoretical density of HA, which is assumed to be 3.156 g/cm^3 and has been used by other researchers (Hing *et al.*, 1999; Rose *et al.*, 2004; Peon *et al.*, 2004).

Image analysis techniques were also used to determine the average porosity of the mesoporous phase of bimodal scaffolds by calculating the ratio of white (pores) versus black (HA material) pixels from the images used in Section 3.5.6 and expressed as a %, using a custom developed macro (included in Appendix D) written for Scion Image^{TM} image analysis software (Scion Corp., Frederick, MD).

3.5.8 Mechanical properties

Compressive mechanical properties of samples were measured using a Zwick mechanical testing machine (Zwick Testing Machines Ltd , United Kingdom) employing a 50 N load cell. Wet samples (⌀ 5 mm) were placed between two platens (Figure 3.26, and a pre-load of 0.1 N was applied at a speed of 0.005 (mm/s) to remove any surface asperities that may be present on the specimen surface. The samples

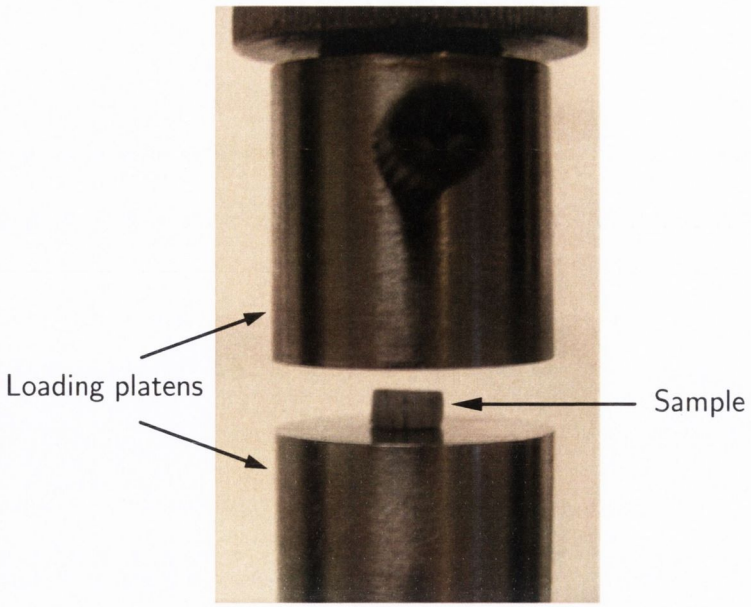

Figure 3.26. Experimental setup for the determination of compressive mechanical properties of HA scaffolds and ABM samples.

were loaded to failure by displacing the top platen at a rate of 0.01 mm/s and the corresponding force was recorded.

3.6 Preparation and Procedures for Cell Culture

3.6.1 Material sterility

To avoid bacterial or fungal contamination all materials that were used during cell culture were sterile and all methods during cell culture were carried out aseptically.

3.6.2 Sterilisation procedure - Equipment

Re-usable equipment, *e.g.* glassware (Schott, Germany), and non-sterile equipment, *e.g.* pipette tips (Sarstedt, Leicester, England), were wrapped in aluminium foil and autoclave tape and autoclaved at 121 °C for 20 min. (Priorclave Ltd., Model EH150, London, England). Instruments were baked at 200 °C overnight in a hotbox oven (Sanyo-Gallenkamp Hotbox Oven, Model OHG050, Loughborough, England). All equipment was sprayed liberally with 70% alcohol before placing inside a lami-

nar flow hood (Astec-Microflow laminar flow workstation, Florida, U.S.A.). Sterile consumables e.g. 50 mL tubes, micro-tubes and petri-dishes (Sarstedt, Leicester, England) were opened only inside the laminar flow hood.

3.6.3 Sterilisation procedure - Reagents

Minimum Essential Eagle's Medium (alpha modified) (α-MEM; Sigma-Aldrich, England) was purchased sterile and all solutions that the medium was supplemented with were sterile filtered using a 0.2 μm cellulose acetate membrane syringe filter (Pall Gellman, Michigan, U.S.A.). Water was autoclaved and all other reagents were stored in autoclaved glass bottles, aliquoted under sterile conditions and were sterile filtered before use.

3.6.4 Culture environment

All culture work was carried out in the laminar flow hood (Astec-Microflow laminar flow workstation, Florida, U.S.A.). All equipment was sprayed liberally with 70% alcohol prior to placing in the hood and disposable latex gloves (Arista Latindo Ind Ltd., Indonesia), also liberally sprayed with alcohol, were worn during all culture procedures. Gloves were changed regularly and the hood was regularly wiped down with alcohol. The ultra-violet (UV) light in the hood was switched on, normally overnight, to further assist sterilisation.

3.6.5 MC3T3-E1 cell culture

MC3T3-E1 mouse clonal osteogenic cells (sub-clone 4) were maintained in α-modified Eagle's medium (α-MEM) supplemented with L-glutamine (2 mM), sodium pyruvate (1 mM), penicillin (100 U/mL), streptomycin (100 μg/mL) and 10 % fetal bovine serum (FBS).

3.6.6 Cell passaging

Upon reaching 80 - 90 % confluency, as assessed by visual inspection under an inverted microscope, (Nikon Labophot, Nikon Instech Co. Ltd. Kanagawa, Japan) cells were passaged at lower densities onto new culture flasks. Flasks were rinsed twice with pre-warmed sterile phosphate buffered saline (PBS; 100mM NaCl, 80mM Na2HPO4, 20 mM Na2H2PO4; Sigma-Aldrich, England). 5 mL of Trypsin EDTA (Sigma-Aldrich, England) was added to each flask to detach the cells from the surface and flasks were incubated at 37 °C for 5 mins. The cultures were examined under an inverted light microscope for detachment and the flask was tapped gently to release any remaining cells. The suspension was added to a 50 mL Falcon^{TM} tube and the flask rinsed twice with 5 mL of supplemented α-MEM, and added to the 50 mL Falcon^{TM} tube. The cell suspension was centrifuged at 300g for 5 mins. at 22 °C. The supernatant was discarded and the pellet re-suspended in 1 mL of supplemented α-MEM. The suspension was triturated three times using a 1 mL pipette to obtain a single cell suspension and the cells were replated onto T75 culture flasks at a fifth of their density before replating. Cultures were maintained in an incubator at 37 °C in 95% air and 5% CO_2 and passaged every 3-4 days.

3.6.7 2D Time-dependent cell attachment

In order to ascertain the time required for cell attachment on 2D surfaces, a time dependent analysis was carried out. HA ceramic substrates (⌀ 5 mm) were inserted into 1.5 mL micro tubes, and tapped lightly into position (before the conical taper) using a tweezers, insuring a good fit within the tube (Figure 3.27. The initial cell density was adjusted to 2.5 x 10^4 cells/cm^2. The cell suspension was pipetted directly onto the ceramic plates contained in micro tubes and placed in an incubator. Time intervals after seeding of 5, 30, 45, 60, 90, 120 and 180 mins. were examined. At each time point, the micro tubes containing the cell seeded ceramic plates were washed in warmed DPBS three times and 400 μL of papain solution was added to

each microtube. Digestion took place at 60 °C overnight, rotating end over end using a rotator wheel (Stuart® Rotator SB3, Lennox Laboratory Supplies Ltd, Ireland). Following digestion, 800 μL of 0.01 % Hoechst was added to each microtube. After light vortexing the samples were transferred to a black 96-well plate in triplicate (300 μL per well), which was read on a fluorescent plate reader (FluoroSkan Assent®) at an excitation of 355 nm and emission of 460 nm.

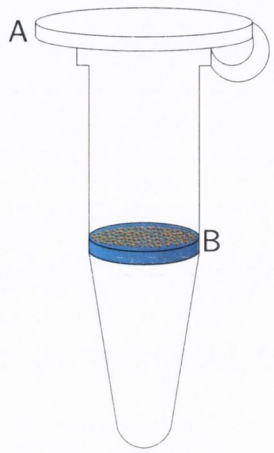

Figure 3.27. Schematic of the experimental arrangement for 2D time-dependent cell attachment. A = microtube, B= cell seeded HA substrate.

3.6.8 Static cell seeding of scaffolds

To minimise the potential of cell suspension flowing around the scaffold volume, thereby reducing the actual number of cells exposed to the scaffold, PDMS silicone chambers were fabricated. These chambers, fabricated through moulding (24 well culture plate using solid PTFE cylinders to form the inner chamber), consisted of a well 12 mm in height with a diameter of 6 mm. Scaffolds to be seeded were placed into each chamber, and a cable tie (previously sterilised by soaking in 70% alcohol) was placed around the periphery of the chamber in order to provide a sufficient seal around the scaffold boundary. Cable ties of different colours were used for ease of labeling. After use, the seeding chambers were washed repeatedly in sterile H_2O, sterilised in 70 % alcohol and stored in a laminar flow hood for future use.

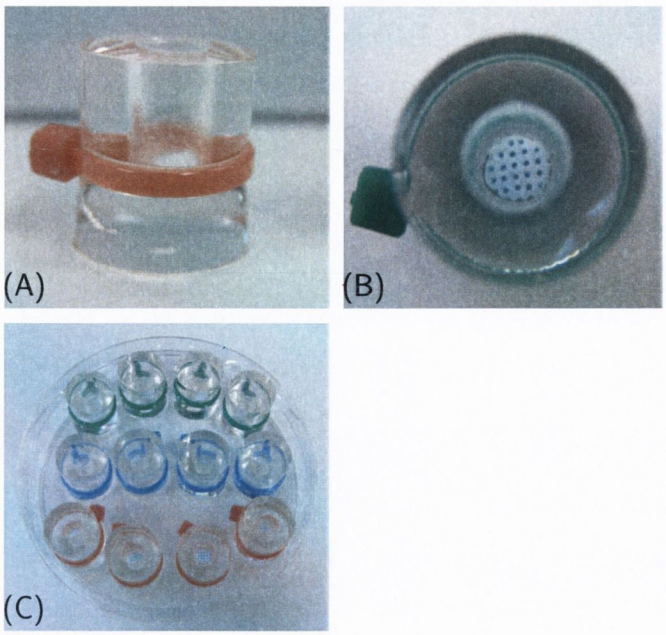

Figure 3.28. PDMS scaffold seeding chambers. (A) & (B) Front and top view of a single PDMS seeding chamber (C) Array of colour coded PDMS seeding chambers

3.6.9 Dynamic rotational cell seeding of scaffolds

In an attempt to increase the degree of cell attachment to freeze-dried scaffolds containing macrochannels, dynamic rotational seeding was employed. PDMS seeding chambers containing scaffolds were placed into the bottom of 30 mL polypropylene tubes, of length 107 mm and diameter 25 mm (Sarstedt, Leicester, England) and seeded with cell suspension (50 μL). The 30 mL tubes were sealed with their respective screw caps and inserted into a rotator wheel (Stuart® Rotator SB3, Lennox Laboratory Supplies Ltd, Ireland), and placed in a hotbox oven. Each tube contained only one scaffold, and rotation was performed clockwise around the central axis of the rotator wheel, with a rotation radius of 10 cm. The rotation speed of the system was set to 25 r.p.m. and the temperature maintained at 37 °C for one hour of rotation. Figure 3.29 illustrates the experimental arrangement employed. Scaffolds were removed from their respective chambers after the one hour time period and assessed using methods described in Sections 3.6.11 and 3.6.13.

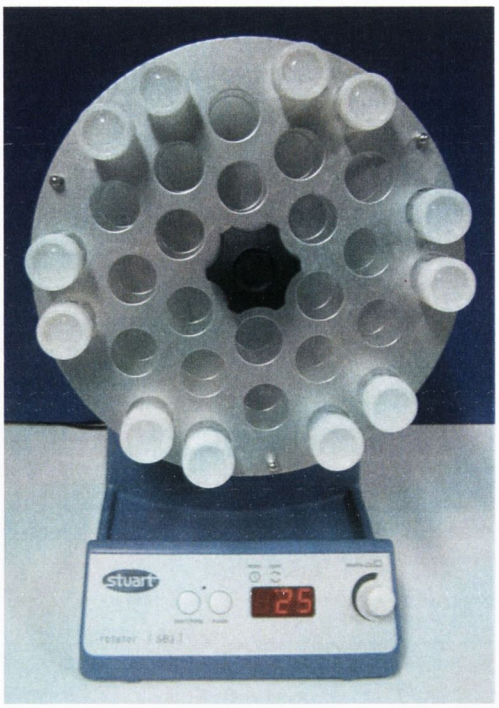

Figure 3.29. Experimental setup for dynamic rotational seeding of HA scaffolds.

3.6.10 XTT cell proliferation and viability assay- standard curve

The TACS^{TM} XTT cell proliferation assay (AMS Biotechnology (Europe) Ltd., United Kingdom) was employed for measurement of cell proliferation and cell viability. XTT, a yellow tetrazolium salt, is cleaved to a water soluble orange formazan dye via the succinate-tetrazolium reductase system in the mitochondria of metabolically active cells, which can be measured by absorbance at 490 (or 450) nm (Roehm *et al.*, 1991). Standard curves were generated by quantifying the signal cultured cells. MC3T3-E1 cells were counted using a hemocytometer and plated in a clear six well plate (Sarstedt, Dublin) at various cell densities(0, 3 x 10^4, 7.5 x 10^4, 15 x 10^4, 3 x 10^5 and 6 x 10^5 cells) in 1 mL of medium. Cells were allowed to attach for 2 hrs. and examined under an inverted light microscope. Before starting incubation with the XTT working solution, sufficient aliquots of XTT reagent and activator (50:1 v/v) were warmed at 37 °C until they were no longer opaque. The two solutions were then mixed, vortexed and immediately used. 500 μL of the working solution was added

to each well of the cell seeded plates and incubated for one hr. at 37 °C under 5 % CO_2. After incubation 100 μL samples were removed from each well (in triplicate) and absorbance values were obtained at 490 nm using a spectrophotometer (Helios Gamma, Thermo Electron Corporation, United Kingdom) and a suprasil® quartz Hellma® absorption cuvette (Cat. 105.202-QS, Sigma-Aldrich, Ireland). Averages of triplicate values were obtained and data expressed as cell number per well versus absorbance.

3.6.11 XTT cell proliferation and viability assay- 2D and 3D

HA flat substrates (2D) or scaffolds (3D) to be assessed with the TACS^{TM} XTT assay were removed from culture and transferred to fresh clear 24-well plates (Sarstedt, Dublin) prior to the assay and incubated with 1 mL of warmed medium. 500 μL of the working solution was added to each well containing a scaffold and a blank well containing medium only as a reference control. Scaffolds and working solution were incubated for one hour and absorbance values were measured as described in Section 3.6.10.

XTT correction factor

It was observed that after incubation of cell seeded HA scaffolds with the XTT reagents, the surfaces of the scaffolds were red in appearance. This was possibly due to the accumulation of the cleaved soluble orange formazan dye within the scaffolds. Due to this observation, it was hypothesised that the determined viable cell numbers were being underestimated and further experiments were carried out to ascertain the degree of this effect.

Three groups of scaffolds (n =3 for each group) were placed in 2.5 mL micro-tubes. One scaffold group was crushed using a forceps. Each of the three groups and one control group (no scaffold) were seeded with 2 x 10^5 cells suspended in 50 μL. After 30 mins. incubation 950 μL of fresh culture medium was added to each group and incubated for a further two hrs. After this time, XTT reagents were

added to each group as described in Section 3.6.10 and incubated for 1 hour. After this time, another scaffold group was then crushed using a forceps. All groups were lightly vortexed and the absorbance values were measured using a spectrophotometer. A summary of the different groups with their respective absorbance values and corresponding cell numbers is given in Table 3.4.

Table 3.4. Summary of the different groups used for XTT correction with respective absorbance values and corresponding cell numbers.

Group	**Absorbance [± SE]**	**Cell number [± SE]**
Control (no scaffold)	0.738 ± 0.016	184500 ± 3971
Fully intact scaffold	0.306 ± 0.006	76417 ± 1446
Scaffold crushed prior to seeding	0.612 ± 0.023	152917 ± 5731
Scaffold crushed after XTT assay	0.766 ± 0.013	191500 ± 3263

As can be seen from Table 3.4 there is a significant difference ($\sim$ factor of 2.5) between the fully intact scaffold group and the other tested groups.

3.6.12 DNA quantification using Hoechst 33258- standard curve

Standard curves were generated by quantifying the signal from known concentrations of DNA from papain digested cells. MC3T3-E1 cells were counted using a hemocytometer. A sample containing 1 x 10^6 cells was centrifuged at 600g for 5 min to obtain a cell pellet. Cells were digested by adding 400 μL of 0.1 % papain in buffer (DPBS, 5mM EDTA pH8, 5mM cysteine-HCl (Sigma-Aldrich, Dublin, Ireland)) to 1.5 mL microtubes. After a gentle vortex, samples were incubated at 60 °C overnight as described by Kim *et al.* (1988). Volumes corresponding to 1 x 10^5 cells, 5 x 10^4 cells, 2 x 10^4 cells, 1 x 10^4 cells, 5 x 10^3 cells, 2 x 10^3 cells and 1 x 10^3 cells, were taken from the digested sample and the final volume for each was made up to 40 μL using papain solution. Samples for each cell number were repeated in triplicate. 800 μL of 0.01 % Hoechst 33258 in buffer (10 x 10mM Tris, 1mM

Na2EDTA, 1M NaCl, pH 7.4) was added to each microtube. After gentle vortexing, the contents of each ependorf were transferred to a black 96-well plate (Sarstedt, Ireland). Plates were analysed on a FluoroSkan Assent® fluorescent plate reader (Thermo Electron Corporation, United Kingdom) The excitation wavelength used was 355 nm and the emission wavelength was 460 nm.

3.6.13 Cell digestion and DNA assay- HA scaffold

Samples were washed three times in warmed DPBS and transferred to 1.5 mL microtubes. 400 μL of papain solution was added to each microtube and the scaffolds were crushed using a forceps. Digestion took place at 60 °C overnight, rotating end over end using a rotator wheel (Stuart® Rotator SB3, Lennox Laboratory Supplies Ltd, Ireland). Digests were centrifuged to pellet the crushed scaffold and 40 μL of the cell digest was subsequently removed from each sample and transferred to empty microtubes. 800 μL of 0.01 % Hoechst was added to each microtube. After light vortexing, the samples were transferred to a black 96-well plate in triplicate (210 μL per well), which was read on a fluorescent plate reader (FluoroSkan Assent®) at an excitation of 355 nm and emission of 460 nm.

3.6.14 Cell seeding suspension volume dependency

An investigation was carried out to assess if the number of cells being seeded and remaining attached onto scaffolds was dependent on the volume of cell suspension delivered to each scaffold. Scaffolds were placed in PDMS chambers (Section 3.6.8), and seeded with various volumes, 25, 50, 100 μL of cell suspension. All suspensions were diluted in a manner providing a final cell number of 3 x 10^5 cells in each volume delivered. Scaffolds were placed in an incubator and cultured for three hours. Scaffolds were removed from culture and washed three times in warmed PBS. The number of cells in each scaffold after the three hour period was assessed through DNA quantification (Section 3.6.13).

3.6.15 Examination of cell proliferation-2D

Proliferation of cells seeded onto flat HA substrates was examined using the TACS^{TM} XTT cell proliferation assay (Section 3.6.11). Flat non-porous HA substrates (⌀ 16 mm, n =6), described in Section 3.3.2, were seeded with cells at a density of 2.5 x 10^4 cells/cm^2 and placed in 24 well plates. For comparison purposes, six wells of a 24 well plate (without HA substrate material) were also seeded with a cell density of 2.5 x 10^4 cells/cm^2. At specific time intervals of culturing (4 hr, 1 day, 3 day, 5 day and 7 days) the flat substrates were assessed. Before each time-point, samples were rinsed with warmed PBS and assessed *via* the XTT assay. The medium of remaining samples in culture was replaced every two days.

3.6.16 MTT assay

An MTT assay was utilized to assess the spatial distribution of cells throughout scaffold constructs. MTT [3-(4,5-dimethylthiazol-2-yl)-2,5-diphenyl tetrazolium bromide] is a water-soluble tetrazolium salt yielding a yellowish solution when prepared in media or salt solutions lacking phenol red. Dissolved MTT is converted to an insoluble purple formazan product by cleavage of the tetrazolium ring by dehydrogenase enzymes. The protocol employed is similar to that used by previous researchers (Yang *et al.*, 1998; Smith *et al.*, 2000; Wendt *et al.*, 2003). Stock MTT (1.0 mg/mL) was prepared by dissolving the salt in phosphate-buffered saline (PBS). The stock MTT was then stored at 4 °C in the dark. Scaffold samples to be assessed were first cut in half and washed in PBS. Scaffolds were then incubated with 2 mL of the MTT stock solution at 37 °C for 2 hours. Viability and distribution were evaluated qualitatively by a dark blue stain, indicating that the reduction of MTT to formazan had occurred. An area in which a dark blue stain was not present denoted an absence of live cells in that specific region.

3.6.17 Static and dynamic culturing of HA scaffolds

Both bimodal and trimodal porous scaffolds were statically seeded with 3 x 10^5 cells as previously described (Section 3.6.8). Both scaffold types were then subjected to either static culturing or dynamic rotational culturing for a 7 day period.

For dynamic rotational culturing, scaffolds were placed into the bottom of 30 mL polypropylene tubes, of length 107 mm and diameter 25 mm (Sarstedt, Leicester, England) with 5 mL of medium. The 30 mL tubes were sealed with their respective screw caps and inserted into a rotator wheel (Stuart® Rotator SB3, Lennox Laboratory Supplies Ltd, Ireland), and placed in a hotbox oven. Each tube contained only one scaffold and rotation was performed clockwise around the central axis of the rotator wheel with a rotation radius of 10 cm. The rotation speed of the system was set to 10 r.p.m. and the temperature maintained at 37 °C. Medium was changed daily due to the absence of gas exchange. Both scaffold groups were assessed after 4 hours and 1, 3, 5 and 7 days of culture to examine cell proliferation *via* a DNA assay (Section 3.6.13). At each of these time points the cell distribution throughout scaffolds was examined qualitatively *via* an MTT assay (Section 3.6.16).

3.6.18 Examination of cellular oxygen consumption

The BD oxygen biosensor system (OBS) (BD Biosciences, England) was employed to determine cellular oxygen consumption rates. The OBS incorporates an oxygen-sensitive ruthenium-based fluorophore (tris 4,7-diphenyl-1,10-phenanthroline ruthenium (II) chloride, or $Ru(DPP)_3Cl_2$) into a silicone rubber matrix in the bottom of each well of an otherwise standard 96 well plate (Guarino *et al.*, 2004). The day before oxygen consumption experiments were initiated, the medium of sub-confluent flasks was changed with fresh medium. MC3T3-E1 cells for analysis were harvested from confluent T75 flasks and resuspended in fresh media (which had been incubated with 5% CO_2 over night), counted using a hameocytometer and serially diluted in order to yield desired cell concentrations.

HA bimodal scaffolds (⌀ 5 mm, height 1 mm), sterilised through autoclaving and

oven baked dry at 125 °C, were seeded with 0.5, 1 and 2 x 10^5 cells and transferred to the plate wells. 200 μL was added to each well containing a HA cell seeded scaffold. Figure 3.30 illustrates the experimental arrangement. The plates were fluorometrically interrogated at various time intervals (0, 12, 36, 60, 156, 228 hrs.). Fluoresence data was collected using a plate reader (Tecan GENios^{TM}) utilising the bottom plate reading configuration. Nominal wavelengths of the bandpass filters were 485 nm for excitation and 620 nm for emission. The corresponding cell number within each bimodal scaffold at each time point was determined using the XTT cell proliferation assay as described in Section 3.6.11.

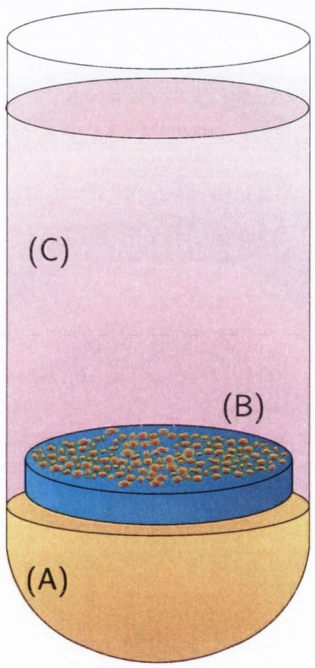

Figure 3.30. Schematic illustrating the experimental arrangement for determining cellular oxygen consumption. (A) Oxygen sensitive silicone rubber matrix (B) Cell-seeded porous bimodal scaffolds (C) Culture medium.

The quenching behaviour of the fluorophore is described by the Stern-Volmer equation (Eqn. 3.10), which relates dissolved oxygen concentrations ($d0_2$) to the ratio of fluorescence intensity at zero oxygen concentration (I_0) and the intensity at the oxygen concentration of interest (I):

$$I_0/I = 1 + K_{SV}[O_2] \tag{3.10}$$

where $[O_2]$ is the oxygen concentration, K_{SV} is the Stern-Volmer constant for the fluorophore, I is the normalised fluorescence intensity at $[O_2]$ and I_0 is the normalised fluorescence intensity for zero oxygen. For experimental convenience the ambient condition is used as the reference yielding:

$$N_{max} = I_0/I_a = 1 + K_{SV}[O_2]_a \tag{3.11}$$

Making the appropriate substitutions into Equation 3.10 and solving for dO_2, yields the oxygen concentration at the well bottom:

$$[O_2] = \frac{[O_2]_a}{N} \times \frac{N_{max} - N}{N_{max} - 1} \tag{3.12}$$

where N is the normalised fluorescence intensity (I/I_a) of the well of interest, N_{max} is the empirically measured maximum ratio known as the dynamic range. The dynamic range is determined empirically from the ratio of fluorescence intensity from two reference conditions. These being the ambient oxygen concentration, $[O_2]_a$ of cell-free medium equilibrated with the incubator atmosphere (37 °C, 5% CO_2) and a zero oxygen control. The ambient oxygen concentration ($[O_2]_a$) is calculated through the use of Henry's Law (Eqn. 3.13):

$$[O_2]_a = \left(\frac{\alpha}{V_m}\right) \times PO_2 \tag{3.13}$$

where $[O_2]_a$ is the concentration of oxygen in solution [mol/L], α is the solubility coefficient of oxygen expressed as volume of gas per volume of water, V_m represents the molar volume of oxygen at standard temperature (0°C) and pressure (1 atm)[L/mol], and PO_2 is the partial pressure of oxygen in the atmosphere [atm]. At 37 °C, the solubility coefficient of oxygen in water is 0.024 and the value for V_m for oxygen is 22.4 L in accordance with Avogadro's theory. The partial pressure of oxygen in air at sea level (0.210 atm) is reduced to 0.186 atm under test conditions by the presence of CO_2 (0.50 atm) and water vapor (0.062 atm) for the incubator atmosphere. Substituting these values into Equation 3.13, yields an ambient oxygen

concentration ($[O_2]_a$) of 200 μM.

The zero oxygen control is obtained from wells containing 100 mM sodium sulphite which scavenges the oxygen from the well and reduces the dO_2 at the well bottom to zero. This approach allows an *in situ* calibration of the system.

The oxygen consumption rate (OCR) can be determined from the steady-state solution of Ficks Law as given in Eqn 3.14, (Guarino *et al.*, 2004; Mamchaoui and Saumon, 2000):

$$OCR = \frac{DSL\triangle P}{h} \tag{3.14}$$

where D is the diffusion coefficient of oxygen in the media (assumed to be 3.0 x 10^{-5} cm^2/s), S is the surface area of the media exposed to the atmosphere (0.32 cm^2 for a 96 well plate), h is the diffusion path length in cm (the distance between the atmosphere and the cells, which is the depth of the media), L is a units conversion factor and $\triangle$P is the difference in oxygen concentration (or partial pressure, in μM) between the air/media interface and the media/cell interface as given by $[O_2]_a$ - $[O_2]$.

3.7 Finite element modelling of *in vitro* oxygen concentration profiles

A mathematical model was developed to determine the distribution of oxygen within scaffold constructs and to assess the influence of macrochannels on the resulting oxygen concentration profiles. The oxygen concentration in a scaffold construct can be described by Eqn. 3.15:

$$\frac{\partial c}{\partial t} = D\frac{\partial^2 c}{\partial x^2} - R \tag{3.15}$$

The diffusing species, oxygen, is assumed to move due to diffusion, with a constant diffusion coefficient D (m^2 s^{-1}). The oxygen concentration is denoted by c (mol m^{-3}). The depth into the scaffold sample is x (μm). The reaction rate, R (mol m^3 s^{-1}), is the rate at which oxygen is consumed by the cells within the mesoporous

domain of the scaffold construct. Figure 3.31 illustrates the domains considered for the finite element model.

The reaction rate, R (mol m^3 s^{-1}) is dependent on the local cell density and on the maximal rate of consumption of oxygen of the cells V_{max} (mol $cell^{-1}$ s^{-1}). As oxygen concentrations, c (mol m^{-3}), become depleted the oxygen consumption rate of the cells alters according to Michaelis-Menten kinetics, with K_m (mol m^3) being the oxygen concentration at half maximal oxygen consumption, giving an equation for R:

$$R = \frac{n_{cell} V_{max} c}{c + K_m} \tag{3.16}$$

3.7.1 Initial and boundary conditions

The scaffold is taken to extend from x =0 to x = L. Due to symmetry (a reasonable assumption based on image analysis) and previous studies (Malda *et al.*, 2004a; Lewis *et al.*, 2005; Radisic *et al.*, 2006), it was sufficient to model only one eighth of the construct and impose symmetrical boundary conditions at the construct centrelines (Figure 3.31).

The initial parameters including initial oxygen concentrations, effective diffusion coefficient (Section 4.2.4), cell numbers (Section 4.3.7) and cellular oxygen consumption rates (Section 4.3.8) obtained from this work were input into the model. Ambient oxygen concentrations (c_0, (mol m^{-3})) were calculated through the use of Henry's Law as described in Section 3.6.18 (Eqn. 3.13). The lateral and top surfaces of the scaffold construct that are in direct contact with the culture medium were assumed to be equal to each other. Various cell densities were confined to specific depths from the surface (250, 500 and 1000 μm). The results for the oxygen concentrations as a function of depth into the sample were plotted.

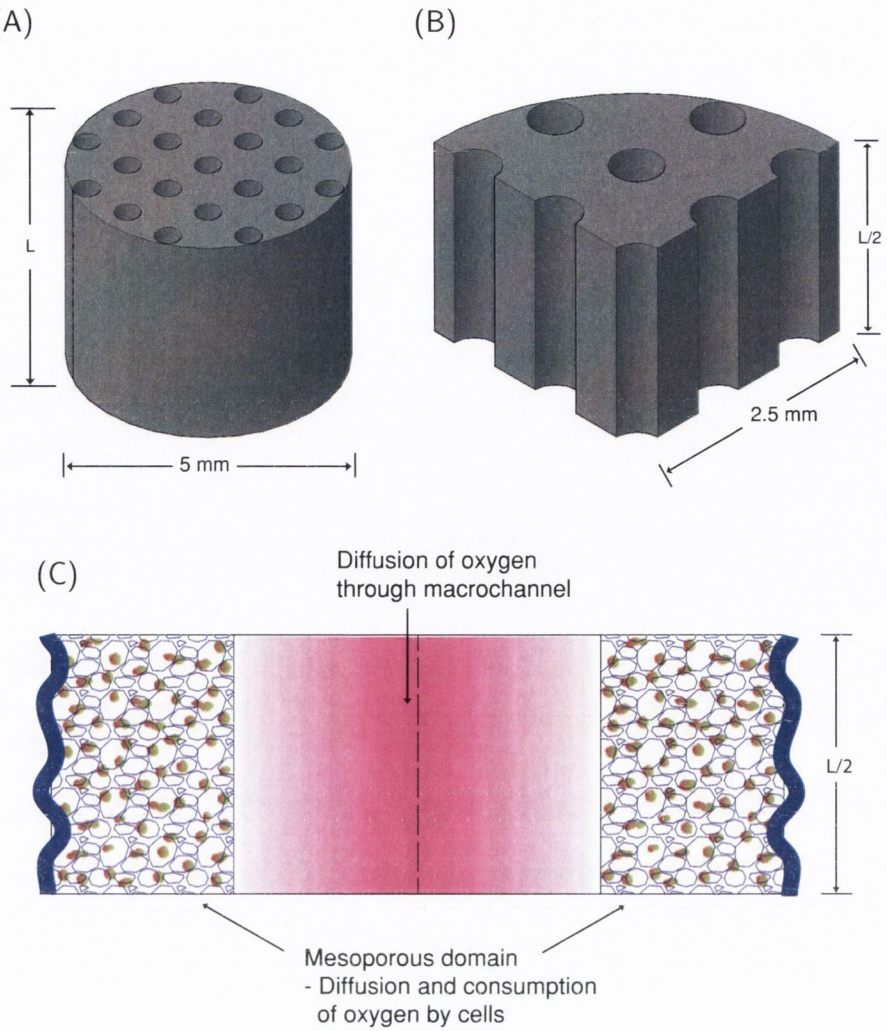

Figure 3.31. Schematics of finite element model geometry (A) Full scaffold with unidirectional macrochannels (B) Modelled geometry, 1/8 section (C) 2D cross-sectional view of a single macrochannel illustrating the oxygen transport and consumption domains.

The initial boundary conditions are:

$$c = c_0 \quad at \quad x = 0$$

$$\frac{\partial c}{\partial x} = 0 \quad at \quad x = \frac{L}{2}$$

3.7.2 Numerical methods

The source term in the diffusion equation follows Michaelis-Menten kinetics and is non-linear. The equations cannot be solved using analytical methods, therefore,

a numerical method was employed to calculate the oxygen gradients using a finite element method and a commercial software package COMSOL Multiphysics^{TM} (3.2). The equations were solved using a stationary non-linear solver, Direct (UMFPACK) solver supplied with COMSOL Multiphysics^{TM} (3.2). The algorithm solves the equation by an affine invariant form of the damped Newton method (Radisic *et al.*, 2005). The maximum number of iterations was set to 25, with a minimum step size of 10^{-4} and the tolerance for convergence was set to 10^{-6}. In order to validate the model, the oxygen profile at the centreline of the constructs with uniform cell density respiring at V_{max}, was compared to the one dimensional analytical solution with zero order kinetics.

3.8 Statistical and error analysis

Numerical and graphical results are reported in the form of mean ± standard error from the mean (SE). All statistical analyses were performed using GraphPad Prism (Version 4.3) software. One way ANOVA with Tukey post-testing and unpaired Student t-tests for individual comparisons were used where indicated. Tukey post hoc statistical analysis methods were performed for image analysis results to permit multiple comparisons between scaffold sections in both the transverse and longitudinal directions.

The standard error (also known as the standard error of the mean) of a sample from a population is the standard deviation of the sampling distribution of the mean, which was calculated by the formula:

$$SE = \frac{\sigma}{\sqrt{n}} \tag{3.17}$$

where σ is an estimate of the standard deviation of the population, and n is the size (number of items) of the sample.

Sources of error encountered in this work were mainly due to either operator error or through background emissions in the case of fluorescence based techniques.

To overcome these operator dependent errors large sample sizes and multiple experiments were conducted and compared. In the case of fluorescence based assays, samples were quantified in triplicate and compared with known standards.

Chapter 4

Results

Contents

4.1 Introduction 129

4.2 Characterisation of scaffold properties 129

4.3 Cellular response to HA scaffolds and substrates 160

4.4 Finite element modelling of *in vitro* oxygen concentration profiles 186

4.1 Introduction

This chapter will present the results obtained from this work in three distinct parts:

(i) Characterisation of scaffold properties

(ii) Cellular response to HA scaffolds

(iii) Finite element analysis of the oxygen environment of HA scaffolds

The terminology used to describe the various scaffold architectures throughout this, and subsequent chapters are defined in Table 4.1.

Table 4.1. Scaffold terms used to define various scaffold architecture types

Scaffold Term	Scaffold Type
Bimodal	Scaffold produced through the freeze drying process containing both micropores and mesopores (Section 3.3.5)
Trimodal	Scaffold produced through the freeze drying process containing both micropores, mesopores and macrochannels (Section 3.3.7)
Foam gel	Scaffold produced through the foam gel method containing both micropores and mesopores (Section 3.3.4)
Cancellous bone	Cancellous bone samples with the organic phase removed though chemical treatment (Section 3.4)

4.2 Characterisation of scaffold properties

4.2.1 Scaffold and pore architecture

Figure 4.1 demonstrates the scaffold architecture produced from the freeze drying process and the post introduction of unidirectional macrochannels produced through CNC machining.

Closer examination by SEM (Figure 4.2), illustrates a finer mesopore structure that exists in the available regions between the unidirectional channels. This mesopore phase is a direct result of the freeze drying process. Figures 4.3 and 4.4 reveal

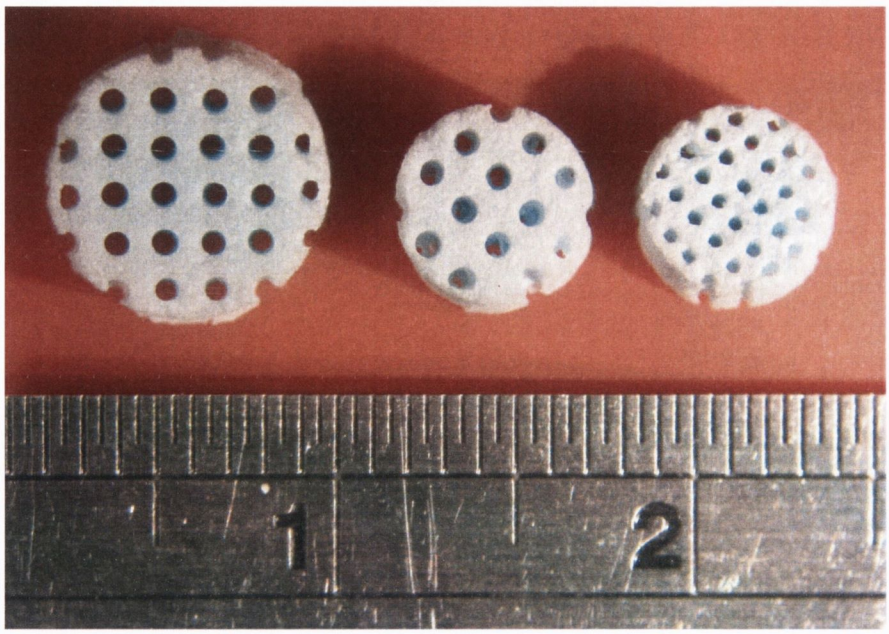

Figure 4.1. Light micrograph of the scaffold architectures of trimodal scaffolds produced through the freeze drying process (L-R) ∅ 8 mm, pore size and spacing of 800 μm, ∅ 5 mm, pore size and spacing of 800 μm and ∅ 5 mm, pore size and spacing of 500 μm.

a closer inspection of these distinct regions. It should be noted that this mesopore structure also contains a degree of microporosity which is highlighted in Figures 4.5 and 4.6. On closer inspection of Figure 4.7, it can be seen that these micropores (indicated by white arrow heads) are approximately 2 - 5 μm in diameter.

A longitudinal cross section of a single unidirectional channel is shown in Figure 4.8 and of multiple channels in Figure 4.9. It is clear from these images that the introduction of macrochannels through CNC machining has not disrupted the mesopore phase at the surface of the channel and thus the mesopores have not become occluded. This is due to the presence of the wax infiltrate and the cutting of material as opposed to piercing of the material, which occurs when attempting to introduce macrochannels through the use of needles as demonstrated in Figure 4.10.

It can also be seen from Figure 4.8 that a dense layer is present. This occurs on the bottom surface of the scaffold discs which was in direct contact with the cooling shelf, and is possibly due to undercooling or settling of HA particles prior to actual freezing and formation of ice crystals. Figures 4.11 and 4.12 reveal greater detail of

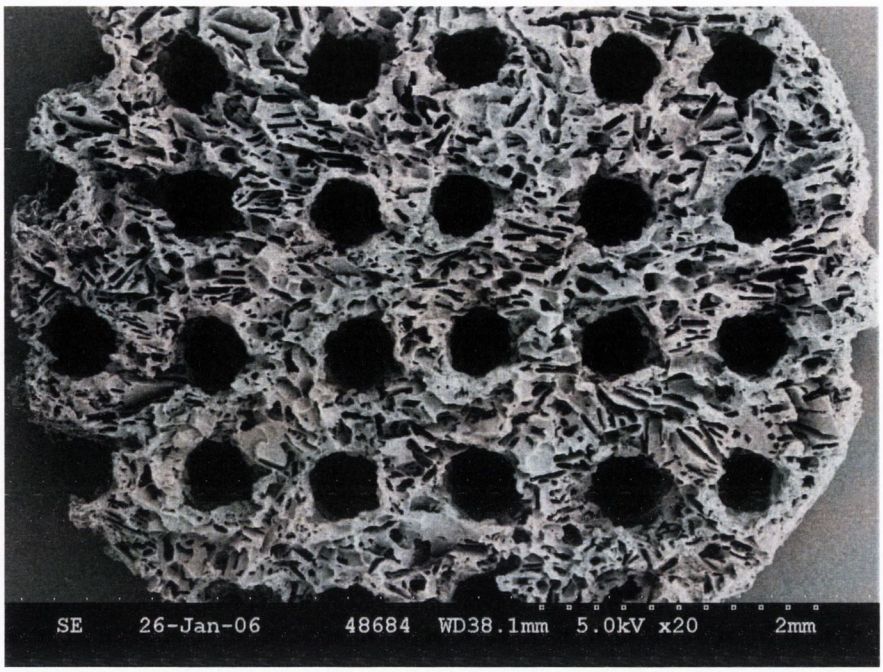

Figure 4.2. SEM of scaffold architecture of ∅ 5 mm with pore size and spacing of 500 μm. Scale bar is 2 mm.

the pore morphology present in this denser layer. This dense layer was removed (using a scalpel blade) from all scaffolds prior to experimental testing. Figure 4.13 (A) and (B) demonstrate the pile up which occurred around the periphery of individual macrochannels. This was possibly due to insufficient removal of the excess material (formed when drilling) prior to sintering. All subsequent samples were subjected to air-jetting to remove excess material prior to sintering.

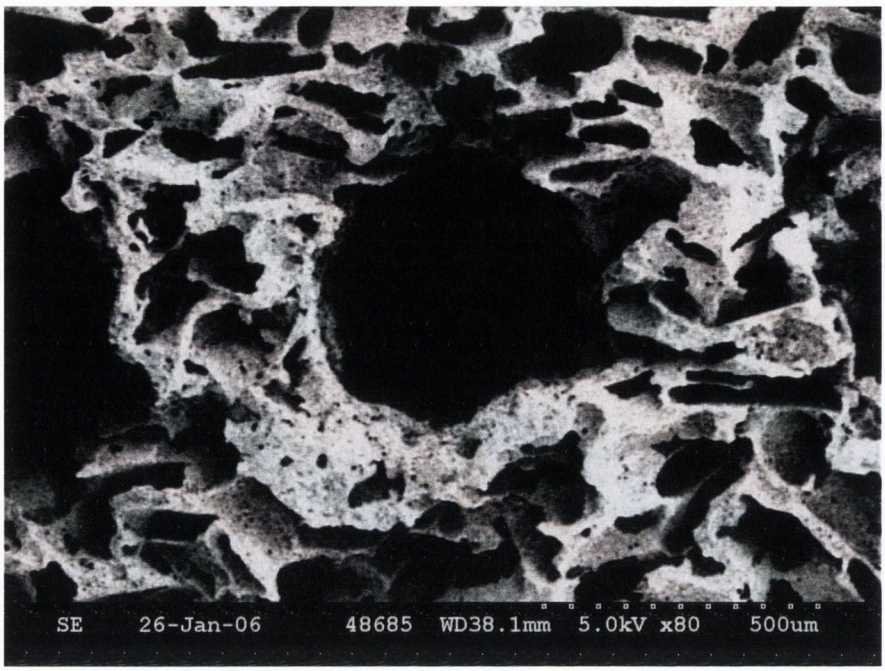

Figure 4.3. Higher magnification (x80) image of a unidirectional channel (∅ 500 μm , surrounded by the mesoporous region, which also contains micropores within the base material. Scale bar is 500 μm.

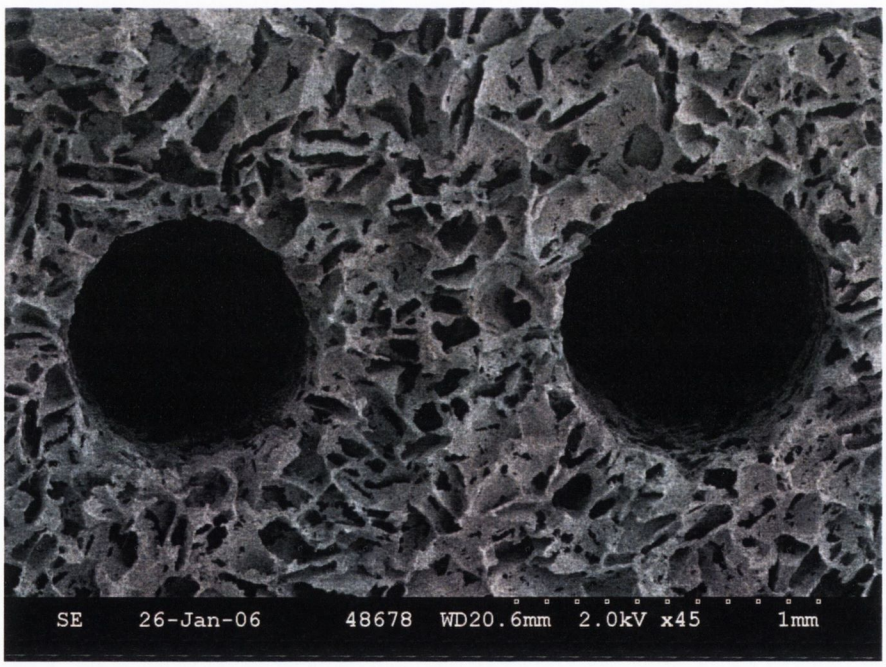

Figure 4.4. SEM showing the top surface region of a trimodal scaffold with unidirectional macrochannels of ∅ 800 μm, with a spacing of 800 μm. Scale bar is 1 mm.

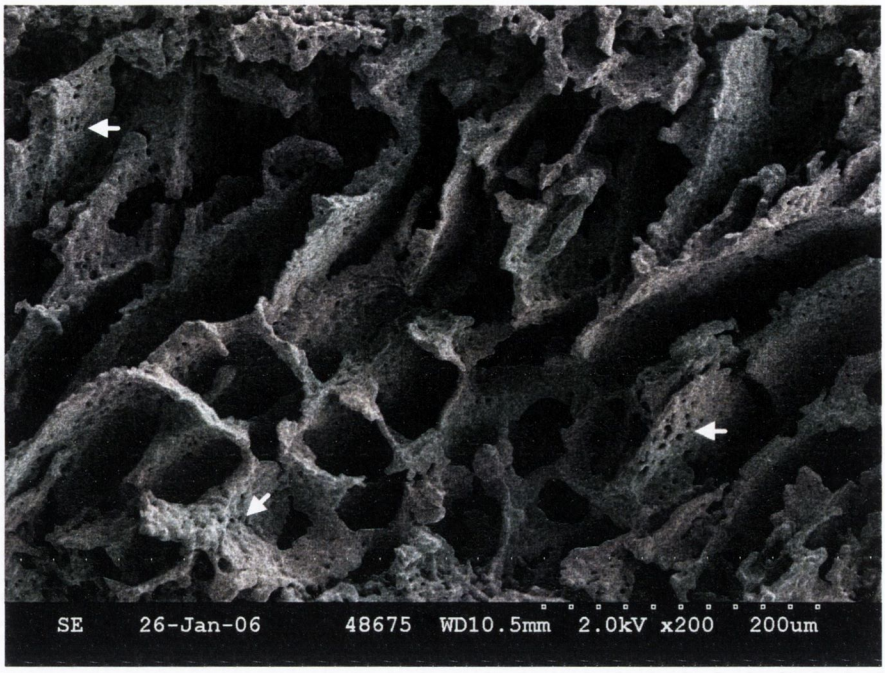

Figure 4.5. SEM illustrating the typical mesoporous architecture obtained through freeze drying. This mesoporous region also contains a degree of microporosity (indicated by white arrowheads) within the struts of the mesopores. Scale bar is 200 μm.

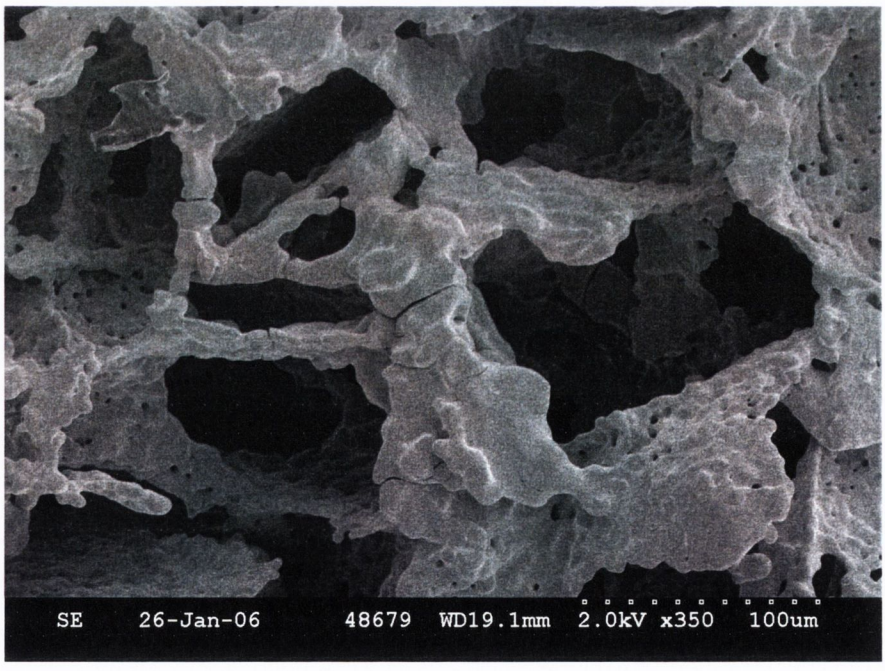

Figure 4.6. Higher magnification (x350) SEM showing meso- and micropores. Note the open, interconnected structure. Scale bar is 100 μm.

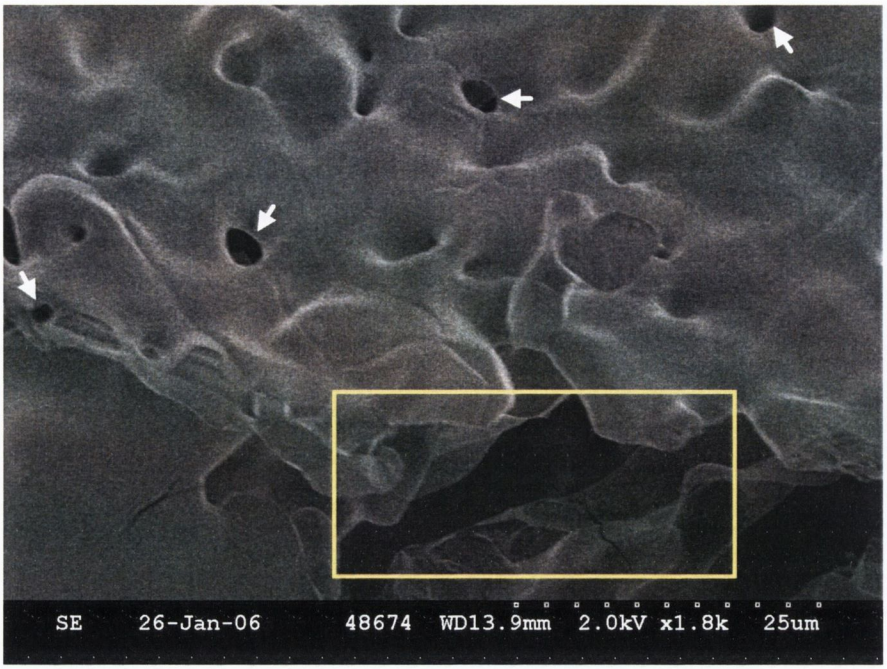

Figure 4.7. High magnification SEM (x1.8k) showing micropores (indicated by white arrow heads) within the base material of a mesopore strut. The region highlighted in yellow is a mesopore. Scale bar is 25 μm.

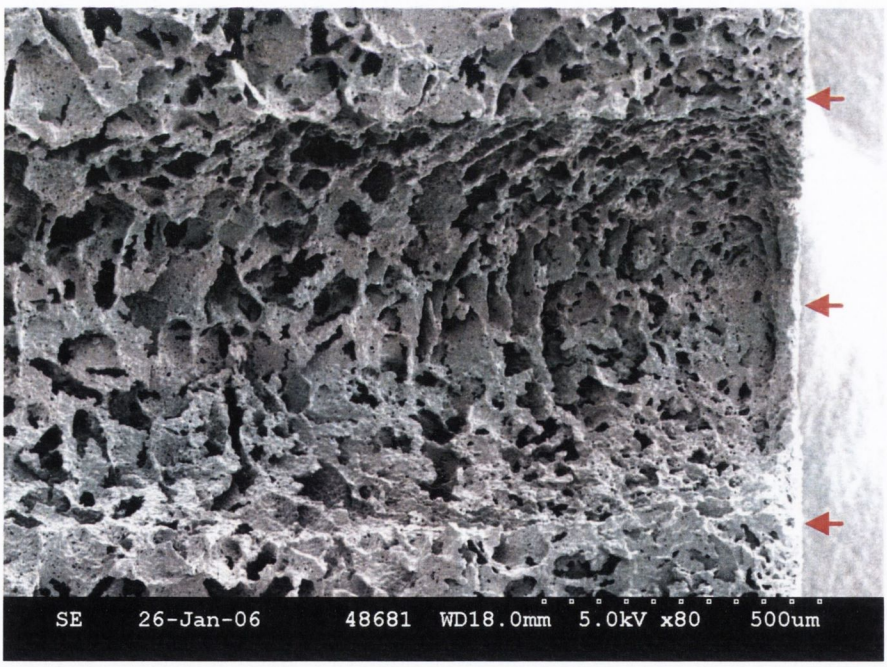

Figure 4.8. SEM of a cross-sectioned macrochannel demonstrating an open interconnected structure, which has not been disrupted through machining. Note the denser layer (indicated by red arrowheads) to the right of the structure. Scale bar is 500 μm.

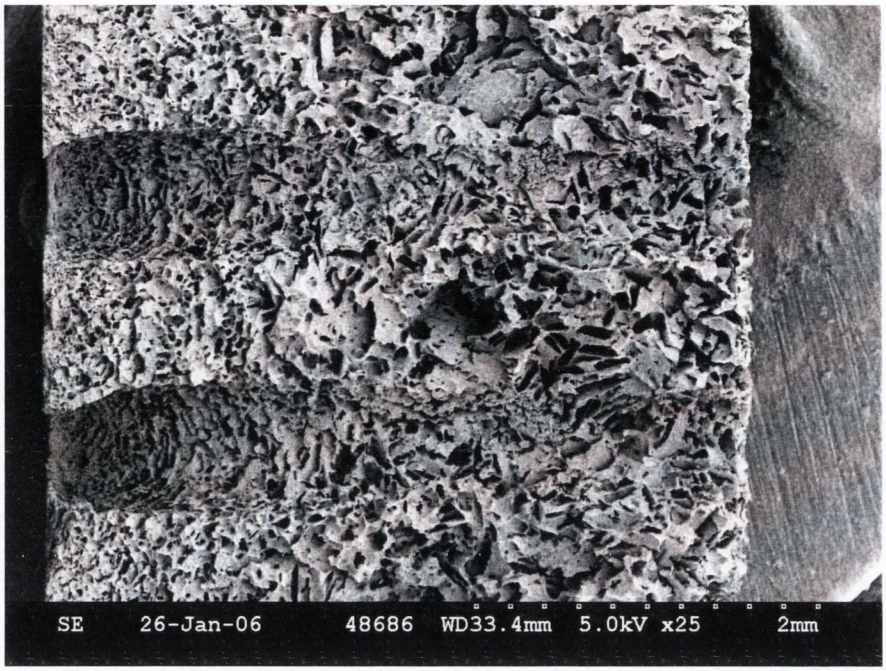

Figure 4.9. SEM of a trimodal scaffold showing two cross-sectioned macrochannels (LHS). Scale bar is 2 mm.

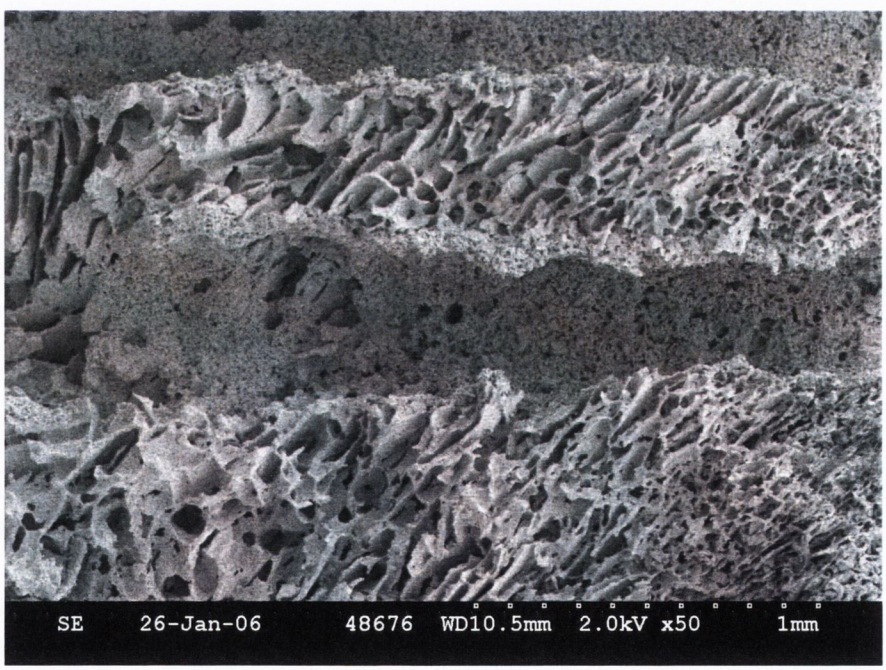

Figure 4.10. SEM showing a disrupted cross-section area of a macrochannel. The mesoporous phase at the surface of the macrochannels has become occluded. This is as of a result introducing the macrochannels by employing needles. Scale bar is 1 mm.

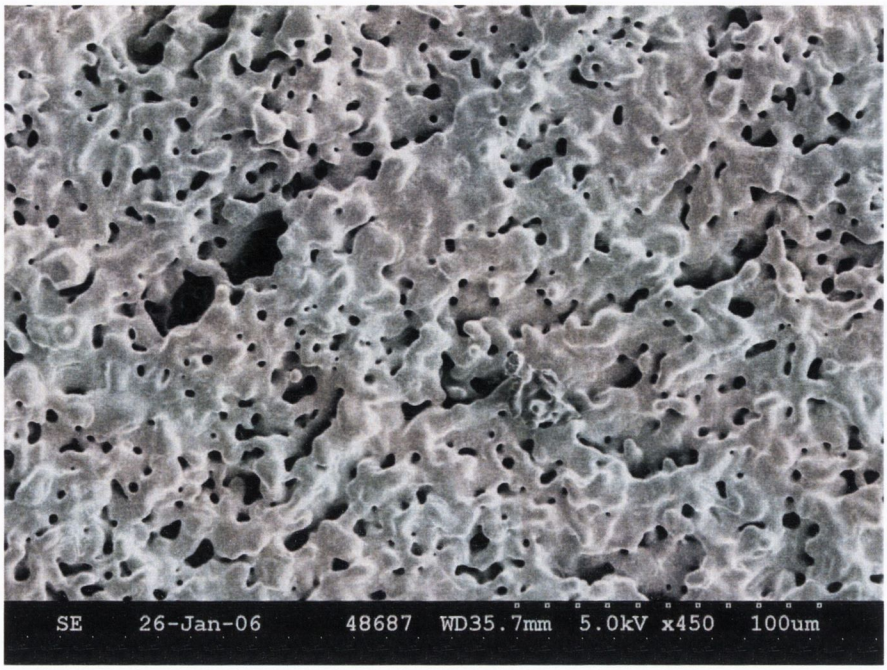

Figure 4.11. SEM showing the bottom surface of a bimodal scaffold typically observed. Note the appearance of a denser structure. This is the side in which cooling was initiated during the freezing cycle. Scale bar is 100 μm.

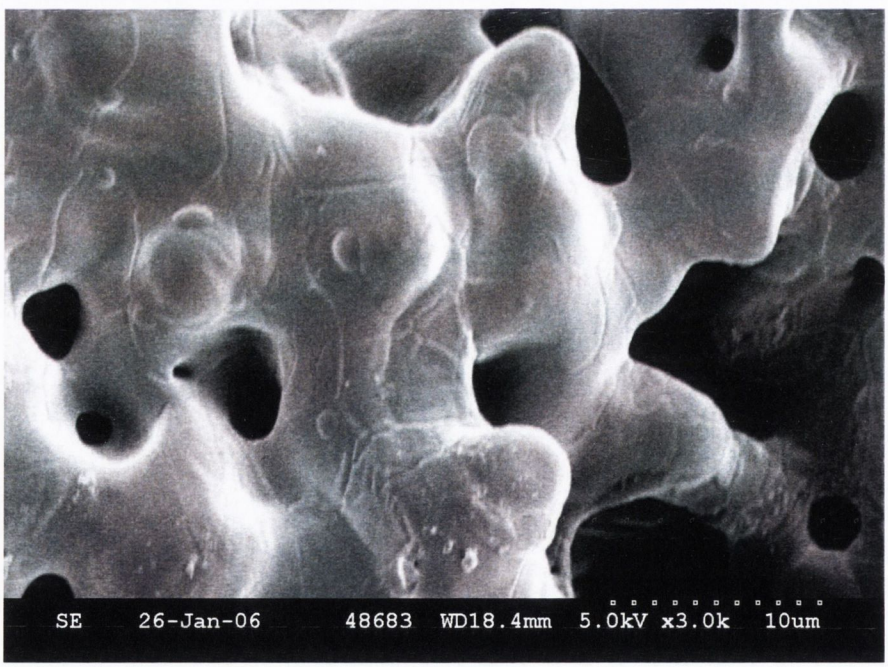

Figure 4.12. Higher magnification (x3k) SEM showing the bottom surface of a bimodal scaffold. Scale bar is 10 μm.

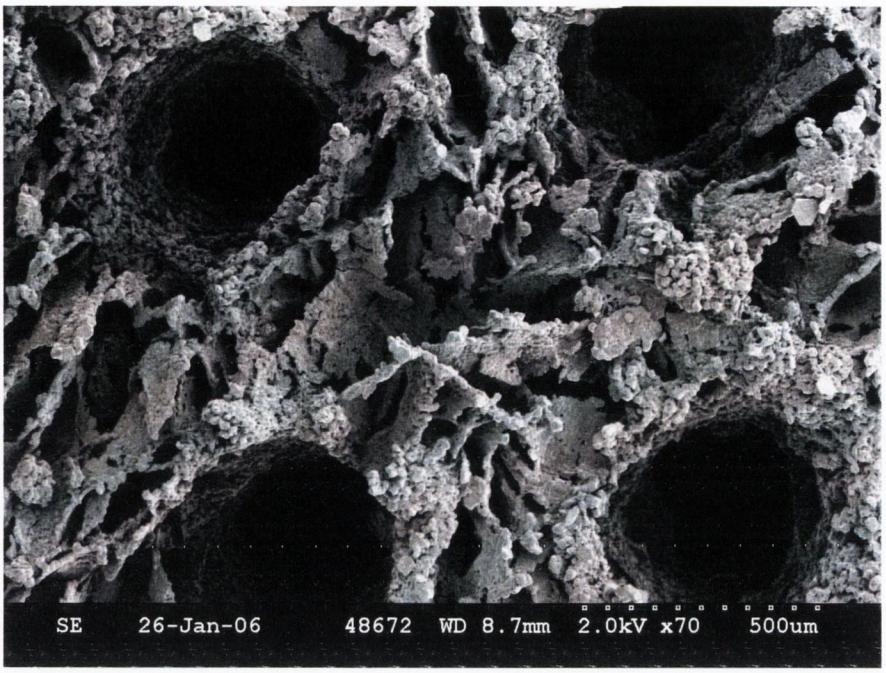

(A)

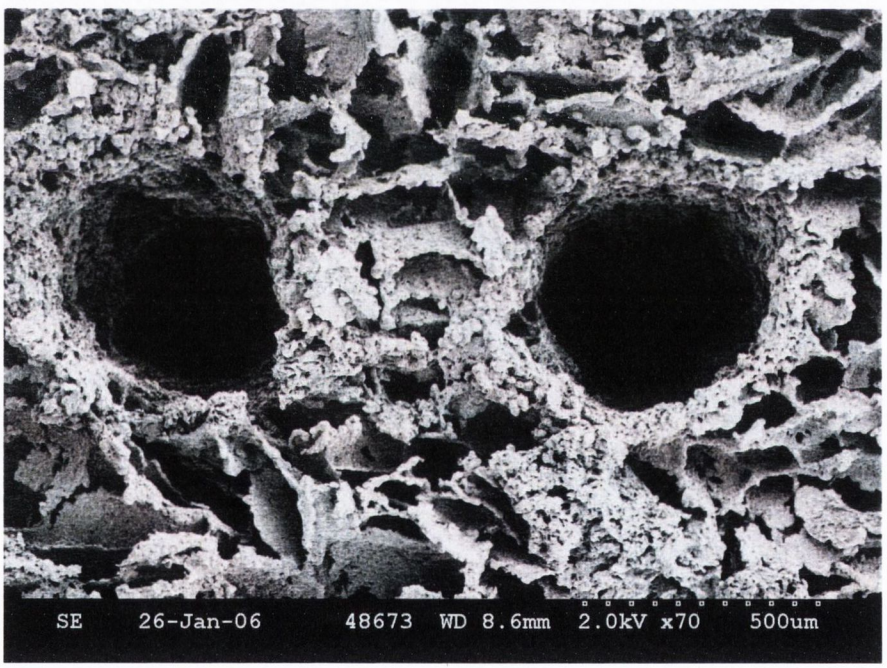

(B)

Figure 4.13. (A) and (B) SEM of a trimodal scaffold showing evidence of pile up occurring around the periphery of the macrochannels. This possibly occurred due to poor wax infiltration of the sample prior to the CNC machining of the macrochannels, or possibly due to insufficient removal of the flash material prior to sintering. Scale bars= 500 μm.

4.2.2 Pore size analysis

The pore architecture of scaffolds produced through the freeze drying technique was determined quantitatively using standard stereological techniques from images of planar sections (x 10) of embedded samples as described in Section 3.5.6. Stero-micrographs (x 4) of sliced scaffold sections obtained from four different scaffolds from the same batch are shown in Figures 4.14 and 4.15. These images reveal that there is variation in the pore size from slice to slice and therefore precise control over the pore size was not attainable. However, as can be seen from these images, variations in pore size do not appear to be localised or concentrated in specific regions, but are more uniformly dispersed. It is therefore typical of a random architecture structure. Also from the longitudinal slices (Figure 4.15) a gradient of varying pore sizes (bottom to top) does not appear to be present in any of the scaffold sections, as is normally found when fabricating scaffolds using the freeze-casting technique (Deville *et al.*, 2006).

Examples of images at higher magnification, again for four different scaffold sections (both transverse and longitudinal directions) are shown in Figures 4.16 and 4.17. In some regions, pores appear to have a more spherical-type morphology, with some longer, flatter pores (dendritic-like) being present also, but such pores do not appear to be localised or concentrated in specific regions. For the longitudinal slices (Figure 4.17) there does not appear to be any bias in the preferred orientation of the pores, indicating that the formation and growth of ice crystals during the freezing cycle was not purely unidirectional. Also, there does not appear to be any noticeable visual difference between the transverse and longitudinal slices.

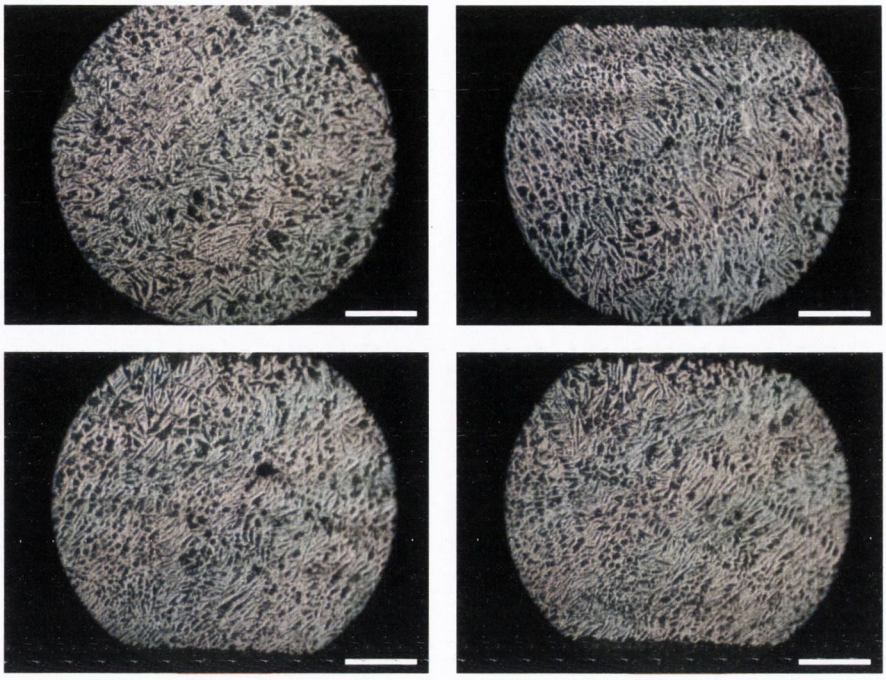

Figure 4.14. Light stereo-micrograph (Magnification x 4) images of scaffolds sliced in the traverse direction. Scale bar is 1 mm.

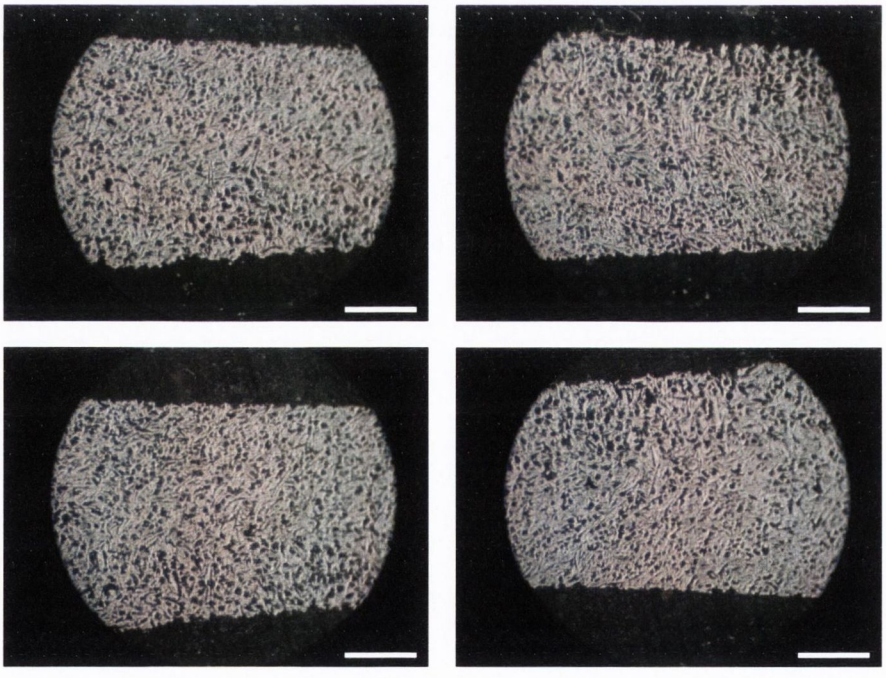

Figure 4.15. Light stereo-micrograph (Magnification x 4) images of scaffolds sliced in the longitudinal direction. Scale bar is 1 mm.

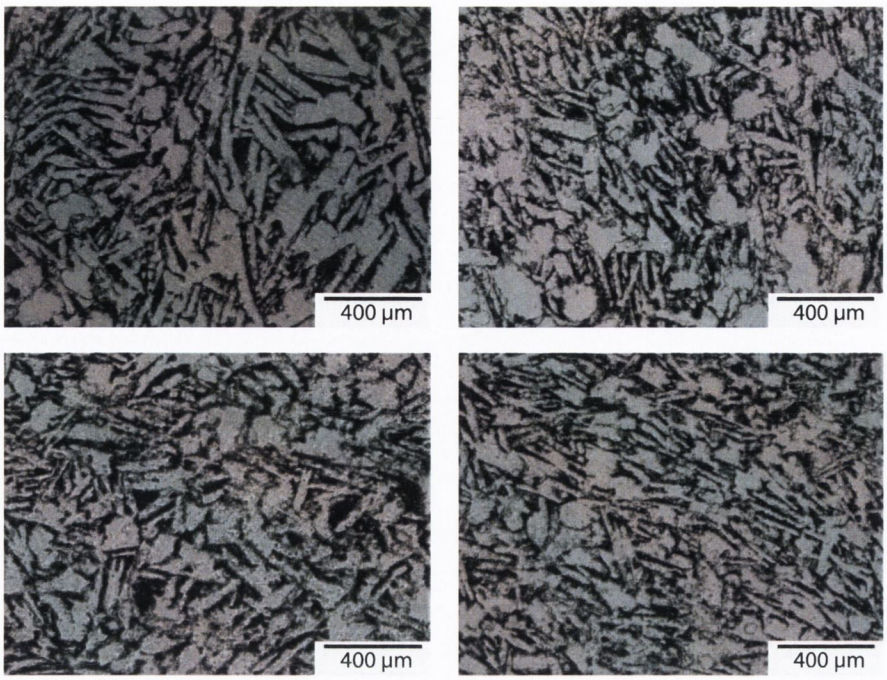

Figure 4.16. Light micrograph (Magnification x 10) images of scaffolds sliced in the traverse direction prior to thresholding used for pore size image analysis. Scale bar is 400 μm.

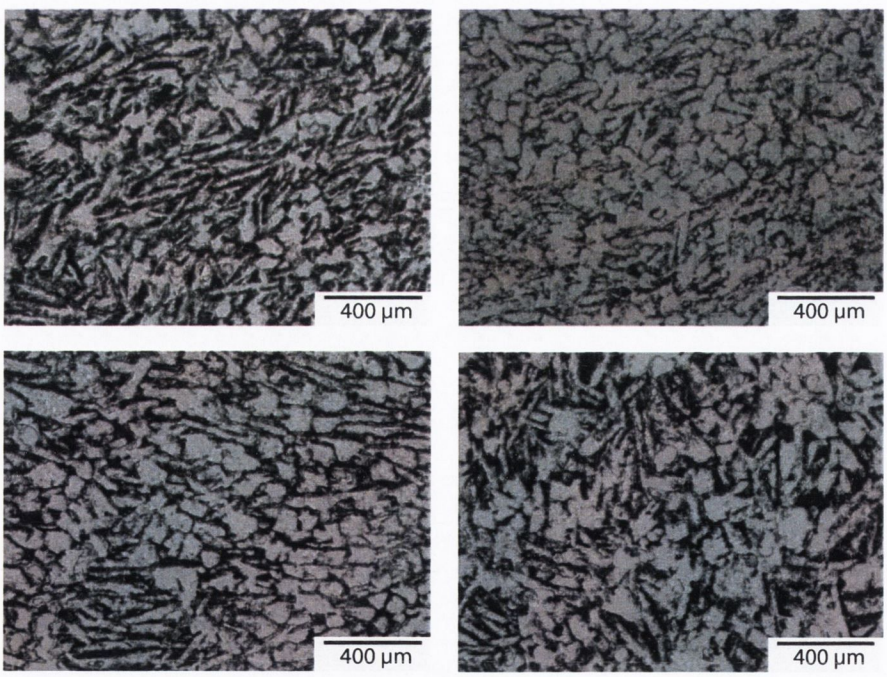

Figure 4.17. Light micrograph (Magnification x 10) images of scaffolds sliced in the longitudinal direction prior to thresholding used for pore size image analysis. Scale bar is 400 μm.

These higher magnification images were analysed using a custom developed linear intercept macro (included in Appendix D) written for Scion Image image analysis software (Scion Corp., Frederick, MD), similar to that as previously described by Freyman *et al.* (2001); O'Brien *et al.* (2004). The macro determines the pixel length of each pore that is bisected, when a series of parallel lines (both horizontal and vertical directions), drawn onto an image intercepts a pore wall (black pixel). The raw data from this procedure was exported to a file and subsequently analysed. An example of thresholded images and their corresponding horizontal and vertical mean pore sizes for scaffolds sliced in the longitudinal and traverse directions is shown in Figure 4.18. Porosity values are also included for each image.

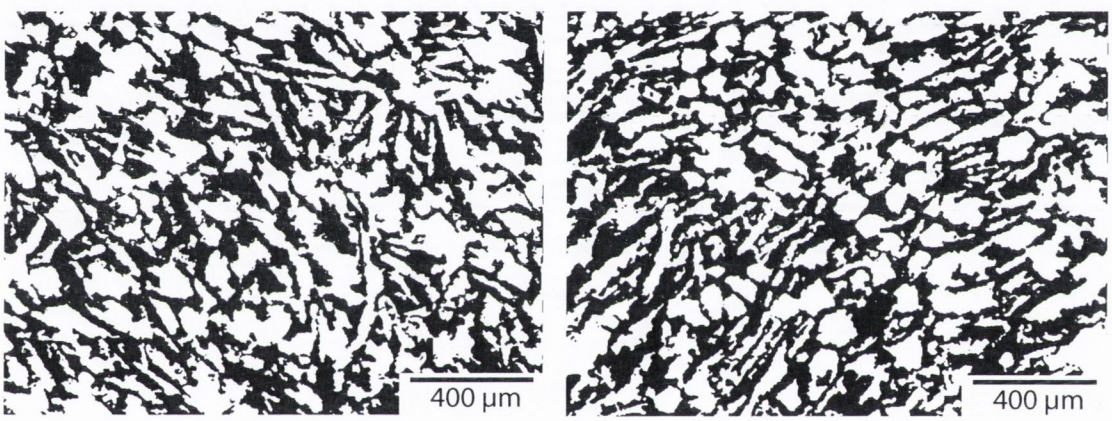

Figure 4.18. Representative images of thresholded scaffold sections used for image analysis. (A) Longitudinal slice, mean horizontal pore size of 56.23 ± 40.87 μm (SD, n=872), mean vertical pore size of 53.18 ± 36.29 μm (SD, n=650), porosity 58.36 % (B) Traverse slice, mean horizontal pore size of 53.63 ± 37.05 μm (SD, n=838), mean vertical pore size of 46.94 ± 29.29 μm (SD, n=695), porosity 56.71 %. Scale bars= 400 μm.

A one-way Anova analysis was carried out on the data obtained from the image analysis to investigate if there was a statistical difference between the mean horizontal and vertical pore size for a given slice. Table 4.2 shows the mean intercept lengths, including their respective SD's, SE's and n number, for vertical and horizontal pore intercept lengths within a given slice of a scaffold. It was found that a statistical difference ($p < 0.01$) did exist between the mean intercept lengths for both the vertical and horizontal directions of samples. However, the statistical significance may have been influenced by the large number (n number ~ 700) of pore intercept lengths determined for a given slice.

However, it must be noted that the differences between the mean pore intercept lengths in the horizontal and vertical directions for a given slice of a scaffold ranged from 0.33 - 15.47 μm and although statistically significant, these variations are unlikely to have a major influence on cellular response. The linear intercept method of measurement may not be the most accurate since the pore intercept lengths measured may not in every case bisect the maximum diameter of a pore being measured.

Since it was found that a statistical difference did exist at this level of hierarchy (between vertical and horizontal pores), it is assumed that this significance would be carried through when combining the vertical and horizontal intercept lengths to yield an average pore size for a given slice, and comparing slices from the same scaffold sample to each other. This assumption was found to be true. Similarly when combining the pore intercept lengths for all slices (n=5) for a given scaffold, and comparing to the mean pore intercept length of other scaffold samples, it was found that a significant difference did exist ($p < 0.01$). The mean intercept lengths (including their respective SD's, SE's and n number) for all scaffolds analysed is shown in Table 4.3.

Table 4.2. Horizontal and vertical mean intercept lengths (MIL) of different scaffold samples in the longitudinal and traverse directions. SD = standard deviation (μm), SE = standard error of the mean (μm) and n= the number of pores bisected.

Sample #	Slice orientation	Measurement direction	MIL [μm]	SD [μm]	SE [μm]	n
1	Longitudinal	Horizontal	46.2	33.1	1.1	866
		Vertical	43.6	30.5	1.2	664
2	Longitudinal	Horizontal	58.1	42.0	1.4	929
		Vertical	53.6	39.3	1.5	734
3	Longitudinal	Horizontal	54.6	43.5	1.4	923
		Vertical	46.6	34.3	1.2	768
4	Longitudinal	Horizontal	56.2	40.9	1.4	872
		Vertical	53.2	36.3	1.4	650
5	Longitudinal	Horizontal	56.1	44.9	1.6	776
		Vertical	52.1	39.4	1.6	598
6	Longitudinal	Horizontal	55.3	41.5	1.3	951
		Vertical	65.0	46.1	1.9	567
7	Longitudinal	Horizontal	59.9	42.3	1.5	765
		Vertical	45.3	28.5	1.1	717
8	Longitudinal	Horizontal	45.8	30.1	0.9	1034
		Vertical	46.2	31.0	1.2	729
9	Longitudinal	Horizontal	63.6	49.2	1.8	777
		Vertical	56.5	42.9	1.7	640
10	Longitudinal	Horizontal	53.8	38.5	1.3	870
		Vertical	54.6	38.7	1.5	636
11	Traverse	Horizontal	45.2	32.0	1.0	1029
		Vertical	60.7	44.4	1.9	557
12	Traverse	Horizontal	51.7	39.2	1.3	921
		Vertical	49.2	39.3	1.5	676
13	Traverse	Horizontal	53.3	39.5	1.3	879
		Vertical	46.5	31.2	1.2	743
14	Traverse	Horizontal	55.3	42.7	1.4	888
		Vertical	58.0	43.1	1.7	626
15	Traverse	Horizontal	52.6	44.0	1.4	999
		Vertical	59.1	47.4	1.9	615
16	Traverse	Horizontal	50.9	37.3	1.3	878
		Vertical	47.6	36.9	1.4	663
17	Traverse	Horizontal	51.3	39.5	1.3	879
		Vertical	45.3	32.1	1.2	740
18	Traverse	Horizontal	53.6	37.1	1.3	838
		Vertical	46.9	29.3	1.1	695

Table 4.3. Mean pore intercept lengths (MIL) of all horizontal and vertical measurements within a sample, separated by slice orientation in the longitudinal and traverse directions. SD = standard deviation (μm), SE = standard error of the mean (μm) and n= the number of pores bisected.

Sample #	Slice orientation	MIL [μm]	SD [μm]	SE [μm]	n
1	Longitudinal	48.9	35.8	0.42	7360
2	Longitudinal	54.0	39.7	0.43	8492
3	Longitudinal	51.7	39.8	0.44	8375
4	Longitudinal	55.7	41.2	0.48	7414
5	Longitudinal	56.7	45.2	0.55	6887
6	Longitudinal	54.4	39.5	0.45	7853
7	Longitudinal	56.5	41.5	0.49	7245
8	Longitudinal	46.6	31.3	0.34	8710
9	Longitudinal	54.7	41.5	0.47	7638
10	Longitudinal	53.2	39.4	0.45	7591
11	Traverse	54.3	43.3	0.50	7486
12	Traverse	52.4	38.0	0.43	7783
13	Traverse	57.7	45.2	0.53	7264
14	Traverse	55.9	48.3	0.55	7688
15	Traverse	53.1	40.3	0.47	7372
16	Traverse	49.0	36.4	0.40	8084
17	Traverse	49.4	35.3	0.37	8969
18	Traverse	49.9	37.7	0.43	7678

To present the data in a more visual form, frequency distribution graphs (Figure 4.19) were employed. These graphs illustrate the range of linear pore intercepts that were measured. The measurements are from a single slice (Slice 1, Samples 4 and 18) as shown in Figure 4.18 (p 141). It should be noted that columns represent the frequency of pore intercepts that were measured, increasing from left to right, and does not necessarily imply that this is a range of pore diameters within in a given slice, since the pore intercept lengths measured may not in every case bisect the

maximum diameter of a pore being measured. The histograms presented suggest that the true pore size (or maximally bisected pores) is possibly closer to ~ 100 μm, up to 200 μm. Pore diameters of these dimensions (100-200 μm) would be more comparable to the pores observed in the scanning electron micrographs (SEM's) (Section 4.2.1).

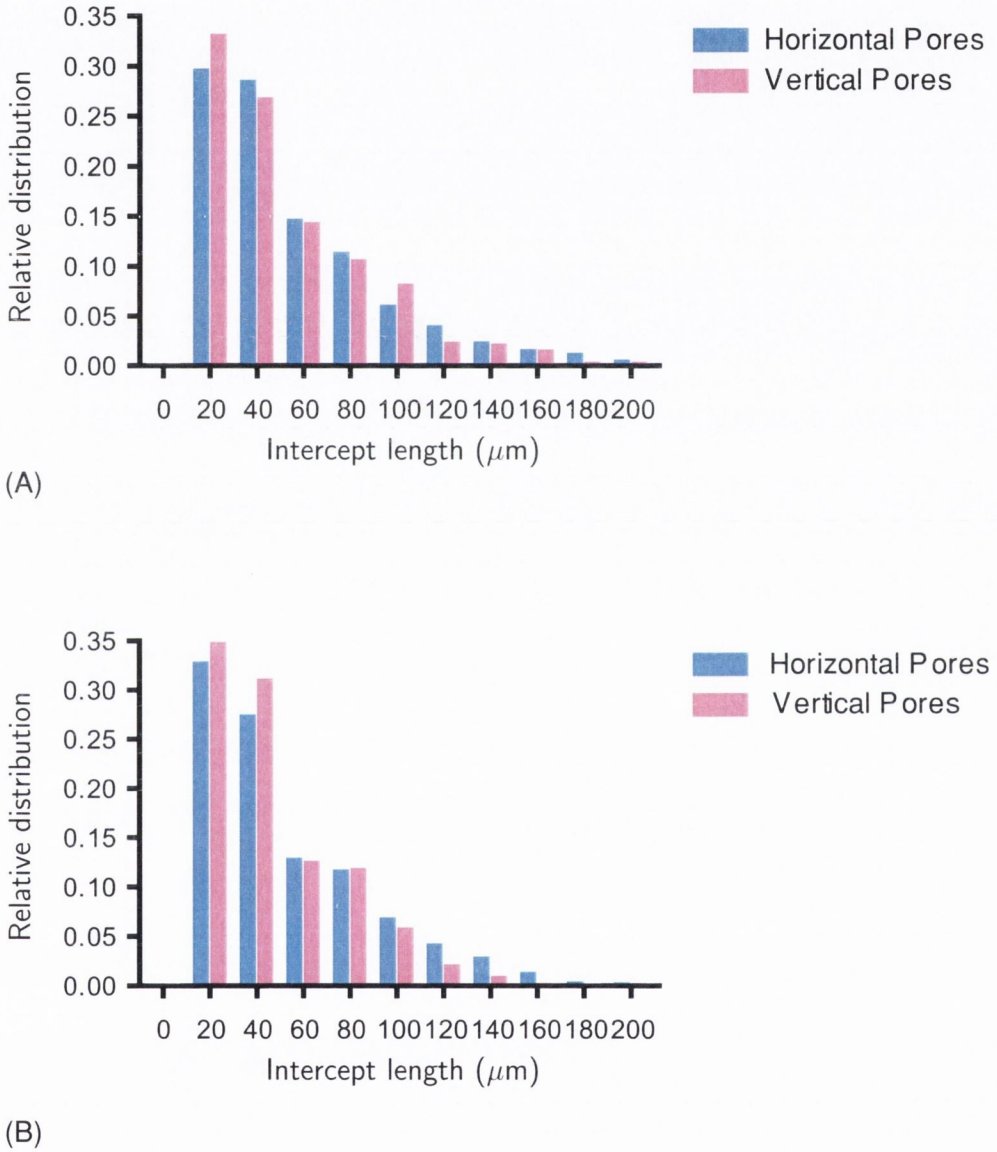

Figure 4.19. Frequency distribution of pore intercept lengths from a single slice for images as shown in Figure 4.18. (A) Longitudinal slice (B) Traverse slice.

A frequency distribution graph based on the combined horizontal and vertical measurements for five separate slices for each scaffold sample is shown in Figure 4.20. As can be seen from Figures 4.19 and 4.20, there is little variation in the pore intercept lengths obtained from either an individual slice, or between scaffold groups.

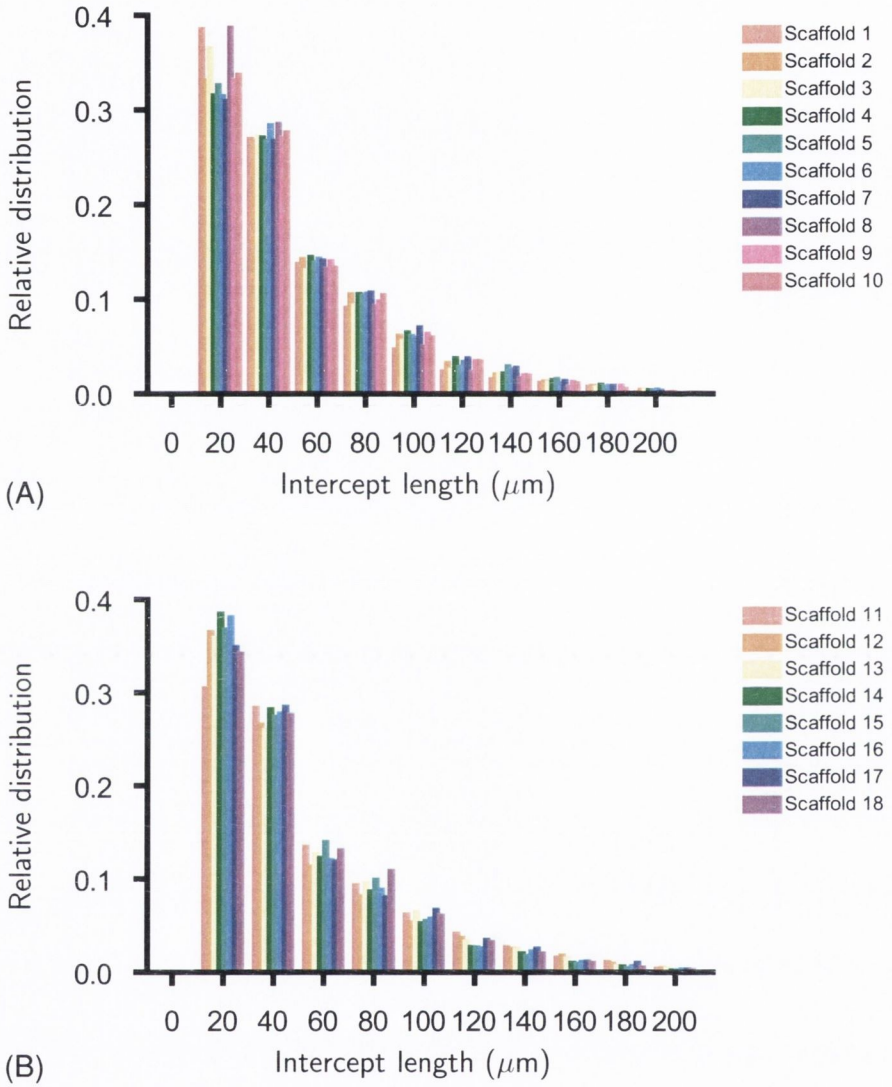

Figure 4.20. Frequency distribution graph based on the combined horizontal and vertical mean intercept measurements. Each bar in the graph represents a mean intercept length for a single sample based on the combined horizontal and vertical measurements from five separate slices. (A) Scaffolds sliced in the longitudinal direction (n=10). (B) Scaffolds sliced in the traverse direction (n=8).

4.2.3 Determination of porosity

Both apparent and real densities were calculated for each sample as described in Section 3.5.7. The apparent density of sintered scaffold samples was calculated from the dry mass and volume and compared to the theoretical density of HA to determine the total porosity (open and closed pores). The average combined scaffold micro- and mesoporosity based on densimetric measurements using the theoretical density of HA (3.156 g/cm^3), yields an average total porosity of 80.5 % (SE=± 0.18, n=11).

The effective porosity, determined from water immersion studies of scaffolds, was similar to the theoretical values obtained, yielding an overall effective porosity of 76.1 % (SE=± 0.65, n=11). Subtraction of the effective porosity from the theoretical porosity yields a value of 4.3 % (SE=± 0.59, n=11), which represents the percentage of closed pores within scaffolds.

The average porosity of the mesoporous phase was also calculated from the ratio of white (pores) versus black (HA material) pixels from the images used in Section 4.2.2. The average mesoporosity based on data obtained from the images was calculated to be 58 % (SE=± 0.38, n=90). Based on the measurements of porosity for the mesoporous phase from the image analysis, and through subtraction from the total effective porosity from densimetric measurements, would imply an open microporous void fraction of approximately 18 %.

For the determination of the porosity of trimodal scaffolds, the percentage of unidirectional channels (determined from image analysis) in a given sample was calculated to be approximately 28 % of the total scaffold volume. From densimetric analysis, the total apparent porosity of trimodal scaffolds was calculated to be 85.1 % (SE=± 0.22, n=11), and the effective porosity determined from water immersion studies was 80.8 % (SE=± 0.66, n=11). This implies that trimodal scaffolds contained approximately 4.24 % (SE=± 0.58, n=11) closed porosity and is similar to that as for bimodal scaffolds. Assuming that the meso- and micro-porosities are in the same ratio for bimodal scaffolds implies that trimodal scaffolds contained $\sim$ 40.3 % mesoporosity and 12.5 % microporosity. A summary of the porosities for both

bimodal and trimodal scaffolds is given in Table 4.4. As can be seen, the presence of macrochannels has only a minor influence ($\sim$ 4.5 %) in increasing the total porosity of trimodal scaffolds compared to bimodal scaffolds.

Table 4.4. Summary of the porosities for both bimodal and trimodal scaffolds. SD = standard deviation (μm), SE = standard error of the mean (μm) and n= the number samples.

Porosity Type	**Value [%]**	**SD [%]**	**SE [%]**	**n**
Bimodal Scaffolds:				
Total apparent porosity	80.5	0.6	0.2	11
Effective porosity	76.1	2.2	0.7	11
Closed porosity	4.3	1.9	0.6	11
Meso porosity (image analysis)	58	3.6	0.4	90
Micro porosity	$\sim$ 18	—	—	—
Trimodal Scaffolds:				
Total apparent porosity	85.1	0.7	0.2	11
Effective porosity	80.8	2.2	0.7	11
Closed porosity	4.3	1.9	0.6	11
Macrochannel porosity	$\sim$ 28	—	—	—
Meso porosity	$\sim$ 40.3	—	—	—
Micro porosity	$\sim$ 12.5	—	—	—

4.2.4 Determination of effective diffusion coefficient

The oxygen diffusion coefficient of bimodal scaffolds was measured according to Section 3.5.1. A sample of the raw data and the calculated diffusion coefficient (D, m^2s^{-1}) (using Eqn. 3.3, p 104) obtained for a specimen are shown in Table 4.5. Figure 4.21 shows the experimental data for this sample and the corresponding analytical solutions for varying diffusion coefficients in the range 2 x 10^{-10} - 1.4 x 10^{-9} m^2s^{-1}.

Table 4.5. Sample data and calculated diffusion coefficient (D, m^2s^{-1}) obtained for a specimen with initial conditions of C_0= 4.5 %, C_1= 19.6 and x= 2.97 mm.

Time [secs.]	**C_x [%]**	**ERF**	**z**	**D [x 10^{-10} m^2s^{-1}]**
300	4.5	—	—	—
600	4.6	0.99	1.92	9.97
900	4.8	0.98	1.65	9.04
1200	5.2	0.95	1.41	9.26
1500	5.5	0.93	1.30	8.71
1800	5.8	0.91	1.21	8.32
2100	6.2	0.89	1.12	8.34
2400	6.5	0.87	1.06	8.12
2700	6.8	0.85	1.01	7.97
3000	7.0	0.83	0.98	7.65

The red line in Figure 4.21 is the experimental plot, and it can be seen that it follows very closely the analytical solution for a diffusion coefficient of 8.0 x 10^{-10} m^2s^{-1}. As can be seen from the graph a good correlation exists at later time points (> 1500 secs.), but not in the earlier parts of the experiment. The over estimation of the change in partial pressure at earlier time points, and subsequently the over estimation of the effective diffusion coefficient is possibly due to the resolution of the oxygen probe that was used to monitor the changes in partial pressures in the lower chamber at given time points, since the oxygen probe cannot measure very small

changes (< 0.1 %) in partial pressures accurately. For these reasons the diffusion coefficients of samples were calculated using the last three experimental measurements obtained. It was found that the oxygen diffusion coefficient of these bimodal scaffolds was equal to 7.9 x 10^{-10} m^2s^{-1} (SE=± 5.3 x 10^{-11}, n=8). According to Haselgrove *et al.* (1993), the diffusion coefficient of oxygen through water at 37 °C is approximately 3.0 x 10^{-9} m^2s^{-1}. This implies that the oxygen diffusion coefficient through the bimodal scaffolds (both the mesoporous and microporous phases) is approximately 26 % (± 1.8 %), of that of water at 37 °C.

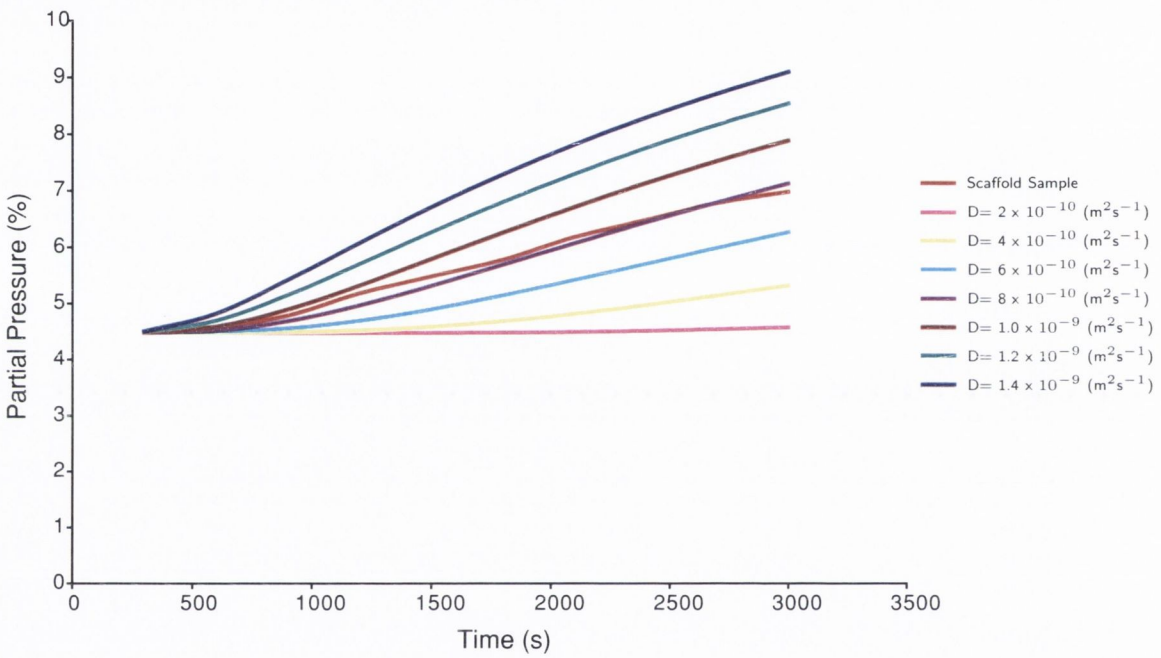

Figure 4.21. Plot of experimental data (Red line) for the change in oxygen partial pressure (%) occurring in the lower chamber versus time (s) of a bimodal scaffold structure. Analytical solutions for varying diffusion coefficients are also plotted for comparison.

4.2.5 Direct permeability analysis

Measurement of permeability values as carried out using a constant head pressure system, employing the relevant formulae as previously outlined in Section 3.5.2. The fluid conductance of each specimen was measured and normalised using the relevant geometric and fluid properties to calculate the permeability. Four specimen types were tested and analysed:

- Trimodal scaffolds
- Bimodal scaffolds
- Cancellous bone samples
- Foam gel scaffolds

The fluid conductance and permeability results are presented in Figures 4.22 and 4.23 respectively, with the data supplied in Tables 4.6 and 4.7. As can be seen from Figure 4.22, there is a statistically significant difference between the fluid conductance values for each specimen type. However, when the results (Figure 4.23) are presented in terms of permeability, which is the fluid conductance normalised by the geometric properties, a large reduction in the difference between trimodal scaffolds and cancellous bone specimens is observed. Of interest from Figures 4.22 and 4.23 is the large difference between the bimodal and trimodal scaffold groups. The permeability of the bimodal scaffolds was calculated to be 9.72 x 10^{-12} m^2 (SE=$\pm$ 3.64 x 10^{-13}, n=12), compared to a value of 1.71 x 10^{-10} m^2 (SE=$\pm$ 6.18 x 10^{-12}, n=11) for trimodal scaffolds which was found to be statistically different ($p < 0.001$). This observation clearly demonstrates the influence of the macrochannels in increasing the permeability for a given scaffold. With respect to fluid conductance, a statistical difference was found to exist between trimodal and cancellous bone samples ($p < 0.001$). However in terms of permeability, it was found that no statistical significant difference existed between trimodal and cancellous bone samples ($p < 0.3740$), although the variances did differ significantly ($p < 0.0007$).

This difference in variation for the cancellous bone samples is possibly due to the architectural variations that may have existed between samples. It can also be seen that the scaffolds produced through the foam gel method have a higher permeability value compared to the bimodal scaffolds (factor of 5), although appreciably lower than that of cancellous bone and trimodal scaffolds (factor of 5). It should also be noted that the permeability values for trimodal scaffolds and cancellous bone scaffolds were approximately 18 times higher than those obtained for the bimodal scaffolds.

Table 4.6. Conductivity data for various scaffold types. SD = standard deviation, SE = standard error of the mean and n= the number samples.

Sample Type	**Mean** $[m^3s^{-1}Pa^{-1}]$	**SD** $[m^3s^{-1}Pa^{-1}]$	**SE** $[m^3s^{-1}Pa^{-1}]$	**n**
Trimodal Scaffolds	1.18×10^{-9}	1.47×10^{-10}	4.44×10^{-11}	11
Bimodal Scaffolds	7.32×10^{-11}	1.01×10^{-11}	2.92×10^{-12}	12
Cancellous Bone	5.77×10^{-10}	1.25×10^{-10}	3.47×10^{-11}	13
Foam-Gel Scaffolds	1.82×10^{-10}	2.59×10^{-11}	7.46×10^{-12}	12

Table 4.7. Permeability data for various scaffold types. SD = standard deviation, SE = standard error of the mean and n= the number samples.

Sample Type	**Mean** $[m^2]$	**SD** $[m^2]$	**SE** $[m^2]$	**n**
Trimodal Scaffolds	1.71×10^{-10}	2.05×10^{-11}	6.18×10^{-12}	11
Bimodal Scaffolds	9.72×10^{-12}	1.26×10^{-12}	3.64×10^{-13}	12
Cancellous Bone	1.78×10^{-10}	6.71×10^{-11}	1.86×10^{-11}	13
Foam-Gel Scaffolds	3.83×10^{-11}	7.66×10^{-12}	2.21×10^{-12}	12

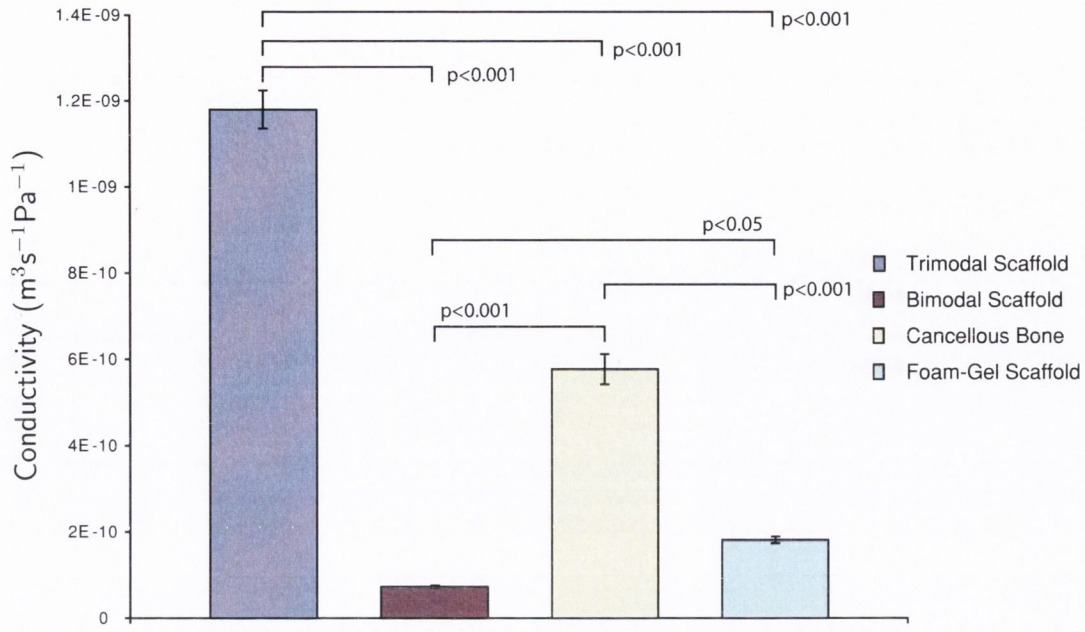

Figure 4.22. Fluid conductivity of various scaffold types. The data represents the mean of samples $\pm$ the standard error of the mean (SE).

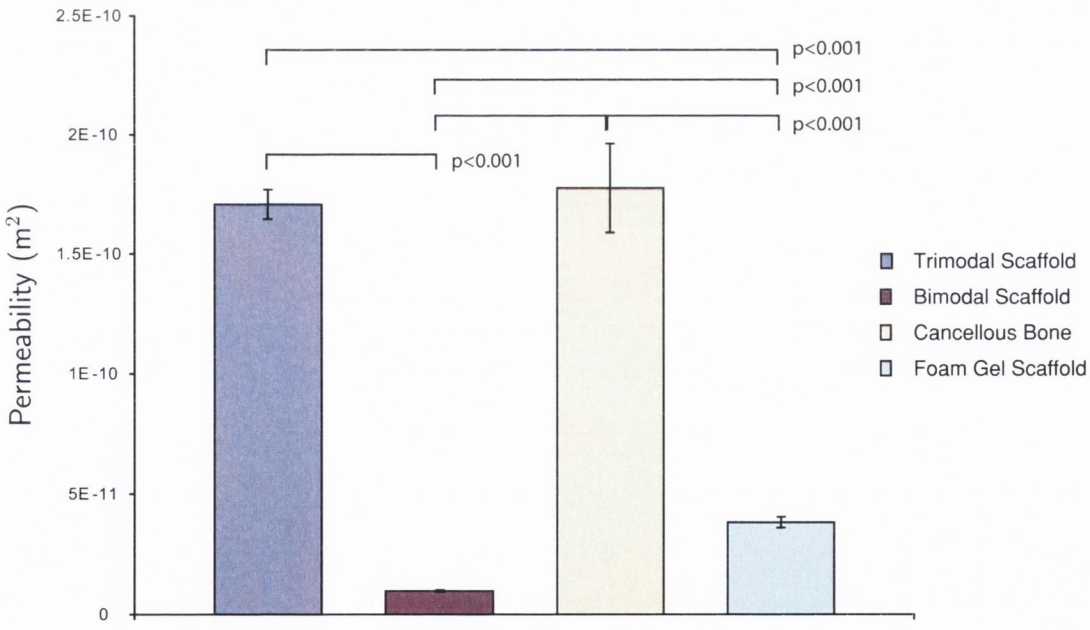

Figure 4.23. Permeability of various scaffold types. The data represents the mean of samples $\pm$ the standard error of the mean (SE).

4.2.6 Mechanical properties

The compressive strength (MPa) of trimodal, bimodal and cancellous bone samples was determined as described in Section 3.5.8. The failure mode for the bimodal and trimodal scaffolds tested appears to be through a series of micro-failures occurring within the struts of the scaffold material as shown in Figure 4.24. These micro-failures result in densification occurring at the surfaces of the specimens until such time as crushing/compaction is no longer sustainable leading to complete destruction of the samples. Interestingly, the cancellous bone samples did not fail in the same manner, but increased to a maximum with an almost elastic response and then rapidly dropped after this point. The cancellous bone samples had a diameter and height of 4 mm. Because of this only very few struts were present within the samples and the typical stress-strain response as shown in Figure 4.24 represents this and is possibly due to bending and ultimate fracture of these few trabeculae struts without densification occurring. Another reason might be due to the cancellous bone tissue being fully dense compared to the scaffold material which contained significant microporosity.

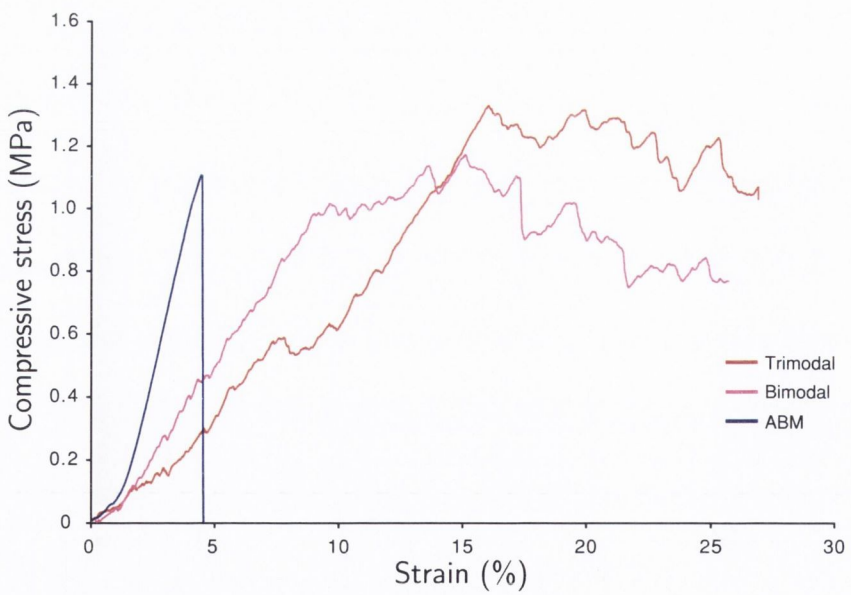

Figure 4.24. Typical stress-strain response of trimodal, bimodal and ABM (Anorganic bone matrix) samples indicating the brittle fracture nature of both bimodal and trimodal scaffolds.

Figure 4.25 and Table 4.8 presents the compressive strength data obtained for the three types of specimens tested. It was found that there was a statistical difference between trimodal and bimodal scaffolds ($p < 0.05$) and between trimodal and cancellous bone $p < 0.01$). No statistical significance was found between bimodal scaffolds and cancellous bone. Interestingly it was observed that trimodal scaffolds had a statistically significantly higher compressive strength compared to that of the bimodal scaffolds.

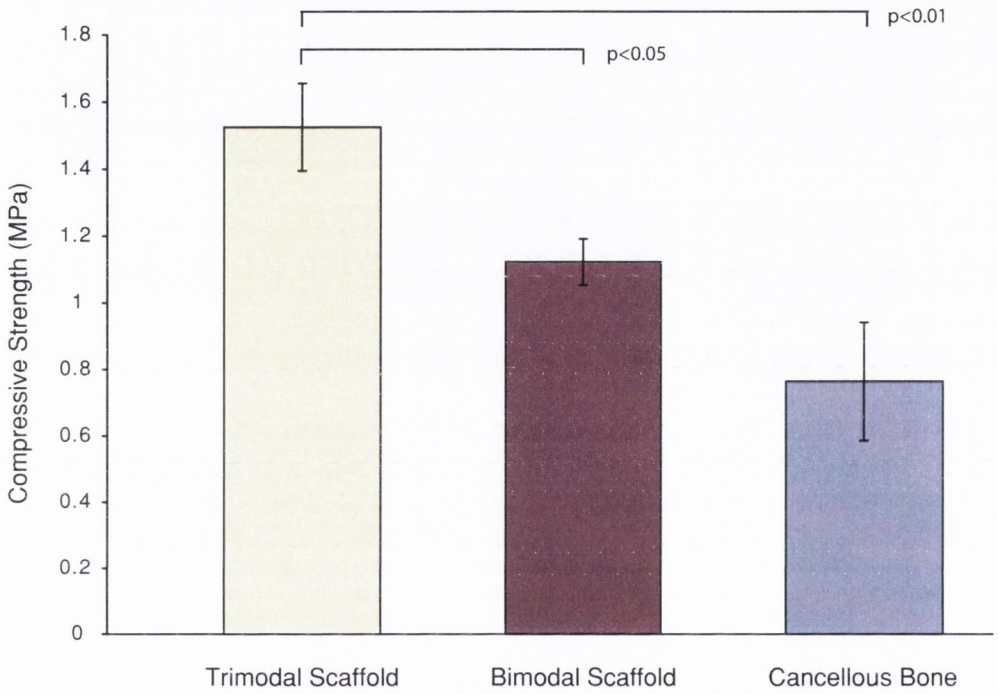

Figure 4.25. Ultimate compressive strengths of porous trimodal, bimodal scaffolds and anorganic cancellous bone. The data represents the mean of samples (n=10) $\pm$ the standard error of the mean (SE).

Table 4.8. Ultimate compressive strength data of porous trimodal, bimodal scaffolds and anorganic cancellous bone. SD = standard deviation, SE = standard error of the mean and n= the number samples.

Sample Type	**Mean [MPa]**	**SD [MPa]**	**SE [MPa]**	**n**
Trimodal Scaffolds	1.53	0.41	0.13	10
Bimodal Scaffolds	1.12	0.22	0.07	10
Cancellous Bone	0.76	0.56	0.18	10

Figure 4.26 and Table 4.9 presents the strain to failure data obtained for the three types of specimens tested. No statistical difference was found between trimodal and bimodal scaffolds, although there was a statistical difference between both scaffold types and cancellous bone and ($p < 0.0001$).

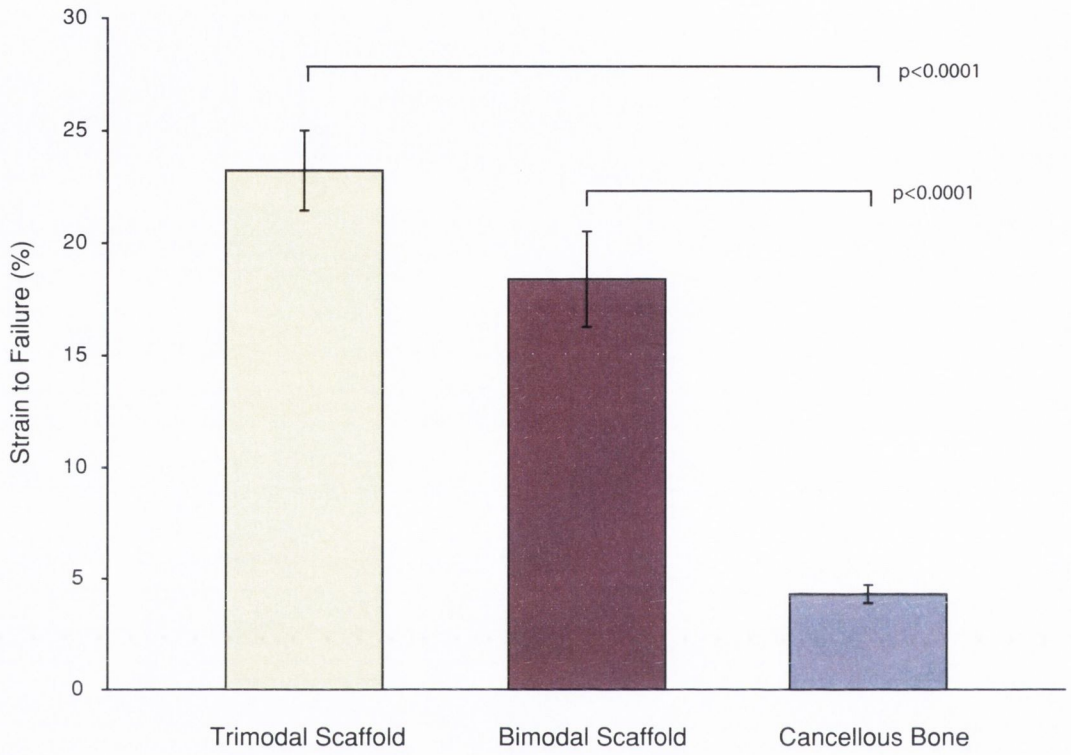

Figure 4.26. Graph of strain to failure for porous trimodal, bimodal scaffolds and anorganic cancellous bone. The data represents the mean of samples (n=10) ± the standard error of the mean (SE).

Table 4.9. Strain to failure data for porous trimodal, bimodal scaffolds and anorganic cancellous bone. SD = standard deviation, SE = standard error of the mean and n= the number samples.

Sample Type	**Mean [%]**	**SD [%]**	**SE [%]**	**n**
Trimodal Scaffolds	23.23	5.60	1.77	10
Bimodal Scaffolds	18.39	6.71	2.12	10
Cancellous Bone	4.29	1.29	0.41	10

Similar compressive strength results were observed by Rose *et al.* (2004) when the insertion of 13 channels (*via* needles) into HA foam-type scaffolds (⌀ 432 μm) enhanced the mechanical strength by almost two-fold when compared with scaffolds without channels. The authors proposed that the increase in mechanical strength may be due to strut formation due to smearing around the channel on insertion of the needles during fabrication. However, for the fabrication of trimodal scaffolds it was demonstrated through SEM imaging (Section 4.2.1) that the macrochannels produced through CNC machining did not possess continuous material around the surface of the channel, and therefore the reasons as proposed by Rose *et al.* (2004) possibly don't apply.

A more likely explanation for the differences in mechanical properties between bimodal and trimodal scaffolds is perhaps due to the modes in which ultimate compressive strength is achieved. Trimodal scaffolds have a higher porosity ($\sim$ 4.5 % greater than bimodal scaffolds) but also contain large pores (*i.e.* macrochannels) that can accommodate greater densification. In many cases it was observed that macrochannels had become occluded to some extent post mechanical testing. Therefore the ultimate compressive strength, although similar to that for bimodal scaffolds, occurs at greater strains. This is perhaps due to the inherent difficulties associated with achieving complete compaction of very small pores (*i.e.* the micro- and meso- porous volume). The presence of macrochannels allows for greater densification (compaction of the micro- and meso- porous volume) thereby producing higher ultimate compressive strengths for trimodal scaffolds. It should be noted that the compressive strength corresponds to the compacted volume for both trimodal and bimodal scaffolds.

Post mechanical testing, the macro architecture of trimodal scaffolds appeared to be intact compared to bimodal scaffolds as shown in Figure 4.27. Although failure of both bimodal and trimodal scaffolds is occurring from the onset of loading and hence are unlikely candidates for load-bearing applications, the ability for these scaffolds to continue to deform up to approximately 15-20 % strain without ulti-

mate failure occurring may prove beneficial in a clinical setting when cutting and manipulating the scaffold shape/size to suit a non load-bearing defect site.

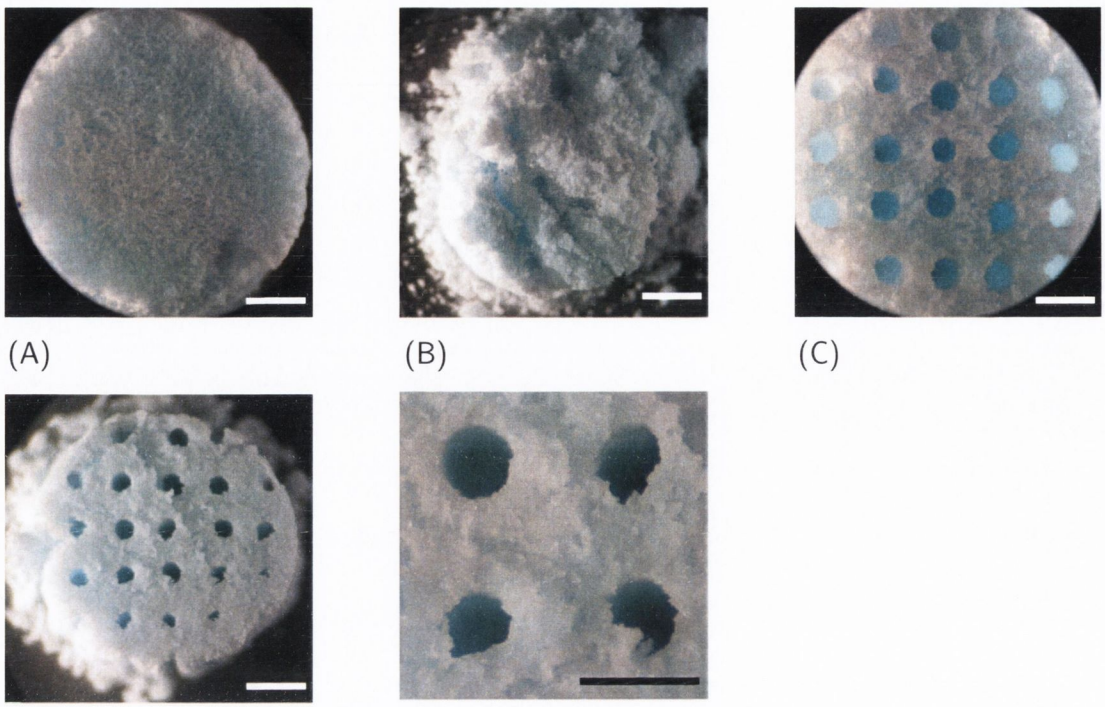

Figure 4.27. (A) and (B) Bimodal scaffold pre- and post- mechanical testing. (C) and (D) Trimodal scaffold pre- and post- mechanical testing. (E) Higher magnification of trimodal scaffold post mechanical testing showing evidence of densification occurring in the mesopore domain between the macrochannels. Scalebar is 1 mm.

4.2.7 Fluid retention properties

In order for both trimodal and bimodal scaffolds to be optimally seeded with cells, the volume of cell suspension to be delivered to the scaffolds should be approximately equal to the maximum fluid capacity of a given scaffold in order to improve cell seeding efficiency. Experimental tests were carried out on both trimodal and bimodal scaffolds to determine the maximum fluid retention capacities using deionised water (Section 3.5.3). Based on the results obtained for scaffolds of ∅ 5 mm and height 4 mm, trimodal scaffolds were capable of retaining up to a maximum of 60 % (SE=± 1.7, n=10) of the scaffold volume. Similarly, bimodal scaffolds were capable of retaining up to a maximum of 67.2 % (SE=± 2.8, n=10) of the scaffold volume. Although a statistical difference ($p < 0.05$) between the maximum fluid retention capacities of the two scaffolds types was observed, with bimodal scaffolds exhibiting slightly higher fluid retentions capacities, this may be attributed to the increased surface tension ability of the bimodal scaffolds, since they have a greater material surface area, forming a layer of water on the top and bottom surfaces of the scaffolds and thus increasing their fluid retention capacity. This phenomenon was observed to occur when conducting the experiments. Interestingly the maximum volume retentions determined are slightly less than their respective effective porosities (trimodal $\sim$ 81%, bimodal $\sim$ 76 %). This is possibly due to the presence of trapped micro air bubbles inside the scaffolds. No external vacuum pressure was applied do these samples to remove any micro air bubbles present in order to simulate the true *in vitro* condition for cell seeding. In light of the results obtained, all *in vitro* experiments involving cell seeding of scaffolds used a volume of 50 μL of cell suspension unless specified otherwise.

4.3 Cellular response to HA scaffolds and substrates

This section presents the results obtained from the *in vitro* cell culturing work of HA scaffolds and non-porous HA substrates. The section deals with time-dependent cell attachment (2D), cell seeding techniques, cell distribution, cell proliferation (2D and 3D) and the determination of cellular oxygen consumption rates.

4.3.1 XTT correction factor

The TACS XTT assay (Section 3.6.10) was used to assess cell proliferation on both 2D flat substrates and 3D bimodal and trimodal constructs. For the 3D scaffolds it was observed that after incubation of cell seeded HA scaffolds with the XTT reagents, scaffolds appeared to be red in appearance and that this was possibly due to the accumulation of the cleaved soluble orange formazan dye within the scaffolds. Due to this observation, it was hypothesised that the determined viable cell numbers were being underestimated and further experiments were carried out to ascertain the degree of this effect (Section 3.6.9). A summary of the different groups and the results obtained are presented in Table 4.10 and the data graphed in Figure 4.28. No significant difference was found to exist between the control group and scaffolds crushed after the XTT assay. There was a statistical difference ($p < 0.0001$) between fully intact scaffolds and scaffolds which were crushed after the XTT assay. Based on the ratio of absorbance from scaffolds crushed after the XTT assay to the absorbance of fully intact scaffolds (See Table 4.10), a correction factor of 2.5 was chosen to correct for viable cell numbers for all experiments involving 3D scaffold constructs. No correction factor was used in determining cell proliferation on HA flat substrates since no accumulation of dye was observed to occur on these substrates.

Table 4.10. Summary of the different groups used for XTT correction with respective absorbance values. SE= standard error of the mean, n = 3 for all groups.

Group	**Absorbance [± SE]**
Control (no scaffold)	0.738 ± 0.02
Fully intact scaffold	0.306 ± 0.01
Scaffold crushed prior to seeding	0.612 ± 0.02
Scaffold crushed after XTT assay	0.766 ± 0.01

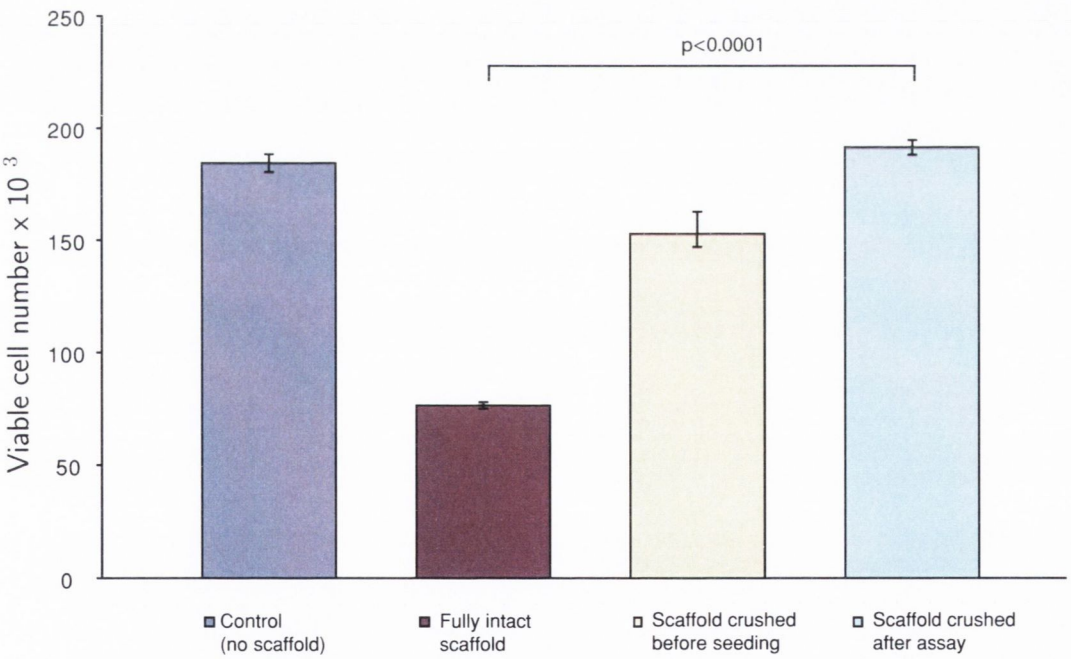

Figure 4.28. Viable cell number for the different groups as presented in Table 4.10. The data represents the mean of triplicate samples ± the standard error of the mean (SE).

4.3.2 2D Time-dependent cell attachment

The purpose of this experiment was to determine the amount of time (after initial cell seeding) before maximum cell attachment occurs. Knowing this information is important for any post-seeding techniques that may be employed to enhance cell distribution or seeding efficiency (*e.g.* perfusion, dynamic rotation) since these techniques must therefore be utilised within this available time frame. A plot of the results obtained for the 2D time-dependent cell attachment of MC3T3-E1 cells to non-porous HA substrates is shown in Figure 4.29.

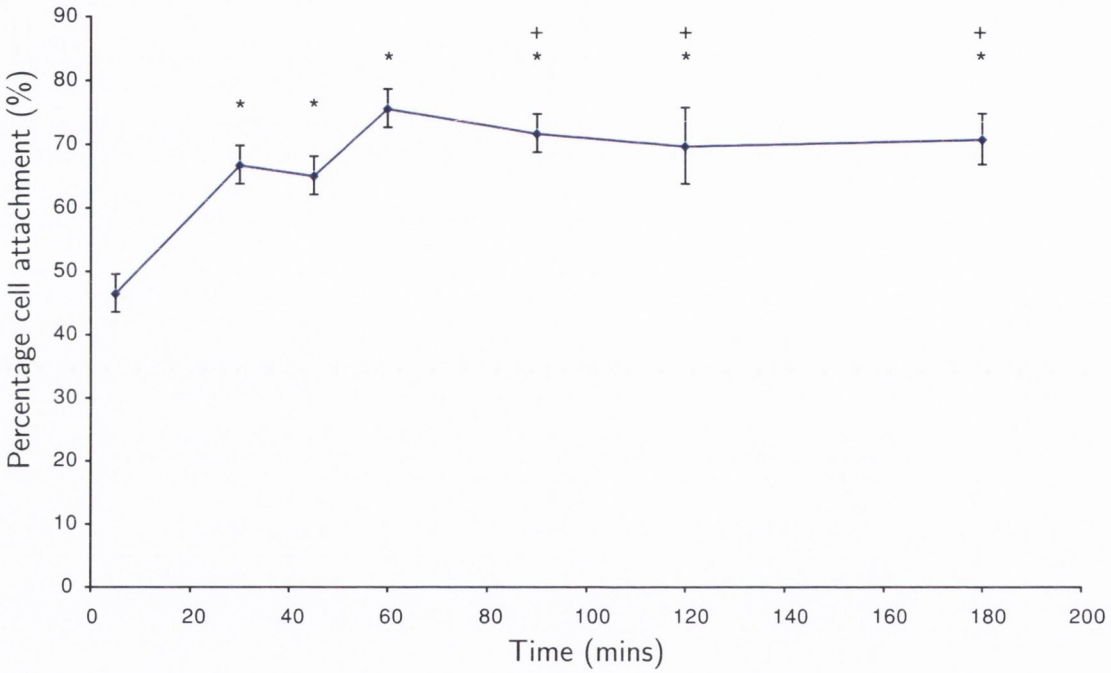

Figure 4.29. Time course of MC3T3-E1 osteoblastic cell attachment to 2D non-porous HA substrates. The data represents the mean of quintuplicate samples ± the standard error of the mean (SE). * indicates significant difference ($p < 0.05$) compared to 5 mins. + indicates no significant difference ($p < 0.05$) compared to 60 mins.

As can be seen MC3T3-E1 cells attached to the HA substrates in an increasing time-dependent manner, from a minimum of 46.6 % (SE=± 2.6, n =5) after 5 mins increasing to a maximum of 75.7 % (SE=± 2.7, n =5) after 60 mins, with a plateau existing after this time point. There was a statistically significant ($p < 0.05$)

difference between the percentage cell attachment measured after 5 mins compared to all subsequent time points. No statistical difference was found between the 60, 90, 120 and 180 min incubations. In this experiment, cells were delivered to the substrate in 20 μL of medium. This was to overcome any time limiting effects of the cell suspension having to come into contact with the HA substrate surface due to gravity. This might explain the relatively high percentage of cell attachment ($\sim$ 46 %) that was found to occur after 5 mins. Based on the data obtained, a minimum time of 60 mins was used for static seeding of scaffold constructs before being transferred to well plates containing medium for further culturing or analysis.

4.3.3 Examination of cell proliferation-2D

For the determination of 2D cell proliferation, MC3T3-E1 cells were seeded and cultured on non-porous HA discs and on culture plastic for comparison purposes (Section 3.6.15). A graph of the determined viable cell number at various time points (4-168 hrs) is shown in Figure 4.30. As can be seen there is an increasing trend in cell number for both substrate materials (culture plastic and HA discs).

However, cell growth on HA discs was lower than on tissue plastic (control) during the culture period. Four hours after seeding there was no statistical significance between the viable cell numbers attached to culture plastic and HA substrates both of which were seeded with 50 x 10^3 cells, and both exhibited approximately 80 % cell attachment. However, as time progresses, there is a statistical difference ($p < 0.05$) between the two groups at each of the subsequent time points. Table 4.11 presents the respective percentage increase per hour [% h^{-1}] of cell numbers for discrete time frames for both HA and control substrates. The greatest percentage increase per hour in cell numbers for both substrates occurs during the first 24 hours of culturing (Control = 12.42 $\pm$ 0.42 % h^{-1}, HA substrate = 6.47 $\pm$ 0.13 % h^{-1}), and decreases thereafter. It is clear from Figure 4.30 and Table 4.11 that the HA substrate inhibited or delayed cell proliferation compared to control surfaces. The growth profiles on control and HA substrates are comparable to those published by

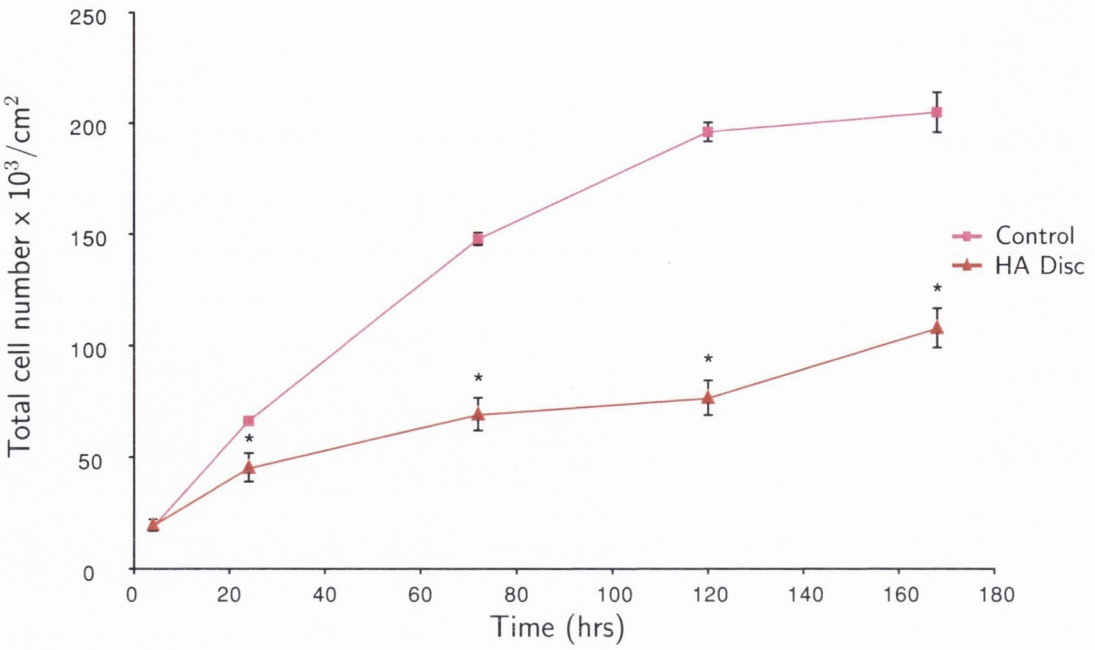

Figure 4.30. Comparative growth kinetics of MC3T3-E1 cells cultured on control and HA substrates with an initial seeding density of 2.5 x 10^3 cells/cm^2. The data represents the mean of sextuplicate samples $\pm$ the standard error of the mean (SE). * indicates significant difference ($P < 0.05$) compared to control at the same time point.

Frayssinet *et al.* (1997) who used a fibroblast cell line (L929 mouse) and similar culturing conditions. Shu *et al.* (2003) also showed that the growth of MC3T3-E1 cells cultured on a HA surface was suppressed in comparison to cells cultured on plastic 24 hrs, four and six days post-seeding, while no differences were observed between plastic and HA in terms of attachment, apoptosis, and necrosis. The authors also demonstrated that bromodeoxyuridine (5-bromo-2-deoxyuridine, BrdU) uptake, used for the detection of proliferating cells, is decreased in cells grown on HA compared with plastic surfaces and that the decrease in growth is consistent with the enhancement of osteoblast differentiation. Other possible reasons for lower proliferation rates of cells cultured on HA discs might include increased calcium and phosphate levels which can induce apoptosis or inhibit cell growth, although this is unlikely due to the minimal dissolution rate of dense sintered HA (Frayssinet *et al.*, 1997). Nevertheless the results obtained for proliferation of MC3T3-E1 cells provide a baseline for determining the influence of various porosities of 3D HA scaffolds.

Table 4.11. Percentage increase per hour (% h^{-1}) of viable cell numbers for discrete time frames, $\triangle$ t (hrs), for both HA and control substrates.

Scaffold Type	$\triangle$ **t [hrs]**	**Percentage per hr.** [% $\mathbf{h^{-1}}$]	$\pm$ **SE**	**n**
Control	4-24	12.42	0.42	6
Control	24-72	2.54	0.02	6
Control	72-120	0.68	0.02	6
Control	120-168	0.09	0.05	6
Control	4-168	2.63	0.29	6
HA substrate	4-24	6.47	0.13	6
HA substrate	24-72	1.20	0.17	6
HA substrate	72-120	0.23	0.05	6
HA substrate	120-168	0.90	0.17	6
HA substrate	4-168	2.92	0.34	6

4.3.4 Static cell seeding of 3D scaffolds

Due to its relative simplicity, static seeding has been utilised by many researchers for various cell types and scaffold configurations. However, due to the complex and tortuous architecture of many single porous domain 3D scaffolds, delivery of a high density of cells with high efficiency and uniformity throughout the scaffold proves difficult. A scaffold has a finite capacity for absorbing fluid, therefore once the scaffold has absorbed this maximum fluid retention volume, any excess medium containing cells may flow around the periphery of the scaffold into the well containing the scaffold construct thereby reducing the actual number of cells exposed to the scaffold and thus producing low seeding efficiencies.

With these existing limitations in mind, PDMS silicone chambers were used for seeding (Section 3.6.8) which had diameters of 6 mm. These closely matched the diameter of the scaffolds of 5 mm to facilitate insertion of scaffolds prior to seeding

and removal of scaffolds post-seeding. Furthermore, cable ties were placed around these PDMS chambers to reduce the excess volume around the periphery of the scaffolds.

A study was carried out to investigate the time required for cells to become attached to bimodal scaffolds. Scaffolds were seeded with 3 x 10^5 cells delivered to the scaffold surface in 50 μL of medium and incubated at 37 °C. At specific time points (30, 60, 120 and 180 mins.), scaffolds were removed from culture and washed three times with PBS using a pasteur pipette and the number of cells within each scaffold was assessed *via* a DNA assay (Section 3.6.13). The results are presented in Figure 4.31 and Table 4.12.

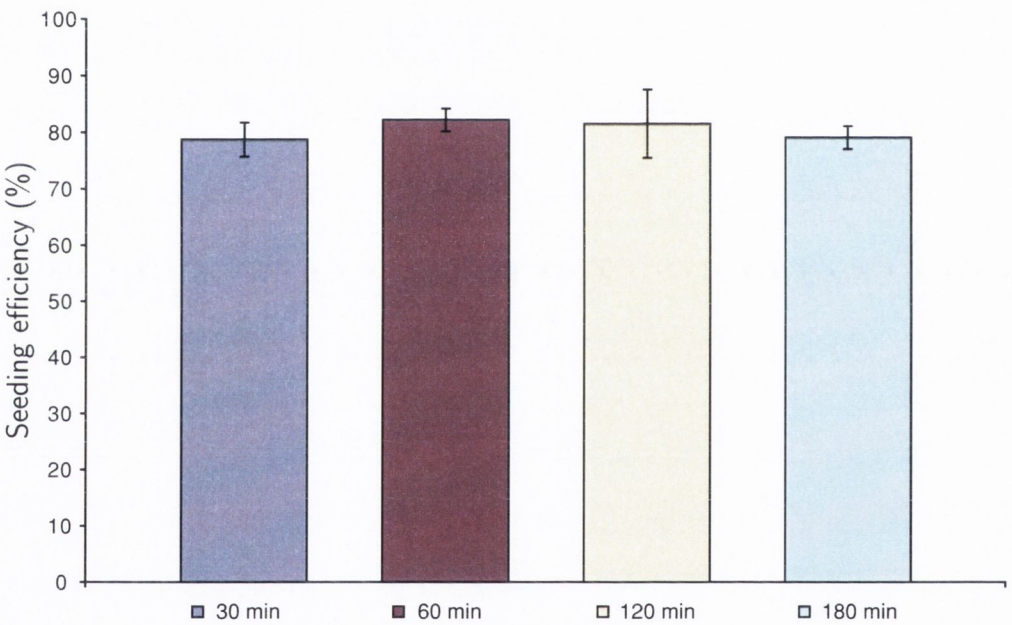

Figure 4.31. Seeding efficiency (%) of cells within bimodal scaffolds post-seeding at 30, 60, 120 and 180 min. The data represents the mean of quintuplicate samples ± the standard error of the mean (SE).

It is evident that the number of cells within bimodal scaffolds remains constant ($\sim$ 80 %) and no statistical difference ($p < 0.05$) was found between any of the groups for any of the time points investigated. However, it should be noted that these data do not necessarily imply that cell adhesion has been attained after 30

Table 4.12. Seeding efficiency (%) of cells of bimodal scaffolds at various time points (30, 60, 120 and 180 min) post-seeding. SE = standard error of the mean, n= number of samples.

Time [mins]	**Seeding efficiency [%]**	**SE [%]**	**n**
30	78.7	2.5	5
60	82.2	2.3	5
120	81.5	6.1	5
180	79.1	2.1	5

minutes. It implies that cells occupied the pores, and could not be removed from the scaffolds through washing. Reflecting on the data obtained from the 2D time-dependent adhesion experiments (Section 4.3.2), it is possible that it may take up to one hour for maximum cell adhesion to be reached.

An investigation was also carried out to assess if the seeding efficiency of trimodal scaffolds was dependent on the volume of cell suspension delivered to each scaffold (Section 3.6.14). Figure 4.32 presents the results obtained 3 hours post-seeding. The same number of cells (3 x 10^5 cells) was delivered to each of the scaffolds while varying the volume of suspension (25, 50 and 100 μL). As can be seen there is a decreasing trend in the number of cells within scaffolds with increasing volume of suspension and these results were found to be statistically significant ($p < 0.05$).

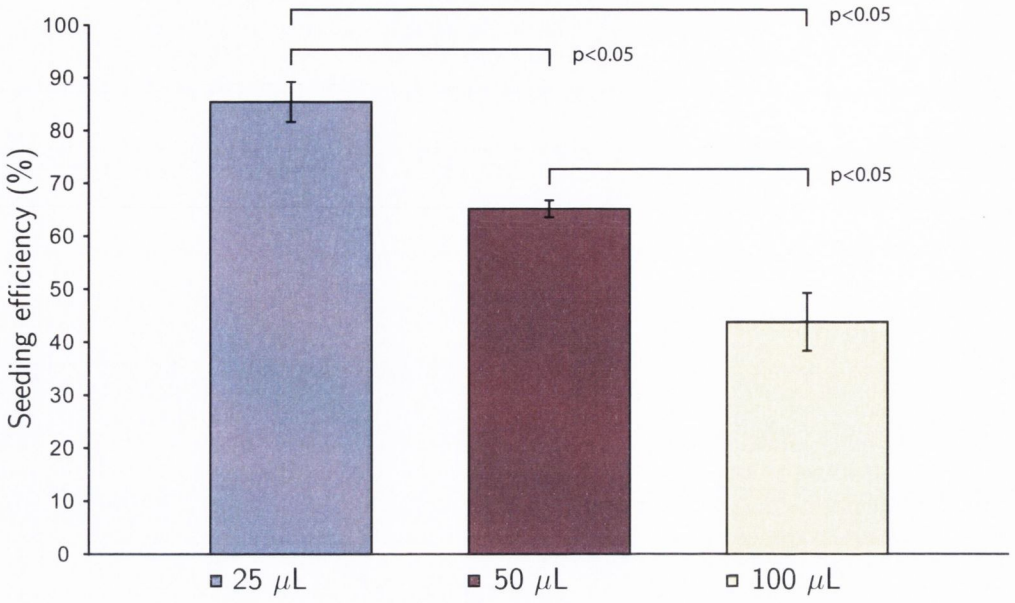

Figure 4.32. Seeding efficiency (%) of cells within trimodal scaffolds 3 hrs post-seeding. All scaffolds were seeded with 3×10^5 while varying the volume of suspension delivered (25, 50 and 100 μL). The data represents the mean of quadruplicate samples $\pm$ the standard error of the mean (SE).

Table 4.13 presents the data for each of the groups investigated. Of interest is the percentage of cells that were found within scaffolds when seeded with 50 μL of cell suspension which was found to be $\sim$ 68 % of the initial seeding density.

Table 4.13. Seeding efficiency (%) of cells within trimodal scaffolds after 3 hrs post-seeding. SE = standard error of the mean, n= number of samples.

Seeding volume [μL]	**Seeding density** [cells]	**Efficiency** $\pm$ **SE** [%]	**n**
25	3×10^5	85.4 ± 4.9	4
50	3×10^5	67.7 ± 2.2	4
100	3×10^5	43.8 ± 3.2	4

Although a lower seeding volume (25 μL) produced higher seeding efficiencies, it is more advantageous that the entire scaffold has been exposed to the cell suspension in order to promote a homogeneous distribution of cells and this is only possible when seeding with volumes approximately equal to the maximum fluid retention capacities of the scaffold being seeded. MTT staining of bimodal scaffolds demonstrated that using low seeding volumes (*i.e.* 25 μL) resulted in poor penetration and distribution of cells into the scaffold volume and they were ultimately confined to the top surface as shown in Figure 4.33.

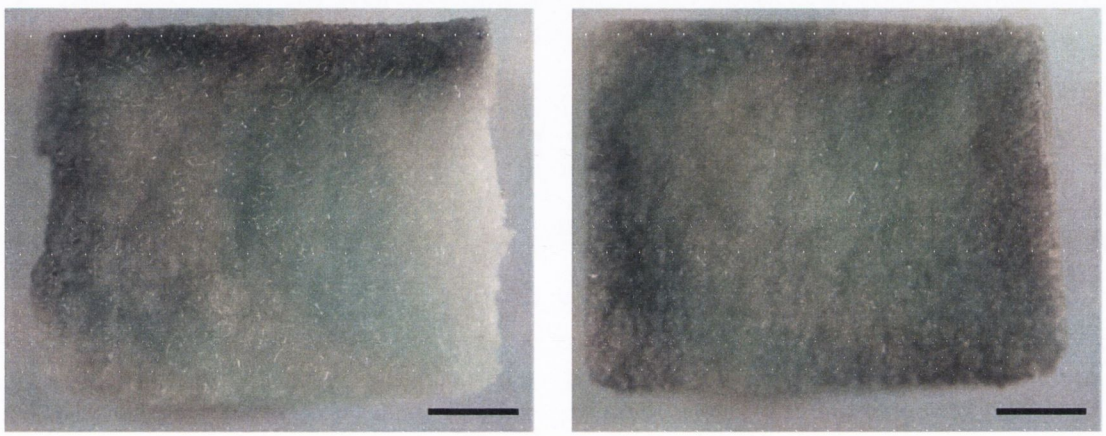

(A) (B)

Figure 4.33. Comparative MTT staining of longitudinal bimodal cross-sections seeded with (A) 25 μL and (B) 50 μL of cell suspension. Scale bar is 1mm.

In contrast, as presented in Figure 4.31 for the same seeding volume (50 μL), the percentage of cells within bimodal scaffolds was higher at $\sim$ 80 %. These results may possibly explain the large variation in seeding efficiencies reported in the literature, and highlight the importance of matching the seeding volume to the fluid retention capacity for a given scaffold. Once a scaffold becomes saturated and has absorbed cell suspension through capillary action, it is likely that any remaining cells in the fluid above the scaffold surface may only rely on gravity to become attached and this may promote inhomogeneous cell seeding, with a larger number of cells attaching on the peripheral surface of the scaffold.

The lower seeding efficiencies observed for trimodal scaffolds compared to bimodal scaffolds ($\sim$ 68 v's 80 %) is possibly due to the presence of the macrochannels. Once the macrochannels become saturated with cell suspension, cells contained within this macrochannel volume may not have been exposed to the mesoporous phase. This may have inhibited cells from attaching, therefore resulting in lower seeding efficiencies. A schematic to illustrate this is shown in Figure 4.34. For this reason, a rotational seeding technique was employed to assess if the seeding efficiency of trimodal scaffolds could be enhanced. This was the focus of the next study.

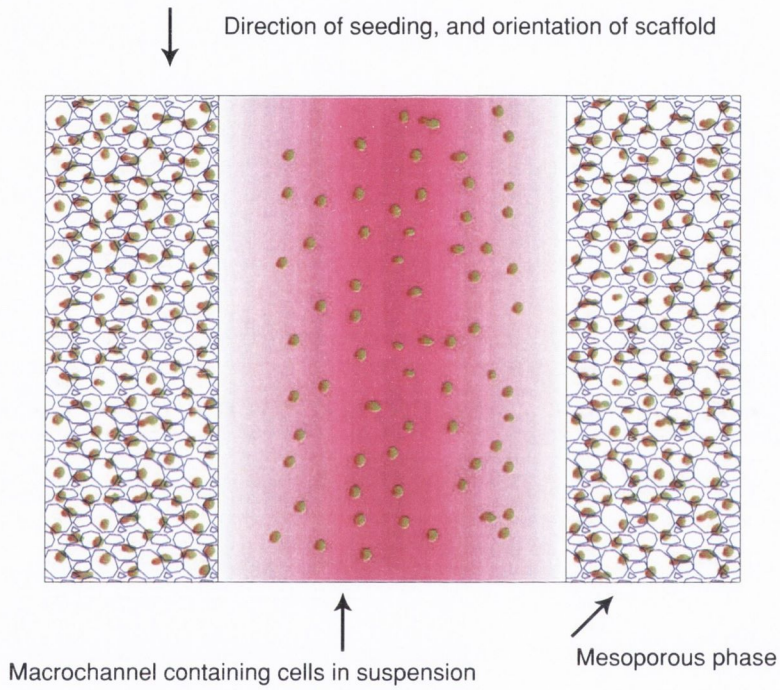

Figure 4.34. Schematic to illustrate a possible reason of lower seeding efficiencies of trimodal scaffolds compared to bimodal scaffolds for the same given seeding volume. Some cells in suspension contained within the macrochannel volume may not have been exposed to the mesoporous phase due to the orientation of the scaffold thus inhibiting cells from attaching, resulting in lower seeding efficiencies.

4.3.5 Dynamic rotational cell seeding of scaffolds

Dynamic rotational cell seeding of trimodal scaffolds was carried out as described in Section 3.6.9 to assess if the seeding efficiency of trimodal scaffolds could be enhanced compared to using the static seeding technique. Three orientations were assessed, normal (no rotation), horizontal (no rotation) and horizontal rotation as illustrated in Figure 4.35.

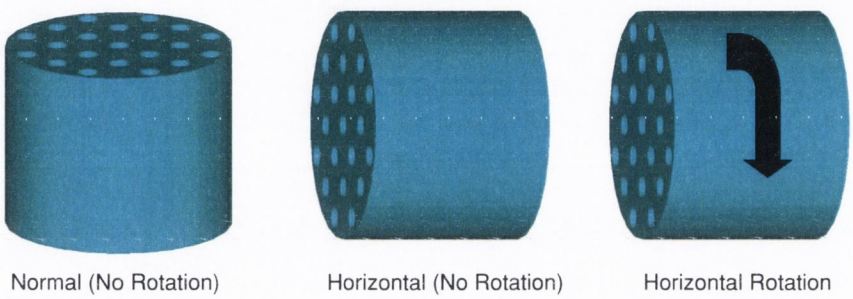

Figure 4.35. Illustration of orientations assessed to enhance seeding efficiency of trimodal scaffolds.

All scaffolds were seeded with 3 x 10^5 cells in 50 μL of medium and assessed after one hour *via* a DNA assay (Section 3.6.13). The results obtained from this experiment are presented in Figure 4.36. As can be seen, there is a decreasing trend in the seeding efficiency from 72.3 % (SE=$\pm$ 1.6, n=6) for the normal (no rotation) orientation, to 64.1 % (SE=$\pm$ 2.4, n=6) for horizontal (no rotation) to 56.3 % (SE=$\pm$ 3.2, n=6) for horizontal rotation. As was observed when removing the samples from their respective chambers, fluid had escaped from the macrochannels of the trimodal scaffolds for samples exposed to both horizontal (no rotation) and horizontal rotation post-seeding, and is possibly the reason for the lower seeding efficiencies observed.

Little or no excess fluid was observed to have existed in the chambers for the normal seeding method. Statistically there was a difference ($p < 0.05$) between the normal orientation and the other two orientations (horizontal and horizontal rotation), although there was no statistical difference ($p < 0.05$) in the seeding ef-

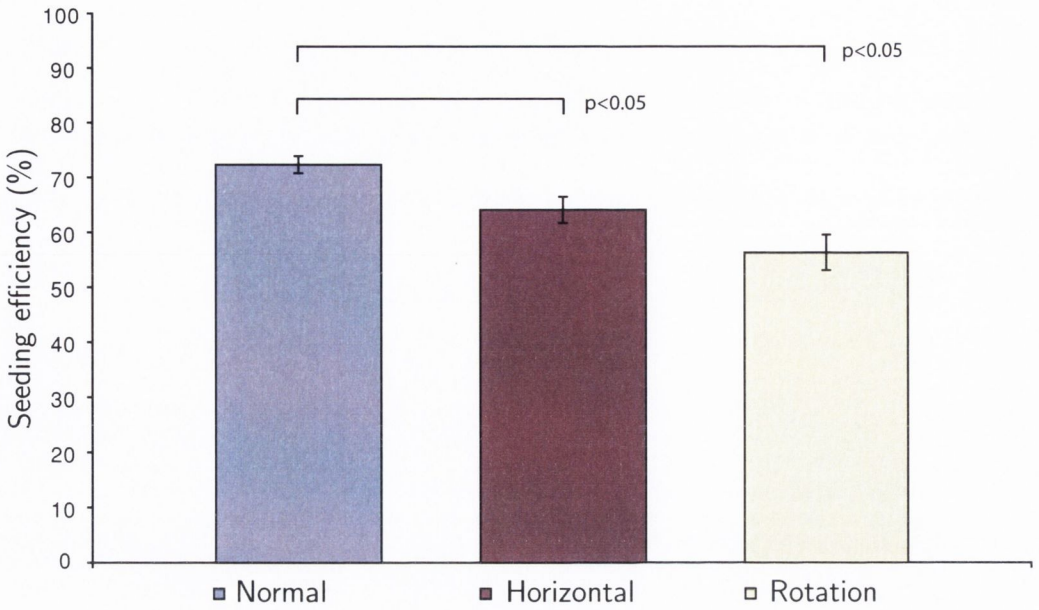

Figure 4.36. Seeding efficiency of trimodal scaffolds subjected to normal, horizontal (no rotation) and horizontal rotation seeding. Scaffolds were seeded with 300 x 10^3 cells in 50 μL of medium. The data represents the mean of sextuplicate samples $\pm$ the standard error of the mean (SE).

ficiency between horizontal (no rotation) and horizontal rotation seeding. Overall, the seeding efficiency of trimodal scaffolds could not be improved upon compared to the normal static method. Therefore the normal static method for seeding trimodal scaffolds for future experiments was utilised. This observation that the presence of macrochannels can have a negative impact on the seeding efficiency of scaffolds may give rise for concern when seeding single regular porous scaffolds with orthogonal channels/struts (reviewed in Section 2.7) without a mesoporous domain which can absorb cell suspension (*i.e.* relying solely on the available surface area of the channels/struts to allow for cell adhesion).

4.3.6 Static and dynamic rotational culturing of scaffolds- Examination of cell distribution

Both bimodal and trimodal scaffold samples were assessed 4 hours post-seeding and after sub-culturing for 1, 3, 5 and 7 days for both static and dynamic rotation conditions as described in Section 3.6.17. An MTT assay (Section 3.6.16) was used to qualitatively assess the spatial distribution of cells throughout scaffold constructs. The results from the MTT staining are shown in Figures 4.37-4.41. A dark blue stain indicates the presence of viable cells, indicating that the reduction of MTT to formazan had occurred. An area in which a dark blue stain was not present denotes an absence of live cells in that specific region. Figure 4.37 shows surface and longitudinal cross-sectional images for both trimodal and bimodal scaffolds 4 hours post-seeding.

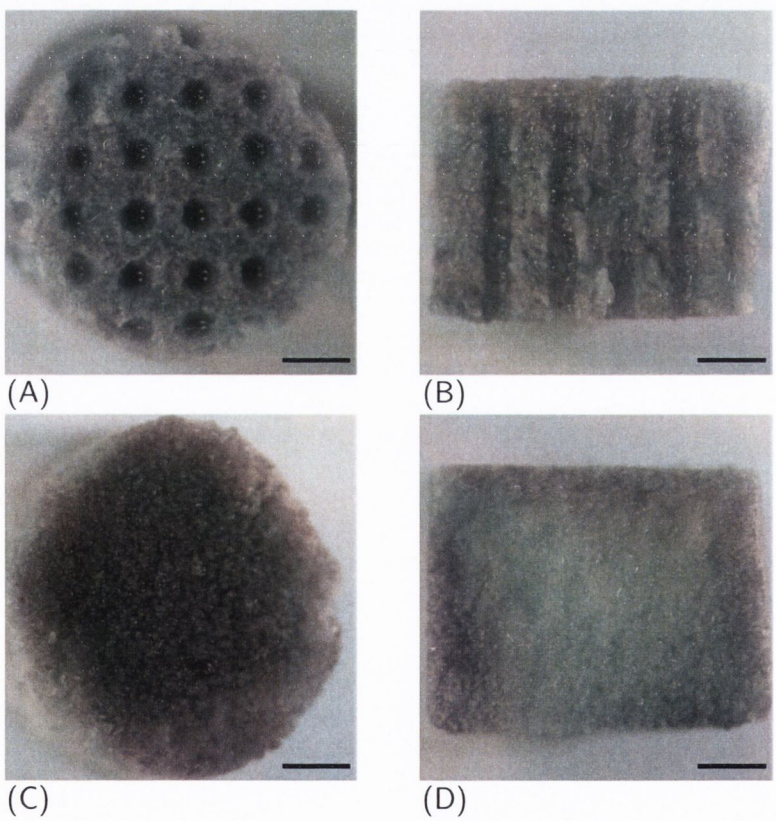

Figure 4.37. Comparative MTT staining of surface and longitudinal cross-sections of trimodal (A, B) and bimodal scaffolds (C, D) 4 hours post seeding. Scale bar is 1mm.

As was observed for seeded bimodal scaffolds, a blue stain was not present throughout the scaffold depth indicating limited penetration of cells through the porous bimodal scaffold material. In contrast, trimodal scaffolds exhibited a uniform blue stain throughout the scaffold depth indicating a homogenous distribution of viable cells.

As can be seen from Figures 4.38-4.41, there is a gradual decrease with time in viable cell distribution with increasing depth away from the surface for both bimodal and trimodal scaffolds subjected to static culturing conditions. For bimodal scaffolds after 7 days of static culture a thin layer of viable cells were observed to exist in the outer periphery of the scaffold volume. Although trimodal scaffolds were initially homogeneously seeded, it can be seen that there is a retreating viable cell front away from the scaffold core with increasing culture time.

In contrast for trimodal scaffolds subjected to dynamic rotational culturing, a homogeneous viable cell distribution was observed throughout the scaffold depth after seven days of continuous rotation. It is also interesting to note that bimodal scaffolds appeared to contain cells at a greater depth away from the surface with increasing time of culturing, showing evidence of cell migration towards the scaffold core. This is possibly due to a more favourable nutrient environment being present due to rotation and mixing of the medium inhibiting concentration gradients from developing. This evidence of cell migration demonstrates that the scaffold architecture is highly interconnected and allows the movement of cells through the mesoporous domain once favourable conditions are present. Even after 7 days of dynamic rotation, a viable cell population was not evident within the centre of bimodal scaffold constructs. The more significant existence and distribution of a viable cell population within trimodal scaffolds compared to bimodal scaffolds is most likely due to the presence of the macrochannels. These macrochannels permitted a more optimised structure for cell seeding and ultimately cell distribution (Figure 4.37) and also more readily facilitated nutrient and metabolic waste transport during dynamic culturing.

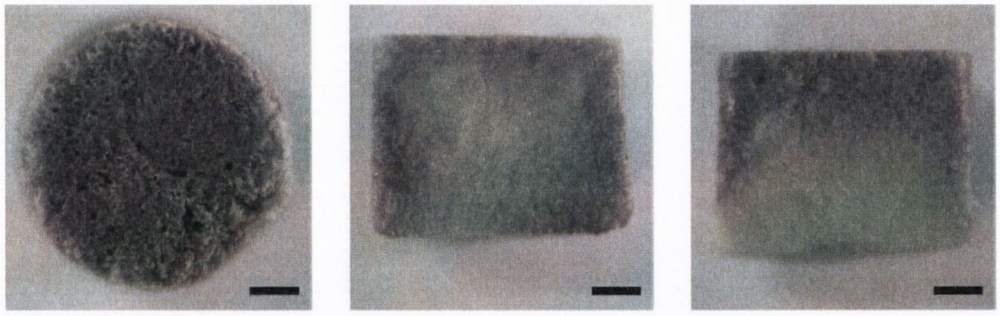

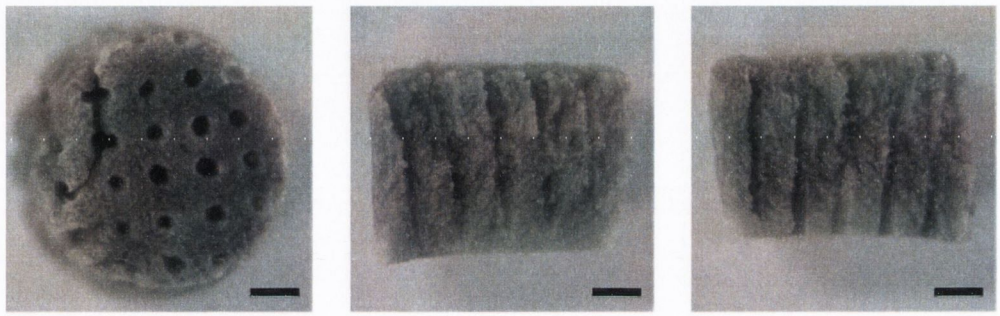

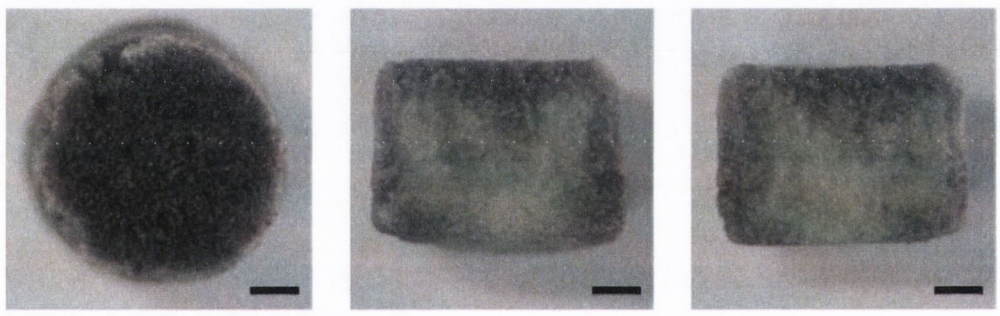

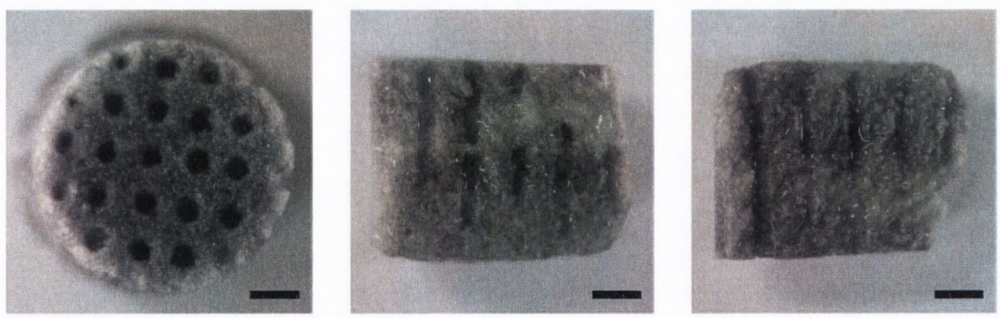

Figure 4.38. Comparative MTT staining of surface and longitudinal cross-sections of bimodal and trimodal scaffolds 1 day post seeding. Scaffolds were subjected to either static or dynamic culturing. Scale bar is 1mm.

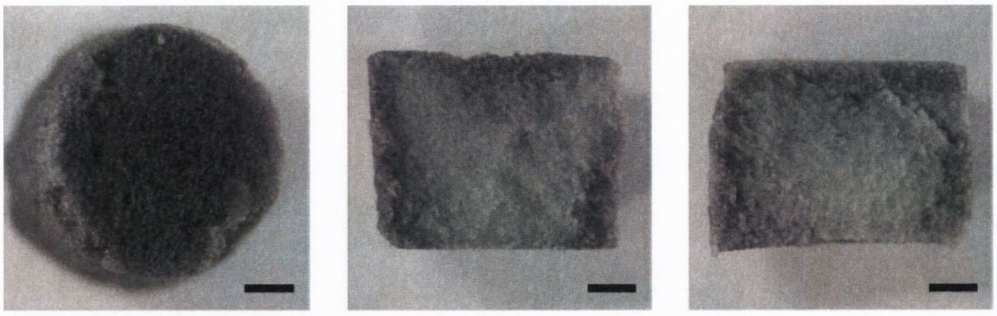

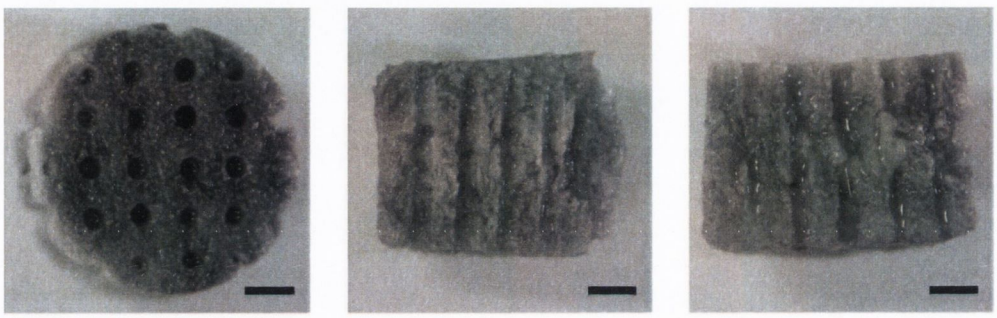

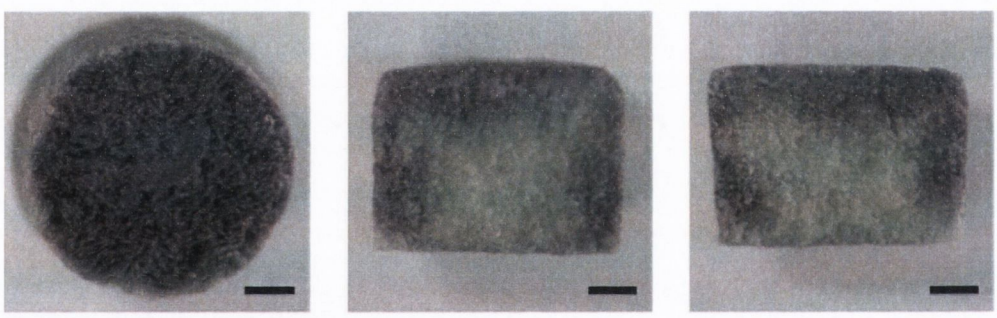

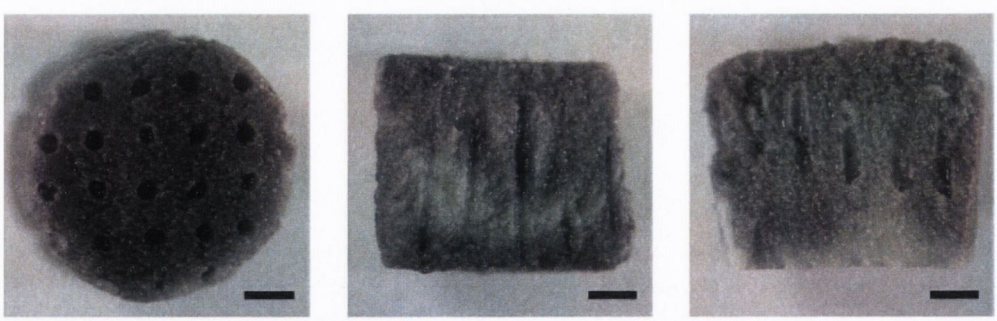

Figure 4.39. Comparative MTT staining of surface and longitudinal cross-sections of bimodal and trimodal scaffolds 3 days post seeding. Scaffolds were subjected to either static or dynamic culturing. Scale bar is 1mm.

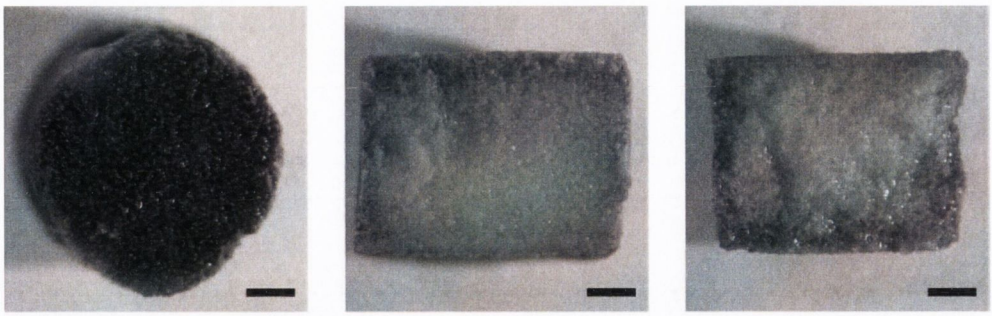

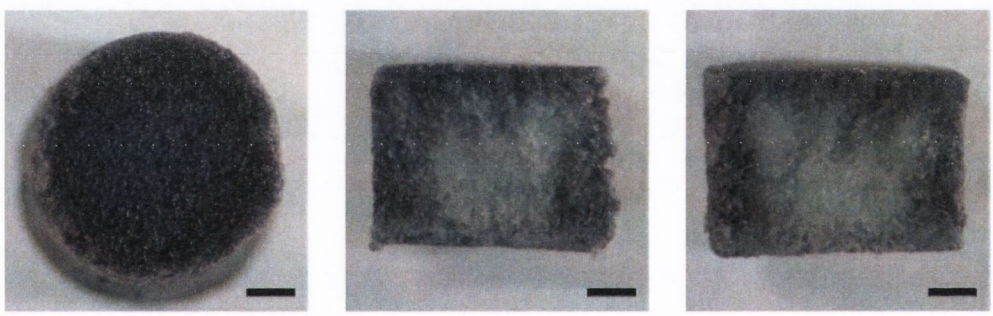

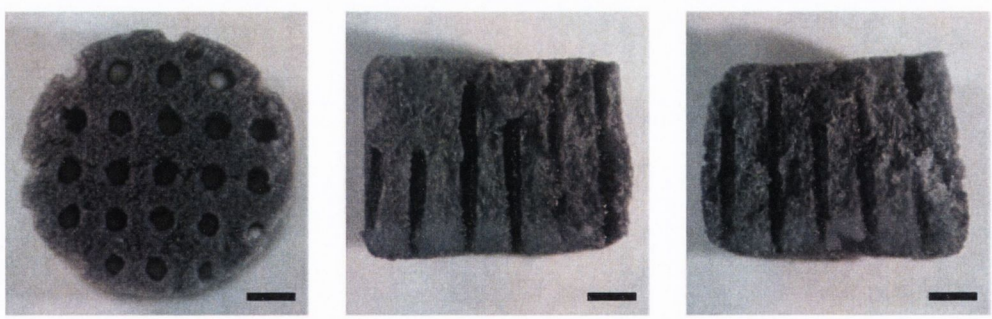

Figure 4.40. Comparative MTT staining of surface and longitudinal cross-sections of bimodal and trimodal scaffolds 5 days post seeding. Scaffolds were subjected to either static or dynamic culturing. Scale bar is 1mm.

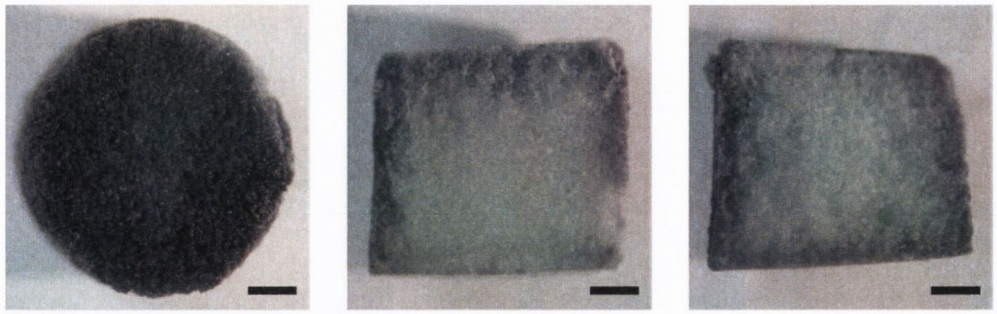

Static bimodal 7 day

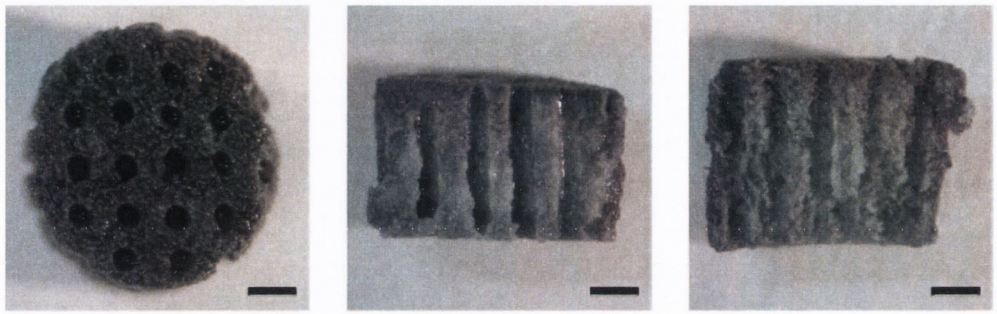

Static trimodal 7 day

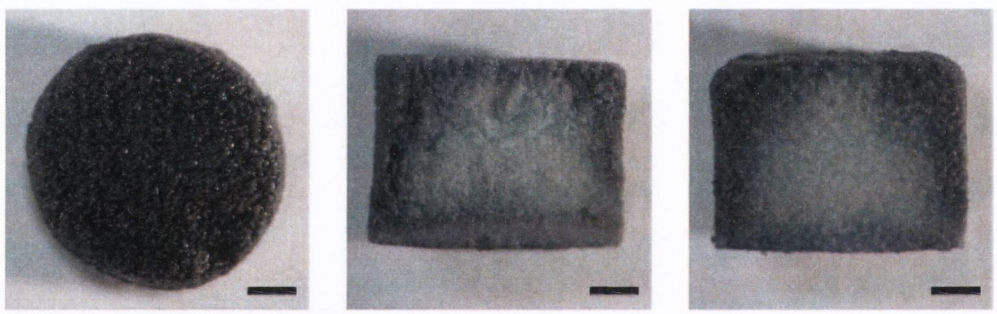

Dynamic bimodal 7 day

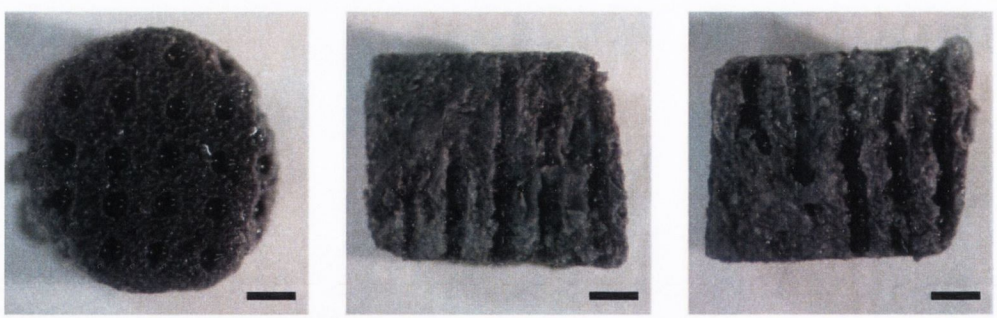

Dynamic trimodal 7 day

Figure 4.41. Comparative MTT staining of surface and longitudinal cross-sections of bimodal and trimodal scaffolds 7 days post seeding. Scaffolds were subjected to either static or dynamic culturing. Scale bar is 1mm.

4.3.7 Static and dynamic rotational culturing of scaffolds- Examination of cell proliferation

Cell numbers within constructs were obtained *via* DNA analysis (Section 3.6.13) in order to examine cell proliferation. A graph of the determined cell number within both trimodal and bimodal scaffolds at 1, 3, 5 and 7 days subjected to either static or dynamic conditions is shown in Figure 4.42.

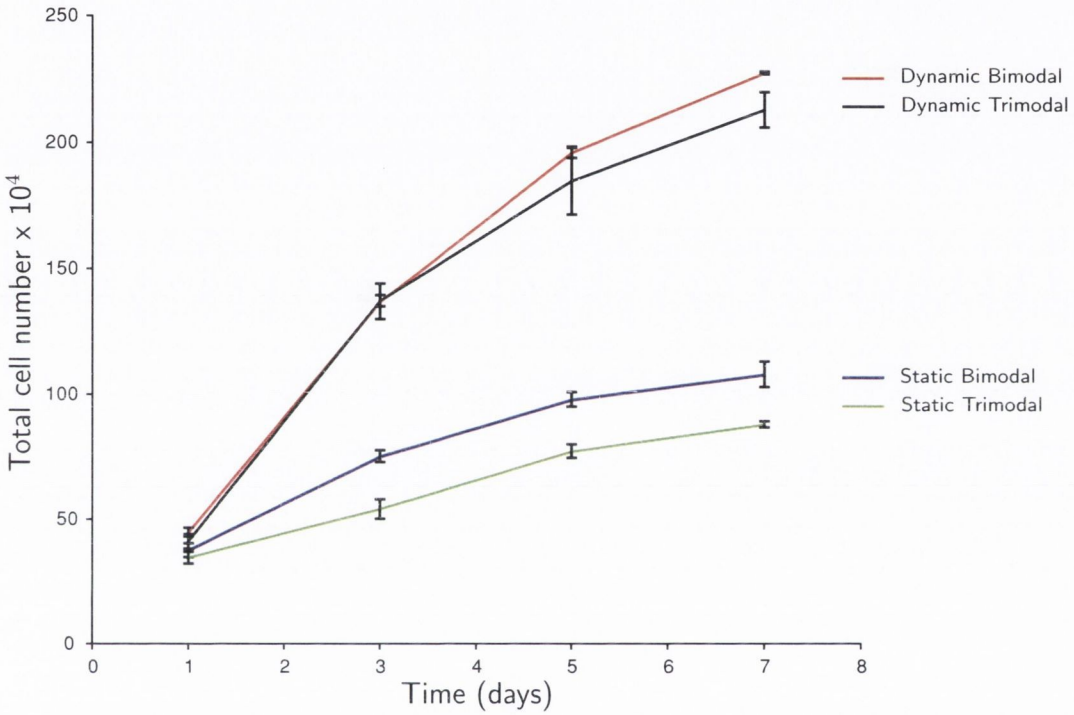

Figure 4.42. Comparative growth kinetics over 7 days of MC3T3-E1 cells cultured on bimodal and trimodal HA scaffolds subjected to either static or dynamic culture conditions. The data represents the mean of triplicate samples $\pm$ the standard error of the mean (SE).

For both bimodal and trimodal scaffolds cultured under static conditions there is an increasing trend in cell number with time. It is interesting to note that the growth profiles for both scaffold types followed a similar trend as was observed for the 2D cultures as presented in Section 4.3.3. After 1 day, no statistical difference in cell number existed between bimodal and trimodal scaffold groups. However for each of the subsequent time points, there were statistically significantly ($p < 0.05$) more cells within bimodal scaffolds compared to trimodal scaffolds. The reason for this

difference in the cell numbers is possibly due to the very different cell distributions between the two scaffold types as presented in Figure 4.38 which influenced the proliferation of cells, with a greater number of cells existing in the outer periphery of bimodal scaffolds compared to trimodal scaffolds.

Comparing dynamic and static culturing conditions it is was observed that there was a greater increase in cell number with time for dynamic culturing. No statistically significant difference existed between any of the scaffolds exposed to either static or dynamic culturing conditions after 1 day. However for subsequent time points there was a statistical difference ($p < 0.01$) between the two culturing conditions. No statistical difference was observed between bimodal and trimodal scaffolds which were dynamically cultured at any of the time points investigated. Comparing static and dynamic bimodal scaffolds, after 7 days of culturing there was a 2.1 fold increase in the number of cells within dynamically cultured compared with statically cultured bimodal scaffolds. Likewise, dynamically cultured trimodal scaffolds exhibited a 2.5 fold increase in cell number compared to statically cultured trimodal scaffolds after 7 days. This increase in cell numbers for dynamic culturing conditions is possibly due to the more effective transfer of nutrients into and metabolic waste away from the scaffold core due to constant rotation and mixing of the medium. This dynamic system would inevitably prevent nutrient or metabolic waste concentration gradients from developing, thereby providing a more homogenous environment. As was presented previously, after 7 days culturing, statically cultured scaffolds (both bimodal and trimodal) exhibited a depleted viable cell distribution, with a core devoid of viable cells within the central regions (Figure 4.41) being evident. Contrastingly, a complete viable cell distribution was observed for dynamically cultured trimodal scaffolds, within which a viable cell distribution was observed throughout the entire scaffold depth.

4.3.8 Examination of cellular oxygen consumption

The measurement of oxygen consumption rate (OCR) of MC3T3-E1 cells cultures on bimodal scaffolds (⌀ 5 mm, height 1 mm) was carried out in accordance with Section 3.6.18. The oxygen concentration values measured at the base of oxygen sensitive wells for three different cell densities (0.5, 1 and 2 x 10^5 cells) is presented in Figure 4.43. As can be seen the oxygen concentration [O_2] in the base of the wells for seeded constructs decreases for all constructs over the time period (0-228 hrs), reaching a plateau at 150 hrs. These curves indicate that cells within the constructs are proliferating and thus decreasing the oxygen concentration in the wells, with the oxygen concentration [O_2] within the wells thereby demonstrating an inversely dependent relationship with cell number. Figure 4.44 and Table 4.14 presents the calculated OCR per cell (fmol min^{-1} $cell^{-1}$) over time for three different initial seeding densities (0.5, 1 and 2 x 10^5 cells).

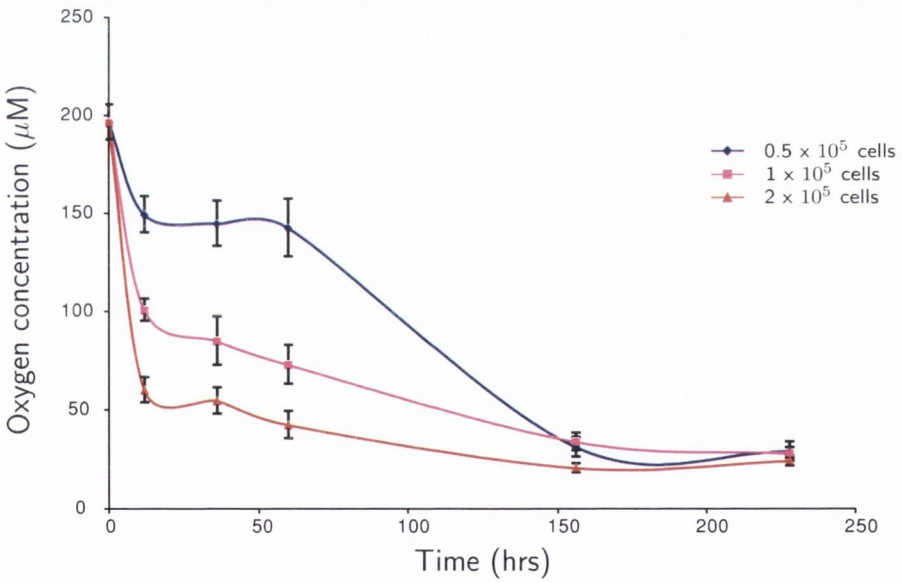

Figure 4.43. The depletion of oxygen concentration (O_2) measured at the base of oxygen sensitive wells for three different cell densities (0.5, 1 and 2 x 10^5 cells) over time (0-228 hrs). The data represents the mean of sextuplicate samples ± the standard error of the mean (SE).

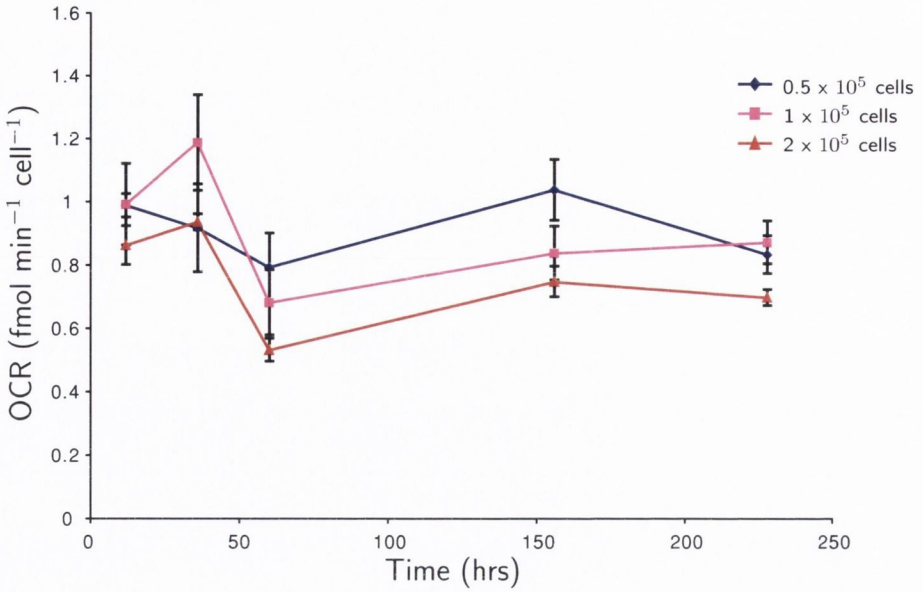

Figure 4.44. Oxygen consumption rate per cell (OCR) (fmol min^{-1} cell^{-1}) over time for three different initial seeding densities (0.5, 1 and 2 x 10^5 cells). The data represents the mean of sextuplicate samples $\pm$ the standard error of the mean (SE).

Table 4.14. Data for the oxygen consumption rate per cell (OCR) (fmol min^{-1} cell^{-1}) at different time points for three different initial seeding densities (0.5, 1 and 2 x 10^5 cells). The data represents the mean of sextuplicate samples. SE= standard error of the mean.

Seeding density	**Time [hrs]**	**12**	**36**	**60**	**156**	**228**
0.5 x 10^5	**OCR [fmol min^{-1} cell^{-1}]**	0.99	0.92	0.80	1.04	0.83
	SE [fmol min^{-1} cell^{-1}]	0.04	0.14	0.11	0.10	0.06
1 x 10^5	**OCR [fmol min^{-1} cell^{-1}]**	0.99	1.19	0.68	0.84	0.87
	SE [fmol min^{-1} cell^{-1}]	0.13	0.15	0.10	0.09	0.07
2 x 10^5	**OCR [fmol min^{-1} cell^{-1}]**	0.86	0.94	0.53	0.75	0.70
	SE [fmol min^{-1} cell^{-1}]	0.06	0.03	0.04	0.05	0.03

The mean OCR of scaffolds was found to be 0.91 fmol min^{-1} $cell^{-1}$ (SE=± .04, n =30), 0.91 fmol min^{-1} $cell^{-1}$ (SE=± .06, n =30) and 0.76 fmol min^{-1} $cell^{-1}$ (SE=± .03, n =30) for respective initial seeding densities of 0.5, 1 and 2 x 10^5 cells. No statistical difference was found to exist in the OCR of scaffolds seeded with an initial seeding density of 0.5 x 10^5 cells at any of the time points investigated. However, statistical differences ($p < 0.05$) in the OCR did exist at some of the time points for the other two seeding densities. For an initial seeding density of 1 x 10^5, a statistical difference ($p < 0.05$) was observed in the OCR between 36 and 60 hours. However, during this time frame significant proliferation was observed to have occurred as is shown in Figure 4.45.

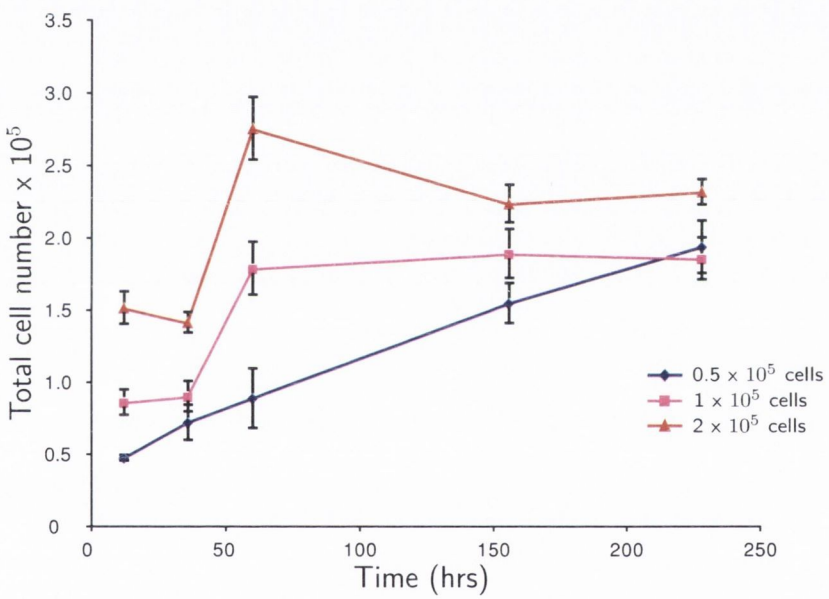

Figure 4.45. Total cell number versus time of MC3T3-E1 cells cultured on porous HA bimodal scaffolds (∅ 5 mm, height 1 mm) initially seeded with three different cell densities (0.5, 1 and 2 x 10^5 cells). The data represents the mean of sextuplicate samples ± the standard error of the mean (SE).

Similarly, for an initial seeding density of 2 x 10^5 cells, statistically significant differences ($p < 0.05$) in the OCR after 36 hours was observed. Comparing the OCR between each group at each time point during the first 36 hours, no statistical difference was observed between any of the cultures. However, statistical differences

were observed for the 2 x 10^5 wells after this time point, whereas no statistical differences were observed between the wells which were initially seeded with 0.5 and 1 x 10^5 cells at any of the time points investigated. There are two possible reasons for these observed differences in OCR.

- Oxygen sensor time-lag
- Cells becoming oxygen starved

With significant cell proliferation occurring, the oxygen demand increases and thus the oxygen becomes more depleted in the base of the wells. According to Guarino *et al.* (2004), the time required for the oxygen-sensitive ruthenium-based fluorophore to reach equilibrium can take up to 6 hours. Since the calculation of OCR depends on the assumption that the system is in equilibrium, if significant proliferation is occurring the system may not have reached equilibrium when measurements were taken and thus skew the calculated oxygen consumption rates.

Also, once the cell number exceeds a critical threshold, the cumulative oxygen demand exceeds the maximum possible diffusive transfer rate. Thus the cells become oxygen starved altering the oxygen consumption rate per cell and surviving via anaerobic glycolysis as previously observed for immortalised cells (McLimans *et al.*, 1968). As is evident in Figure 4.45, greater cell proliferation was observed to occur in scaffolds initially seeded with 1 and 2 x 10^5 cells between 36 and 60 hours. compared to scaffolds initially seeded with 0.5 x 10^5 cells. This may have been due to the lower oxygen concentrations initially experienced in these cultures which may have triggered a signalling for cell proliferation as has been similarly observed *in vitro* by Brighton *et al.* (1991) for rat calvarial bone cells and by Ren *et al.* (2006) for bone marrow stromal cells. Purposely designed experiments would be required to investigate this effect further and was not within the scope of this investigation. Although theoretically this effect of low oxygen concentrations stimulating cell proliferation might appear advantageous, work by Salim *et al.* (2004) has shown that short-term anoxic (< 0.02 % O_2) treatment of primary osteoblasts and mesenchymal precursors inhibited *in vitro* bone nodule formation and extracellular calcium deposition.

In contrast, exposure to hypoxic (2 % O_2) conditions had little effect on osteogenic differentiation. These observations are in good agreement with the work of Brighton *et al.* (1991) who observed that cells exposed to low oxygen concentrations (1 - 9 %) favoured bone cell proliferation, whereas high oxygen concentrations (9 - 21 %) favoured macromolecular synthesis (alkaline phosphatase activity, collagen and proteoglycan synthesis). The calculated mean oxygen consumption rates (OCR's) for the cultures seeded with an initial density of 0.5 and 1 x 10^5 cells were identical 0.91 fmol min^{-1} $cell^{-1}$ (SE=± .04, n =30) and 0.91 fmol min^{-1} $cell^{-1}$ (SE=± .06, n =30), and compare favourably to those obtained by Guarino *et al.* (2004) for the same immortalised cell line (MC3T3-E1 cells) cultured on polysaccharide scaffolds (0.80 fmol min^{-1} $cell^{-1}$) under similar culturing conditions.

4.3.9 Summary of cellular response to hydroxyapatite scaffolds

In summary, it was shown that although the cell seeding efficiency was higher for lower seeding volumes, the distribution of cells was confined to the top surface of the scaffolds. Therefore the most optimum approach was to adopt a seeding volume that closely matched the saturation capacity of the scaffold. Although the seeding efficiency decreased (from 85.4 % to 67.7 %), cells penetrated the mesoporous domain to a greater extent thus producing a better cell distribution. In addition, over saturation of the scaffold did not enhance cell distribution and decreased cell seeding efficiency to a greater extent (43.8 %).

The presence of macrochannels significantly enhanced the distribution of cells compared to bimodal scaffolds for the same given seeding volume, although the cell seeding efficiency was decreased. Rotational seeding was observed to have a negative impact on the seeding efficiency of trimodal scaffolds, and the seeding efficiency could not be improved. Qualitatively, a homogeneous distribution of cells were observed throughout the entire depth of trimodal scaffolds four hours post-seeding, and did not appear to be localised or concentrated in a specific region. Conversely, limited cell penetration was observed for bimodal scaffolds with the majority of

cells being confined to the outer peripheral regions of the mesoporous domain. This work has shown that when seeding three-dimensional porous scaffolds, appropriately matching the seeding volume to the saturation capacity of the scaffold is the most optimum approach in terms of promoting homogeneous cell seeding and maintaining relatively high seeding efficiencies ($\sim$ 70 %). This work has also shown that high seeding efficiencies alone may not be the best measurable outcome for evaluation purposes of cell seeding and should only be used in conjunction with initial cellular distributions.

The differences observed in viable cell distributions and cell proliferation for static and dynamic culturing conditions provide a greater depth of knowledge for development of more clinically relevant regimes for culturing scaffolds *in vitro*. The aim of *in vitro* scaffold based tissue engineering in recent years has endeavored to initially homogeneously seed scaffolds with cells and, subject to some form of culturing, to allow proliferation to develop. This study has shown that although a trimodal scaffold architecture surpasses a purely bimodal in terms of facilitating homogenous seeding, it requires dynamic culturing such as rotational culturing to maintain uniform cell viability throughout the scaffold depth with increasing culturing time. Although the focus of this work was not to develop a bioreactor device, a simple but effective system has been employed which shows that constant rotation of trimodal scaffold constructs can maintain superior cell depth viability compared to bimodal scaffolds and increase the extent of cell proliferation (2.1 - 2.5 fold) compared to static culturing.

4.4 Finite element modelling of *in vitro* oxygen concentration profiles

A numerical model was developed in order to assess the influence of active viable cells on the resulting oxygen concentration profiles when cultured on both bimodal and trimodal HA porous scaffolds (Section 3.7). The models presented in this section represent oxygen concentration profiles for various cell densities confined to specific

depths from the surface (homogeneous, 250, 500 and 1000 μm). It is assumed that the oxygen transport is by diffusion alone and that cells consume the available oxygen according to their oxygen consumption rate (0.91 fmol min^{-1}).

These models do not attempt to model the influence on cell proliferation or cell death due to the developing oxygen profiles, but use the *in vitro* experimental distributions of viable cells observed from the static culturing experiments (Section 4.3.6) at each time point of interest. Cell numbers were obtained from Section 4.3.7 for static culturing conditions relying solely on a diffusion-based regime. The models were solved numerically using the finite element method and a commercial software package COMSOL Multiphysics (ver 3.2). Geometries were generated and meshed using the fine or extra fine parameter settings. At each time point to be assessed (1, 3, 5 and 7 days), models were initialised with new cell density distributions as determined experimentally and solved for the oxygen concentration distributions at steady-state. The models therefore represent a quasi-static approach for specified time-points due to the changing cell density distributions. The input model parameters and the various cell distributions assessed from the *in vitro* static culturing experiments are presented in Tables 4.15 and 4.16.

Table 4.15. Model parameters used to calculate the oxygen concentration profiles in bimodal and trimodal scaffolds.

Parameter	**Value**	**Source**
Scaffold radius	2.5 mm	Measured
Macrochannel radius	250 μm	Measured
Scaffold height	4 mm	Measured
V_{max}	0.91 fmol $min^{-1}cell^{-1}$	Measured
k_m	5 x 10^{-3} mol m^{-3}	Haselgrove *et al.* (1993)
D_{medium}	3.0 x 10^{-9} m^2 s^{-1}	Haselgrove *et al.* (1993)
$D_{mesoporous}$	7.9 x 10^{-10} m^2 s^{-1}	Measured

V_{max}: Cellular oxygen consumption rate
k_m: Michaelis-Menten constant defined as the oxygen concentration at half maximal oxygen consumption
D_{medium}: Diffusion coefficient of oxygen through culture medium at 37 °C
$D_{mesoporous}$: Effective diffusion coefficient of oxygen through the mesoporous domain at 37 °C

Table 4.16. Cell density parameters used to determine oxygen concentration profiles for bimodal and trimodal scaffolds for various time points.

Bimodal	**Day**	**Viable cell depth (μm)**	**Cell density (cells m^{-3})**
	1	1000	7.76 x 10^{12}
	3	1000	1.55 x 10^{13}
	5	500	3.18 x 10^{13}
	7	250	6.25 x 10^{13}
Trimodal			
	1	Homogeneous	8.13 x 10^{12}
	3	Homogeneous	1.27 x 10^{13}
	5	500	3.5 x 10^{13}
	7	250	7.1 x 10^{13}

Based on these input parameters, oxygen concentration distributions were predicted for the 3D geometry. The planar plots presented herein represent the oxygen concentration distributions across the longitudinal cross-section of bimodal and trimodal scaffolds as illustrated in Figure 4.46.

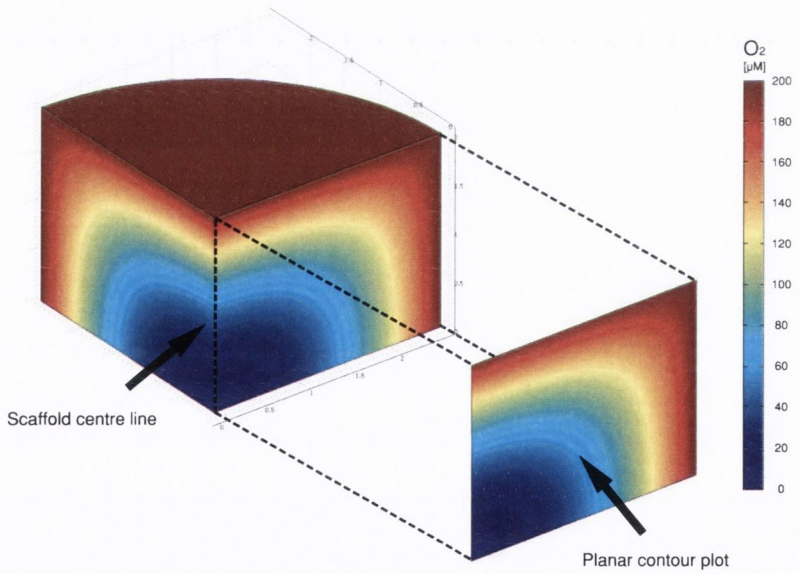

Figure 4.46. Illustration of the 3D scaffold geometry to highlight the longitudinal plane and centre line from which oxygen concentrations were extracted for planar plots.

Planar plots of oxygen concentration distributions for the various time points investigated for bimodal scaffolds are presented in Figures 4.47-4.50 and for trimodal scaffolds in Figures 4.51-4.54. Similarly the oxygen concentration profiles along the centreline of scaffolds at each of these time points is presented in Figure 4.55. Model parameters and cell density distributions are defined in Tables 4.15 and 4.16.

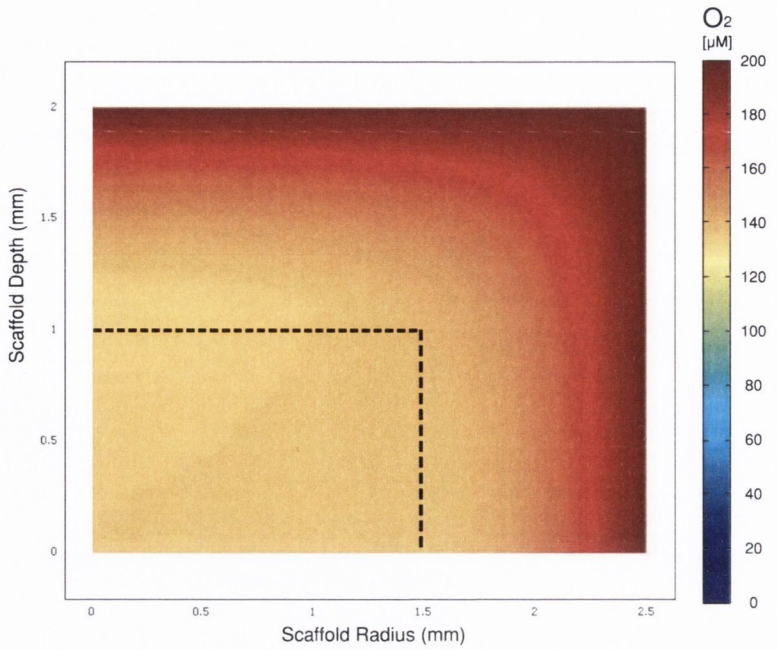

Figure 4.47. Day 1 oxygen concentration distribution for bimodal scaffolds. Experimentally, at this time point viable cells were observed at a depth of 1mm from the fluid-scaffold interface. No cellular activity was therefore modelled within the dashed region.

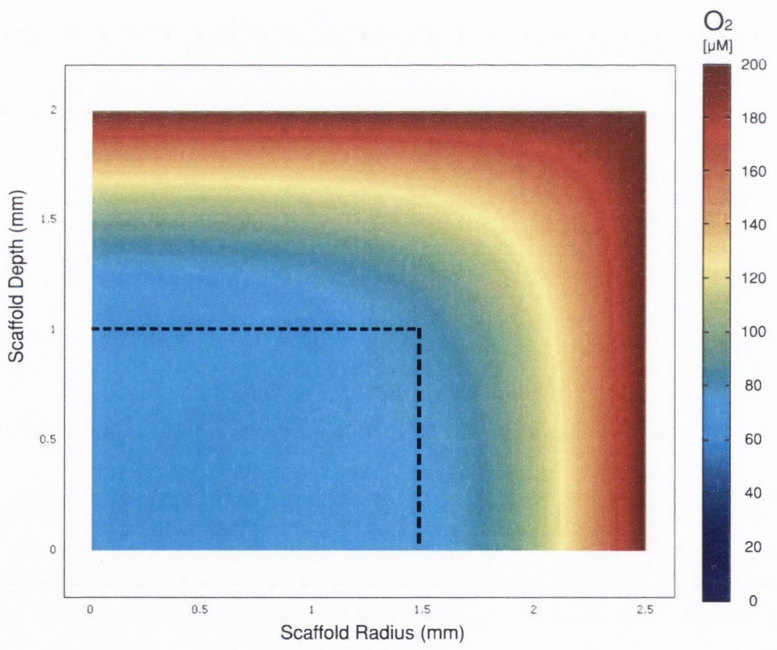

Figure 4.48. Day 3 oxygen concentration distribution for bimodal scaffolds. Experimentally, at this time point viable cells were observed at a depth of 1mm from the fluid-scaffold interface. No cellular activity was therefore modelled within the dashed region.

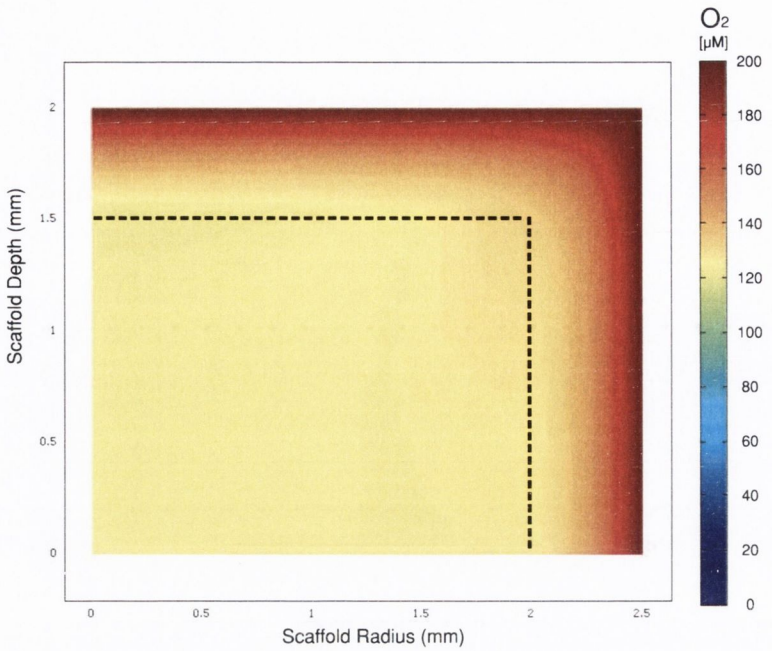

Figure 4.49. Day 5 oxygen concentration distribution for bimodal scaffolds. Experimentally, at this time point viable cells were observed at a depth of 500 μm from the fluid-scaffold interface. No cellular activity was therefore modelled within the dashed region.

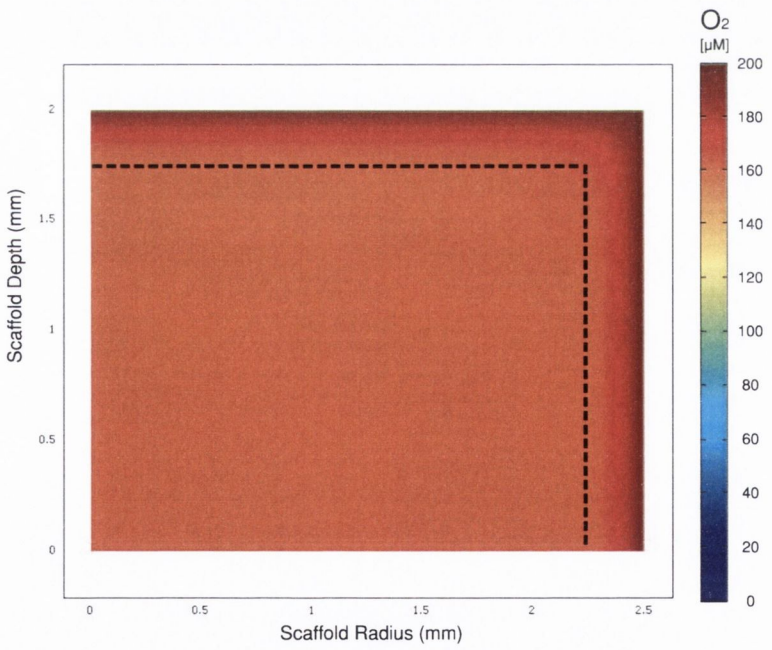

Figure 4.50. Day 7 oxygen concentration distribution for bimodal scaffolds. Experimentally, at this time point viable cells were observed at a depth of 250 μm from the fluid-scaffold interface. No cellular activity was therefore modelled within the dashed region.

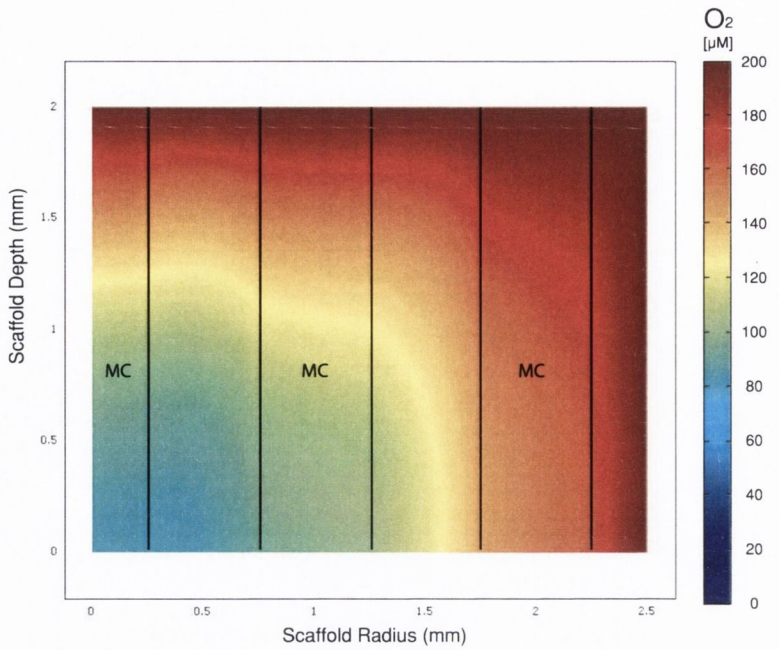

Figure 4.51. Day 1 oxygen concentration distribution for trimodal scaffolds. Experimentally, at this time point viable cells were observed throughout the entire depth of the scaffold. A homogeneous cell distribution was therefore modelled. Solid lines represent the macrochannel (MC) domain.

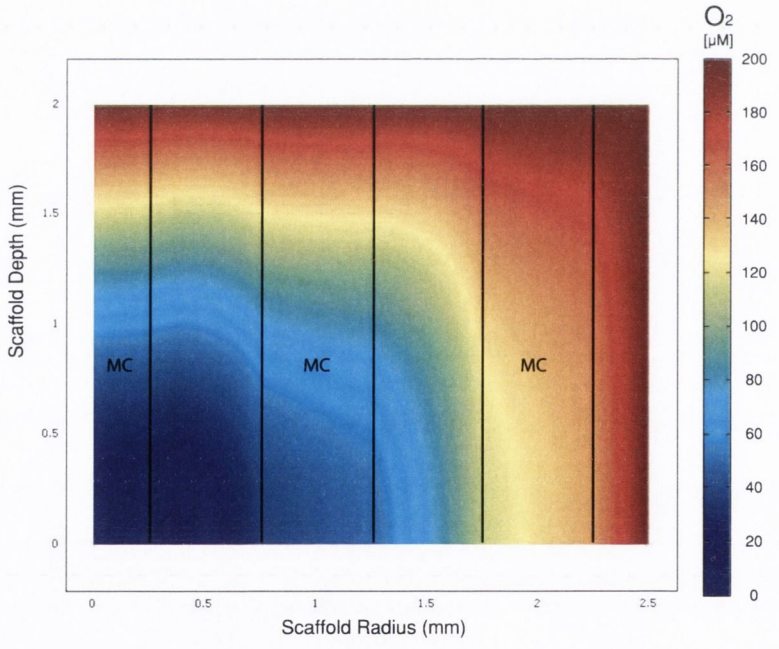

Figure 4.52. Day 3 oxygen concentration distribution for trimodal scaffolds. Experimentally, at this time point viable cells were observed throughout the entire depth of the scaffold. A homogeneous cell distribution was therefore modelled. Solid lines represent the macrochannel (MC) domain.

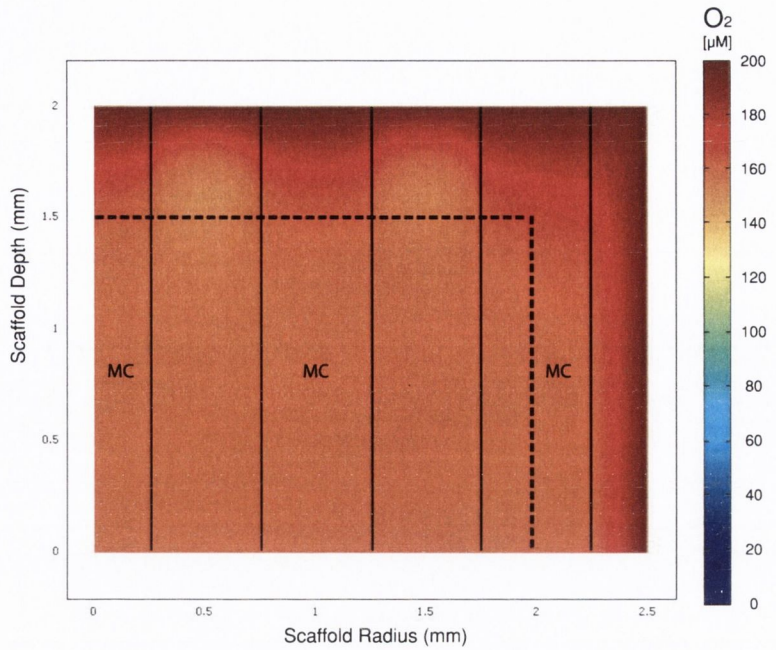

Figure 4.53. Day 5 oxygen concentration distribution for trimodal scaffolds. Experimentally, at this time point viable cells were observed at a depth of 500 μm from the fluid-scaffold interface. No cellular activity was therefore modelled within the dashed region. Solid lines represent the macrochannel (MC) domain.

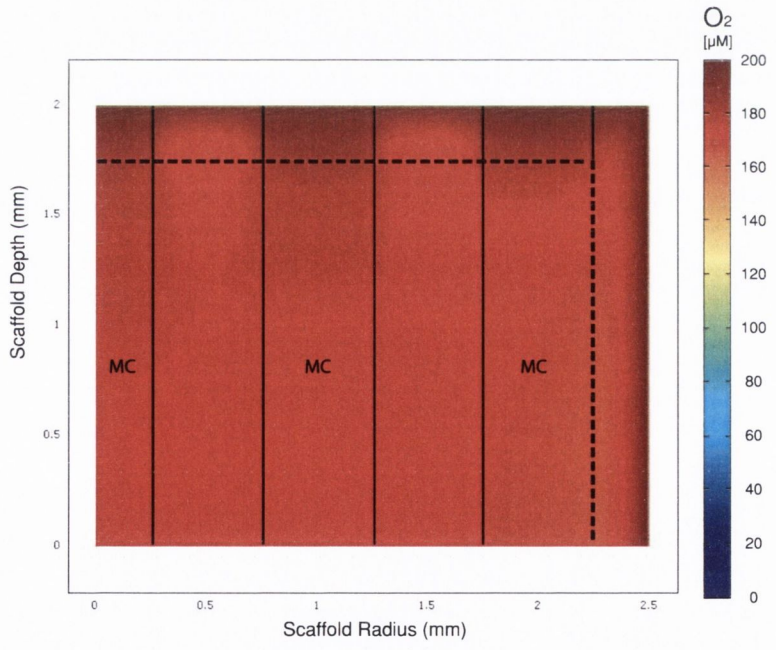

Figure 4.54. Day 7 oxygen concentration distribution for trimodal scaffolds. Experimentally, at this time point viable cells were observed at a depth of 250 μm from the fluid-scaffold interface. No cellular activity was therefore modelled within the dashed region. Solid lines represent the macrochannel (MC) domain.

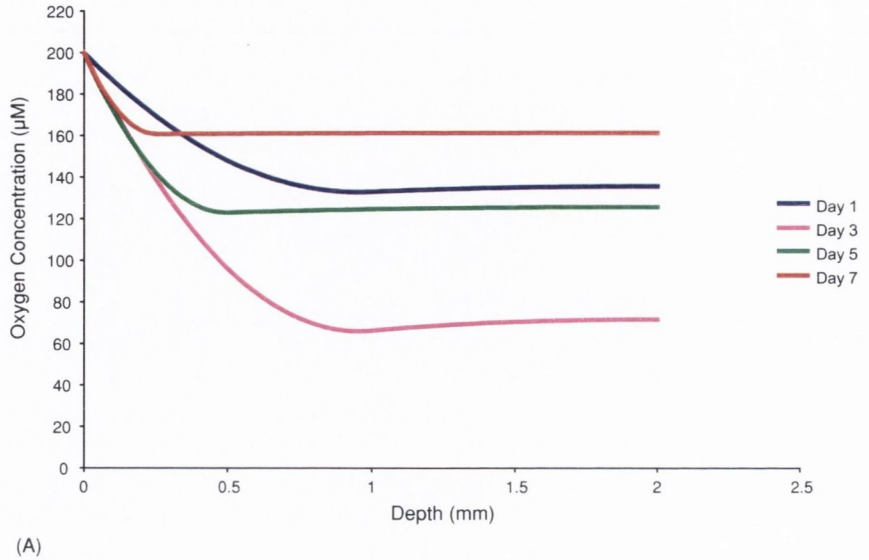

(A)

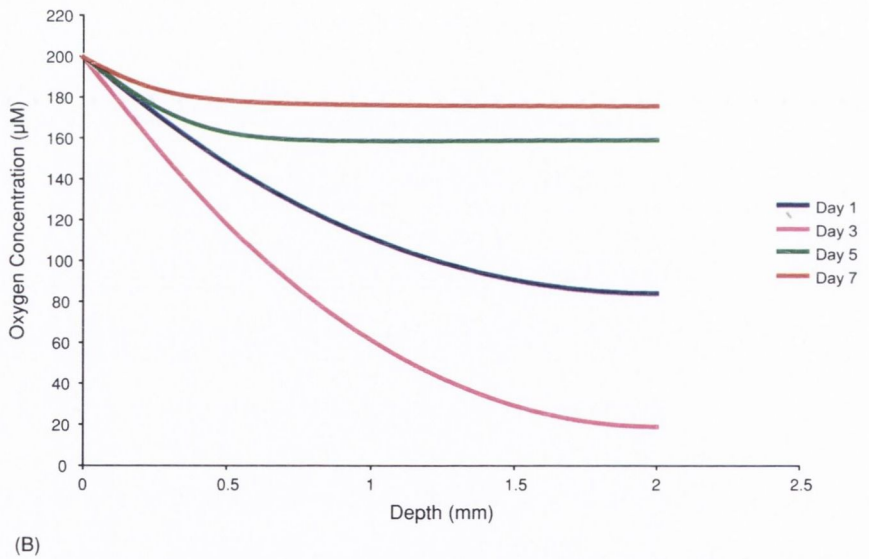

(B)

Figure 4.55. Changes in oxygen concentration along the centre line of scaffold constructs for various time points (1, 3, 5 and 7 days) (A) Bimodal and (B) Trimodal.

For bimodal scaffolds oxygen concentrations were predicted to decrease from $\sim$ 133 μM at day 1 to $\sim$ 66 μM at day 3 as presented in Figure 4.55 A. However from day 3 to day 5, the oxygen concentrations predicted were higher than those predicted on day 3 (123 vs. 66 μM) and approaching those predicted for day 1, yet the viable cell depth was observed to decrease. Similarly for day 7, higher oxygen concentrations were again observed compared to day 5 (161 vs. 123 μM) and represents the highest oxygen concentration predicted by the model. Despite the higher oxygen concentrations predicted, the viable cell depth distribution was observed to decrease with increasing culturing time from $\sim$ 1mm to 250 μm for bimodal scaffolds.

Similarly for trimodal scaffolds (Figure 4.55 B), from day 1 to day 3, a decrease in the oxygen concentration was predicted, with minimums of $\sim$ 84 and 20 μM respectively. Similar to bimodal scaffolds after day 3 there is a reversal in the predicted oxygen concentrations with higher oxygen concentrations of $\sim$ 158 μM predicted for day five. Similarly for the day seven model, higher oxygen concentrations were predicted with a minimum of $\sim$ 176 μM, representing the highest oxygen concentration predicted by the model at any of the time points.

From the oxygen consumption experiments (Section 4.3.8), it was shown that MC3T3-E1 cells remained viable (determined *via* XTT assay) in low oxygen concentration environments of between 24 and 29 μM (Figure 4.43, p 181). Based on these results, low levels of oxygen cannot solely be responsible for the observed necrotic core formation as was observed experimentally in bimodal and trimodal scaffolds. The finite element models predict that similar minimum oxygen concentrations existed in the centre of trimodal scaffolds at day three. For both scaffold types much higher oxygen concentrations were predicted for the other various time points investigated (Figures 4.47 -4.54). The models predict that minimum oxygen concentrations of $\sim$ 66 μM for bimodal and $\sim$ 20 μM for trimodal scaffolds occurred at day three. The retreating viable cell population is more likely to be due to another limiting diffusive molecule such as glucose or possibly a build up of metabolic

waste products within the central regions of the scaffolds resulting in cell necrosis.

Solution convergence was tested by examining the stability of solutions as mesh parameters were varied. No significant changes were observed in the oxygen profile (Figure 4.56) when increasing the mesh size from 35138 to 460812 elements. As can be seen from Figure 4.56 all three solution curves for increasing mesh size are coincident.

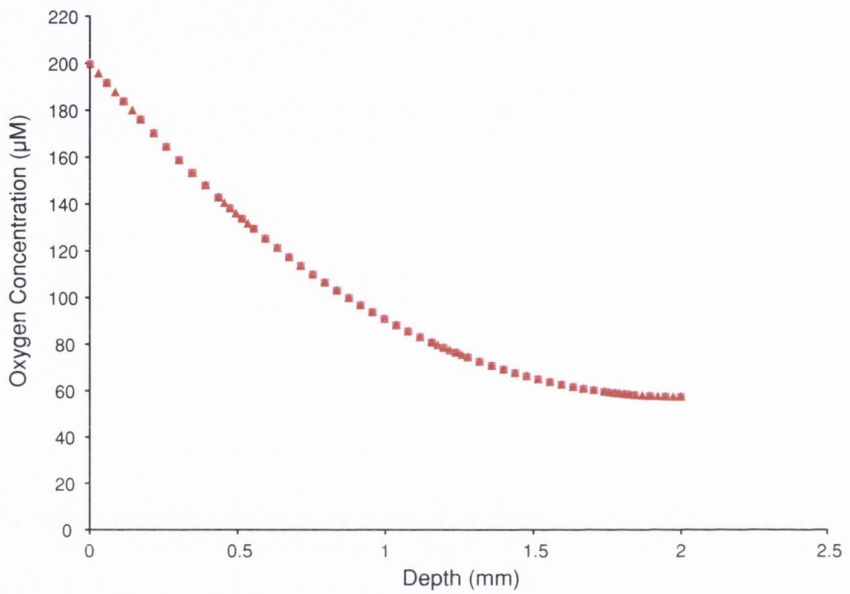

Figure 4.56. Solution convergence test using increasing mesh refinements from 35138 to 460812 elements. Graph represents oxygen concentration change with depth for a homogeneous cell distribution. All three solution curves are coincident.

Figure 4.57 demonstrates the sensitivity of the oxygen concentration results to cell density for both bimodal and trimodal scaffolds. Various homogeneous cell densities ranging from 5 to 9 x 10^{12} [cells m^{-3}] in increments of 1 x 10^{12} [cells m^{-3}] were assessed for both scaffold types. It should be noted that this is an artificial analysis since homogeneous seeding was never achieved for bimodal scaffolds. As can be seen, trimodal scaffolds are capable of maintaining much higher oxygen concentrations compared to bimodal scaffolds for the same given cell density within the mesoporous region. This is an expected observation since the macrochannels were incorporated in order to provide a direct path for diffusion to occur. For a

cell density of 9 x 10^{12} [cells m^{-3}], the minimum oxygen concentration calculated for bimodal scaffolds at a depth of 2 mm is $\sim$ 8 μM, compared to $\sim$ 95 μM for trimodal scaffolds. It can also be seen that bimodal scaffolds are more sensitive to changing cell densities with larger variations existing in the oxygen concentrations between the maximum and minimum cell densities assessed. For bimodal scaffolds at a depth of 2 mm this difference in concentration is $\sim$ 85 μM compared to $\sim$ 46.8 μM for trimodal scaffolds.

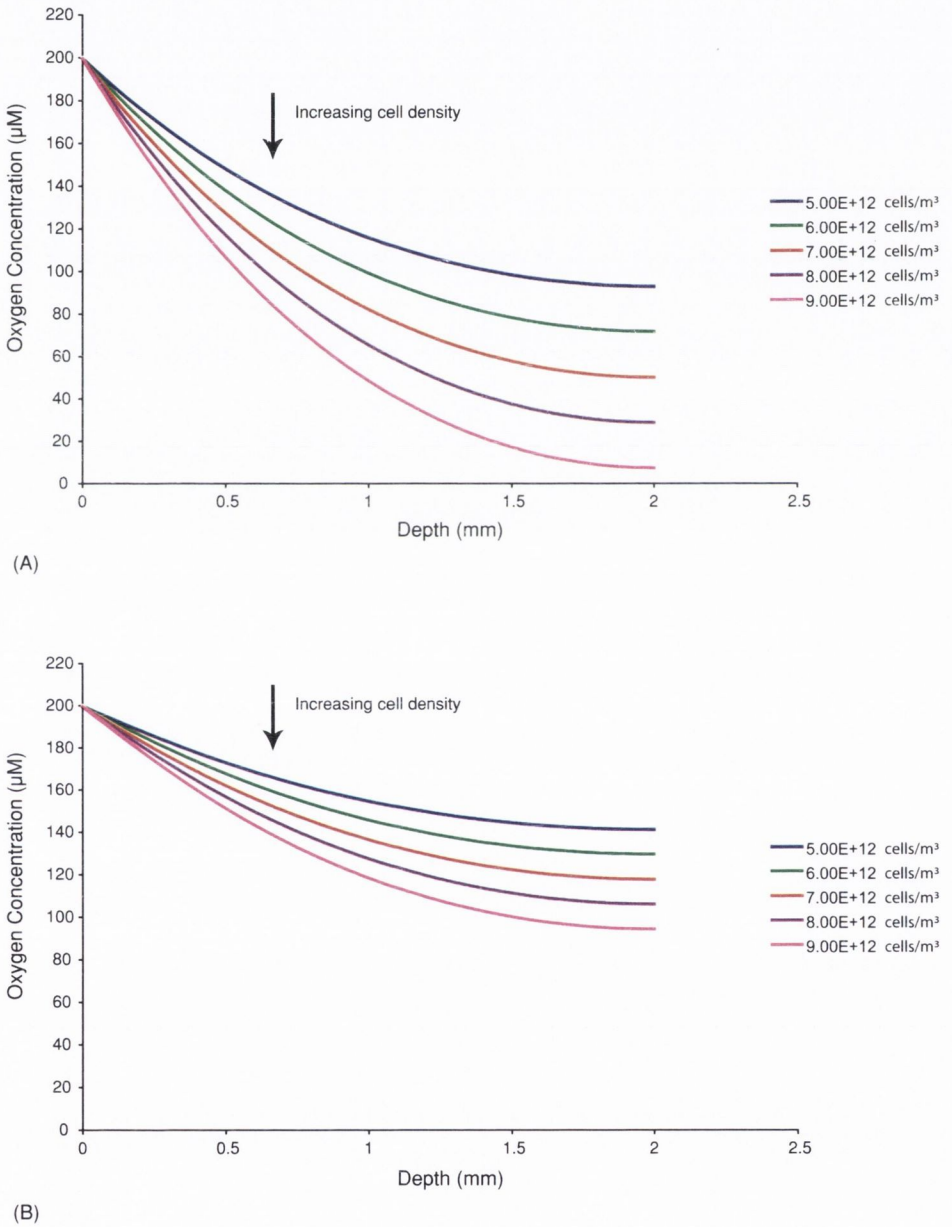

Figure 4.57. Cell density sensitivity analysis for (A) Bimodal and (B) Trimodal scaffolds.

4.4.1 Summary

The function of the finite element models were to assess if oxygen was a limiting factor during static culturing conditions for bimodal and trimodal scaffolds, and to assess if oxygen alone could be responsible for the formation of a necrotic core as observed experimentally. The models were also used to demonstrate the effectiveness of incorporating macrochannels to increase the core oxygen concentration. It was shown that the presence of macrochannels had a positive influence in minimising the concentration gradients compared to bimodal scaffolds for the same cell density distributions.

Even with the presence of high density distribution of cells in the outermost periphery, the results from the numerical models cannot fully explain the lack of cell viability within the central regions of the scaffold constructs. Sufficiently high concentrations of oxygen were shown to exist beyond the depth of the viable cell layers. Based on this evidence it is proposed that oxygen alone cannot be solely responsible for the formation of a necrotic core, which leads to the possibility that secondary diffusive molecules such as either glucose or lactic acid (metabolic waste products) are responsible for the limited cell depth viability as observed experimentally.

It is therefore feasible to propose that regardless of the scaffold architecture (*i.e.* bimodal or trimodal), diffusion based culturing will lead to the formation of a necrotic core, and that oxygen alone cannot be responsible for this effect.

Chapter 5

Discussion

Contents

5.1 Introduction 200

5.2 Scaffold fabrication and architecture 201

5.3 Permeability of scaffolds 205

5.4 Diffusion coefficients 208

5.5 Mechanical properties 210

5.6 Cell seeding 212

5.7 Dynamic vs. static culturing 216

5.8 Finite element modelling of *in vitro* oxygen concentration profiles 218

5.1 Introduction

The impetus of this work was to advance the fundamental work in bone tissue engineering and accelerate the development of scaffolds for *in vivo* applications. Many of the current strategies involve the implantation of seeded scaffold constructs that may have been cultured *in vitro* either statically or with the assistance of a bioreactor for a period of time. As has been observed by many researchers, a recurring limitation of bone tissue scaffolds is that bone has been shown to form only in the outer 300 μm - 500 μm region of scaffolds resulting in the formation of a necrotic core with limited cell viability. This is primarily believed to be due to the lack of nutrient delivery into and waste removal from the inner regions of the scaffold construct (Ishaug-Riley *et al.*, 1998). Many of the commercially available bone substitute products mimic the natural architecture of cancellous bone which is hypothesised to be optimal for the formation of new tissue when implanted *in vivo*. However, bone can be considered as an initially random porous structure that has been remodelled throughout an individual's life in response to *in vivo* stimuli. It's architecture is in effect an end result of the *in vivo* remodelling process. Therefore, it may not necessarily provide a suitable architecture in terms of cell seeding and maintaining uniform nutrient concentrations throughout the scaffold. Other strategies have included the fabrication of scaffolds with a single porous domain created through a wide variety of techniques including particulate leaching, gas foaming, fiber bonding, freeze drying, foam-gel and more recently solid free-form fabrication. From a biomaterials viewpoint, many researchers have focused on the physical characteristics of scaffolds such as porosity, pore size, interconnectivity and mechanical properties. Currently a lack of knowledge exists on the optimal approach for the conditioning of scaffolds prior to *in vivo* implantation such as initial cell seeding and subsequent short term *in vitro* culture.

This work includes the development of a novel porous HA scaffold architecture for bone tissue engineering applications. Experimental investigations focused on physical scaffold characteristics which are likely to influence initial cell seeding distribution and subsequent cellular viability during short-term *in vitro* culturing. It

was hypothesised that this could be best achieved through the development of a multi-domain porous scaffold (*i.e.* a scaffold providing a discrete domain for cell occupancy and a separate domain for nutrient delivery) with the specific objectives to embody in one scaffold the structures required to optimise cell seeding, cell proliferation and migration and potentially to facilitate vascularisation once implanted *in vivo*.

5.2 Scaffold fabrication and architecture

As presented herein (Sections 2.5.4 and 2.10.3), there is sufficient evidence from the literature to support the advancement of fabricating multi-domain porous scaffolds. Traditional scaffold fabrication techniques (Section 2.6) and more recently solid free form fabrication (SFF) (Section 2.7) have been used to develop many scaffolds of varying complex architectures with the sole purpose of providing a porous body with typical porosities ranging from 40-90 %. This work explored the potential use of some of these techniques including particulate leaching (Section 3.2.7), SLS rapid prototyping (Section 3.3.3), foam gel method (Section 3.3.4) and the freeze-drying technique (Section 3.3.5) to create porous scaffold structures. For the purpose of this work the aforementioned techniques, with the exception of the freeze-drying technique, proved to be limited in developing a multi-domain porous architecture scaffold with physically relevant structural characteristics such as macrochannel diameter and spacing.

Attempts to introduce an array of macrochannels into structures produced through either particulate leaching or the foam gel method, proved difficult in terms of maintaining structural integrity. This is possibly due to the use of a macrochannel spacing of 500 μm which provided insufficient material between adjacent macrochannels to maintain structural integrity since the pore sizes of the mesoporous phase were in the 200-400 μm range. This limitation did not exist when the freeze-drying technique was employed due to the fine mesoporous architecture produced. Although the macrochannel diameter and spacing can be altered during the fabrication pro-

cess, a diameter and spacing of 500 μm was chosen based on the findings of several researchers (Section 3.5.6) showing that greater bone formation was observed in implants containing channels approximately equal to this dimension. For these reasons, preliminary work utilising particulate leaching and foam-gel were abandoned in favour of adopting the freeze-drying technique in conjunction with CNC machining macrochannels for producing scaffolds.

As was observed through SEM imaging, the introduction of macrochannels through CNC machining has not disrupted the mesoporous domain phase at the surface of the channel and thus the mesopores have not become occluded (Figures 4.8 and 4.9). This is due to the presence of the wax infiltrate and the cutting of material as opposed to piercing of the material. Introduction of macrochannels via the insertion of needles (piercing) resulted in the disruption and thus occlusion of the mesoporous domain as was shown in Figure 4.10.

The total apparent porosity (densimetric measurements) of trimodal scaffolds was calculated to be 85.1 % (SE=$\pm$ 0.22, n=11), and the effective porosity determined from water immersion studies was 80.8 % (SE=$\pm$ 0.66, n=11). This implies that trimodal scaffolds contained approximately 4.24 % (SE=$\pm$ 0.58, n=11) closed porosity. The percentage of unidirectional macrochannels was calculated to be approximately 28 % of the total scaffold volume. The presence of macrochannels had only a minor influence ($\sim$ 4.5 %) in increasing the total porosity of trimodal scaffolds compared to bimodal scaffolds (Table 4.4).

The purpose of providing macrochannels within a porous scaffold is three-fold. Firstly they aid in the initial seeding distribution of cells throughout the depth of the scaffold. Secondly they provide the most direct diffusion route to the interior of the scaffold to provide sufficient oxygen and nutrients to the proliferating cells which can migrate into the mesoporous phase. Thirdly, they provide sufficient open porosity to permit vascularisation of the macrochannels once implanted *in vivo*. Further development of multi-domain porous scaffolds may benefit from the advances in solid free-form technologies (SFF) in the future, allowing greater flexibility and

higher spatial resolution.

This work has demonstrated that it is possible to produce a highly interconnected mesoporous structure using the freeze-drying technique. The primary focus of employing this technique was to enable the fabrication of a multi-domain porous scaffold when coupled with the introduction of macrochannels through CNC machining. However precise control over the architecture of the mesoporous phase was not achieved. As was observed from SEM imaging and image analysis, various pore shapes consisting of either an elongated or partially spherical morphology were produced. However these different pore shapes were not found to be localised or concentrated in specific regions and did not appear to vary throughout the scaffold depth. There also did not appear to be a bias in the preferred orientation of pores between the longitudinal and transverse direction (Figures 4.14 and 4.15), indicating that the formation and growth of ice crystals during the freezing cycle was not purely unidirectional. The variation in pore-morphology is possibly due to inhomogeneous cooling producing temperature gradients within the slurry during the cooling and subsequent freezing cycle. O'Brien *et al.* (2004) showed that through controlling the rate of freezing a more homogeneous pore architecture of collagen-glycosaminoglycan (CG) scaffolds could be produced. O'Brien *et al.* (2005) also showed that the pore size of freeze dried structures can also be controlled by the final freezing temperature, with a lower temperature producing pores with a smaller mean pore diameter. Koch *et al.* (2003) showed that the pore size of porous alumina ceramics produced through freeze-drying increases strongly with decreasing cooling rates. Although this work used the same constant cooling regime as O'Brien *et al.* (2004) with a final freezing temperature of -40 °C, homogenous spherical-type pores could not be obtained. A final freezing temperature of -10 °C was also investigated but similar variations in pore morphology were observed. This variation in pore morphology is most likely due to different thermal properties and thus freezing kinetics of a HA suspension compared to a CG slurry as used by O'Brien *et al.* (2004). Fabrication optimisation in this regard was not within the scope of this present investigation and necessitates

further work in order to produce a porous structure with a more homogenous pore morphology. A negative aspect of the freeze-drying technique which was observed in this work and similarly by other researchers (Koch *et al.*, 2003; Deville *et al.*, 2006) is the formation of a dense layer on the surface of the structure. This denser layer formation was observed to occur on the bottom surface of the green-body discs which were in contact with the cooling shelf and is possibly due to undercooling of the suspension or settling of HA particles prior to actual formation of ice crystals. When using ceramic materials this dense layer is easily removed either pre- (wax embedded samples) or post- sintering. However, other researchers have shown that a similar dense layer is formed using different materials such as collagen mixtures, which may not be as easily removed and therefore may influence important characteristics such as cell seeding penetration, nutrient diffusion and permeability (Yeong *et al.*, 2004; Waller, 2004).

As presented in Section 4.2.2, the pore architecture of the mesoporous domain was analysed from high magnification sections (x 10) of embedded samples using a custom developed linear intercept macro (included in Appendix D) written for Scion Image image analysis software (Scion Corp., Frederick, MD). The macro determines the pixel length of each pore that is bisected, when a series of parallel lines (both horizontal and vertical directions), drawn onto an image intercepts a pore wall (black pixel).

Using this procedure the mean intercept length of scaffolds was determined to be 53 μm (SE=$\pm$ 0.74, n=18). However, as was demonstrated from frequency distribution graphs (Figures 4.19 and 4.20), the true pore size (or maximally bisected pores) was possibly closer to $\sim$ 100 μm, up to 200 μm. The linear intercept method of measurement may not be the most accurate form of measurement of pore sizes, since the pore intercept lengths measured may not in every case bisect the maximum diameter of a pore being measured, thus reducing the overall mean pore length. Pore diameters ($\sim$ 100-200 μm), would be more comparable to the pores observed in the scanning electron micrographs (SEM's) (Section 4.2.1).

The total apparent porosity of bimodal scaffolds was calculated to be 80.5 % (SE=± 0.18, n=11), and the effective porosity determined from water immersion studies was 76.1 % (SE=± 0.66, n=11), implying that bimodal scaffolds contained approximately 4.3 % (SE=± 0.59, n=11) closed porosity.

As was observed through SEM imaging (Figures 4.5, 4.6 and 4.7), the mesoporous structure contained a degree of microporosity whose pores were approximately 2 - 5 μm in diameter. The average porosity of the mesoporous phase calculated from the ratio of white (pores) versus black (HA material) pixels from the images used in Section 4.2.2 and was found to be 58 % (SE=± 0.38, n=90). Through subtraction from the total effective porosity, an open microporous void fraction of approximately 18 % for bimodal scaffolds ($\sim$ 12.5 % for trimodal) was estimated. This is a significant amount of porosity to be present and further work is required to investigate the reduction or elimination of this porosity through modification of the sintering regime.

5.3 Permeability of scaffolds

Permeability of tissue engineering scaffolds has long since been regarded as an important physical property of scaffolds. Permeability measurements of many porous scaffold materials have been conducted, with the general consensus that a more permeable scaffold construct is more beneficial in terms of enhancing nutrient delivery and metabolic waste removal during *in vitro* culturing with the ultimate aim of facilitating vascularisation post *in vivo* implantation.

From the literature a wide range of permeability values have been obtained for many different scaffold types. The most common unit employed in describing permeability is κ which is the fluid conductance normalised by the geometric and fluid properties and is normally expressed in units of (m^2). Many researchers also report experimental data in terms of fluid mobility K (m^4/Ns) which is defined as the material permeability normalised by the viscosity of the fluid μ (Pas) (O'Brien *et al.*, 2007). Most experiments employ water as the permeating fluid with the

viscosity of water being $\sim$ 0.001 Pas. Therefore in order to easily equate these similar quantities, the fluid mobility (K) is equivalent to permeability (κ) x 10^{-3}.

The fluid conductance of bimodal scaffolds was found to be 7.32 x 10^{-11} $m^3s^{-1}Pa^{-1}$, which was approximately sixteen times lower than that of trimodal scaffolds (1.18 x 10^{-9} $m^3s^{-1}Pa^{-1}$) and approximately eight times lower than that of cancellous bone (5.77 x 10^{-10} $m^3s^{-1}Pa^{-1}$). Trimodal scaffolds exhibited a significantly higher fluid conductance (Figure 4.22) than any of the other sample types, which was found to be statistically significant ($p < 0.001$). This finding demonstrates that the primary path of fluid flow is through the macrochannels which provide a path of least resistance.

Hui *et al.* (1996) observed that the fluid conductance of cylindrical trabecular bone grafts was found to be the best predictor of their clinical success as scaffolds in the rabbit tibial diaphysis. The authors observed that the graft-host union was not affected by the effect of the length, porosity or orientation of the graft alone, but rather by their simultaneous effects expressed as conductance. A threshold conductance was found to be approximately 1.5 x 10^{-10} $m^3s^{-1}Pa^{-1}$. Compared to the conductivity results obtained in this work, bimodal scaffolds with a conductivity value of 7.32 x 10^{-11} $m^3s^{-1}Pa^{-1}$ (SE=$\pm$ 2.92 x 10^{-12}, n=12), would be below (factor of 2) this critical threshold conductance.

In this work, the permeability of the bimodal scaffolds was calculated to be 9.72 x 10^{-12} m^2 (SE=$\pm$ 3.64 x 10^{-13}, n=12) compared to a value of 1.71 x 10^{-10} m^2 (SE=$\pm$ 6.18 x 10^{-12}, n=11) for trimodal scaffolds. The permeability of trimodal scaffolds was therefore approximately 18 times greater than that of bimodal scaffolds. This expected increase in permeability is due the presence of the macrochannels which provide a path of least resistance to the flow of the perfusing fluid. The permeability of cancellous bone samples, 1.78 x 10^{-10} m^2 (SE=$\pm$ 1.86 x 10^{-11}, n=13), was well within the range reported by other researchers (Nauman *et al.*, 1999).

Compared to fluid conductance, when the results are expressed in terms of permeability, a significant reduction in the difference between trimodal scaffolds and

cancellous bone specimens was observed. Statistically, no significant difference was found to exist between trimodal scaffolds and cancellous bone samples ($p = 0.3740$).

Although the permeability of bimodal scaffolds was significantly lower (two to three orders of magnitude) than all the other sample types developed in this work, it was found to be similar to other scaffold types that have been used by other researchers (Agrawal *et al.*, 2000; Radisic *et al.*, 2005).

Radisic *et al.* (2005) evaluated the permeability of porous poly(glycerol-sebacate) scaffold fabricated by means of the particulate salt leaching technique and obtained a value of $8.1 \pm 0.4 \times 10^{-12}\ m^2$. This value of permeability, which is approximately three orders of magnitude lower than that of cancellous bone is similar to the values obtained in this study for bimodal scaffolds.

In another study by Li *et al.* (2003), the permeabilities of various ceramic porous structures including commercially available scaffolds, bone and coral were measured. These porous structures of varying porosity (50-80%) had a range of permeabilities between 0.03 and $0.53 \times 10^{-9}\ m^2$.

Agrawal *et al.* (2000) determined the permeability for PLGA scaffolds (50:50) fabricated through particulate salt leaching ranged from 2.1 to $16.1 \times 10^{-12}\ m^2$.

O'Brien *et al.* (2007) measured the permeability of collagen-glycosaminoglycan (CG) scaffolds (dry porosity of 99.5 %) of varying pore sizes controlled through the fabrication process. Values of fluid mobility ranged from 0.660 to 1.387×10^{-10} (m^4/Ns) for scaffolds with pore sizes of 96 and 151 μm respectively. Assuming the viscosity of the permeating fluid to be 0.001 Pas and converting to permeability (m^2) these values range from 0.660-1.387 $10^{-13}\ m^2$, which is approximately three orders of magnitude less than the permeability of trimodal scaffolds and cancellous bone, and two orders of magnitude less than bimodal scaffolds.

The results of this work supports the hypotheses that multi-domain architectures enhance both fluid conductance and permeability compared to single random porous domain structures by providing a path of least resistance for fluid flow. From an *in vivo* perspective, the presence of unidirectional macrochannels would also provide

a path of least resistance, thereby providing an effective route to facilitate *in vivo* vascularisation and promoting the ingrowth and formation of new tissue.

5.4 Diffusion coefficients

Many researchers fail to measure or take account of the tortuosity of a scaffold architecture, and thus over estimate the true effective oxygen diffusion coefficients (D_{eff}) being investigated. Of significant interest in this work was the determination of the effective oxygen diffusion coefficients of the bimodal (meso- and micro-) pore domains (effective porosity of $\sim$ 76 %). This was found to be equal to 7.9 x 10^{-10} m^2s^{-1} (SE=$\pm$ 5.3 x 10^{-11}, n=8). This value is approximately 26 % ($\pm$ 1.8 %) of that of water at 37 °C. Malda *et al.* (2004a) estimated the effective diffusion coefficient through polyethylene glycol terephthalate/polybutylene terephthalate (PEGT/PBT) polymer scaffold (80 % porosity) fabricated through a compression moulding and salt leaching method as being 3.8 x 10^{-10} m^2s^{-1} which is approximately 13 % of the diffusion coefficient through water at 37 °C. This diffusion coefficient appears to be low for an 80 % porous scaffold and would possibly indicate a scaffold which has poor interconnectivity or high pore tortuosity.

The effective diffusion coefficient (assuming complete interconnectivity) through a porous body is directly proportional to porosity and inversely proportional to tortuosity (Cussler, 1997). Tortuosity values for porous structures typically range from 2-6, averaging about three (Cussler, 1997). For bimodal scaffolds, the tortuosity can be calculated from the measured effective diffusion coefficient and known porosity, and is estimated to be approximately 2.9. Moreira and Coury (2004) measured the tortuosity of SiC-Al_2O_3 ceramic foams fabricated through the polyurethane foam reticulate method. It was found that for a foam with a pore size of 360 μm and porosity of 76 % the tortuosity was 1.84 and decreased to 1.6 for foams with pore diameters of 2.3 mm and 94 % porosity. Based on these values it is clear that the tortuosity of a porous body does not change significantly with increasing porosity and therefore has a negligible influence on the effective oxygen diffusion coefficient

through a porous structure. Most scaffold structures have porosities ranging from 60 to 90+ %. Therefore it is probable that the maximum effective diffusion coefficient of oxygen through a porous scaffold structure will never exceed $\sim$ 60 % (assuming a tortuosity value of 1.6 and porosity of 95 %) of that of water at 37 °C. This presents a significant challenge in maintaining nutrient- and minimising metabolic waste- concentrations with increasing depth away from the scaffold surface. Since the effective diffusion coefficient is more sensitive to the tortuosity term, future scaffold developments should focus on minimising structural tortuosity and maximising interconnectivity rather than porosity in order to enhance the effective diffusion coefficients of species. From literature, the diffusion coefficients of glucose and lactate through water at 37 °C are 0.92 x 10^{-9} m^2s^{-1} (Torzilli *et al.*, 1987) and 1.4 x 10^{-9} m^2s^{-1} (Holm *et al.*, 1981) respectively. Assuming no molecular influences, the relative effective diffusion coefficients of both glucose and lactate can be inferred through the relationship of porosity and tortuosity. Based on this relationship the effective diffusion coefficients of glucose through the mesoporous domain can be estimated to be approximately 2.4 x 10^{-10} m^2s^{-1} and 3.6 x 10^{-10} m^2s^{-1} for lactate.

As was discussed previously, polymer scaffolds fabricated through the particulate salt leaching technique produced scaffolds with a less porous surface layer (Figure 3.9, p 86). This dense layer was also evident when fabricating HA scaffolds using the freeze-drying and foam-gel techniques. This dense layer was removed from bimodal scaffolds prior to experimental measurements. Other researchers (Waller, 2004; Deville *et al.*, 2006) have also observed thin films to be present on scaffold structures and it may be hypothesised that the presence of these films on the surfaces of scaffolds in conjunction with limited pore interconnectivity may also have a negative impact on the effective diffusion coefficients unless they are removed. The presence of proliferating cells on the surfaces of these scaffolds may also inevitably produce an impeding barrier, thereby reducing the effective diffusion coefficient further and inhibit subsequent *in vivo* vascularisation post implantation. Developing a

porous scaffold architecture containing macrochannels of sufficient diameter to prevent cell occlusion (within the mesoporous domain) from developing is most likely to overcome this barrier formation.

5.5 Mechanical properties

Ceramics have been widely used due to their high biocompatibility and resemblance to the natural inorganic component of bone and teeth (Chang *et al.*, 2000; Chu *et al.*, 2002). However, despite their favourable biological properties the inherent brittleness of porous ceramics resulting in low strength and toughness severely limit their use for clinical applications.

The compressive strength (MPa) and strain to failure (%) of bimodal, trimodal and cancellous bone samples was presented in Section 4.2.6. In this work the compressive strengths for trimodal scaffolds was found to be 1.53 MPa (SE=± 0.13, n=10), 1.12 MPa (SE=± 0.07, n=10) for bimodal scaffolds and 0.76 MPa (SE=± 0.18, n=10) for cancellous bone.

The failure mode for the bimodal and trimodal scaffolds tested appeared to be through a series of micro-failures occurring within the struts of the scaffold material (Figure 4.24). These micro-failures resulted in densification occurring at the surfaces of the specimens until such time as crushing/compaction was no longer sustainable leading to complete destruction of the samples. Conversely cancellous bone samples did not fail in the same fashion but increased to a maximum with an almost elastic response and then rapidly dropped after this point.

A statistical difference ($p < 0.05$) between the compressive strength of bimodal and trimodal scaffolds was found to exist, with trimodal scaffolds exhibiting greater compressive strengths. This difference is perhaps due to the modes in which ultimate compressive strength is achieved. Trimodal scaffolds contain large pores (*i.e.* macrochannels) that can accommodate greater densification. Due to the inherent difficulties associated with achieving complete compaction of very small pores, the presence of macrochannels allow for greater densification thereby producing higher

ultimate compressive strengths for trimodal scaffolds.

Although failure of both bimodal and trimodal scaffolds occurs from the onset of loading, the ability for these scaffolds to continue to deform up to approximately 15-20 % strain without ultimate failure occurring may prove beneficial in a clinical setting when cutting and manipulating the scaffold shape/size to suit a non load-bearing defect site.

From a scaffold design perspective it is favourable to have a high degree of porosity to provide an available volume for new matrix deposition and nutrient delivery and allow full ingrowth of new tissue greater. However, as the porosity of a porous ceramic scaffold increases the overall mechanical properties decrease exponentially (Liu, 1997). Due to the low compressive strengths and brittle nature of both bimodal and trimodal scaffolds observed in this work, it is highly unlikely that they would be suitable candidates for load-bearing applications. For development of scaffolds for load bearing applications the relationship of compressive strength with porosity warrants further investigation.

For non-load bearing applications the mechanical properties of scaffolds are not necessarily critical. They relate solely to the clinical requirements of the surgeon to allow manipulation and shaping of the scaffold of the scaffold to appropriately match the geometry of the defect site. This is typically done with a scalpel which requires either a low strength or low fracture toughness. This makes both bimodal and trimodal scaffolds ideal candidates for such purposes. The primary function of a scaffold during the early stages post-implantation is to ensure seeded cells remain viable and to facilitate vascularisation. For low strength porous scaffolds it may be necessary to employ external fixators or mesh cages to support the defect site.

Development of scaffolds for bone tissue engineering with sufficient mechanical properties presents many challenges and poses difficulties with respect to design criteria. The two competing criteria of developing a mechanically suitable yet highly porous scaffold is difficult to achieve. Compromises are therefore necessary and must be made in the design and fabrication processes. This may inevitably lead to the

production of scaffolds for different functional uses, *i.e.* load- and non load- bearing scaffold constructs for bone tissue engineering purposes.

5.6 Cell seeding

The primary focus with respect to the cell seeding investigations was to develop upon the widely employed static seeding method. This technique is often associated with low seeding efficiencies and non-uniform cell distributions within scaffolds, which is partially due to the manual- and operator-dependent nature of the process (Wendt *et al.*, 2005).

A study to gain an appreciation and assess the time-dependent nature of cell attachment to flat HA substrates was carried out. As presented in Figure 4.29 it was observed that MC3T3-E1 cells attached to HA substrates in an increasing time-dependent manner, from a minimum of 46.6 % (SE=$\pm$ 2.6, n =5) after 5 mins increasing to a maximum of 75.7 % (SE=$\pm$ 2.7, n =5) after 60 mins, with a plateau existing for subsequent time points 90, 120 and 180 min. Of significant interest is the short duration (1 hour) that was required for relatively high cell attachment to occur. With respect to seeding of three-dimensional scaffolds, this observation indicates that the time-frame to adopt secondary procedures (*e.g.* dynamic rotation or perfusion) in order to influence cell distribution or percentage attachment of cells is limited. Similar observations were made by Stephan *et al.* (1999) when seeding anorganic bovine matrix with primary culture neonatal rat osteoblastic cells with an increasing trend in cell attachment up to 90 minutes post-seeding.

Similar studies were also carried out to assess if a similar time-dependent trend existed when statically seeding three-dimensional bimodal scaffolds. It was observed that the number of cells within scaffold constructs remained constant ($\sim$ 80 %, Table 4.12) and no statistical difference ($p < 0.05$) was found between any of the groups for any of the time points investigated (30, 60, 120 and 180 mins). However, it should be noted that this data does not necessarily imply that cell adhesion has been attained after 30 minutes. It is more likely that cells occupying the pores could not be removed

through washing. Reflecting on the data obtained from the 2D cell attachment study, it is possible that maximum cell attachment would take a minimum of 1 hour to occur. This observation could prove useful from a clinical perspective to reduce the time required for cell seeding of constructs prior to immediate *in vivo* implantation.

For seeding of three-dimensional scaffolds it was hypothesised that the cell seeding inefficiencies commonly observed are related to the volume of cell suspension being delivered to the scaffold, with higher seeding volumes producing lower seeding efficiencies. As presented in Figure 4.32 and Table 4.13, this hypothesis was confirmed by experiments which showed there was a decreasing trend in the number of cells within scaffolds with increasing volume of cell suspension delivered from a maximum of 85.4 % (SE=$\pm$ 4.9, n =4) for a seeding volume of 25 μL decreasing to 67.7 % (SE=$\pm$ 2.2, n =4) for 50 μL and 43.8 % (SE=$\pm$ 3.2, n =4) for 100 μL. Once a scaffold becomes saturated with cell suspension, it is likely that any remaining cells in the fluid above the scaffold surface may only rely on gravity to become exposed to the scaffold material and attach, which possibly explains the decreasing efficiency trend observed.

The data obtained may also explain the large variations in cell seeding efficiency data observed in the literature. Furthermore, it is probable that the remainder of cells relying on gravity to become attached may promote inhomogeneous cell distributions, with a larger number of cells attaching to the peripheral surface of the scaffold.

Although lower seeding volumes were found to yield in higher seeding efficiencies, limited cell penetration was found to exist thus producing poor cell distributions, with the majority of cells being confined to the top surface of the scaffolds as was shown in Figure 4.33. Based on this work, when seeding three-dimensional porous scaffolds, appropriately matching the seeding volume to the saturation capacity of the scaffold is the most optimum approach in terms of promoting homogeneous cell seeding while maintaining relatively high seeding efficiencies ($\sim$ 70 %). This work has also shown that high seeding efficiencies alone may not be the best measurable

outcome for evaluation purposes and should only be used in conjunction with initial cellular distributions.

Experiments showed that the cell seeding efficiency of bimodal scaffolds was greater than those observed for trimodal scaffolds ($\sim$ 85 vs. 70 %). As depicted in Figure 4.34, this was believed to be due to the presence and the orientation of the macrochannels during seeding, limiting the number of cells being exposed and thereby attaching to the mesoporous phase. Therefore a rotational seeding technique was investigated to assess if the seeding efficiency of trimodal scaffolds could be enhanced. It was shown that the percentage cell attachment of trimodal scaffolds could not be enhanced by the adoption of a rotational seeding technique. Results showed (Figure 4.36) that there was a decreasing trend in the seeding efficiency from normal static seeding (no rotation), 72.3 % (SE=$\pm$ 1.6, n =6), to horizontal (no rotation), 64.1 % (SE=$\pm$ 2.4, n =6), to horizontal rotation 56.3 % (SE=$\pm$ 3.2, n =6). This decrease in seeding efficiency may possibly be due to cell suspension escaping from the macrochannels when subjected to dynamic rotational conditions. This result highlights the difficulties associated when seeding scaffolds containing macrochannel architectures and gives rise for concern when seeding single regular porous scaffolds with orthogonal channels/struts (reviewed in Section 2.7) which do not provide a mesoporous domain to permit the absorbtion of cell suspension and thereby relying solely on the available surface area of the channels/struts to facilitate cell adhesion to occur.

As was observed from the MTT staining of scaffolds 4 hours post-seeding (Figure 4.37), it was shown that trimodal scaffolds exhibited superior cell distribution throughout the entire scaffold depth compared to bimodal scaffolds. This enhancement is due to the presence of the macrochannels within the mesoporous phase, allowing the cell suspension to be more easily absorbed into the mesoporous domain. This highlights one of the significant benefits of incorporating unidirectional macrochannels into porous scaffold architectures. In contrast, bimodal scaffolds exhibited limited cell penetration, with a greater density of cells being observed on

the top surface and the outer peripheral regions (< 1mm) of the scaffolds. Comparing the top surfaces of both bimodal and trimodal scaffolds (Figure 4.37 A and C), it can be seen that for bimodal scaffolds a darker blue stain is present which indicates a greater number and therefore density of cells are present. This intensity of stain was not observed for trimodal scaffolds, with both cross-sectional and top surfaces of trimodal scaffolds exhibiting similar stain intensity. This demonstrates that trimodal scaffolds were more homogeneously seeded compared to bimodal scaffolds. The relatively poor penetration of cells into bimodal scaffolds is similar to the observations made by Wendt *et al.* (2003) when statically seeding porous β-TCP ceramic scaffolds. A porous scaffold is somewhat analogous to a porous filter system, with the specific objective to permit cells to flow through the porous domain and attach. However, once the material is saturated and with no external assistance (e.g. vacuum or perfusion) gravity alone is insufficient in forcing cells through the material. Researchers have adopted many techniques such as oscillating perfusion (Wendt *et al.*, 2003), orbital shaking (Rose *et al.*, 2004) or low-pressure systems (Wang *et al.*, 2006) to enhance seeding efficiency and ultimate cell distribution. Although these techniques were shown to enhance initial cell seeding efficiency and distribution to a degree they add further and unnecessary complication which might not prove advantageous or practical from a clinical perspective.

In terms of scaffold design, the presence of macrochannels from an *in vitro* seeding perspective proved positive and beneficial in terms of initial cell distribution and negative in terms of seeding efficiency compared to bimodal scaffolds. The overall qualitative results of cellular distribution within trimodal scaffolds using the static seeding method proved to be a highly effective and simple method compared to the cellular distributions obtained for seeding of bimodal scaffolds under identical conditions. These observations can only be due to the presence of macrochannels providing a path of least resistance for the absorbtion of the cell suspension throughout the mesoporous domain without the use of secondary perfusion- or vacuum- type systems.

5.7 Dynamic vs. static culturing

The purpose of this study was to determine the influence of dynamic culturing compared to static culturing which relies solely on a diffusion. It was hypothesised that dynamic culturing conditions would enhance cellular proliferation and cell viability within scaffold constructs due to enhanced nutrient supply and more efficient metabolic waste removal. It was also hypothesised that due to the presence of the macrochannels, trimodal scaffolds would exhibit superiority in terms of cellular proliferation and prevent cell death within the core of scaffolds compared to bimodal scaffolds.

The data obtained for cell numbers obtained from DNA analysis at various time points (1, 3, 5 and 7 days) was presented in Figure 4.42. Cell numbers in both static and dynamic cultures increased from day 1 to day 7 although a statistically significant difference ($p < 0.01$) for cell proliferation existed between static and dynamic flow culture conditions, with dynamic cultures exhibiting superiority at each time point. Comparing static and dynamic bimodal scaffolds, after 7 days of culturing there was a 2.1 fold increase in the number of cells within dynamic cultures compared to static cultures. Similarly after 7 days, dynamically cultured trimodal scaffolds exhibited a 2.5 fold increase in cell number compared to static cultures

This significant increase in cell number for the dynamic culturing conditions for both bimodal and trimodal scaffolds is most likely due to enhanced nutrient supply and more efficient metabolic waste removal from the interior regions of scaffold constructs due to constant mixing of the medium caused by rotation of the constructs. This constant mixing is likely to have prevented detrimental nutrient and metabolic waste concentrations from developing around and within the interior regions of scaffolds. Due to this, a more favourable environment was promoted in which cells could remain viable and therefore proliferate to a greater extent compared to static cultures. Interestingly, comparing trimodal and bimodal scaffolds at each specific time point there was no statistically significant difference in cell number within scaffolds which were dynamically cultured.

From the MTT staining (Figures 4.38 - 4.41) of these scaffold groups over time, very different viable cell distributions were observed to emerge and develop with increasing time. After seven days static culturing, it was evident that a depleting viable core was beginning to develop within trimodal type scaffold structures which had initially been shown to be homogeneously seeded. In the case of bimodal scaffolds after seven days of static culturing, a more dramatic depleted viable core had developed with viable cells observed to exist within the outer periphery ($\sim$ 500 μm) of these scaffold types. It is therefore feasible to hypothesise that under static culturing conditions, nutrient transport and waste-product efflux was insufficient to maintain cell viability in the interior regions of both these scaffold types.

For dynamic rotational culturing, trimodal scaffolds exhibited a homogeneous viable cell distribution throughout the entire scaffold depth after seven days of continuous rotation. In contrast for bimodal scaffolds even after 7 days of dynamic rotation, a viable cell population was not found to have developed within the centre of scaffold constructs. The existence and distribution of a viable cell population throughout the depth of trimodal scaffolds compared to bimodal scaffolds is most likely due to the presence of the macrochannels. These macrochannels permitted a more optimised structure for cell seeding and ultimately cell distribution (Figure 4.37) and also more readily facilitated nutrient and metabolic waste transport during dynamic culturing.

For dynamic culturing conditions, although bimodal scaffolds initially exhibited poor viable cell distributions, it was observed that significant cell migration occurred when scaffolds were subjected to dynamic culture conditions. This observation highlights that the mesoporous architecture of these scaffolds produced though the freeze-drying technique was not inhibiting in terms of pore size and pore interconnectivity. Also, the similar cell proliferation profiles which were observed for static or dynamic cultures imply that the slight architectural variations of the mesoporous domain that existed (Sections 4.2.1 and 4.2.2) did not significantly influence cell proliferation to any large extent. From the data and observations obtained, it

could be proposed that cell proliferation is more dependent on the culturing conditions.

From an *in vivo* perspective, the evidence provided from the static culturing experiments may give rise for significant concern when developing bone tissue-engineering strategies. It is clear from the literature that when a scaffold is initially implanted into a defect site a somewhat hostile nutrient environment exists (Brighton and Krebs, 1972; Kalfas, 2001; Muschler *et al.*, 2004). In the early stages of scaffold implantation, prior to vascularisation, a cell seeded scaffold relies solely on the diffusion of oxygen through the blood itself. The presence of a scaffold will reduce the effectiveness of this nutrient delivery and metabolic waste removal, since a porous construct will have an effective diffusion coefficient value less than that of the blood itself. Therefore it is pertinent to maximise diffusional effectiveness of scaffolds and to subsequently enhance rapid vascularisation in order to encourage cell migration and maintain cell depth viability. By providing a path of least resistance, the presence of macrochannels may facilitate this to occur post implantation and during the progressive fracture healing process.

5.8 Finite element modelling of *in vitro* oxygen concentration profiles

Due to the high metabolic demands of osteoblast-like cells during proliferation and subsequent tissue formation, effective delivery of nutrients and removal of metabolic waste products has been considered a critical factor for successful bone tissue engineering strategies.

Comparing the numerous experiments in the literature for other scaffold and cell types, the recurring trend of limited cell depth viability appears to be predominant and inevitable for static culture based systems (Shea *et al.*, 2000; Botchwey *et al.*, 2003; Malda *et al.*, 2004a; Lewis *et al.*, 2005; Dunn *et al.*, 2006). Cellular consumption of oxygen and other nutrients at the fluid-scaffold interface will inevitably result in the formation of gradients, thereby providing lower oxygen tensions within the

central core of the scaffold.

In this work it was proposed that the presence of macrochannels would significantly enhance the cell viability distribution during static culturing, by providing sufficiently high oxygen concentrations at the centre of trimodal scaffolds. However, as was observed from MTT staining, the presence of macrochannels were themselves insufficient to maintain full cell depth viability, with similar cell depth viabilities observed for both bimodal and trimodal scaffolds after seven days of static culturing ($\sim$ 250-500 μm).

Results obtained from the finite element analysis were presented in Section 4.4. These models were developed in order to assess the influence of macrochannels on the resulting oxygen concentration profiles, due solely to the diffusion of oxygen from the surrounding culture medium and consumption of the available oxygen by cellular activity during *in vitro* static culturing. The models were also used to assess the oxygen concentration gradients due to cell density distribution. From the qualitative determination of cell viability distribution within both bimodal and trimodal scaffolds during static culturing (Section 4.3.6), it was shown that there was a preferential growth of cells in the outer periphery of scaffolds. The finite element models represent these cell distributions and the resulting oxygen concentration profiles for various cell densities confined to specific depths from the surface (homogeneous, 250, 500 and 1000 μm). This work did not attempt to simulate cell proliferation based on the local oxygen tension, as has been performed by other researchers (Lewis *et al.*, 2005; Dunn *et al.*, 2006). The finite element analysis therefore provides an analytical representation of the oxygen concentration profiles that occur during static culturing at specific time points (1, 3, 5 and 7 days), due solely to the measured cellular distributions in a diffusion-based regime. These models do not account for the possible reduction in the effective diffusivity of the mesoporous domain, which could potentially occur as the cells proliferating on the periphery of the scaffold block the pores resulting in pore occlusion. This is a reasonable assumption to make based on the short time culturing duration of seven days. In addition, stereo-microscopy

imaging provided no evidence that pore occlusion had occurred.

The results obtained from the numerical modelling indicate that the oxygen concentration profiles that ensue due to the oxygen consumption demand of osteoblast-like cells cannot fully explain the lack of cell viability with increasing depth into the scaffold. Sufficiently high concentrations of oxygen were shown to exist beyond the depth of the viable cell layer.

Comparing bimodal and trimodal scaffolds, it was shown that the presence of the macrochannels had a positive influence in minimising the concentration gradients compared to bimodal scaffolds, and that trimodal scaffolds were less sensitive to changing cell densities (Figure 4.57).

For bimodal scaffolds oxygen concentrations were predicted to decrease from $\sim$ 133 μM at day 1 to $\sim$ 66 μM at day 3 (Figure 4.55 A). However from day 3 to day 5, the oxygen concentrations predicted were higher than those predicted on day 3 (123 vs. 66 μM) and approaching those predicted for day 1, yet the viable cell depth was observed to decrease (1000 to 500 μm). Similarly for day 7, higher again oxygen concentrations were predicted compared to day 5 (161 vs. 123 μM). Despite the higher oxygen concentrations predicted, the viable cell depth distribution was observed to decrease with increasing culturing time from $\sim$ 1mm to 250 μm after seven days for bimodal scaffolds.

Similarly for trimodal scaffolds (Figure 4.55 B), from day 1 to day 3, a decrease in the oxygen concentration was predicted, with minimums of $\sim$ 84 and 20 μM respectively. Similar to bimodal scaffolds after day 3 a reversal in the oxygen concentrations was predicted with higher oxygen concentrations of $\sim$ 158 μM predicted for day five. Similarly for day seven higher oxygen concentrations were predicted with a minimum of $\sim$ 176 μM, representing the highest oxygen concentration predicted by the model at any of the time points. However, the viable cell depth distribution retreated from being initially homogeneously to being confined to the outer 250 μm periphery at seven days.

In essence, although the finite element models predicted sufficiently high oxygen

concentrations at various time points, the persistent retreat of the viable/non-viable cell boundary from the centre remained for both scaffold types. No correlation appears to be present between oxygen concentration and viable cell depth.

From oxygen consumption experiments (Section 4.3.8), it was shown that MC3T3-E1 cells remained viable (determined *via* XTT assay) in low oxygen concentration environments of between 24 and 29 μM (Figure 4.43, p 181).

Other researchers have also shown that osteoblast-like cells remain viable when exposed to relatively low oxygen concentrations. For example, Salim *et al.* (2004) assessed *in vitro* osteoblast-like immortalised cells (MC3T3-E1), primary osteoblasts and mesenchymal stem cell bone nodule formation following exposure to 21 % O_2 (ambient oxygen), 2 % O_2 (hypoxia), and < 0.02 % O2 (anoxia). It was shown that hypoxia had little effect on subsequent osteogenic differentiation. In contrast, short-term anoxic treatment of primary osteoblasts and mesenchymal precursors inhibited subsequent *in vitro* bone nodule formation and extracellular calcium deposition. However this was not observed for the MC3T3-E1 cell line. It was also shown *via* cell viability assays that bone nodule inhibition was not caused by immediate or delayed cell death. No significant differences in viability were observed immediately after 3, 6, 12, or 24 hours of anoxic exposure, or after two days of reoxygenation.

Based on this, low levels of oxygen cannot solely be responsible for the observed necrotic core formation. Higher oxygen concentrations were predicted by the finite element models at various time points yet the viable cell depth progressively diminished from day 1 to day 7 for both scaffold types.

Based on the finite element models the retreating viable cell population observed experimentally is more likely due to another limiting diffusive molecule such as glucose or possibly a build up of metabolic waste products within the central regions of the scaffolds creating a toxic environment resulting in cell death.

Botchwey *et al.* (2003) developed numerical models to evaluate the diffusion of glucose during static culture within porous scaffolds. Results showed that passive glucose diffusion alone was insufficient to maintain minimum glucose concentration

beyond a depth of a few hundred microns.

Further experiments are required to determine the influence of glucose concentrations and metabolic waste products on cell viability and subsequent proliferation. With this information further numerical modelling focusing on the diffusion limitations of glucose and metabolic waste products will be feasible.

However the existing limitation still remains with static culturing. Although experiments in conjunction with numerical analysis may isolate the critical diffusing molecule, it still remains a significant challenge to successfully culture scaffolds based solely on a diffusive environment while maintaining full scaffold depth cell viability. Accordingly it is necessary to employ some form of dynamic culturing regime to overcome these diffusion limitations. As was seen from the dynamic culturing study, continuous rotation significantly enhanced cell proliferation and viability throughout the scaffold depth.

The hypothesis proposed that oxygen is the limiting diffusing molecule, and that steep gradients result in the formation of a necrotic core. However, although experimentally the formation of a necrotic core did develop, the numerical models show that sufficiently high levels of oxygen were present within the interior regions of the scaffold, and therefore oxygen alone cannot be the critical diffusing molecule.

One of the main advantages of finite element models is that they allow for parametric studies to be easily performed. Such models can be utilised as a tool for optimisation of scaffold geometry, with the specific goal of determining the theoretically ideal unidirectional macrochannel diameter and spacing that would predict the highest concentration of a diffusing species (in this case oxygen) within the core of the modelled scaffold in a tissue-engineering system. These models can also serve as a tool for use by other researchers to establish a correct relationship between oxygen availability and cell survival rate. In conjunction, the overall mechanical properties of a multi-domain porous system must be taken into consideration with quantification of the mechanical properties for different macrochannel array patterns. These models also serve as a template to explore and investigate cell survival and matrix

production for other diffusing species such as glucose and metabolic waste products. An iterative engineering approach such as this may permit the development of scaffolds which can facilitate high nutrient diffusion concentrations with appropriate mechanical properties.

Chapter 6

Conclusions and future work

Contents

6.1 Summary of project 224

6.2 Future work 227

6.1 Summary of project

The impetus of this work was to advance the fundamental work in bone tissue engineering and accelerate the development of scaffolds for *in vivo* applications. A recurring limitation of bone tissue scaffolds is that bone has been shown to form only in the outer 250 - 500 μm region of scaffolds resulting in the formation of a necrotic core with limited cell viability. This is primarily believed to be due to the lack of nutrient delivery into and waste removal from the inner regions of the scaffold construct (Ishaug-Riley *et al.*, 1998). Other scaffold limitations involve poor cell seeding efficiency resulting in inhomogeneous cellular distributions.

It was hypothesised that many of the existing limitations could be overcome through the development of a multi-domain porous scaffold (*i.e.* a scaffold providing a discrete domain for cell occupancy and a separate domain for nutrient delivery) with the specific objective to embody in one scaffold, the structures required to optimise cell seeding, cell proliferation and migration and potentially to facilitate

vascularisation once implanted *in vivo*.

This work has developed a novel technique employing freeze-drying and CNC machining for developing trimodal scaffold architectures resulting in discrete domains for cell proliferation and nutrient delivery, with overall porosities of approximately 85%. The mesoporous phase formed through the freeze drying process provides a discrete domain for cell attachment and proliferation. The function of incorporating unidirectional macrochannels was to facilitate homogeneous cell seeding and provide a direct route for diffusion of critical nutrient molecules and removal of metabolic waste products.

Characterisation of scaffold's properties was performed and showed comparable compressive strengths to cancellous bone and high permeability values. The compressive strengths of both bimodal and trimodal scaffolds was found to be approximately 1.12 MPa and 1.53 MPa respectively, with strain to failure ranging between 15-20 %. The incorporation of macrochannels (*i.e.* trimodal scaffolds) was shown to significantly influence both the fluid conductance and permeability of scaffolds with an 18 fold increase in permeability compared to bimodal scaffolds, and similar permeability values compared to cancellous bone.

Effective diffusion coefficients for the bimodal phase were also determined and compare favourably with theoretical values, with an average effective diffusion coefficient of 7.9 x 10^{-10} m^2s^{-1} which is approximately 26 % of that of water at 37 °C, and similar to values in the literature for other scaffold types.

It has been demonstrated that the introduction of the macrochannels facilitates more homogeneous cell seeding, and also maintains high oxygen concentrations throughout the scaffold depth, compared to scaffolds without macrochannels.

The presence of macrochannels significantly enhanced the distribution of cells compared to bimodal scaffolds for the same given seeding volume, although the cell seeding efficiency was decreased.

This work has shown that when seeding three-dimensional porous scaffolds, appropriately matching the seeding volume to the saturation capacity of the scaffold is

the most optimum approach in terms of promoting homogeneous cell seeding while maintaining relatively high seeding efficiencies ($\sim$ 70 %).

Although a trimodal scaffold architecture surpasses a purely bimodal in terms of facilitating homogenous seeding, it requires dynamic culturing such as rotational culturing to maintain uniform cell viability throughout the scaffold depth with increasing culturing time. When dynamically cultured, it has been demonstrated that trimodal scaffold constructs can maintain superior cell depth viability compared to bimodal scaffolds and increase the extent of cell proliferation ($\sim$ 2 fold) compared to static culturing.

The function of the finite element models was to assess if oxygen was a limiting factor during static culturing conditions for bimodal and trimodal scaffolds, and to assess if oxygen alone could be responsible for the formation of a necrotic core as observed experimentally. The models were also used to demonstrate the effectiveness of incorporating macrochannels to increase the core oxygen concentration. The accuracy of these models was improved by employing experimentally measured cellular oxygen consumption rates, effective diffusion coefficients and cell distributions at each time point. It was shown that the presence of macrochannels had a positive influence in minimising the concentration gradients compared to bimodal scaffolds for the same cell density distributions.

Even with the presence of a high density distribution of cells in the outermost periphery, the results from the numerical models cannot fully explain the lack of cell viability within the central regions of the scaffold constructs. Sufficiently high concentrations of oxygen were shown to exist beyond the depth of the viable cell layers. Based on this evidence it is proposed that oxygen alone cannot be solely responsible for the formation of a necrotic core, which leads to the possibility that secondary diffusive molecules such as either glucose or metabolic waste products (*e.g.* CO_2, lactate and urea) are responsible for the limited cell depth viability observed experimentally.

It is therefore feasible to propose that regardless of the scaffold architecture

(*i.e.* bimodal or trimodal), diffusion based culturing will lead to the formation of a necrotic core, and that oxygen alone cannot be responsible for this effect.

This work also shows that "conditioning" cell seeded scaffolds through *in vitro* static culturing prior to *in vivo* implantation may not be an effective tissue engineering strategy. The *in vivo* environment prior to vascularisation appears to be inadequate for maintaining a homogeneously distributed cell population. Therefore a more appropriate strategy may be to reduce the concentration of transplanted cells, or incorporate a specific cell type to promote angiogenesis through effective cell seeding and dynamic culturing prior to *in vivo* implantation. Another option may be to limit the geometrical dimensions of the scaffold thereby reducing the inevitable influence of diffusion limitations.

In this scenario the trimodal scaffold developed in this work offers distinct advances to current scaffold designs. The *in vivo* work assessing this novel trimodal scaffold architecture on vascularisation and diffusion of other species warrants further investigation and is outlined in the next section.

6.2 Future work

As was evident from this thesis, precise control of the pore size of mesoporous phase was unattainable for HA based systems. The variation in pore morphology is most likely due to inhomogeneous cooling of the HA suspension, leading to the formation of non spherical type ice crystals. Further investigations are required with possible modification of the cooling cycle such as final freezing temperature and cooling rates in order to fabricate a mesoporous architecture with a more homogeneous pore architecture.

As was demonstrated, the mechanical properties of both bimodal and trimodal scaffolds are currently insufficient for load bearing applications. The influence of final sintering temperatures in order to remove the presence of microporosity which may lead to enhanced compressive strengths should be assessed. In addition, characterisation of the relationship between mechanical properties and overall porosity

of the mesoporous phase should be performed in order to develop more clinically suitable implantable scaffolds.

From an *in vivo* perspective, the presence of unidirectional macrochannels may provide a path of least resistance to fluid flow, thereby providing an effective route to facilitate *in vivo* vascularisation and promoting the ingrowth and formation of new tissue. The ultimate assessment of these novel trimodal architectures relies on *in-vivo* implantation into a defect site, and subsequent analysis of the ingrowth and formation of new tissue compared to bimodal scaffold architectures alone.

As this work has shown relying solely on a diffusion based system will inevitably result in limited cell depth viability. This has significant consequences with respect to the implantation of cell-seeded scaffolds. During the initial stages of healing (inflammation), the primary source of nutrients to the central region of an implanted scaffold is supplied by the surrounding tissues until such time as vascularisation occurs. Based on this progression of events, it may be feasible and necessary to perform some secondary seeding of cells to encourage the formation of new blood vessels (angiogenesis). Formation of blood vessels may overcome some of these diffusion limitations and result in greater penetration and formation of new bone tissue, while maintaining core cell viability.

In this work HA was chosen as the base material due its high biocompatibility and its wide use in clinical applications and also due to the fact that it is one of the main constituents of natural bone. However the slow resorption rates of HA may be undesirable from a purely tissue-engineering perspective. The techniques as described in this thesis for the fabrication of bimodal or trimodal scaffold architectures are not just limited to HA, and can be used in conjunction with many other ceramic materials such as α- or β- tricalcium phosphates. Such flexibility may be beneficial and more clinically desirable. However, employing such materials may prove difficult due to the associated poor mechanical performance of such materials as demonstrated by other researchers.

Further studies regarding the effect of other critical molecules such as glucose

and metabolic waste products on the viability of cells are required to isolate the critical diffusing molecule in order to prevent the formation of necrotic cores within scaffolds. Additionally, due to the hostile environment into which scaffolds are typically transplanted, information regarding the typical basal and transient local concentrations of the available nutrients in the surrounding tissues are required. In conjunction with this information, the use of diffusion-reaction based finite element models will become a more powerful and robust tool. Such models may allow the calculation of optimum seeding densities prior to implantation in order to provide more favourable nutrient conditions to prevent the formation of necrotic cores.

Bibliography

Agrawal, C. M., McKinney, J. S., Lanctot, D., and Athanasiou, K. A., 2000. Effects of fluid flow on the in vitro degradation kinetics of biodegradable scaffolds for tissue engineering. *Biomaterials*, **21**(23):2443–2452.

Al-Souhail, A., Claffey, N., Toner, M., Tancred, D. C., and Carr, A. J., 2000. An *in vivo* study of a novel bone graft for oral surgical applications. In Prendergast, Lee, and Carr, eds., *Proceedings of the 12th Conference of the European Society of Biomechanics*, page 240. Royal Academy of Medicine in Ireland. ISBN 0-9538809-0-7.

Allen, C. B., Schneider, B. K., and White, C. W., 2001. Limitations to oxygen diffusion and equilibration in in vitro cell exposure systems in hyperoxia and hypoxia. *Am J Physiol Lung Cell Mol Physiol.*, **281**(4):L1021–7.

Allen, J. W. and Bhatia, S. N., 2003. Formation of steady-state oxygen gradients in vitro. *Biotechnology and Bioengineering*, **82**(3):253–262.

Almarza, A. J. and Athanasiou, K. A., 2004. Seeding techniques and scaffolding choice for tissue engineering of the temporomandibular joint disk. *Tissue Eng.*, **10**(11-12):1787–1795.

Anil-Kumar, P. R., Varma, H. K., and Kumary, T. V., 2005. Rapid and complete cellularization of hydroxyapatite for bone tissue engineering. *Acta Biomater.*, **1**(5):545–552.

Anselme, K., 2000. Osteoblast adhesion on biomaterials. *Biomaterials*, **21**(7):667–681.

Asahina, I., Watanabe, M., Sakurai, N., Mori, M., and Enomoto, S., 1997. Repair of bone defect in primate mandible using a bone morphogenetic protein (bmp)-hydroxyapatite-collagen composite. *J Med Dent Sci*, **44**(3):63–70.

Baksh, D. and Davies, J. E., 2000. *Bone Engineering*, chapter Design strategies for 3-dimensional in vitro bone growth in tissue engineering scaffolds, pages 488–495. University of Toronto Press, Toronto, Canada.

Balis, U. J., Behnia, K., Dwarakanath, B., Bhatia, S. N., Sullivan, S. J., Yarmush, M. L., and Toner, M., 1999. Oxygen consumption characteristics of porcine hepatocytes. *Metab Eng.*, **1**(1):49–62.

Begley, C. T., Doherty, M. J., Mollan, R. A. B., and Wilson, D. J., 1995. Comparative study of the osteoinductive properties of bioceramic, coral and processed bone graft substitutes. *Biomaterials*, **16**(15):1181–1185.

Bose, S., Suguira, S., and Bandyopadhyay, A., 1999. Processing of controlled porosity ceramic structures via fused deposition. *Scripta Materialia*, **41**(9):1009–1014.

Botchwey, E. A., Pollack, S. R., El-Amin, S., Levine, E. M., Tuan, R. S., and Laurencin, C. T., 2003. Human osteoblast-like cells in three-dimensional culture with fluid flow. *Biorheology*, **40**:299–306.

Boyan, B. D., Hummert, T. W., Dean, D. D., and Schwartz, Z., 1996. Role of material surfaces in regulating bone and cartilage cell response. *Biomaterials*, **17**:137–146.

Boyde, A., Corsi, A., Quarto, R., Cancedda, R., and Bianco, P., 1999. Osteoconduction in large macroporous hydroxyapatite ceramic implants: evidence for a complementary integration and disintegration mechanism. *Bone*, **24**(6):579–589.

Brighton, C. T. and Krebs, A. G., 1972. Oxygen tension of healing fractures in the rabbit. *J Bone Joint Surg Am.*, **54**(2):323–332.

Brighton, C. T., Schaffer, J. L., Shapiro, D. B., Tang, J. J., and Clark, C. C., 1991. Proliferation and macromolecular synthesis by rat calvarial bone cells grown in various oxygen tensions. *J Orthop Res.*, **9**(6):847–854.

Burg, K. J. L., Porter, S., and Kellam, J. F., 2000. Biomaterial developments for bone tissue engineering. *Biomaterials*, **21**(23):2347–2359.

Cao, W. and Hench, L. L., 1996. Bioactive materials. *Ceramics International*, **22**:493–507.

Carrier, R. L., Rupnick, M., Langer, R., Schoen, F. J., Freed, L. E., and Vunjak-Novakovic, G., 2002. Effects of oxygen on engineered cardiac muscle. *Biotechnol Bioeng.*, **78**(6):617–625.

Cartmell, S. H., Porter, B. D., Garcia, A. J., and Guldberg, R. E., 2003. Effects of medium perfusion rate on cell-seeded three dimensional bone constructs in vitro. *Tissue Eng.*, **9**(6):1197–1203.

Cerroni, L., Filocamo, R., Fabbri, M., Piconi, C., Caropreso, S., and Condo, S. G., 2002. Growth of osteoblast-like cells on porous hydroxyapatite ceramics: an in vitro study. *Biomol. Eng.*, **19**(2-6):119–124.

Chang, B. S., Lee, C. K., Hong, K. S., Youn, H. J., Ryu, H. S., Chung, S. S., and Park, K. W., 2000. Osteoconduction at porous hydroxyapatite with various pore configurations. *Biomaterials*, **21**(12):1291–1298.

Chistolini, P., Ruspantini, I., Bianco, P., Corsi, A., Cancedda, R., and Quarto, R., 1999. Biomechanical evaluation of cell-loaded and cell-free hydroxyapatite implants for the reconstruction of segmental bone defects. *Journal of Materials Science: Materials in Medicine*, **10**:739–742.

Chow, D. C., Wenning, L. A., Miller, W. M., and Papoutsakis, E. T., 2001. Modeling po_2 distributions in the bone marrow hematopoietic compartment. i. krogh's model. *Biophys J*, **81**(2):675–684.

Chu, T. M., Halloran, J. W., Hollister, S. J., and Feinberg, S. E., 2001. Hydroxyapatite implants with designed internal architecture. *Journal of Materials Science: Materials in Medicine*, **12**(6):471–478.

Chu, T. M., Orton, D. G., Hollister, S. J., Feinberg, S. E., and Halloran, J. W., 2002. Mechanical and in vivo performance of hydroxyapatite implants with controlled architectures. *Biomaterials*, **23**:1283–1293.

Ciapetti, G., Ambrosio, L., Marletta, G., Baldini, N., and Giunti, A., 1996. Human bone marrow stromal cells: In vitro expansion and differentiation for bone engineering. *Biomaterials*, **27**(36):6150–6160.

Collins, P. C., Nielsen, L. K., Patel, S. D., Papoutsakis, E. T., and Miller, W. M., 1998. Characterization of hematopoietic cell expansion, oxygen uptake, and glycolysis in a controlled, stirred-tank bioreactor system. *Biotechnol Prog.*, **14**(3):466–472.

Croll, T. I., Gentz, S., Mueller, K., Davidson, M., OConnor, A. J., Stevens, G. W., and Cooper-White, J. J., 2005. Modelling oxygen diffusion and cell growth in a porous, vascularising scaffold for soft tissue engineering applications. *Chemical Engineering Science*, **60**(17):4924–4934.

Cussler, E. L., 1997. *Diffusion, Mass Transfer in Fluid Systems*. Cambridge University Press, second edition. ISBN 0-521-45078-0.

Cypher TJ, G. J., 1996. Biological principles of bone graft healing. *J Foot Ankle Surg.*, **35**(5):413–417.

Cyster, L. A., Grant, D. M., Howdle, S. M., Rose, F. R., Irvine, D. J., Freeman, D., Scotchford, C. A., and Shakesheff, K. M., 2005. The influence of dispersant concentration on the pore morphology of hydroxyapatite ceramics for bone tissue engineering. *Biomaterials*, **26**(7):697–702.

Deligianni, D. D., Katsala, N. D., Koutsoukos, P. G., and Missirlis, Y. F., 2001. Effect of surface roughness of hydroxyapatite on human bone marrow cell adhesion, proliferation, differentiation and detachment strength. *Biomaterials*, **22**:87–96.

Dennis, J. E., Haynesworth, S. E., Young, R. G., and Caplan, A. I., 1992. Osteogenesis in marrow-derived mesenchymal cell porous ceramic composites transplanted subcutaneously: effect of fibronectin and laminin on cell retention and rate of osteogenic expression. *Cell Transplant.*, **1**(1):23–32.

Deville, S., Saiz, E., and Tomsia, A. P., 2006. Freeze casting of hydroxyapatite scaffolds for bone tissue engineering. *Biomaterials*, **27**(32):5480–5489.

Dong, J., Kojima, H., Uemura, T., Kikuchi, M., Tateishi, T., and Tanaka, J., 2001a. In vivo evaluation of a novel porous hydroxyapatite to sustain osteogenesis of transplanted bone marrow-derived osteoblastic cells. *J Biomed Mater Res.*, **57**(2):208–216.

Dong, J., Uemura, T., Kojima, H., Kikuchi, M., Tanaka, J., and Tateishi, T., 2001b. Application of low pressure system to sustain in vivo bone formation in osteoblast/porous hydroxyapatite composite. *Mater Sci Eng C*, **17**(1-2):37–43.

Ducheyne, P. and Qiu, Q., 1999. Bioactive ceramics: the effect of surface reactivity on bone formation and bone cell function. *Biomaterials*, **20**(23):2287–2303.

Dunn, J. C., Chan, W. Y., Cristini, V., Kim, J. S., Lowengrub, J., Singh, S., and Wu, B. M., 2006. Analysis of cell growth in three-dimensional scaffolds. *Tissue Eng.*, **12**(4):705–716.

Engin, N. O. and Tas, A. C., 1999. Manufacture of macroporous calcium hydroxyapatite bioceramics. *Journal of the European Ceramic Society*, **19**(13-14):2569–2572.

Frayssinet, P., Rouquet, N., Fages, J., Durand, M., Vidalain, P. O., and Bonel, G., 1997. The influence of sintering temperature on the proliferation of fibroblastic cells in contact with ha-bioceramics. *Journal of Biomedical Materials Research*, **35**:337–347.

Freyman, T. M., Yannas, I. V., and Gibson, L. J., 2001. Cellular materials as porous scaffolds for tissue engineering. *Progess in Materials Science*, **46**(3-4):273–282.

Galban, C. J. and Locke, B. R., 1999. Analysis of cell growth kinetics and substrate diffusion in a polymer scaffold. *Biotechnol. Bioeng*, **65**(2):121–132.

Gauthier, O., Bouler, J. M., Aguado, E., Pilet, P., and Daculsi, G., 1998. Macroporous biphasic calcium phosphate ceramics: influence of macropore diameter and macroporosity percentage on bone ingrowth. *Biomaterials*, **19**:133–139.

Griffith, C. K., Miller, C., Sainson, R. C., Calvert, J. W., Jeon, N. L., and George, C. C. H. S. C., 2005. Diffusion limits of an in vitro thick prevascularized tissue. *Tissue Eng.*, **11**(1-2):257–266.

Grynpas, M. D., Pilliar, R. M., Kandel, R. A., Renlund, R., Filiaggi, M., and Dumitriu, M., 2002. Porous calcium polyphosphate scaffolds for bone substitute applications in vivo studies. *Biomaterials*, **23**:2063–2070.

Guarino, R. D., Dike, L. E., Haq, T. A., Rowley, J. A., Pitner, J. B., and Timmins, M. R., 2004. Method for determining oxygen consumption rates of static cultures from microplate measurements of pericellular dissolved oxygen concentration. *Biotechnol Bioeng.*, **86**(7):775–787.

Hadlock, T., Sundback, C., Hunter, D., Cheney, M., and Vacanti, J. P., 2000. A polymer foam conduit seeded with schwann cells promotes guided peripheral nerve regeneration. *Tissue Eng.*, **6**(2):119–127.

Haselgrove, J. C., Shapiro, I. M., and Silverton, S. F., 1993. Computer modeling of the oxygen supply and demand of cells of the avian growth cartilage. *Am J Physiol.*, **265**(2):C497–506.

Hench, L. L. and Ethridge, E. C., 1982. *Biomaterials- An Interfacial Approach*, volume 4 of *Biophysics and Bioengineering Series*. Academic Press.

Heppenstall, R. B., Grislis, G., and Hunt, T. K., 1975. Tissue gas tensions and oxygen consumption in healing bone defects. *Clin Orthop Relat Res.*, **106**:357–365.

Hershey, D. and Karhan, T., 1968. Diffusion coefficients for oxygen transport in whole blood. *AIChE Journal*, **14**(6):969–972.

Heywood, H. K., Bader, D. L., and Lee, D. A., 2006. Rate of oxygen consumption by isolated articular chondrocytes is sensitive to medium glucose concentration. *J Cell Physiol.*, **206**(2):402–410.

Hing, K. A., Best, M., and Bonfield, W., 1999. Characterization of porous hydroxyapatite. *J Mater Sci Mater Med.*, **10**(3):135–145.

Hollister, S. J., Chu, T. M., Halloran, J. W., and Feinberg, S. E., 2000. *Bone mechanics*, chapter Design and manufacture of bone replacement scaffolds, pages 36–1. Boca Raton, FL: CRC Press.

Hollister, S. J., Lin, C. Y., Saito, E., Lin, C. Y., Schek, R. D., Taboas, J. M., Williams, J. M., Partee, B., Flanagan, C. L., Diggs, A., Wilke, E. N., Lenthe, G. H. V., Muller, R., Wirtz, T., Das, S., Feinberg, S. E., and Krebsbach, P. H., 2005. Engineering craniofacial scaffolds. *Orthod Craniofac Res.*, **8**(3):162–173.

Holm, S., Maroudas, A., Urban, J. P., Selstam, G., and Nachemson, A., 1981. Nutrition of the intervertebral disc: solute transport and metabolism. *Connect Tissue Res.*, **8**(2):101–119.

Howe, D. F., Svare, C. W., and Tock, R. W., 1974. Some effects of pore diameter on single pore bony ingression patterns in teflon. *J Biomed Mater Res.*, **8**(6):399–406.

Hui, P. W., Leung, P. C., and Sher, A., 1996. Fluid conductance of cancellous bone graft as a predictor for graft-host interface healing. *J. Biomechanics*, **29**(1):123–132.

Hulbert, S. F., Morrison, S. J., and Klawitter, J. J., 1972. Tissue reaction to three ceramics of porous and non-porous structures. *J Biomed Mater Res.*, **6**(5):347–374.

Hutmacher, D. W., 2000. Scaffolds in tissue engineering bone and cartilage. *Biomaterials*, **21**(24):2529–2543.

Hutmacher, D. W., 2001. Scaffold design and fabrication technologies for engineering tissues- state of the art and future perspectives. *J. Biomater. Sci. Polymer Edn*, **12**(1):107–124.

Ishaug-Riley, S. L., Crane-Kruger, G. M., Yaszemski, M. J., and Mikos, A. G., 1998. Three-dimensional culture of rat calvarial osteoblasts in porous biodegradable polymers. *Biomaterials*, **19**:1405–1412.

Ito, Y., Tanaka, N., Fujimoto, Y., Yasunaga, Y., Ishida, O., Agung, M., and Ochi, M., 2004. Bone formation using novel interconnected porous calcium hydroxyapatite ceramic hybridized with cultured marrow stromal stem cells derived from green rat. *J Biomed Mater Res A.*, **69**(3):454–461.

Janssen, F. W., Oostra, J., Oorschot, A., and van Blitterswijk, C. A., 2006. A perfusion bioreactor system capable of producing clinically relevant volumes of tissue-engineered bone: in vivo bone formation showing proof of concept. *Biomaterials*, **27**(3):315–323.

Jun, I. K., Koh, Y. H., and E.Kim, H., 2006. Fabrication of ultrahigh porosity ceramics with biaxial pore channels. *Materials Letters*, **60**(7):878–882.

Kalfas, I. H., 2001. Principles of bone healing. *Neurosurg Focus.*, **10**(4):E1.

Karande, T. S., Ong, J. L., and Agrawal, C. M., 2004. Diffusion in musculoskeletal tissue engineering scaffolds: design issues related to porosity, permeability, architecture, and nutrient mixing. *Ann Biomed Eng.*, **32**(12):1728–1743.

Kieswetter, K., Schwartz, Z., Dean, D. D., and Boyan, B. D., 1996. The role of implant surface characteristics in the healing of bone. *Crit Rev Oral Biol Med.*, **7**(4):329–45.

Kim, H. W., Knowles, J. C., and Kim, H. E., 2004. Hydroxyapatite/poly(epsilon-caprolactone) composite coatings on hydroxyapatite porous bone scaffold for drug delivery. *Biomaterials*, **25**(7-8):1279–1287.

Kim, Y. J., Sah, R. L. Y., Doong, J. Y. H., and Grodzinsky, A. J., 1988. Fluorometric assay of dna in cartilage explants using hoechst 33258. *Analytical Biochemistry*, **174**:168–176.

Koch, D., Andresen, L., Schmedders, T., and Grathwohl, G., 2003. Evolution of porosity by freeze casting and sintering of sol-gel derived ceramics. *J. sol-gel sci. technol.*, **26**(1-3):149–152.

Koh, Y. H., Jun, I. K., and Kim, H. E., 2006. Fabrication of poly(ϵ-caprolactone)/hydroxyapatite scaffold using rapid direct deposition. *Materials Letters*, **60**(9-10):1184–1187.

Koh, Y. H., Kim, H. W., Kim, H. E., and Halloran, J. W., 2002. Fabrication of macrochannelled-hydroxyapatite bioceramic by a coextrusion process. *J. Am. Ceram. Soc.*, **85**(10):2578–2580.

Laurencin, C. T., Ambrosio, A. M. A., Borden, M. D., and Cooper, J. A., 1999. *Annu. Rev. Biomed. Eng.*, chapter Tissue engineering: Orthopedic applications, pages 19–46. Annual Reviews. Palo Alto, CA.

Laurencin, C. T. and Lu, H. H., 2000. *Bone Engineering*, chapter Polymer-ceramic composites for bone-tissue engineering, pages 462–472. University of Toronto Press, Toronto, Canada.

Leong, K. F., Cheah, C. M., and Chua, C. K., 2003. Solid freeform fabrication of three-dimensional scaffolds for engineering replacement tissues and organs. *Biomaterials*, **24**(13):2363–2378.

Lewandrowski, K. U., Gresserb, J. D., Wiseb, D. L., and Trantolo, D. J., 2000. Bioresorbable bone graft substitutes of different osteoconductivities: a histologic evaluation of osteointegration of poly(propylene glycol-co-fumaric acid)-based cement implants in rats. *Biomaterials*, **21**(8):757–764.

Lewis, M. C., Macarthur, B. D., Malda, J., Pettet, G., and Please, C. P., 2005. Heterogeneous proliferation within engineered cartilaginous tissue: the role of oxygen tension. *Biotechnol Bioeng.*, **91**(5):607–615.

Li, S., Wijn, J. R. D., Li, J., Layrolle, P., and Groot, K. D., 2003. Macroporous biphasic calcium phosphate scaffold with high permeability/porosity ratio. *Tissue Eng.*, **9**(3):535–548.

Lin, A. S. P., Barrows, T. H., Cartmel, S. H., and Guldberg, R. E., 2003. Microarchitectural and mechanical characterization of oriented porous polymer scaffolds. *Biomaterials*, **24**:481–489.

Liu, D. M., 1997. Influence of porosity and pore size on the compressive strength of porous hydroxyapatite ceramic. *Ceramics International*, **23**:135–139.

Malda, J., Rouwkema, J., Martens, D. E., Comte, E. P. L., Kooy, F. K., Tramper, J., van Blitterswijk, C. A., and Riesle, J., 2004a. Oxygen gradients in tissue-engineered pegt/pbt cartilaginous constructs: measurement and modeling. *Biotechnol Bioeng.*, **86**(1):9–18.

Malda, J., van den Brink, P., Meeuwse, P., Grojec, M., Martens, D. E., Tramper, J., J, J. R., and van Blitterswijk, C. A., 2004b. Effect of oxygen tension on adult articular chondrocytes in microcarrier bioreactor culture. *Tissue Eng.*, **10**(7-8):987–994.

Malda, J., Woodfield, T. B., van der Vloodt, F., Kooy, F. K., Martens, D. E., Tramper, J., van Blitterswijk, C. A., and Riesle, J., 2004c. The effect of pegt/pbt scaffold architecture on oxygen gradients in tissue engineered cartilaginous constructs. *Biomaterials*, **25**(26):5773–5780.

Malik, M. A., Puleo, D. A., Bizios, R., and Doremus, R. H., 1992. Osteoblasts on hydroxyapatite, alumina and bone surfaces in vitro: morphology during the first 2 h of attachment. *Biomaterials*, **13**(2):123–128.

Mamchaoui, K. and Saumon, G., 2000. A method for measuring the oxygen consumption of intact cell monolayers. *Am J Physiol Lung Cell Mol Physiol.*, **278**(4):L858–863.

Martin, I., Padera, R. F., Vunjak-Novakovic, G., and Freed, L. E., 1998. In vitro differentiation of chick embryo bone marrow stromal cells into cartilaginous and bone-like tissues. *Journal of Orthopaedic Research*, **16**:181–189.

Martin, I., Wendt, D., and Heberer, M., 2004. The role of bioreactors in tissue engineering. *Trends in Biotechnology*, **22**(2):80–86.

Martini, F. H., 2001. *Fundamentals of Anatomy & Physiology*, volume 5. Prentice Hall.

Mastrogiacomo, M., Scaglione, S., Martinetti, R., Dolcini, L., Beltrame, F., Cancedda, R., and Quarto, R., 2006. Role of scaffold internal structure on in vivo bone formation in macroporous calcium phosphate bioceramics. *Biomaterials. 2006 Jun;27(17):3230-7. Epub 2006 Feb 20*, **27**(17):3230–3237.

McLimans, W. F., Blumenson, L. E., and Tunnah, K. V., 1968. Kinetics of gas diffusion in mammalian cell culture systems. ii. theory. *Biotechnology and Bioengineering*, **10**(6):741–763.

Metzen, E., Wolff, M., Fandrey, J., and Jelkmann, W., 1995. Pericellular p_{O_2} and o_2 consumption in monolayer cell cultures. *Respir Physiol.*, **100**(2):101–106.

Mikos, A. G., Sarakinos, G., Lyman, M. D., Vacanti, D. E. I. J. P., and Langer, R., 1993. Prevascularization of porous biodegradable polymers. *Biotechnology and Bioengineering*, **42**:716–723.

Moore, M. J., Friedman, J. A., Lewellyn, E. B., Mantila, S. M., Krych, A. J., Ameenuddin, S., Knight, A. M., Lu, L., Currier, B. L., Spinner, R. J., Marsh, R. W., Windebank, A. J., and Yaszemski, M. J., 2006. Multiple-channel scaffolds to promote spinal cord axon regeneration. *Biomaterials*, **27**(3):419–429.

Moreira, E. A. and Coury, J. R., 2004. The influence of structural parameters on the permeability of ceramic foams. *Braz. J. Chem. Eng. vol.21 no.1 So Paulo Jan./Mar. 2004*, **21**(1):23–33.

Moretti, M., Prina-Mello, A., Reid, A. J., Barron, V., and Prendergast, P. J., 2004. Endothelial cell alignment on cyclically-stretched silicone surfaces. *Journal of Materials Science: Materials in Medicine*, **15**(10):1159–1164.

Murphy, W. L., Dennis, R. G., Kileny, J. L., and Mooney, D. J., 2002. Salt fusion: An approach to improve pore interconnectivity within tissue engineering scaffolds. *Tissue Engineering*, **8**(1):43–52.

Muschler, G. F., Nakamoto, C., and Griffith, L. G., 2004. Engineering principles of clinical cell-based tissue engineering. *J Bone Joint Surg Am.*, **86-A**(7):1541–1558.

Nauman, E. A., Fong, K. E., and Keaveny, T. M., 1999. Dependence of intertrabecular permeability on flow direction and anatomic site. *Annals of Biomedical Engineering*, **27**:517–524.

Nehring, D., Adamietz, P., Meenen, N. M., and Portner, R., 1999. Perfusion cultures and modeling of oxygen uptake with three-dimensional chondrocyte pellets. *Biotechnology Techniques*, **13**:701–706.

Obradovic, B., Meldon, J. H., Freed, L. E., and Vunjak-Novakovic, G., 2000. Glycosaminoglycan deposition in engineered cartilage: experiments and mathematical model. *Bioengineering, Food, and Natural Products*, **46**(9):1860–1871.

O'Brien, F. J., Harley, B. A., Waller, M. A., Yannas, I. V., Gibson, L. J., and Prendergast, P. J., 2007. The effect of pore size on permeability and cell attachment in collagen scaffolds for tissue engineering. *Technology and Health Care*, **15**(1):3–17.

O'Brien, F. J., Harley, B. A., Yannas, I. V., and Gibson, L., 2004. Influence of freezing rate on pore structure in freeze-dried collagen-gag scaffolds. *Biomaterials*, **25**(6):1077–1086.

O'Brien, F. J., Harley, B. A., Yannas, I. V., and Gibson, L. J., 2005. The effect of pore size on cell adhesion in collagen-gag scaffolds. *Biomaterials*, **26**(4):433–441.

O'Kelly, K. U., 1999. *On the microstructure and mechanical properties of cancellous bone*. Ph.D. thesis, University College Dublin, Ireland.

Peon, E., Fuentes, G., Delgado, J. A., Morejon, L., Almirall, A., and Garcia, R., 2004. Preparation and characterization of porous blocks of synthetic hydroxyapatite. *Lat. Am. Appl. Res.*, **34**(4):225–228.

Pettersen, E. O., Larsen, L. H., Ramsing, N. B., and Ebbesen, P., 2005. Pericellular oxygen depletion during ordinary tissue culturing, measured with oxygen microsensors. *Cell Prolif.*, **38**(4):257–267.

Pisu, M., Lai, N., Cincotti, A., Delogu, F., and Cao, G., 2003. A simulation model for the growth of engineered cartilage on polymeric scaffolds. *International Journal of Chemical Reactor Engineering*, **1**:Article A38.

Radisic, M., Deen, W., Langer, R., and Vunjak-Novakovic, G., 2005. Mathematical model of oxygen distribution in engineered cardiac tissue with parallel channel array perfused with culture medium containing oxygen carriers. *Am J Physiol Heart Circ Physiol. 2005 Mar;288(3):H1278-89*, **288**(3):H1278–H1289.

Radisic, M., Malda, J., Epping, E., Geng, W., Langer, R., and Vunjak-Novakovic, G., 2006. Oxygen gradients correlate with cell density and cell viability in engineered cardiac tissue. *Biotechnol Bioeng.*, **93**(2):332–343.

Ren, H., Cao, Y., Zhao, Q., Li, J., Zhou, C., Liao, L., Jia, M., Zhao, Q., Cai, H., Han, Z. C., Yang, R., Chen, G., and Zhao, R. C., 2006. Proliferation and differentiation of bone marrow stromal cells under hypoxic conditions. *Biochem Biophys Res Commun.*, **347**(1):12–21.

Rice, R. W., 1993. Comparison of stress concentration versus minimum solid area based mechanical property-porosity relations. *Journal of Materials Science*, **28**(8):2187–2190.

Roehm, N. W., Rodgers, G. H., Hatfield, S. M., and Glasebrook, A. L., 1991. An improved colorimetric assay for cell proliferation and viability utilizing the tetrazolium salt xtt. *J Immunol Methods.*, **142**(2):257–265.

Rose, F. R., Cyster, L. A., Grant, D. M., Scotchford, C. A., Howdle, S. M., and Shakesheff, K. M., 2004. In vitro assessment of cell penetration into porous hydroxyapatite scaffolds with a central aligned channel. *Biomaterials*, **25**(24):5507–5514.

Roy, T. D., Simon, J. L., Ricci, J. L., Rekow, E. D., Thompson, V. P., and Parsons, J. R., 2003. Performance of hydroxyapatite bone repair scaffolds created via three-dimensional fabrication techniques. *J Biomed Mater Res A*, **67**(4):1228–37.

Sachlos, E. and Czernuszka, J. T., 2003. Making tissue engineering scaffolds work. review on the application of solid freeform fabrication technology to the production of tissue engineering scaffolds. *European Cells and Materials*, **5**:29–40.

Salgado, A. J., Continho, O. P., and Reis, R. L., 2004. Bone tissue engineering: state of the art and future trends. *Macromol. Biosci.*, **4**(8):743–765.

Salim, A., Nacamuli, R. P., Morgan, E. F., Giaccia, A. J., and Longaker, M. T., 2004. Transient changes in oxygen tension inhibit osteogenic differentiation and runx2 expression in osteoblasts. *J Biol Chem. 2004 Sep 17;279(38):40007-16. Epub 2004 Jul 19*, **279**(38):4000740016.

Shea, L. D., Wang, D., Franceschi, R. T., and Mooney, D. J., 2000. Engineered bone development from a pre-osteoblast cell line on three-dimensional scaffolds. *Tissue Engineering*, **6**(6):605–617.

Sherwood, J. K., Riley, S. L., Palazzolo, R., Brown, S. C., Monkhouse, D. C., Coates, M., Griffith, L. G., Landeen, L. K., and Ratcliffe, A., 2002. A three-dimensional osteochondral composite scaffold for articular cartilage repair. *Biomaterials*, **23**(24):4739–4751.

Shu, R., McMullen, R., Baumann, M. J., and McCabe, L. R., 2003. Hydroxyapatite accelerates differentiation and suppresses growth of mc3t3-e1 osteoblasts. *J Biomed Mater Res A.*, **67**(4):1196–1204.

Simon, J. L., Roy, T. D., Parsons, J. R., Rekow, E. D., Thompson, V. P., Kemnitzer, J., and Ricci, J. L., 2003. Engineered cellular response to scaffold architecture in a rabbit trephine defect. *J Biomed Mater Res A*, **66**(2):275–282.

Singh, I., 1978. The architecture of cancellous bone. *Journal of Anatomy*, **27**(2):305–310.

Smith, C. L., MacDonald, M. H., Tesch, A. M., and Willits, N. H., 2000. In vitro evaluation of the effect of dimethyl sulfoxide on equine articular cartilage matrix metabolism. *Vet Surg.*, **29**(4):347–357.

Stephan, E. B., Jiang, D., Lynch, S., Bush, P., and Dziak, R., 1999. Anorganic bovine bone supports osteoblastic cell attachment and proliferation. *J Periodontol.*, **70**(4):364–369.

Taboas, J. M., Maddox, R. D., Krebsbach, P. H., and Hollister, S. J., 2003. Indirect solid free form fabrication of local and global porous, biomimetic and composite 3d polymer-ceramic scaffolds. *Biomaterials*, **24**:181–194.

Tadic, D. and Epple, M., 2004. A thorough physicochemical characterisation of 14 calcium phosphate-based bone substitution materials in comparison to natural bone. *Biomaterials*, **25**(6):987–994.

Tamai, N., Myoui, A., Tomita, T., Nakase, T., Tanaka, J., Ochi, T., and Yoshikawa, H., 2002. Novel hydroxyapatite ceramics with an interconnective porous structure exhibit superior osteoconduction in vivo. *J Biomed Mater Res.*, **59**(1):110–117.

Tancred, D. C., 1996. *A new bone replacement material*. Ph.D. thesis, University College Dublin, Ireland.

Tancred, D. C., Carr, A. J., and McCormack, B. A. O., 1998a. Development of a new synthetic bone graft. *J. Mater. Sci. Mater. Med.*, **9**:819–823.

Tancred, D. C., McCormack, B. A. O., and Carr, A. J., 1998b. A synthetic bone implant macroscopically identical to cancellous bone. *Biomaterials*, **19**(24):2303–2311.

Torzilli, P. A., Adams, T. C., and Mis, R. J., 1987. Transient solute diffusion in articular cartilage. *J Biomech.*, **20**(2):203–214.

Vunjak-Novakovic, G., Martin, I., Obradovic, B., Treppo, S., Grodzinsky, A. J., Langer, R., and Freed, L. E., 1999. Bioreactor cultivation conditions modulate the composition and mechanical properties of tissue-engineered cartilage. *Journal of Orthopaedic Research*, **17**(1):130–138.

Waller, M. A., 2004. *Mechanical characterisation of tissue engineering scaffolds and constucts*. Master's thesis, Trinity College Dublin, Ireland.

Wang, J., Asou, Y., Sekiya, I., Sotome, S., Orii, H., and Shinomiya, K., 2006. Enhancement of tissue engineered bone formation by a low pressure system improving cell seeding and medium perfusion into a porous scaffold. *Biomaterials*, **27**(13):2738–2746.

Wendt, D., Jakob, M., and Martin, I., 2005. Bioreactor-based engineering of osteochondral grafts: from model systems to tissue manufacturing. *J Biosci Bioeng.*, **100**(5):489–494.

Wendt, D., Marsano, A., Jakob, M., Heberer, M., and Martin, I., 2003. Oscillating perfusion of cell suspensions through three-dimensional scaffolds enhances seeding efficiency and uniformity. *Biotechnology and Bioengineering*, **84**(2):205–213.

Williams, J. M., Adewunmi, A., Schek, R. M., Flanagan, C. L., Krebsbach, P. H., Feinberg, S. E., Hollister, S. J., and Das, S., 2005. Bone tissue engineering using polycaprolactone scaffolds fabricated via selective laser sintering,. *Biomaterials 26*, **26**(23):4817–4827.

Wintermantel, E., Mayer, J., Blum, J., Eckert, K. L., Lscher, P., and Mathey, M., 1996. Tissue engineering scaffolds using superstructures. *Biomaterials*, **17**(2):83–91.

Woesz, A., Rumpler, M., Stampfl, J., Varga, F., Fratzl-Zelman, N., Roschger, P., Klaushofer, K., and Fratzl, P., 2005. Towards bone replacement materials from calcium phosphates via rapid prototyping and ceramic gelcasting. *Materials Science and Engineering: C*, **25**(2):181–186.

Woodfield, T. B. F., Malda, J., de Wijn, J., Pters, F., Riesle, J., and van Blitterswijk, C. A., 2004. Design of porous scaffolds for cartilage tissue engineering using a three-dimensional fiber deposition technique. *Biomaterials*, **25**(18):4149–4161.

Xiong, Z., Yan, Y., Zhang, R., and Sun, L., 2001. Fabrication of porous poly(l-lactic acid) scaffolds for bone tissue engineering via precise extrusion. *Scripta Materialia*, **45**:773–779.

Yamada, S., Heymann, D., Bouler, J. M., and Daculsi, G., 1997. Osteoclastic resorption of calcium phosphate ceramics with different hydroxyapatite/β-tricalcium phosphate ratios. *Biomaterials*, **18**(15):1037–1041.

Yang, H., Acker, J., Chen, A., and McGann, L., 1998. In situ assessment of cell viability. *Cell Transplant.*, **7**(5):443–451.

Yang, J., Webb, A. R., and Ameer, G. A., 2004. Novel citric acid-based biodegradable elastomers for tissue engineering. *Adv Mater 16 (2004), pp. 511516*, **16**(6):511–516.

Yang, J., Webb, A. R., Pickerill, S. J., Hageman, G., and Ameer, G. A., 2006. Synthesis and evaluation of poly(diol citrate) biodegradable elastomers. *Biomaterials*, **27**(9):1889–1898.

Yang, S., Leong, K. F., Du, Z., and Chua, C. K., 2001. The design of scaffolds for use in tissue engineering. part i. traditional factors. *Tissue Engineering*, **7**(6):679–689.

Yaszemski, M. J., Payne, R. G., Hayes, W. C., Langer, R., and Mikos, A. G., 1996. Evolution of bone transplantation: molecular, cellular and tissue strategies to engineer human bone. *Biomaterials*, **17**(2):175–185.

Yeong, W. Y., Chua, C. K., Leong, K. F., and Chandrasekaran, M., 2004. Rapid prototyping in tissue engineering: challenges and potential. *Trends Biotechnol.*, **22**(12):643–652.

Yoon, J. J., Kim, J. H., and Park, T. G., 2003. Dexamethasone-releasing biodegradable polymer scaffolds fabricated by a gas-foaming/salt-leaching method. *Biomaterials*, **24**(13):2323–2329.

Yoshikawa, T., 2000. Bone reconstruction by cultured bone graft. *Materials Science and Engineering: C*, **13**(1-2):29–37.

Yuan, H., Yang, Z., de Bruijn, J. D., de Groot, K., and Zhang, X., 2001. Material-dependent bone induction by calcium phosphate ceramics: a 2.5-year study in dog. *Biomaterials*, **22**(19):2617–2623.

Zein, I., Hutmacher, D. W., Tan, K. C., and Teoh, S. H., 2002. Fused deposition modeling of novel scaffold architectures for tissue engineering applications. *Biomaterials*, **23**:1169–1185.

Appendix A

SEM micrographs of PDDC scaffolds

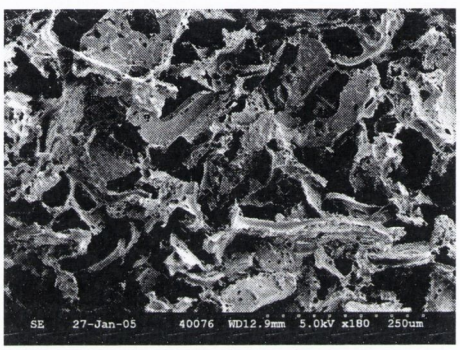

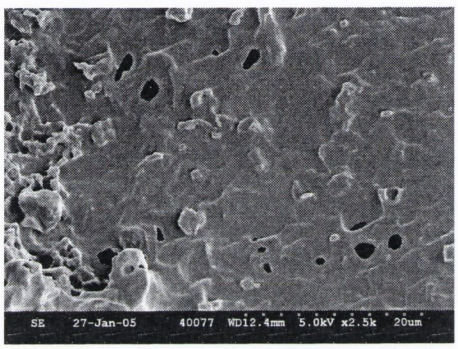

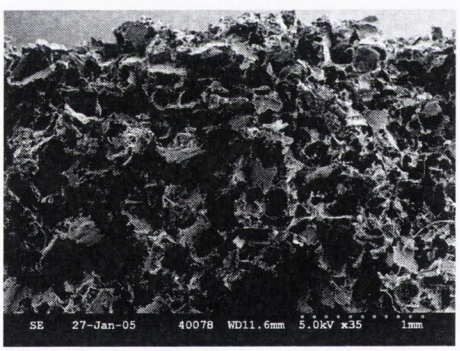

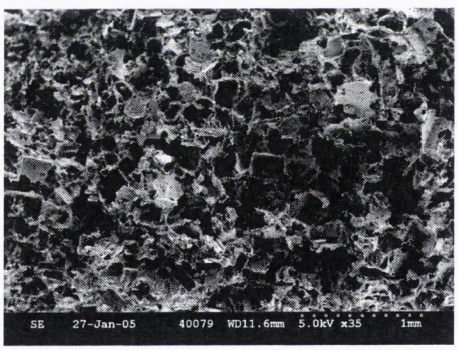

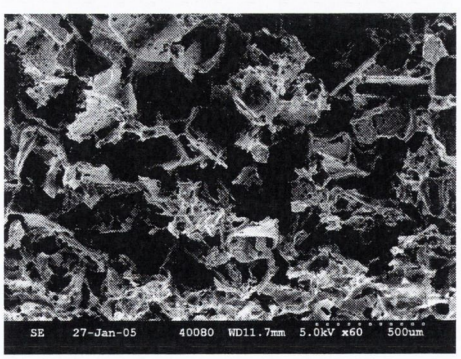

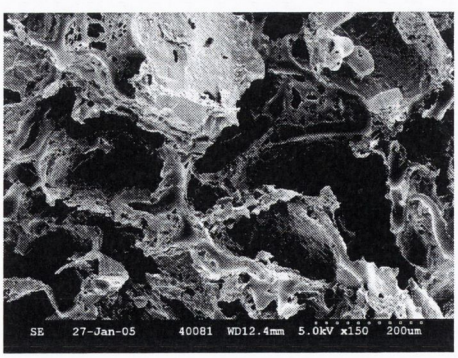

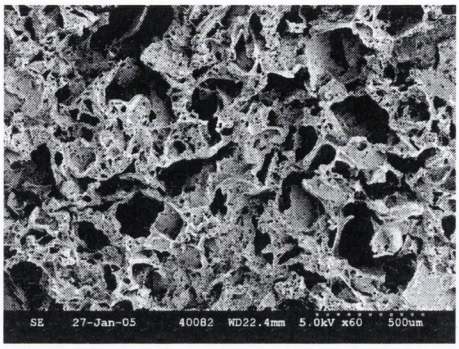
SE 27-Jan-05 40082 WD22.4mm 5.0kV x60 500um

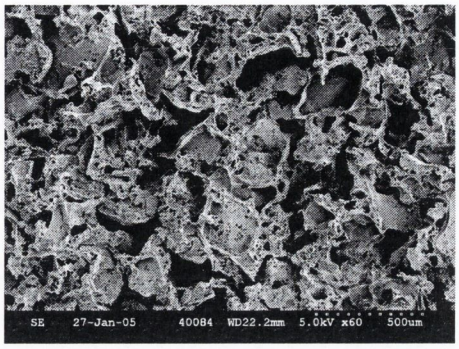
SE 27-Jan-05 40084 WD22.2mm 5.0kV x60 500um

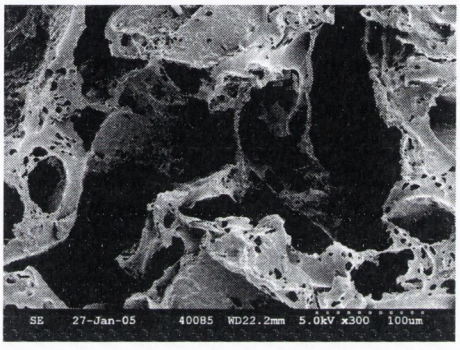
SE 27-Jan-05 40085 WD22.2mm 5.0kV x300 100um

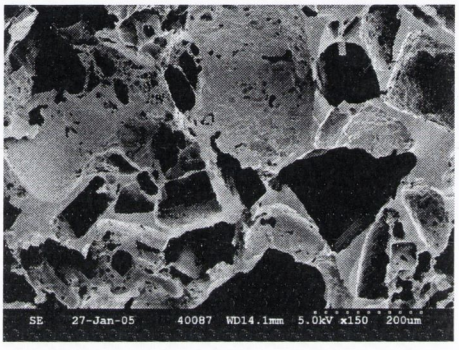
SE 27-Jan-05 40087 WD14.1mm 5.0kV x150 200um

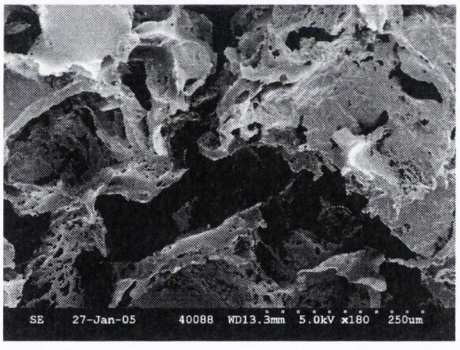
SE 27-Jan-05 40088 WD13.3mm 5.0kV x180 250um

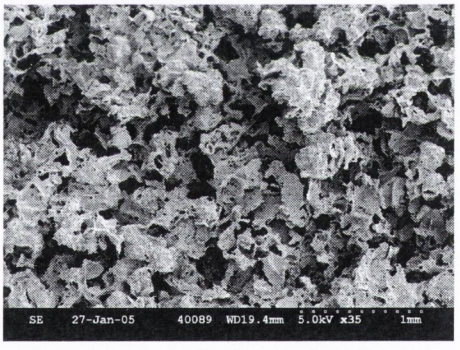
SE 27-Jan-05 40089 WD19.4mm 5.0kV x35 1mm

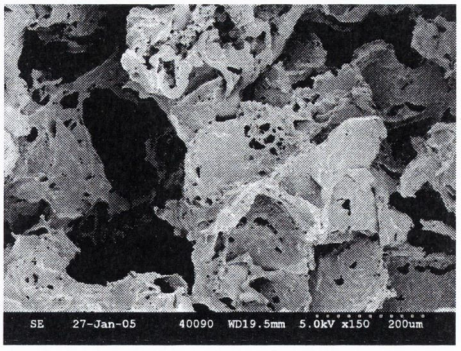
SE 27-Jan-05 40090 WD19.5mm 5.0kV x150 200um

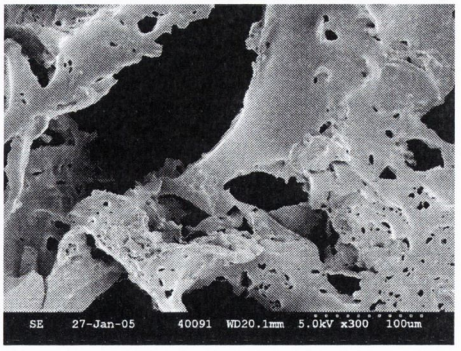
SE 27-Jan-05 40091 WD20.1mm 5.0kV x300 100um

Appendix B

Hydroxyapatite powder data

SPECIMEN: Hydroxyapatite Powder Batch P220 Sintered

RELEASE NUMBER: N/A

This specimen has been examined using X-ray diffraction methods according to SOP 046 and has the following properties...

COMPOSITION: Hydroxyapatite with a trace of calcium oxide phosphate *.

RELATIVE CRYSTALLINITY: 105% (as compared to Biotal standard powder).

d-spacings: see enclosed XRD trace.

d-spacing	two theta	d-spacing	two theta
4.070	21.84	2.810	31.84
3.881	22.92	2.780	32.20
3.502	25.44	2.717	32.96
3.444	25.87	2.631	34.08
3.168	28.17	2.528	35.52
3.079	29.00		
2.996	29.82 *	3.052	29.26 *
2.872	31.14 *	2.894	30.90 *

Name(Print)..P.J. Lowe

Signature..

Date...15/02/01

Checked inwards by:-S Morrey

Date:-19/2/01

STAFFORDSHIRE UNIVERSITY
SCHOOL of SCIENCES
DEPARTMENT of PHYSICS
COLLEGE ROAD
STOKE-on-TRENT
ST42DE

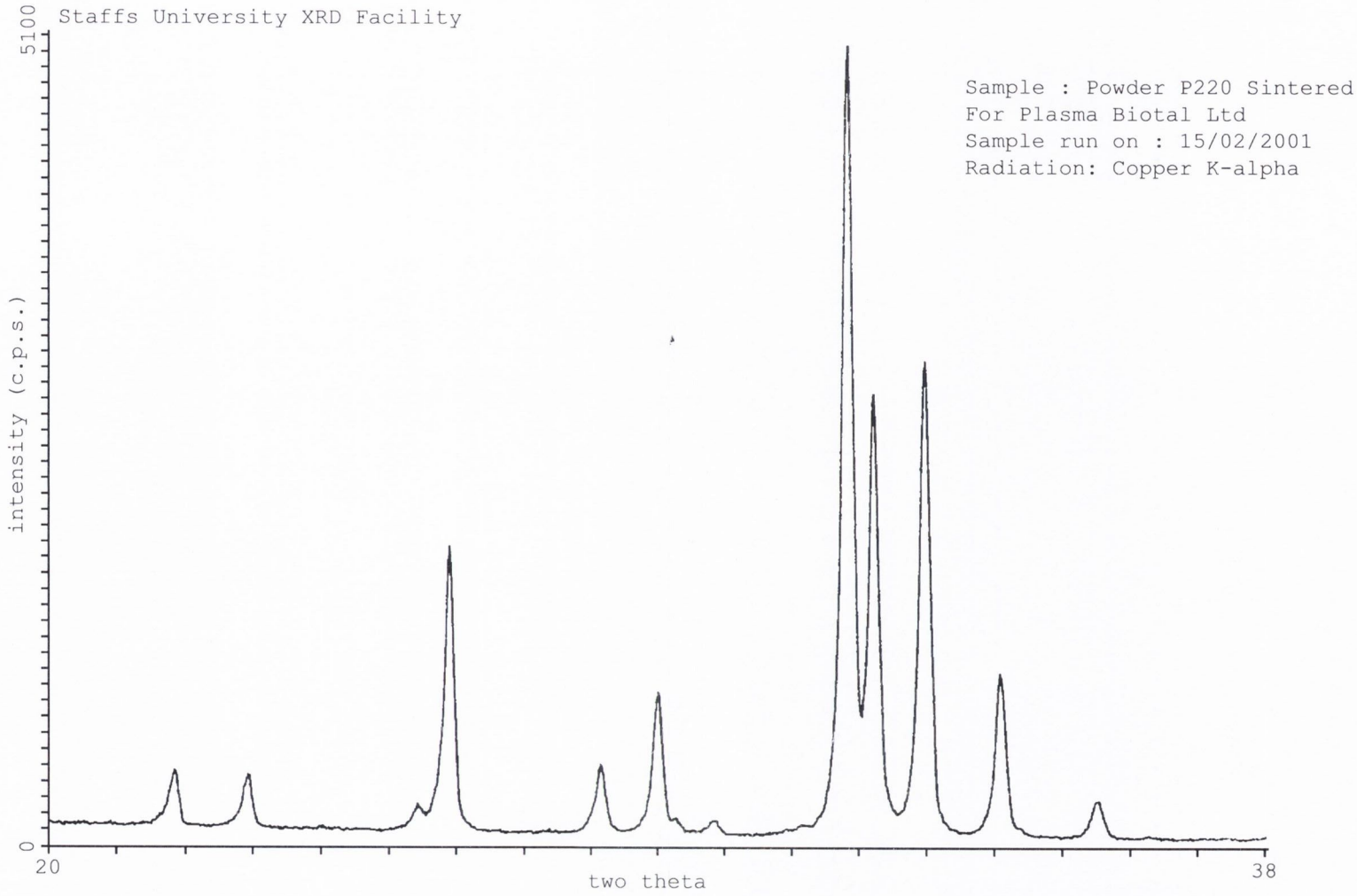
Staffs University XRD Facility
5100
0
intensity (c.p.s.)
20
38
two theta
Sample : Powder P220 Sintered
For Plasma Biotal Ltd
Sample run on : 15/02/2001
Radiation: Copper K-alpha

MALVERN Instruments M7.09 Mon 23 Jun 2003 Time 12:54 pm

P220S CAPTAL S

Size microns	% under	% in band	Size microns	% under	% in band
118	100	0.00	11.1	94.5	6.16
102	100	0.00	9.62	88.3	8.04
88.1	100	0.00	8.30	80.3	8.15
76.0	100	0.00	7.16	72.1	8.50
65.6	100	0.00	6.18	63.6	9.71
56.6	100	0.00	5.33	53.9	11.1
48.8	100	0.00	4.60	42.8	11.3
42.1	100	0.00	3.97	31.6	9.48
36.3	100	0.00	3.42	22.1	7.18
31.3	100	0.00	2.95	14.9	5.25
27.0	100	0.00	2.55	9.65	3.47
23.3	100	0.00	2.20	6.18	1.95
20.1	100	0.01	1.90	4.23	1.11
17.4	100	0.27	1.64	3.13	0.71
15.0	99.7	1.52	1.41	2.42	0.46
12.9	98.2	3.75	1.22	1.96	

Result source=Sample
Record No. = 0
Focal length = 63 mm.
Presentation =pil
Volume distribution
Beam length = 2.0 mm.
Obscuration =0.3663
Volume Conc. = 0.0312 %
Log. Diff. = 4.178
Model indp

D(v,0.5) = 5.05 µm
D(v,0.9) = 9.96 µm
D(v,0.1) = 2.58 µm
D(4,3) = 5.68 µm
D(3,2) = 4.11 µm
Span = 1.46
Spec. surf. area
1.4611 sq.m./cc.

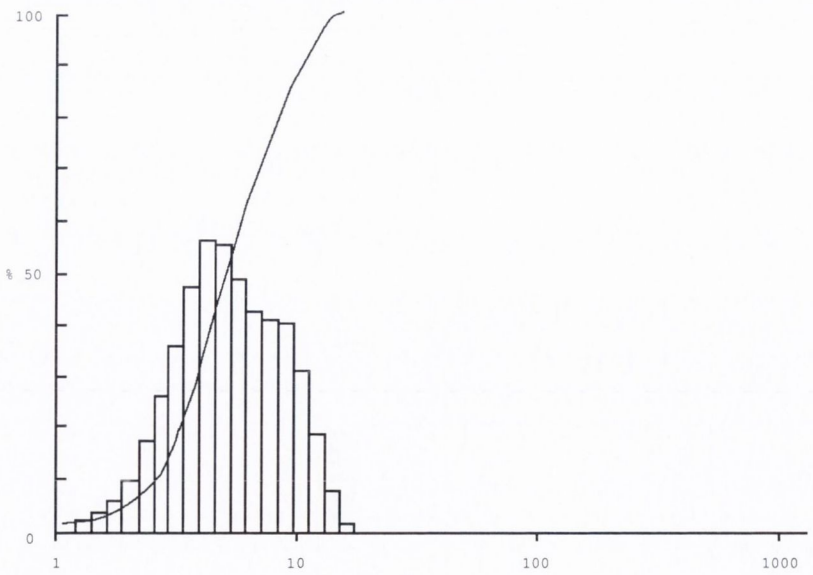

Appendix C

CNC machining G-code

Mill CAM Designer - ctb11.MCD)
(18/1/2006)
(Post fanucm:1.20 24 June 1994)
G21
[BILLET X100 Y90 Z6
[EDGEMOVE X0 Y0
[TOOLDEF T1 D1
G91G28X0Y0Z0
M6T1
G43H1
M3S3000
G90X2Y2
Z1
G91 G99 G81 X1 Z-8 K60 F100
X-1Y1
G91 G99 G81 X1 Z-8 K60 F100
X-1Y1
G91 G99 G81 X1 Z-8 K60 F100
X-1Y1
G91 G99 G81 X1 Z-8 K60 F100
X-1Y1

⋮ ⋮ ⋮

⋮ ⋮ ⋮

F100 X-1Y1 G91 G99 G81 X1 Z-8 K60 F100
X-1Y1
G91 G99 G81 X1 Z-8 K60 F100
X-1Y1
G91 G99 G81 X1 Z-8 K60 F100
X-1Y1
G80
m30
End Machine Cycle

Appendix D

Image analysis code

```
Macro 'Scaffold Image Analysis';

    var {Declared variables}
hinc, vinc, hcount, vcount, hlines, vlines, rnum, cnum: integer;
width, height, porewidth, poreheight, i, j, h, v: integer;
strSM:string;
porecolour, nPixels, mean, mode, min, max,
ScaffoldPorosity, MinPixel, scale1: real;
HorizontalMean,SigmaSquaredHorizontal, StandardDevHorizontal, SEMHorizontal:
real;
VerticalMean, SigmaSquaredVertical, StandardDevVertical, SEMVertical: real;



    {**********Mean Intercept Algorithm**********}

    {Clears Results array with zeros}
begin
SetCounter(2000);
SetUser1Label('HorPores');
SetUser2Label('VertPores');

    for i:=0 to 1999 do
begin
rUser1[i+1]:=0;
rUser2[i+1]:=0;
rMean[i+1]:=0;
end;

    AutoThreshold;
Smooth;
ReduceNoise;
MakeBinary;
GetPicSize(width,height);
```

```
width:=width;
height:=height-36;
{Accounts for scale bar area, to avoid inclusion in calculations}
MakeRoi(0, 0, width, height);

    strSM:=GetString('Scaffold pores shown as black or white (b/w)?');
SetCursor('watch');
if strSM='w'then
porecolour:=0
else
porecolour:=255;

    scale1:=GetNumber('Enter the scale as pixels/mm:', 1,0);
MinPixel:=GetNumber('Enter minimum pixel size to be detected:', 2,0);
h:= GetNumber('Enter the number of horizontal lines:', 10, 0);
v:= GetNumber('Enter the number of vertical lines:', 10, 0);
hlines:= h-2; vlines:= v-1;

    rnum:=0;
cnum:=0;
hinc:= trunc(height/h);
vinc:= trunc(width/v);
hcount:=1;
vcount:=1;

    for i:= 1 to hlines do
begin
porewidth:=0;
rnum:= rnum + hinc;
GetRow(0, rnum, width);

    for j:= 1 to width do
begin
if Linebuffer[j] = porecolour then
porewidth:= porewidth +1;
if (Linebuffer[j+1] <> Linebuffer[j]) AND (porewidth > MinPixel) then begin
rUser1[hcount]:=((porewidth/scale1)*1000)*1.5;
hcount:=hcount+1;
porewidth:=0;
end;
end;
j:= j +1;
end;

    for i:= 1 to vlines do
begin
poreheight:=0;
cnum:=cnum + vinc;
```

```
GetColumn(cnum, 0, height);

    for j:= 1 to height do
begin
if Linebuffer[j] = porecolour then
poreheight:= poreheight + 1;
if (LineBuffer[j+1] <> Linebuffer[j]) AND (poreheight > MinPixel) then begin
rUser2[vcount]:=((poreheight/scale1)*1000)*1.5;
vcount:=vcount + 1;
poreheight:=0;
end;
end;
j:= j+1;
end;

    ShowResults;




    {**********Porosity Calculation**********}

    Measure; GetResults(nPixels, mean, mode, min, max);
ScaffoldPorosity:=100*((histogram[porecolour])/(histogram[0] + histogram[255]));




    {**********Statistical Analysis**********}

    hcount:=hcount-1;
vcount:=vcount-1;

    rMean[hcount]:=0;
for i:=1 to hcount do begin
rMean[hcount]:=rMean[hcount] + rUser1[i];
end;

    for i:=1 to vcount do begin
rMean[vcount]:=rMean[vcount] + rUser2[i];
end;

    HorizontalMean:=rMean[hcount]/hcount;
VerticalMean:=rMean[vcount]/vcount;

    {Horizontal Variance Array}
rStdDev[hcount]:=0;
```

```
for i:=1 to hcount do begin
rStdDev[i]:=Sqr(rUser1[i]- HorizontalMean);
end;

    {Sum of Horizontal Variance Array}
rMean[hcount]:=0;
for i:=1 to hcount do begin
rMean[hcount]:=rMean[hcount] + rStdDev[i];
end;

    SigmaSquaredHorizontal:=rMean[hcount]/hcount;
StandardDevHorizontal:=sqrt(SigmaSquaredHorizontal);
SEMHorizontal:= StandardDevHorizontal/sqrt(hcount);

    {Vertical Variance Array}
rStdDev[vcount]:=0;
for i:=1 to vcount do begin
rStdDev[i]:=Sqr(rUser2[i]- VerticalMean);
end;

    {Sum of Vertical Variance Array}
rMean[vcount]:=0;
for i:=1 to vcount do begin
rMean[vcount]:=rMean[vcount] + rStdDev[i];
end;

    SigmaSquaredVertical:=rMean[vcount]/vcount;
StandardDevVertical:=sqrt(SigmaSquaredVertical);
SEMVertical:= StandardDevVertical/sqrt(vcount);




    {**********************Output Results******************}
    NewTextWindow('Scaffold Analysis Results');
Writeln('Mean Horizontal Length','','SEM','','STDEV','','n number','','Mean Vertical Length','','SEM','','STDEV','','n number','','Scaffold Porosity':6:2);
Writeln('(microns)','', '(microns)','','(%)':6:2);
Writeln('');
Writeln(HorizontalMean,'',SEMHorizontal,'',StandardDevHorizontal,'',hcount,
'',VerticalMean,'',SEMVertical,'',StandardDevVertical,'',vcount,'',ScaffoldPorosity);
Writeln('');
Writeln('Pore colour was set to: ', strSM);
Writeln('Scale set to: ', scale1, 'pixels/mm');
Writeln('Minimum pixel length used for measurements: ', MinPixel);
Writeln('Minimum pore size to be detected:, ((MinPixel*1000)/scale1),'microns');
Writeln('Horizontal lines set to: ', h);
Writeln('Vertical lines set to: ', v);
```

```
Writeln('Number of horizontal intercepts: ', hcount);
Writeln('Number of vertical intercepts: ',vcount);
Writeln('');
Writeln('The image width is', width, 'pixels');
Writeln('The image height is', height, 'pixels');
   SetCursor('arrow');

   {To Export Results files}
begin
SetExport('Measurements');
SetOption; Export('filename');
end;

   {**********************End Output Results*******************}

   end; {Macro End}
```

Appendix E

Threshold images of HA scaffolds

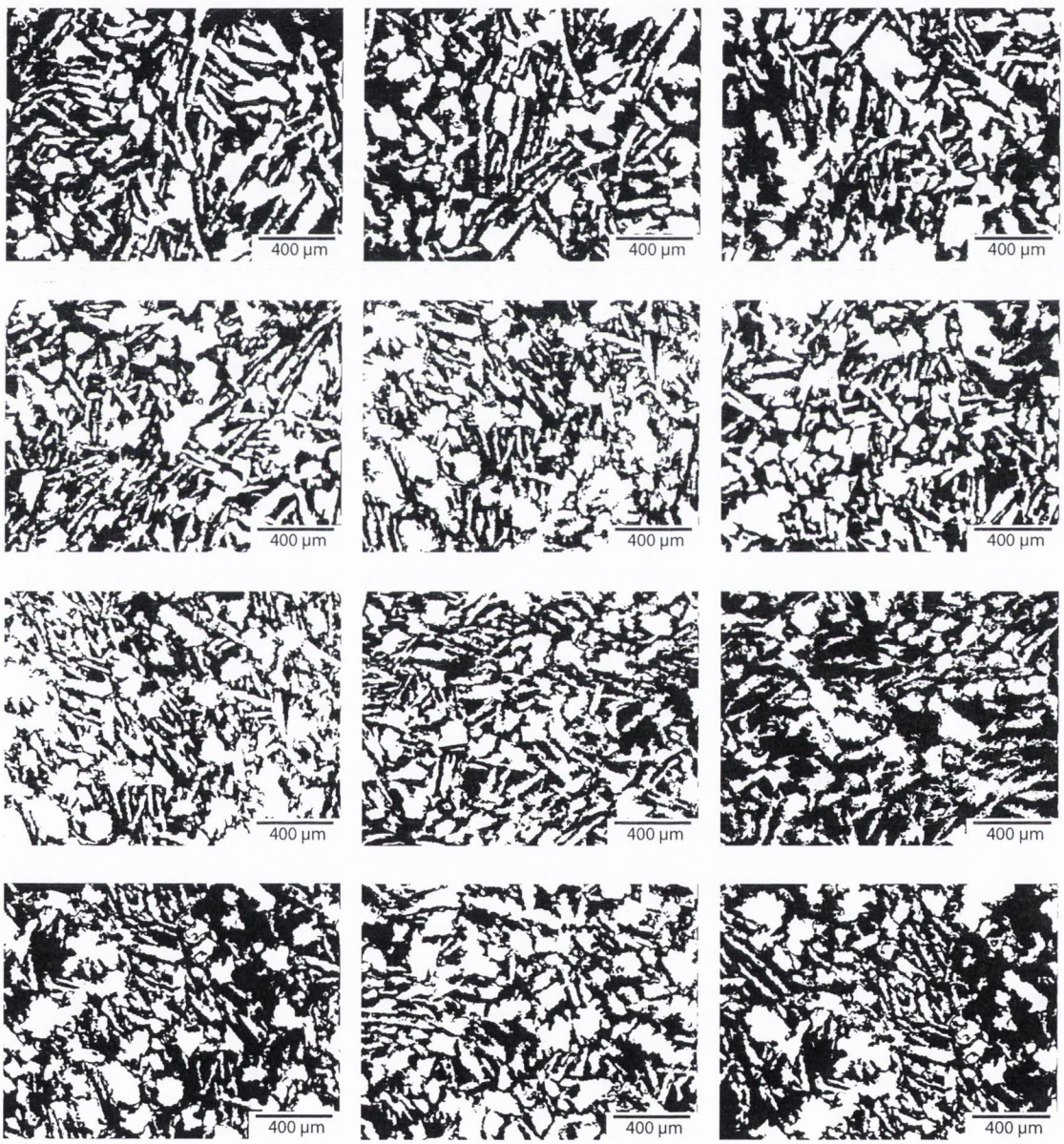

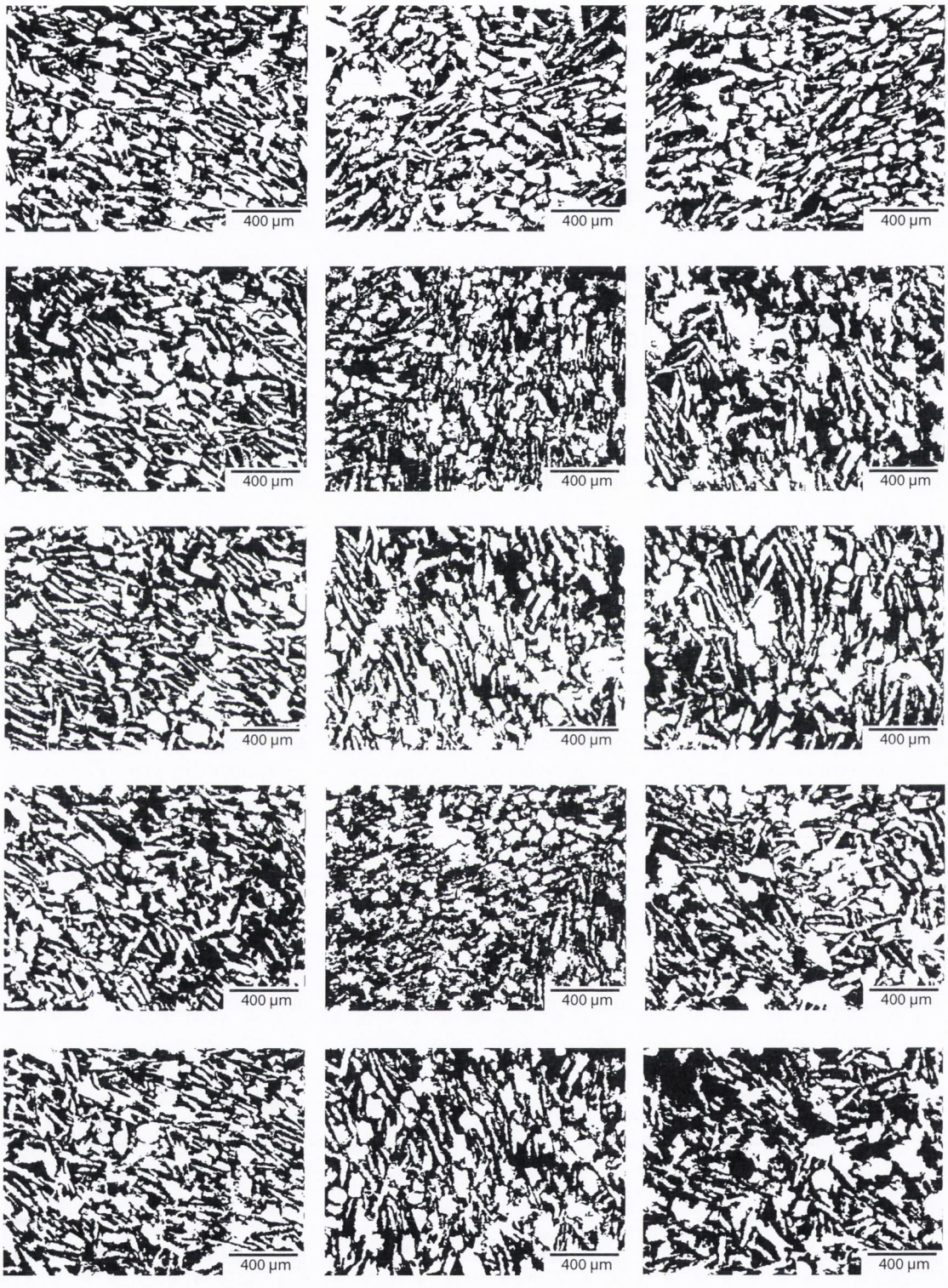
400 µm
400 µm
400 µm
400 µm
400 µm
400 µm
400 µm
400 µm
400 µm
400 µm
400 µm
400 µm
400 µm
400 µm
400 µm

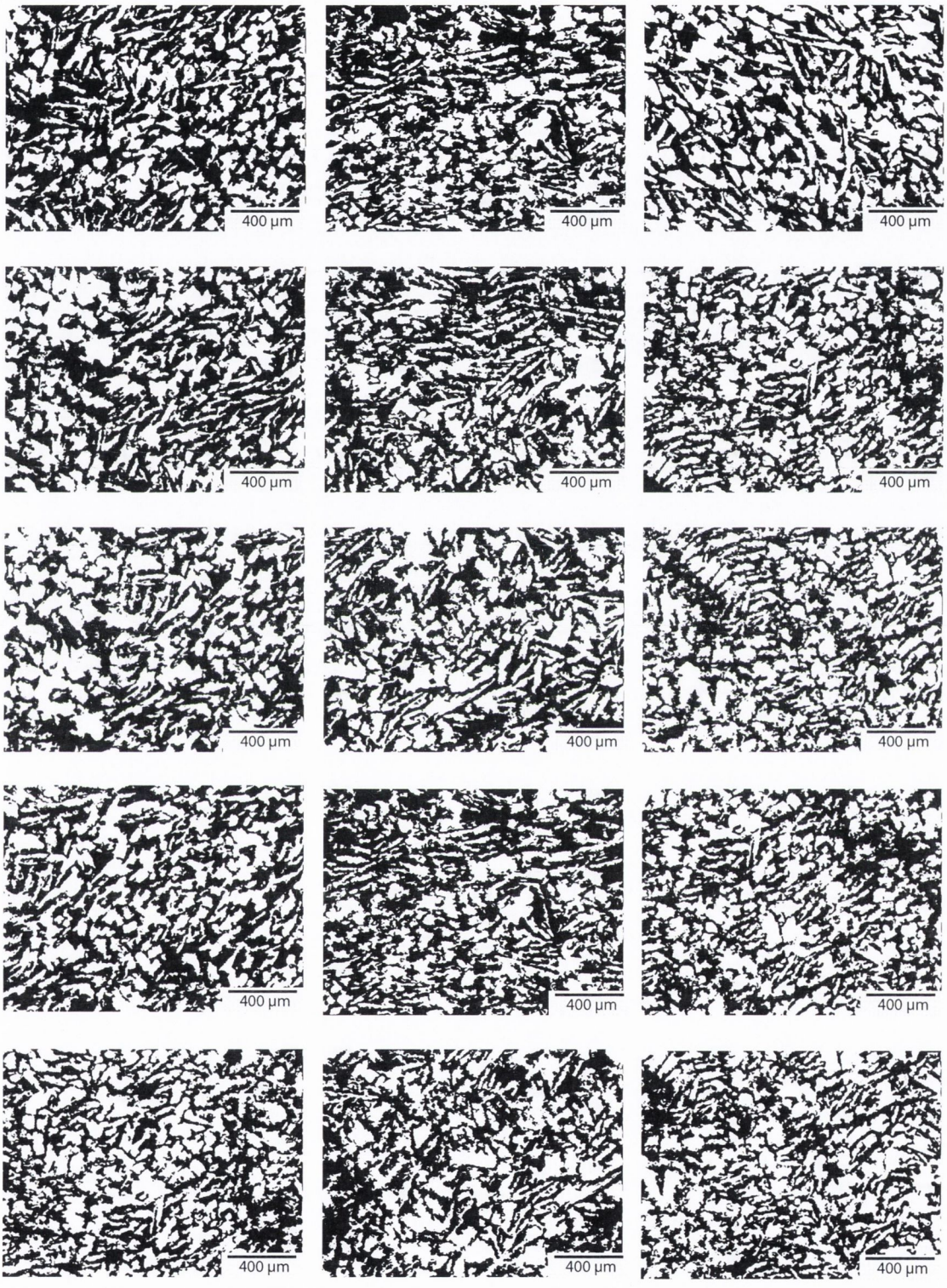
400 µm
400 µm
400 µm
400 µm
400 µm
400 µm
400 µm
400 µm
400 µm
400 µm
400 µm
400 µm
400 µm
400 µm
400 µm

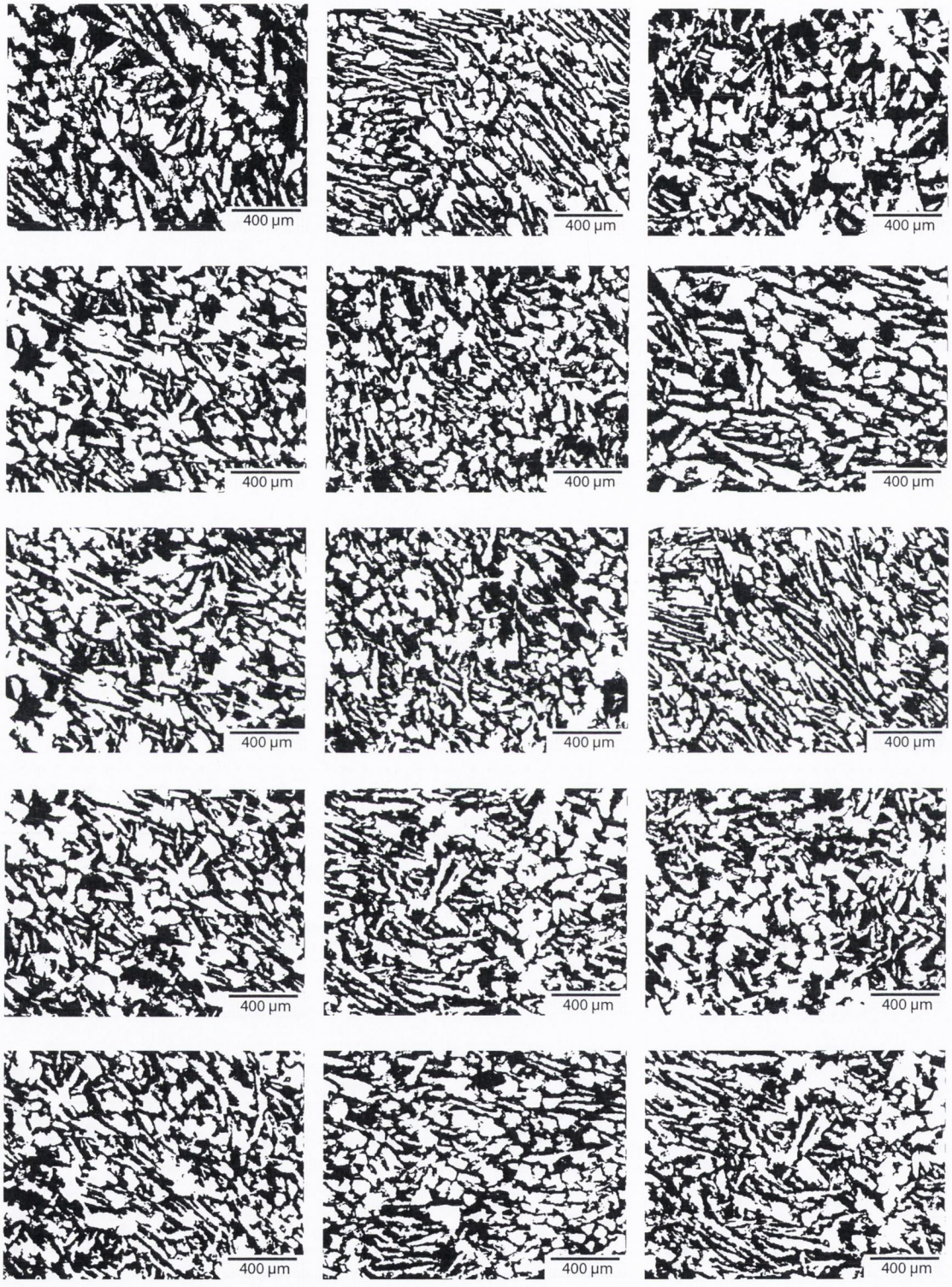
400 µm